

Investigating Exciton Correlations Using Coherent Multidimensional Optical Spectroscopy

by

Daniel Burton Turner

B.A. Chemistry and B.A. Mathematics
Concordia College, 2004

Submitted to the Department of Chemistry
in partial fulfillment of the requirements for the degree of

DOCTOR OF PHILOSOPHY

at the

MASSACHUSETTS INSTITUTE OF TECHNOLOGY

June 2010

© Massachusetts Institute of Technology 2010. All rights reserved.

Author
Department of Chemistry
May 6, 2010

Certified by.....
Keith A. Nelson
Professor of Chemistry
Thesis Supervisor

Accepted by.....
Robert W. Field
Chairman, Department Committee on Graduate Students

This doctoral thesis has been examined by a committee of the Department of Chemistry as follows:

Professor Mounji G. Bawendi

Chairperson

Professor Keith A. Nelson

Thesis Supervisor

Professor Robert W. Field

Investigating Exciton Correlations Using Coherent Multidimensional Optical Spectroscopy

by

Daniel Burton Turner

Submitted to the Department of Chemistry
on May 6, 2010, in partial fulfillment of the
requirements for the degree of
DOCTOR OF PHILOSOPHY

Abstract

The optical measurements described in this thesis reveal interactions among bound electron-hole pairs known as excitons in a semiconductor nanostructure. Excitons are quasiparticles that can form when light is absorbed by a semiconductor. Exciton interactions gained prominence in the 1980s when unexpected signals were observed in studies of carrier dynamics. The presence of exciton interactions in semiconductors motivated an ongoing, focused research effort not only because the materials had valuable commercial applications but also because the interactions could be used to test fundamental theories of many-body physics.

Laser light provides a coherent electric field with a well defined phase. In linear spectroscopy, an electric field that is resonant with an exciton transition will induce coherent oscillations of electronic charge density. The charges will oscillate at the transition frequency with a well defined phase, and these oscillations will radiate a signal that has an amplitude proportional to the incident field amplitude and has the same direction as the incident light. If the laser light is intense, its field may induce a high density of excitons, and the field can interact with those excitons to induce transitions to higher-energy states composed of multiple interacting excitons. Many-body interactions among the excitons can predictably modify—or unpredictably scramble—the quantum phase of the exciton. The interactions can produce signals that have amplitudes proportional to high powers of the incident field amplitude, and the signal fields often propagate in directions different than the incident field. The signal fields contain information—often encoded in their phases—that can reveal the nature of the higher-energy states and the many-body interactions that produced them. Thus, many-body interaction studies rely on measurements of exciton phases that are reflected in the optical phases of coherent signals. These measurements require a tool that can detect optical coherence before the exciton phases are scrambled by the environment. Coherent ultrafast optical spectroscopy is that tool.

The spectra displayed in this work were measured by an experimental apparatus that separates the electric fields as needed into different laser beams with controllable directions; it controls the optical phase, arrival time, and polarization of the femtosecond light pulse(s) in each of those beams; it then recombines all of the beams at the

sample to generate the signal field; and finally it measures the signal field, including its phase. Using this instrument, we isolated—with a high degree of selectivity—signals that arose from different numbers of field interactions and from different microscopic origins using various beam geometries and pulse timing sequences.

In this thesis, we present electronic spectra measured at varying orders in the electric field to isolate and measure the properties of excitons and their many-body interactions. As the number of electric fields is increased and the resulting higher-order signals are generated, interactions involving increasing numbers of particles can be measured. The vast majority of previous work focused on the interactions manifest in third-order signals. This thesis not only includes new insights gained from third-order signals, but also includes new phenomena observed in fifth-order and seventh-order signals. We measure signals due to four-particle correlations in the form of bound biexcitons and unbound-but-correlated exciton pairs. We also measure signals due to six-particle correlations in the form of bound triexcitons. Although we searched for them, there were no signals due to eight-particle correlations, indicating that the set of multiexciton states truncates. We thus measured the properties and the extent of many-body interactions in this system.

The spectra presented here reveal a large set of excitonic many-body interactions in GaAs quantum wells and answer questions about the many-body interactions posed decades ago. The optical apparatus constructed to perform these measurements will soon be used to measure correlations in a range of systems, including other semiconductors and their nanostructures, molecular aggregates, molecules, and photosynthetic complexes. Because future technologies such as entangled photon sources, advanced photovoltaics, and quantum information processing will rely on these types of materials and their many-body correlations, it is important to develop techniques to measure their microscopic interactions directly.

Thesis Supervisor: Keith A. Nelson
Title: Professor of Chemistry

Acknowledgments

It is with great pleasure that I reflect on the last five years and attempt to express my sincere gratitude to all of the people who have made the work and struggles not only possible, but also enjoyable. Keith Nelson has been a fantastic research advisor. His support and encouragement have been unwavering, and his enthusiasm for science is contagious. His kind and generous disposition—and his oft-repeated phrase, ‘come on in’—make him one of those people with whom it is truly a pleasure to work.

The skilled members of the Nelson group have been remarkable colleagues and friends, especially the FWM team. Kathy Stone has been a great teacher, coworker, and confidante. Her mentorship and patient guidance have made me a more careful scientist. I fondly recall the times we spent learning about lasers, pulse shaping, and spectroscopy together. Kenan Gundogdu—with his infectious enthusiasm and kindness—taught me much about spectroscopy, semiconductors, and life. Patrick Wen, a rising member of the FWM team, is a fantastic scientist, and he contributed a great deal to the calculations presented here. Dylan Arias, too, has really taken to the FWM lab. His knack for making experiments work is truly impressive. Kathy, Kenan, Patrick, and Dylan all helped keep the lasers lasing, the helium flowing, and the data acquisition computers running, and they had great ideas about how to improve manuscripts. Eric Statz and Darius Torchinsky were two other brilliant and patient senior graduate students who spent a lot of time teaching me about optics and lasers. Ka-Lo Yeh was a special coworker who was always available to lend an ear, and although Brad Perkins has only been with the group a short time, he has given me a lot of good advice. Christoph Klieber has been in the group through thick and thin, and I am grateful for his friendship. It has been a pleasure to work with the other past and present members of the Nelson group, Andrei Tokmakoff, and many members of his group as well. Special thanks go to Gloria Pless and Li Miao for their administrative contributions. Josh Lessing, Kevin Jones, Lisa Marshall, and Galia Debelouchina were wonderful classmates and fellow TAs the first year. Josh’s tales—tall or not, no one knows—were always fascinating.

During this five-year journey, I was able to explore strange new places and seek out new civilizations. In Stresa I made many new friends, including Catherine Kealhofer and Naomi Ginsberg. I will never forget the incredible adventure my fellow travelers and I had in the Prosper-Haniel coal mine as part of the YCC exchange to Essen, Germany. Our hosts—especially Caroline Bishof—were gracious and welcoming. Thanks to Maaïke Milder and Alexandra Nemeth for housing me on other travels, Prof. Thomas Feurer for hosting me in Bern, and Cindy Bolme for the hiking trip in Los Alamos.

Emily and I have enjoyed living with, mentoring, and of course feeding the students of H-entry in MacGregor House for the past three years. The occasional stressful situation paled in comparison to the overflowing humor, entertainment and friendship that this collection of forty-eight MIT undergraduates provided. Thanks go to Jessica Nesvold, Josh Ramos, and Ashaki Jacquet for volunteering for the thankless task of entry chair; Aaron Thom and Peter Lu have been sources of inspiration in the gym. Arkajit Dey, you will do great things. Milena Andzelm deserves recognition for

keeping our plants alive while we were traveling. Many students have come and stayed, while others have come and gone, but all helped make the entry and MacGregor House a supportive and pleasant community.

Our friends and fellow musicians at Park Street Church have been wonderful. My fellow choir members—Bryan Bilyeu (MIT alum!), Heidi Bone, Mike Brescia (MIT alum!), Prof. Tom Brooks, Roy and Norma Brunner, Philip and Mandy Bush, Dan and Rebecca Draper, Andrew and Sarah Frey, Heather Gregg, Dr. Pavel Hejzlar (former MIT!), Liana Hill, Jonathan Hornbeck, Sarah Johnson, Dr. Barry (current MIT!) and Julianne Johnston, Tekhyung Lee (current MIT!), Phil Mell, Jeffrey Miller, Ruben Muresan, Dan and Jenn Schmunk, and Ted and Lorien Urban—deserve thanks for making the choir a welcoming place that has allowed me to continue in the tradition of The Concordia Choir, whose mission it is “. . . to uphold the sacred choral tradition through the uncompromising and unrelenting collaborative pursuit of musical integrity and spiritual expression”.

There are many authors, of fiction and otherwise—Wendell Berry, Philip Corbett, Charles Dickens, C. S. Lewis, Donald Miller, John Piper, Michael Pollan, Ayn Rand, Michael Schut, Henry David Thoreau, and Wil Wheaton—who have inspired me in one way or another. Reading the carefully constructed words, wisdoms, and witticisms of others is one of life’s greatest pleasures.

Others have provided timely encouragement and friendship for which I am grateful. Arlyn DeBruyckere, Amrita Bijoor, John Buncher, Mike Carls, Dr. René Clausen, the Colvin family, Prof. Steven Cundiff, Mary Froemming, Matt and Sarah Gunderson, Prof. Mark Jensen, Rev. Dan and Cheryl Moose, Dan Scheer, Dexter Sederquist, Megan Wilson, Prof. Martin Zanni, sporcle.com, and so many more have impacted my life in important ways. Prof. Darin Ulness is responsible for showing me the path of scientific research, and his guidance and support are truly appreciated.

My family is full of remarkable people. I want to thank my parents, Dan and Linda Turner, for letting me move ‘clear across the country’. They are also the hardest working people I know; my life of ease is a direct result of their hard work. Thankfully, they are finally starting to take life at a more leisurely pace. My brothers—Ramsey, Joe, James, and Tim—and my sisters-in-law Jenny and Carla, are sources of encouragement, support, and constant entertainment. My grandparents, Dorothy Turner and Dale and Dorothy Holen, have also been extremely supportive. Mike and Nan Crary have been the best parents-in-law imaginable, and their support for our adventures has been important. Thanks to the rest of the Crary family—Nathan, Jessica, Betha, and ‘my friend Paul’—for letting me steal Emily away to Boston.

Finally, my wife Emily has been an unwavering source of loving support. Thank you for cheerfully embarking on this journey with me. Our travels to New Hampshire, Toronto, and Las Vegas were special. Together, we have somehow maintained the best of our bucolic roots (sometimes literally, with the garden in our bedroom windows) while still enjoying life in a bustling city. As we approach our fifth wedding anniversary—and our tenth year together—your beauty, intelligence, artistic talents, perseverance, and steadfast calmness continue to amaze me. Let’s go for a walk.

Contents

1	Introduction	11
1.1	Many-body phenomena	11
1.2	Coherent fields and signals	12
1.3	Excitons: quantum objects	14
1.4	Coherent exciton dynamics	17
1.5	Exciton many-body interactions	18
1.6	Two-dimensional optical spectroscopy	23
1.7	Outline of this thesis	25
2	Nonlinear optical spectroscopy	27
2.1	Nonlinear polarization	29
2.1.1	Macroscopic description	30
2.1.2	Microscopic origins	33
2.2	Sum-over-states model	36
2.3	Bloch equations	40
2.4	Nonlinear exciton equations	45
2.5	Material properties of GaAs	50
2.6	Summary	54
3	Experimental Methods	55
3.1	Shaping femtosecond pulses	55
3.2	COLBERT construction	57
3.3	Extended-cavity oscillator	61
3.4	COLBERT alignment	63
3.5	Two-dimensional Fourier beam shaping	63
3.6	Diffraction-based spatiotemporal pulse shaping	67
3.7	Pulse shaper resolution	71
3.8	Rotating frame detection	72
3.9	Calibrating COLBERT	74

3.9.1	Greyscale to phase shift calibration	74
3.9.2	Wavelength to pixel calibration	76
3.9.3	Aberration-induced temporal modulation correction	76
3.9.4	Carrier frequency calibration	78
3.9.5	Delay-dependent amplitude modulation correction	78
3.9.6	Global phase calibration	79
3.10	Spectral interferometry	80
3.11	Phase cycling procedures	84
3.12	Operation COLBERT: Performing a measurement	86
3.13	Limitations of the COLBERT spectrometer	89
3.14	Summary	90
4	Two-particle correlations: excitons	91
4.1	Exciton resonance energies and strengths	91
4.2	Exciton lifetimes	94
4.3	Cross peaks between excitons	96
4.4	Exciton correlation spectra	99
4.5	Exciton quantum beats in a 3D spectrum	106
4.6	Hints of higher-order correlations	109
5	Four-particle correlations	111
5.1	Third-order two-quantum coherences	111
5.2	Fifth-order two-quantum rephasing spectra	119
5.3	Fifth-order two-quantum rephasing of mixed biexcitons	125
5.4	Simulated fifth-order two-quantum correlation spectra	125
5.5	Hints of even higher-order correlations	126
6	Six-particle correlations	129
7	Eight-particle correlations	135
8	Conclusions	137
8.1	Summary	137
8.2	Outlook	139
A	Analysis of cascade contamination	143
B	Spectrum from the nonlinear exciton equations	145

Chapter 1

Introduction

I perceive the universe as a single equation, and it is so simple.

— The fictional character Lt. Reginald Barclay in the television series *Star Trek: The Next Generation* episode “The Nth Degree”.

1.1 Many-body phenomena

The world in which we live is remarkably complex. Oftentimes, complexity results when groups of objects interact through simple rules. For instance, a snowflake is a collection of water molecules; each intermolecular interaction is a ‘simple’ hydrogen bond, but the aggregate is beautiful¹. Moreover, small changes to the initial conditions or to the simple rules can cause strikingly different collective properties to emerge. Carbon is one example. By changing the conditions under which carbon atoms aggregate, materials with distinct properties can result: graphite, diamond, and fullerenes. Other examples of complex many-body phenomena in physics include planetary motion and Efimov trimers [1], and two examples from life science are animal aggregation [2–4] and biological networking [5, 6]. Although the underlying physical laws need not be simple, there are many systems for which the sum seems to be greater than the parts.

But complexity—often in the form of coordinated motion—is a problem for the physicist who desires a predictive scientific theory. Isaac Newton was among the first to consider such problems in his *Principia* in the late 1600s. When attempting to describe the trajectory of a collection of celestial bodies ($N \geq 3$) mathematically,

¹Some argue that what we perceive as complexity is merely the result of a change in scope: Individual water molecules seem inconsequential when appreciating the complexities of a snowflake, but individual snowflakes seem inconsequential when viewing a snowdrift.

he discovered that although the individual trajectory of each planet or star could be written in differential form using his laws of motion, the coupled, transcendental nature of the *set* of equations made finding an algebraic solution difficult, and usually impossible. Solutions that could be found required approximations or numerical integration techniques, and often the solution depended highly on the initial location and initial velocity of each body.

Atomic physics, a field more closely related to the work of this thesis, provides another classic example that illustrates how it is often difficult to predict coordinated motion, even when the number of interacting particles is small. Although exact algebraic expressions for hydrogen atom wavefunctions can be found, the electron-electron repulsion term in the helium atom Hamiltonian prevents analytic solutions to the Schrödinger equation. Approximations result in solutions, and the solutions can then be compared to experiments.

This thesis describes experiments designed to measure the properties of collective states that can result from interactions among excitons in a semiconductor nanostructure. Just as water molecules can aggregate to form snowflakes—or as hydrogen atoms can bind to form hydrogen molecules—excitons can aggregate to form more complex objects such as biexcitons. Our experiments on GaAs quantum wells show that excitons can interact in pairs to form either bound biexcitons or unbound two-exciton complexes, that excitons can interact in triples to form bound triexcitons, and that excitons cannot interact to a significant extent in quadruples. Each of these many-body interactions is investigated in detail using coherent ultrafast spectroscopy techniques. In this chapter, we describe the coherent spectroscopy of excitons qualitatively. The quantitative treatment follows in the remainder of the thesis.

1.2 Coherent fields and signals

We use ultrafast spectroscopy to observe exciton interactions by measuring how the material responds to optical excitation in the form of femtosecond (10^{-15} second) optical pulses. Similar to how high-speed cameras [7] and stroboscopes [8, 9] take microsecond photographic ‘snapshots’ of ballistic projectile impacts, our device takes femtosecond *spectroscopic* ‘snapshots’ of transient material dynamics. The two measurements are thematic analogs only. In high-speed photography, the light reflects off the projectile but does not perturb it significantly, whereas in nonlinear spectroscopy the laser pulses interact with the sample. The electric fields provided by the pulses interact with the electronic charge density in the sample to first induce and then measure a material response.

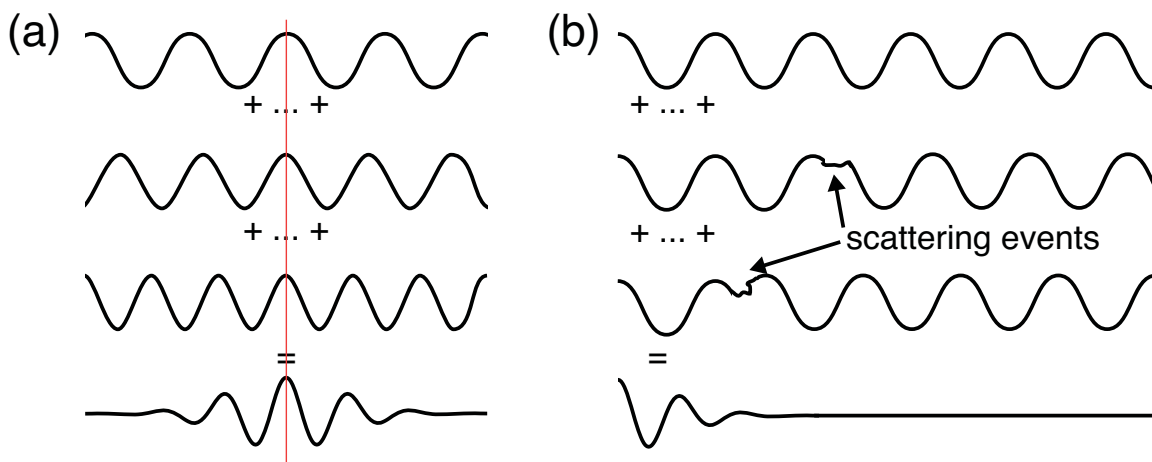


Figure 1-1: Wave interference. (a) Coherent waves of different frequencies are in-phase at one point in time (red line). Constructive interference occurs at that point; at other times, destructive interference diminishes the field. (b) Scattering events cause arbitrary phase shifts and diminish the field.

Light waves are oscillating electromagnetic fields, and each spectrum displayed in this thesis is the result of subtle changes in the electric component of those field oscillations due to light-matter interactions. Many-body interactions can manifest themselves in all wave parameters, including frequency, polarization, and amplitude, but are especially evident in the phase of the wave. The phase of an oscillating wave is that fraction of a full period which offsets the wave from its specified value at some point, usually $t = 0$ [10]. Having a wave with a well defined phase shift—and almost always that phase shift should be zero—is critical in time domain measurements. If the phase fluctuates, information about the function is lost.

In physics, the adjective *coherent* means that the phase of a wave is well defined. It can also mean that the phases of two or more waves are related in some unchanging or controlled fashion. This term is most often used to describe the temporal nature of a femtosecond pulse, but it can also describe other properties of the femtosecond pulse such as spatial mode or polarization. If two laser beams form a stable interference pattern when overlapped, they have a constant phase relationship and are thus deemed coherent.

Coherence is especially important in ultrafast spectroscopy because the femtosecond pulse itself requires many ($\sim 10^6$) frequencies that have a stable phase relationship [11]. The relationship is such that each frequency has its maximum value at one point in time², for example $t = 0$, as illustrated in Fig. 1-1(a). At this point, the field is

²This is not to say that ultrafast measurements *must* be performed with femtosecond pulses. Quasi-cw ‘noisy’ light spectroscopy [12–15] uses essentially incoherent nanosecond pulses but achieves

enhanced because all of the frequencies constructively interfere, but at values away from this point, destructive interference diminishes the field. Although the field is diminished, the frequencies are still coherent because the phase relationship is maintained. Given a long enough time—the repetition rate of the laser—the frequencies will once again constructively interfere and create another pulse³. This is one example of a broader principle: coherent fields of different frequencies can destructively interfere to decrease a signal. This effect appears in later chapters as inhomogeneous broadening.

On the other hand, random dynamic interactions—scattering events—between a wave and its environment introduce phase fluctuations that destroy the coherent relationship, as illustrated in Fig. 1-1(b). It is not feasible to describe each scattering event mathematically because we do not have complete information about all of the time-dependent forces acting on the waves. Instead, we use a statistical description of the scattering events in the form of a *dephasing time*. This is the characteristic timescale describing the average duration of the coherence. Most of the signals in this thesis were measured in the coherent regime as scattering events were in the process of destroying the signal coherence to measure the duration of the many-body interactions.

In our experiments, we excite the many-body interactions coherently using a series of laser pulses and then ‘watch’, using other laser pulses, how quickly the excitations lose their phase relationship. Most of the many-body interactions dephase within a few picoseconds (10^{-12} seconds).

1.3 Excitons: quantum objects

In atoms, the electrons exist in localized atomic orbitals having discrete energy levels⁴. In the tight-binding approach to conceptualizing a solid material such as a covalently bonded semiconductor⁵, the atoms are arranged in a three-dimensional spatially periodic fashion and the outermost (valence) atomic orbitals overlap slightly [17]. The electrons in the overlapping atomic orbitals are effectively shared throughout the lattice in interatomic bonds where most of the electron density is found between adjacent atomic nuclei [18–24]. In this manner, the overlapping atomic orbitals can be recast as valence bands. In the free-electron approach, the Schrödinger equation can be solved

femtosecond resolution using noise correlations. This has been called ‘the ultimate poor man’s femtosecond spectroscopy’, see Ch. 10 App. B in Ref. [16].

³More accurately, the time period between pulses is the inverse of the repetition rate.

⁴An electron in a valence orbital of a Ga atom fills a volume of $\sim 10^{-3}$ nm³.

⁵Although GaAs is a canonical example of a covalently bonded material, it is slightly ionic.

using solutions based on Bloch waves with a phase that depends on the electron wave vector [25]. In either approach, electron energies are no longer related to the quantum numbers of the atomic orbitals but are instead related to the electron wave vector, \mathbf{k} , through the dispersion relation of the material, $E(\mathbf{k})$. Fitting a dispersion curve near the Γ -point ($\mathbf{k} = 0$) results in a parabola with a characteristic curvature; this is interpreted in terms of an effective mass. Effective mass is intimately connected to spatial delocalization.

When a photon with enough energy is incident on the solid, it can excite an electron from the valence band into the conduction band. This excitation changes the spatial distribution of the electron. Both valence band and conduction band electrons have probability densities with spatially extended envelopes⁶. In addition to this envelope, the wavefunction of a valence band electron is strongly modulated by the nuclei while the wavefunction of a conduction band electron is weakly modulated by the nuclei. In the simplest picture of a conduction band electron, the wavefunction is not modulated at all.

The excited electron leaves a vacancy in the valence band. This positive charge has the same spatial distribution as a valence-band electron. This volume of excess positive charge is called a hole. In many materials, the energetic electron in the conduction band is attracted by the Coulomb force (also called electrostatic force) to the hole. This attraction stabilizes the electron-hole pair, which is called an exciton. The degree of stabilization is reflected in the value of the exciton binding energy.

The wavefunction of an exciton is similar to that of a hydrogen atom; both species are the result of binding between one negative charge and one positive charge. The similarities between excitons and hydrogen atoms have been explored in detail elsewhere [26, 27]. Here it is sufficient to say that excitons are larger—in the sense that the electron and hole constituents are delocalized—and significantly less tightly bound than hydrogen atoms. Characteristic binding energies of several systems are listed in Table 1.1. The dramatic differences between hydrogen atoms and excitons in GaAs are due to screening by other charged particles in the semiconductor, and the amount of screening is quantified by the dielectric constant of the material.

Excitons are found in many systems. These charge-neutral microscopic quasiparticles are often used in transport applications, and they are usually placed into one of two broad classes based on the size of the exciton and the strength of the binding between the electron and the hole. Frenkel excitons are small, tightly bound excitons usually observed in organic systems such as light-harvesting complexes, molecular crystals, or molecular aggregates. More delocalized, loosely bound Wannier excitons

⁶An electron in a 10 nm GaAs quantum well fills a volume of $\sim 10^3$ nm³.

Table 1.1: Characteristic energies of several systems.

System	Energy
Hydrogen atom (H) ionization	13600 meV
Hydrogen molecule (H_2) dissociation	4500 meV
Trihydrogen molecule (H_3) binding	not stable
Trihydrogen cation (H_3^+) dissociation [37]	4500 meV
Water-water hydrogen bond (H_2O-H_2O) dissociation	250 meV
GaAs quantum well exciton (H) binding	10 meV
GaAs quantum well biexciton (HH) binding	1 meV

are often found in inorganic systems such as semiconductors. Wherever they are found, their small constituent effective masses mean that excitons are governed by the laws of quantum mechanics.

The properties of excitons are determined by the material in which they reside. Although changing materials is one way to obtain excitons with different properties, an alternative way to alter the exciton properties is to use nanostructuring techniques to change the size or shape of the material [28]. In this manner, the size of the exciton is limited by the spatial dimensions of the object, not by the Coulomb interaction between the electron and hole. The confined exciton often has remarkable size-dependent optical properties. Many types of nanostructures have been synthesized. Early structures were quantum wells—one dimension of confinement—and quantum dots [29, 30]—three dimensions of confinement. Quantum rods, wires and tubes, with two dimensions of confinement, can also be fabricated. Exciting new frontiers for nanofabrication include ‘nanoshells’ [31], ‘nanorattles’ [32, 33], ‘nanobones’ [34], and nanoparticles able to deliver pharmaceuticals [35, 36]. The sample studied in this thesis is GaAs that has been fabricated into a 10 nm wide quantum well. This confines the exciton in one dimension to just below its natural Bohr radius, results in a slightly increased binding energy relative to bulk GaAs, and causes the two degenerate valence bands to split energetically.

In short, electrons in GaAs take advantage of their quantum mechanical nature (the particle-wave duality) when they are essentially freed from their atomic orbitals and to form valence bands; spatially, they are delocalized like waves over a large spatial region. Photoexcited electrons are attracted to the nuclei even less. The promotion of an electron to the conduction band leaves an excess positive charge in the valence band, a hole. The Coulombic attraction between the positively charged hole and the negatively charged electron results in binding between the two particles. The attraction between particles with opposite charge (and the repulsion between particles with similar charge) is the ‘simple rule’ that will lead to the complex behaviors—

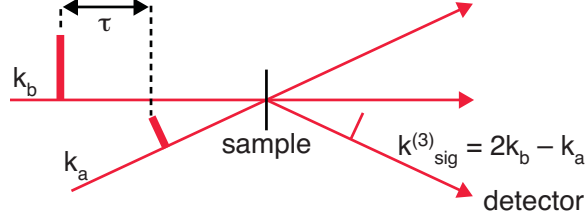


Figure 1-2: Third-order ‘self-diffraction’ measurement. Field E_a , which propagates in a direction \mathbf{k}_a , forms exciton coherences. After a time delay τ , the first interaction by field E_b —propagating in direction \mathbf{k}_b —forms spatially periodic exciton populations, and its second interaction generates rephasing exciton coherences which radiate signal in the phase-matched direction, $2\mathbf{k}_b - \mathbf{k}_a$.

many-body interactions—measured in this thesis.

1.4 Coherent exciton dynamics

The history of coherent spectroscopic experiments on excitons in semiconductor quantum wells is well documented (hundreds of publications) and has been reviewed several times [27, 38–41]. Therefore we provide only a brief summary here. Studies of semiconductor nanostructures began in the 1980s when time-domain experiments were performed in the coherent regime immediately after photoexcitation to measure the transient exciton dynamics. The intent was to understand the distinct physical processes that led to exciton dephasing. These measurements were performed at the same time that nonlinear spectroscopy theories were being developed [16], and the studies tested theories about the coherent responses [42, 43]. Although the first experiments did not have sufficient time resolution to measure exciton dephasing, the strong signals motivated continued efforts [44–48]. Additional experiments with shorter pulses established the exciton dephasing time in GaAs, but left many questions unanswered [49, 50].

Experiments performed on a variety of semiconductor nanostructures under different experimental conditions noted some of the contributions to exciton dynamics and dephasing, including:

1. coherent oscillations due to excitons in different wells [51–55],
2. coherent oscillations due to excitons in the same well [56, 57],
3. exciton-phonon scattering [58, 59],
4. exciton–free-carrier scattering [60–65],
5. disorder and localization [66, 67],
6. the AC Stark effect [68, 69],

7. magnetic field effects [70].

Importantly, the observed signal oscillations due to excitons in the same well—the second item above—were in fact due to quantum beats caused by quantum mechanical coupling between exciton states, and they were not due to macroscopic polarization interference effects [51, 71].

Most of these measurements were conducted as two-beam, four-wave-mixing measurements as shown in Fig. 1-2. Two laser beams, in directions given by wave vectors \mathbf{k}_a and \mathbf{k}_b , were focused to a spot in the sample. The field provided by the femtosecond optical pulse in beam \mathbf{k}_a generated exciton coherences; the electric field E_a induced coherent oscillations of electronic charge density that oscillated at the exciton frequency with a well defined phase. After a variable delay, τ , the field in beam \mathbf{k}_b interacted twice with the sample; its first interaction generated spatially periodic exciton populations by stopping the coherent oscillations because this field interaction completed the two dipole operations necessary to absorb the energy from the photon. Then, the second interaction by field E_b again generated exciton coherences. These coherent oscillations had the same frequency but opposite sign as the initial exciton coherences, so that dephasing due to inhomogeneity was reversed [72]. These coherences radiated signal in the phase-matched direction [73], and that signal was measured using a detector. In this manner, the initial field created coherences that evolved during time period τ , and the final fields were used to ‘watch’ these decaying oscillations.

The studies revealed that although exciton resonances dominate the nonlinear response, strong exciton-phonon and exciton-free-carrier scattering result in a loss of exciton coherence even at low temperatures. Thus, current studies are performed at temperatures below 10 K to extend the duration of the exciton coherences, and pulses no shorter than about 100 fs in duration are used to minimize the number of excited free-carriers.

1.5 Exciton many-body interactions

Most of the preceding observations were explainable using simple models—such as the optical Bloch equations described in Sec. 2.3—that included a small number of energy levels for the exciton states but did not contain particle interaction mechanisms. Although these models matched experiments rather well, there were a few pieces of experimental evidence suggesting that the third-order nonlinear response deviated from the simple models. The most obvious deviation was the anomalous signal observed at ‘negative’ delay times in self-diffraction measurements as illustrated in

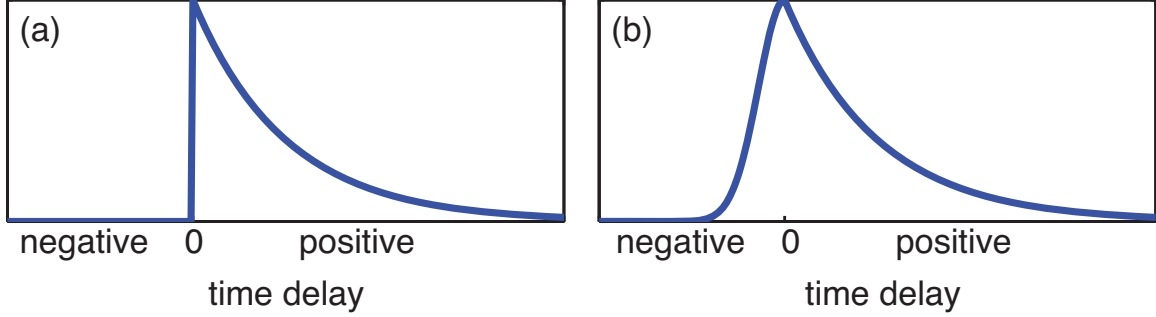


Figure 1-3: Third-order self-diffraction signals. (a) Predicted signal without exciton interactions. No signal is observed at ‘negative’ delays when field E_b interacts before field E_a . (b) Including exciton interactions, negative-delay signals can be predicted. The existence of these negative-delay signals has motivated research on many-body interactions for decades.

Fig. 1-3. The simple models predict that there should be no signal emitted in the self-diffraction experiment when pulse \mathbf{k}_b interacts with the sample before pulse \mathbf{k}_a , but experiments showed that signal did exist [74, 75]. In fact, the signal at negative delays was nearly as strong as that observed at positive delays. It was surmised that the signals arose when the first two field interactions induced nonradiative two-quantum coherences from which the third field interaction generated single-exciton coherences that radiated in the signal direction. The two-quantum oscillations are coordinated four-particle motions that are nonradiative because they do not have an associated dipole moment. Other observations, such as unexpected signals when the optical polarization direction between the two beams was varied [76–81], also could not be explained using the non-interacting exciton model.

These experiments illustrated the sensitivity of the coherent nonlinear response to many-body interactions, and the deviations from the simple model provided an opportunity to explore exciton many-body interactions. Microscopic theories were developed that did not involve re-diagonalization to an exciton basis. The complete treatment has been called the nonlinear exciton equations, the semiconductor Bloch equations, or the dynamics controlled truncation approach. All three techniques treat the electrons, holes, and their interactions explicitly, although the semiconductor Bloch equations work in a momentum basis while the other two approaches use a site basis. Additionally, in the exciton representation, physical insights were gained by modifying the optical Bloch equations. The modified equations phenomenologically included mean-field many-body interactions such as local field and excitation-induced effects.

Local field effects (LFE) were initially implicated as the source of the negative-delay signal [74, 75]. We will see in Sec. 2.3 how these effects are incorporated

mathematically. Physically, signals due to local fields are produced in the following manner. The initial field due to field \mathbf{k}_b produces a first-order polarization which radiates as a free-polarization decay. The free-polarization decay time is governed not by the pulse duration but rather by the exciton dephasing rate. This radiated field—now picoseconds in duration rather than femtoseconds—can then drive new excitations in the sample, and the new excitations can produce signal in the phase-matched direction once the second pulse arrives.

Other measurements showed that increasing the laser intensity caused the exciton coherences to dephase more quickly and the exciton emission energy to shift. Although the excitation-induced dephasing (EID) effect was noticed in early measurement [82, 83], only later was it interpreted as a many-body interaction. An excitation-induced energy shift (EIS) was also noticed [84, 85], and its signature in the coherent response was measured [86]. These two phenomena can be understood physically in terms of exciton-density-dependent changes to the linewidth (EID) and central component (EIS) of frequency ‘gratings’, periodic variations in amplitude as a function of frequency formed by two phase-coherent pulses with a relative delay. EID and EIS can also be understood physically in terms of the free polarization decay above, where the second field interaction from pulse \mathbf{k}_b produces spatially modulated excited state populations, but now regions with dense populations decay more quickly than regions with sparse populations [41]. These two many-body interactions are also described in Sec. 2.3.

The coupling between excitons and free carriers is another type of many-body interaction. Signals due to exciton–free-carrier scattering can often dominate the nonlinear response, and these signals are present in many experiments described in this thesis. A spectral feature due to interactions between excitons and free electron-hole pairs was reproduced by including an EID term in the modified optical Bloch equations [87]. As mentioned above, we often tune the pulse spectrum to excite the fewest possible number of free carriers to prevent rapid dephasing of the coherent signal.

While mean-field many-body interactions aided the interpretation of the experimental results, they could not describe the material response completely. Biexciton contributions were also explored. Just as excitons are analogous to hydrogen atoms, H, biexcitons are analogous to hydrogen molecules, H₂. They are perhaps the most straightforward way to interpret the negative delay signal [88, 89]. First observed as biexciton-exciton emission in a photoluminescence measurement [90], a biexciton is produced when a pair of excitons bind. For binding to occur, the constituent ex-

citons must have opposite spin⁷. The biexciton binding energy in GaAs quantum wells is about 1 meV [91]. Biexcitons are just one member of a class of four-particle correlations. Correlations among multiple charged particles are essential features of many systems and processes including quantum dot lasers [92], quantum logic gates [93], light harvesting complexes [94], scintillators [95], high-harmonic generation [96], entangled photon sources [97], and perhaps soon exciton-polariton condensation [98].

Although the progress in isolating and understanding the various many-body interactions was substantial, numerous open questions remained. The next section describes additional insights learned using two-dimensional spectroscopy, a recent significant advance in experimental methodology. Before progressing to that topic, we describe in more detail the physical process involved in generating nonlinear signals due to excitons and their interactions. It is difficult to provide a real-space description of coordinated four-particle motion that is both accurate and lucid. Although challenging, it is important to understand coordinated several-particle motion because most many-body interactions, including LFE, EID, EIS, biexcitons, and exciton-free-carrier scattering, can be interpreted as four-particle motions. Essentially, a single coherent electric field interaction will induce motions of electronic charge density in the sample. The motions are oscillations along a spatial coordinate related to the incident field polarization; charges that oscillate in this manner emit radiation⁸. A second field interaction can have several effects. Since this discussion focuses on exciton interactions, we consider the situation in which this second field induces more complex motions, such as a quadrupolar motion. This motion involves four particles—two electrons and two holes—but does not have an associated dipole moment so it does not radiate light. A third field, however, can interact with the particles involved in the quadrupole to induce charge oscillations that do radiate. By varying the time at which the third field interacts, the quadrupole motion can be tracked by its influence on the radiated signal, specifically the phase of the signal.

We can describe this in more detail using concepts from quantum mechanics; an illustration is given Fig. 1-4. As discussed above, the absorption of a photon with enough energy can promote an electron from the valence band to the conduction band. Both the electron and the residual positive charge to which it is attracted—the hole—are delocalized throughout the space of the material. In the language of

⁷In the ground-state spin configuration, the two electrons have opposite spins, as do the two holes.

⁸If this were the only field interaction and we placed a spectrometer in the appropriate position, this notion could be used to understand a linear absorption measurement. The emitted field is phase-shifted with respect to the incident field, causing a diminished amplitude at the resonance frequency. The phase shift is described by the Maxwell equation presented in Sec. 2.1.1.

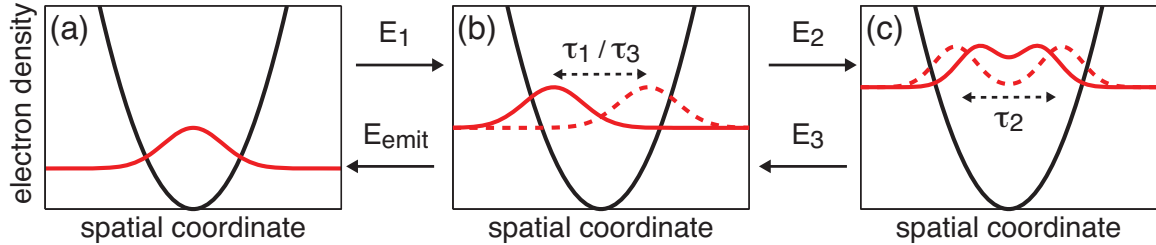


Figure 1-4: Hypothetical two-quantum signal in a slightly anharmonic potential. (a) Initially, the system is in the ground state; the wavepacket is stationary. (b) Field E_1 creates a coherent superposition. The wavepacket oscillates during time period τ_1 between the left (solid) and right (dashed) sides of the potential. (c) Field E_2 creates the two-quantum coherent superposition. Although the wavepacket moves during time period τ_2 between the solid and dashed positions, there is no change in the average spatial position. Field E_3 projects the two-quantum motion back to a one-quantum wavepacket as in (b). This motion emits the signal field, E_{emit} , during time period τ_3 , returning the system to the ground state (a). These fields can be related to the self-diffraction experiment: fields E_1 and E_2 correspond to the two interactions by field E_b , and field E_3 corresponds to the interaction by field E_a .

light-matter interactions, absorbing a photon requires two electric field interactions of opposite conjugation ($+\mathbf{k}$ and $-\mathbf{k}$). A single light-matter interaction—for instance the electric field interaction due to field E_b in the self-diffraction experiment—will induce a superposition between the ground state and the exciton state. If the electric field is coherent, this superposition will have a well defined phase and can be described as a spatial wavepacket of electron density. Unlike the smooth Gaussian wavepackets presented in Fig. 1-4 or those discussed in introductory quantum mechanics⁹, in a semiconductor this wavepacket will have a complex spatial distribution since it involves electronic charge density that is distributed across many lattice sites and modulated by the nuclei and their bonds at each site. In both cases, the average spatial position of the wavepacket oscillates as a function of time. These oscillations in electron charge density will radiate light. The second field interaction—if it has the same conjugation as the first field and if it acts before the initial motion has stopped—can cause motions that oscillate at twice the frequency. But this motion, although oscillatory, would not involve a time-dependent variation in the average spatial position of charge density. Thus this motion—described above as a quadrupolar motion—would not radiate. Spatially, this could correspond to a symmetric motion reminiscent of a molecular ring-breathing mode. If the four particles involved in the motion had the appropriate spin pairings such that the energy of the

⁹These wavepackets typically involve many excited states with well defined amplitudes and phases.

four-particle correlation would be lowered¹⁰, the frequency of the four-particle motion would decrease slightly. The third field can interact with this wavepacket to cause new electronic charge density oscillations that have a time-dependent average spatial position. These final oscillations emit the signal field in the phase-matched direction. This process has been compared to the nuclear spin precessions of multiple-quantum NMR [99].

1.6 Two-dimensional optical spectroscopy

The advent of two-dimensional optical spectroscopy has heralded a new era of investigation into exciton many-body interactions. Multidimensional Fourier-transform spectroscopy was developed in the 1970s and 1980s in the context of nuclear magnetic resonance (NMR) [100–104], in which a series of radio frequency pulses manipulated the nuclear spins of each active nucleus in the sample. By varying the times at which the pulses interact and detecting the full signal field at each delay point, signal oscillations can be mapped and phases in multiple times periods can be correlated. **Two-dimensional spectra are powerful primarily because the presence of a cross peak immediately reveals a quantum correlation.** In almost all cases, the existence of a cross peak between different absorption and emission frequencies is direct evidence that two eigenstates are coupled quantum mechanically. Two-dimensional NMR revolutionized synthetic chemical characterization procedures because it provided important molecular structure information encoded in the cross peaks: if two atoms were spatial neighbors in a molecule, their spins coupled, and that coupling resulted in a cross peak. In this way, features that overlapped in one-dimensional spectra were separated using the new dimension, and this separation revealed molecular structural information [105].

Although multidimensional NMR spectroscopy has existed for decades, only since the late 1990s have similar methods been applied to other regions of the spectrum. The slow adoption of multidimensional techniques was due to the fact that as the frequency of radiation increases, it becomes increasingly difficult to maintain the necessary phase stability [106]. Moreover, laser beams are used to deliver the pulses in the optical regime. Laser beams have a directionality component determined by the wave vector of the beams not relevant in NMR, where the sample length is shorter than the wavelength. Two-dimensional Fourier-transform infrared (2D IR) spectroscopy is now an important tool that uses vibrational transitions to reveal information on

¹⁰This small energy change is the binding energy of the biexciton.

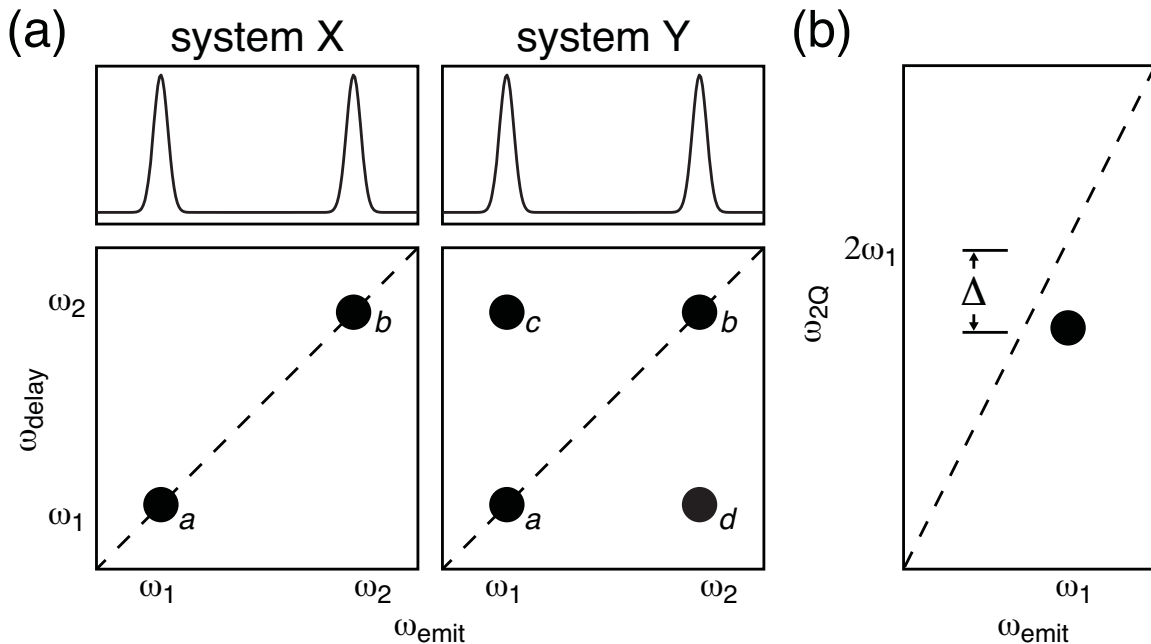


Figure 1-5: The power of two-dimensional spectroscopy. (a) System X has two uncorrelated eigenstates while system Y has two correlated eigenstates. The linear spectra (top) are identical. The two diagonal peaks (*a* and *b*) reveal the energies of eigenstates $|1\rangle$ and $|2\rangle$, respectively. The cross peaks (*c* and *d*) present in the 2D spectrum of system Y indicate that the two eigenstates are coupled. The dashed line indicates the $\omega_{\text{delay}} = \omega_{\text{emit}}$ diagonal. (b) A two-quantum measurement. The peak is located slightly below the two-quantum diagonal, $\omega_{2Q} = 2\omega_{\text{emit}}$. A small frequency shift—in our sample due to a binding energy—is indicated by Δ .

topics as diverse as molecular anharmonicities [107–111], hydrogen bond dynamics [112–116], protein and peptide dynamics [117–119], dye-sensitized solar cells [120], and amyloid fiber formation [121]. Since the first report in 1998 [122] and subsequent method development [123–137], many 2D Fourier-transform optical (2D FTOPT) spectroscopy studies have been conducted to explore phenomena such as excitonic many-body interactions [87, 99, 138–153], coherent intrachain energy migration in conjugate polymers [154, 155], higher-lying excited states of molecules [156, 157], energy dissipation in beta-carotene [158], exciton resonances in molecular aggregates [134, 159–162] and nanotubes [163], and how electronic charge is shuttled among chromophores in light-harvesting complexes [164–169]. Finally, efforts are underway to extend multidimensional methods below the IR to the THz regime [170, 171] and above the visible to the ultraviolet and x-ray regime [172, 173].

In multidimensional FTOPT spectroscopy, a series of femtosecond laser pulses is used to create and manipulate coherent superpositions of system eigenstates. After all the pulses have interacted, the system emits a signal in a direction that conserves

energy and quasi-momentum. Crucially, the full signal field—both its phase and amplitude—is detected. During a measurement, an input field(s) is delayed temporally, and the signal field is measured at each delay point. Repeated measurements are collated and then Fourier transformed to create the 2D spectrum. This spectrum correlates oscillations during time periods τ_{delay} and τ_{emit} as peaks along frequency axes ω_{delay} and ω_{emit} , as shown in Fig. 1-5(a). Related to Fig. 1-4, $\tau_{delay} = \tau_1$ and $\tau_{emit} = \tau_3$. In the example 2D spectra, the diagonal peaks reveal the eigenstate energies; although not described in this example, their lineshapes contain dephasing information. If cross peaks exist—as in system Y—the two states are coupled. In Fig. 1-5(b), we illustrate a different 2D measurement in which the pulse-timing sequence was changed to induce oscillations derived from two quanta of the same eigenstate. In this example, the two-quantum coherence oscillated at slightly less than twice the frequency of a single exciton, due to a binding energy for the two-exciton (biexciton) state. Related to Fig. 1-4, $\tau_{2Q} = \tau_2$ and $\tau_{emit} = \tau_3$. As in many cases, most of the unexpected spectral features revealed in the 2D and 3D FTOPT spectra presented in the following chapters were due to many-body interactions. The spectra were measured at varying nonlinear orders in the electric field under varying conditions to explore several different many-body interactions.

The nonlinear signal field can contain many possible contributions that we can isolate with even more specificity by tuning the parameters of each laser field. Recent advances in experimental techniques now make it possible to specify each parameter of each laser field, including the polarization, wave vector, temporal duration, optical phase, and frequency content. Pulse sequences originally developed in NMR are now applied routinely to the optical regime to accomplish specific tasks. For example, third-order photon echo (*rephasing*) measurements—analogous to spin echo measurements in NMR—can separate inhomogeneous dephasing (due to static disorder) from homogeneous dephasing (dynamic phase fluctuations due to scattering). In many cases, this control over the pulse parameters allows us to discriminate against all of the signals except for the specified one.

1.7 Outline of this thesis

The rest of this thesis—which describes both the development of new spectroscopic methods and the application of those methods to isolate and learn about exciton interactions—is organized as follows. Chapter 2 reviews the nonlinear polarization and outlines three theoretical approaches used to describe its microscopic origin. Chapter 3 describes the construction, calibration, and operation of the experimental

apparatus, and it includes a description of the data analysis procedures. Chapter 4 contains spectra performed to reveal properties of single, non-interacting excitons. We extract exciton parameters such as absorption energies, emission energies, sample inhomogeneity, dephasing times, and exciton lifetimes. We also observe several features due to many-body interactions. In Chapters 5–7 we isolate and measure four-particle, six-particle, and eight-particle correlations, respectively. The results are organized by the number of particles interacting, regardless of the order of the nonlinear signal required to make the measurement. Chapter 8 both summarizes the results on GaAs quantum wells and describes future experiments.

Chapter 2

Nonlinear optical spectroscopy

Optical spectroscopy is a tool used to probe electronic resonances in atomic, molecular, semiconductor, and biological systems. Linear spectroscopy involves only one electric field interaction, and the broad features present in most linear spectra hide important information about microscopic phenomena such as exciton-exciton and exciton-phonon interactions.

Intense electric fields—almost always from a laser, where modern pulsed lasers can reach peak intensities on the order of terawatts (10^{12} W)—can interact with matter to produce nonlinear signals¹. The link between lasers and nonlinear optics was established when the first optical nonlinearity [174] was observed less than one year after the laser was developed [175]. Nonlinear signals are often visually appealing because they can contain new frequencies or propagate in new directions—or both. Nonlinear optical signals created by a sequence of intense laser pulses can be used to produce multidimensional spectra, which in turn can provide detailed information about the sample.

There are two methods commonly used to describe how input electric fields, E_{in} , create output signal fields, E_{out} . The parallel sets of terminology can be confusing, so they are depicted graphically in Fig. 2-1. In both methods E_{in} creates a polarization, P , which is converted by one of Maxwell's equations, ME , to E_{out} . As we will show, the mathematics of this final step do not change the time-dependence of the signal significantly, so usually only the polarization is calculated.

In the first method—outlined in the top two steps of Fig. 2-1—only the macro-

¹These fields are intense, but even when focused, the experiment still takes place in the perturbative limit because the electric field of a typical sample is orders of magnitude greater. In our experiments, the pulse energy is about 10 pJ, the pulse duration is about 100 fs, and the beam is focused to a spot size of about 10^{-5} cm²; the radiative flux is on the order of 10^7 W/cm². On the other hand, the electric field intensity in a hydrogen atom is on the order of 10^{17} W/cm².

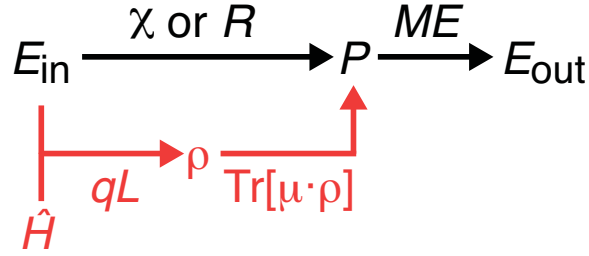


Figure 2-1: An illustration of the mathematical procedure used to calculate a nonlinear signal field from the input field(s). In the macroscopic-only picture, which excludes the steps colored red, the input electric field, E_{in} , interacts with the material described by either its susceptibility, χ , or its response function, R , to create a polarization, P . This polarization—an oscillating charge distribution inside a material—is a source term in a Maxwell equation, ME , which generates the output electric field, E_{out} . The case is similar when the quantum nature of the material is considered by following the steps colored red. The system response can be calculated in the density matrix formalism, ρ , whose time dependence is governed by the quantum-Liouville equation, qL . This equation incorporates both the system Hamiltonian, \hat{H} , and E_{in} . The polarization can be computed by taking the trace over the dipole operator, $\text{Tr}[\mu \cdot \rho]$, and the signal field can be calculated as before.

scopic properties of the sample are considered. These properties are encoded in the elements of the susceptibility tensor, χ , or equivalently, the response function tensor, R . Input electric fields, incorporated perturbatively, can create a nonlinear polarization if the appropriate tensor element is nonzero.

The second method—using the red-colored steps in Fig. 2-1 and ignoring χ and R —is used to learn about the quantum nature of the excited chromophores. The microscopic system is usually formulated in terms of the density matrix, $\rho(t)$. The time dynamics of the density matrix are governed by the quantum-Liouville equation, qL . This equation uses a system Hamiltonian, \hat{H} , and it incorporates the input field interactions perturbatively. The Hamiltonian can be simple or complicated, and we will see examples of both in this chapter. The density matrix is propagated over all of the field interactions. The trace operation is then performed after projection by the dipole operator, yielding a result proportional to the macroscopic polarization: $P \propto \text{Tr}[\mu \cdot \rho]$. The density matrix approach explicitly treats the system Hamiltonian, which includes both mixed and pure quantum states of the system, and can include the effects of temperature and coupling to the environment.

The standard approach to understanding nonlinear optical spectroscopy can be confusing because many sources use both methods and interchange terminology in the following manner. The macroscopic-only view is used to determine the directions in which signals will propagate—the phase matching conditions—using the frequency domain susceptibilities. Meanwhile, the time-dependence of the polarization is com-

Table 2.1: Jones vector representation of optical polarization

Linear horizontal	$\begin{bmatrix} 1 \\ 0 \end{bmatrix}$	Linear vertical	$\begin{bmatrix} 0 \\ 1 \end{bmatrix}$
Right circular	$\frac{1}{\sqrt{2}} \begin{bmatrix} 1 \\ -i \end{bmatrix}$	Left circular	$\frac{1}{\sqrt{2}} \begin{bmatrix} 1 \\ i \end{bmatrix}$

puted using the density matrix. This discussion is then often cast in terms of response functions, R .

In Sec. 2.1, we first review the nonlinear optical polarization and its microscopic origins. We then survey three theoretical approaches used to compute multidimensional spectra from the density matrix through the nonlinear optical polarization in Secs. 2.2–2.4. We review these concepts with some detail because the array of measurements presented in the following chapters demands that we have a command of the material so that we can traverse the ever-changing experimental conditions with ease. Finally, in Sec. 2.5 we discuss how the nonlinear optical methodology applies to the sample.

2.1 Nonlinear polarization

In this section we review how observed signals, E_{out} , can be computed from the macroscopic polarization, P_{NL} , through one of Maxwell’s equations. We then use the density matrix, ρ , to relate the quantum mechanics of the microscopic chromophores to the macroscopic polarization. The approach is semiclassical; the electric field is treated classically but the material response is treated using quantum mechanics. A classical electric field—a real-valued oscillating wave—can be decomposed using the Euler relations into a sum of two exponentials, and can thus be expressed as

$$\mathbf{E}_n(\mathbf{r}, t) = \hat{\mathbf{e}}_n(t) \tilde{E}_n(t) (e^{i(\mathbf{k}_n \mathbf{r} - \omega_n t)} + c.c.), \quad (2.1)$$

where \tilde{E}_n is a slowly-varying envelope (perhaps a Gaussian), ω_n is the frequency, \mathbf{k}_n is the wave vector, and $\hat{\mathbf{e}}_n$ —which can vary with time—is a unit vector describing the optical polarization of the beam. Beam polarizations can be expressed using Jones vectors, see Table 2.1.

2.1.1 Macroscopic description

For the moment, the discussion remains entirely in the macroscopic realm. Throughout most of the discussion, we suppress detailed tensor descriptions to ease interpretation. An input electric field, \mathbf{E}_{in} , can create an electronic charge distribution in a material—a polarization, \mathbf{P} —through the material susceptibility, χ , as given by

$$\mathbf{P}(\mathbf{r}, \omega) = \chi(\omega)\mathbf{E}_{in}(\mathbf{r}, \omega). \quad (2.2)$$

Susceptibilities are frequency-domain tensors that are connected to time-domain *response function* tensors through a Fourier transform

$$R(t) = \mathcal{F}[\chi(\omega)] \quad (2.3)$$

$$\mathbf{P}(\mathbf{r}, t) = \int_0^\infty d\tau R(\tau)\mathbf{E}_{in}(\mathbf{r}, t - \tau). \quad (2.4)$$

The value of \mathbf{P} can be expressed as a dipole moment per unit volume. \mathbf{E}_{in} creates an electronic charge distribution which can have a complicated temporal and spatial nature. If \mathbf{E}_{in} is coherent, the charge distribution can oscillate with a well defined phase over macroscopic distances. Oscillating charges radiate electric fields, hence the polarization acts as a source term in the Maxwell equation

$$\nabla^2\mathbf{E}_{out}(\mathbf{r}, t) - \frac{1}{c^2}\frac{\partial^2}{\partial t^2}\mathbf{E}_{out}(\mathbf{r}, t) = \frac{4\pi}{c^2}\frac{\partial^2\mathbf{P}(\mathbf{r}, t)}{\partial t^2}, \quad (2.5)$$

to radiate the signal field $\mathbf{E}_{out}(\mathbf{r}, t)$. Using Eqn. 2.5, the coherent signal field can be calculated in a straightforward fashion from the sample polarization. For a thin sample of length l , the time dependence of the signal field at frequency ω_s in the phase-matched direction, \mathbf{k}_{sig} , at a specified detector location is given by

$$E_{out}(t) = i\frac{2\pi\omega_s l}{nc}P(t)\text{sinc}\left(\frac{\Delta kl}{2}\right)e^{i\Delta kl/2}. \quad (2.6)$$

The signal field and the polarization differ only slightly. There is a $\frac{\pi}{2}$ phase shift between them; the amplitude is modulated according to the phase-mismatch Δk ; if the phase-mismatch or the pathlength, or both, is large, the final exponential term can cause an additional phase shift; and the two quantities have different units. The time-dependent oscillations in $P(t)$ will be altered by at most constant phase and amplitude factors. Thus in most cases the task of calculating the signal field is reduced to calculating just the polarization. For an example of when it is important to calculate the full field, see Ref. [176].

Material response information is encoded in the values of the elements of χ , and this information is reported in the total polarization, $\mathbf{P}(\mathbf{r}, t)$. If a signal is generated in a new direction or with a new frequency, the total polarization must contain a nonlinear component,

$$\mathbf{P}(\mathbf{r}, t) = \mathbf{P}^{(1)}(\mathbf{r}, t) + \mathbf{P}_{\text{NL}}(\mathbf{r}, t). \quad (2.7)$$

The microscopic origin of this nonlinear polarization, \mathbf{P}_{NL} , must be treated for the specific system under study, and this ultimately provides insights into the system behavior [16, 177, 178]. For now, we remain in the macroscopic realm and assume that the input electric fields are capable of producing a nonlinear polarization because we observe such signals in the laboratory. The polarization can be expanded as a power series in the field by

$$\mathbf{P} = \mathbf{P}^{(1)} + \mathbf{P}^{(2)} + \mathbf{P}^{(3)} + \dots, \quad (2.8)$$

where the linear ($\mathbf{P}^{(n=1)}$) and nonlinear ($\mathbf{P}^{(n>1)}$) polarizations are defined in terms of their respective susceptibilities and the input fields by

$$\mathbf{P}^{(1)}(\omega) = \chi^{(1)} \mathbf{E}_{in}(\omega), \quad (2.9)$$

$$\mathbf{P}^{(2)}(\omega) = \chi^{(2)} \mathbf{E}_{in}^2(\omega), \quad (2.10)$$

$$\mathbf{P}^{(3)}(\omega) = \chi^{(3)} \mathbf{E}_{in}^3(\omega), \quad (2.11)$$

and so on for higher orders. The n^{th} -order induced polarization, $\mathbf{P}^{(n)}$, can then be written in the time domain as a convolution between the n^{th} -order response function, $R^{(n)}$, and n input electric field(s)

$$\begin{aligned} \mathbf{P}^{(n)}(\mathbf{r}, t) &= \int_0^\infty d\tau_n \int_0^\infty d\tau_{n-1} \dots \int_0^\infty d\tau_1 R^{(n)}(\tau_n, \tau_{n-1}, \dots, \tau_1) \\ &\quad \times \mathbf{E}_n(\mathbf{r}, t - \tau_n) \mathbf{E}_{n-1}(\mathbf{r}, t - \tau_n - \tau_{n-1}) \dots \mathbf{E}_1(\mathbf{r}, t - \tau_n - \tau_{n-1} - \dots - \tau_1). \end{aligned} \quad (2.12)$$

If the directionality can be ignored, then Eqn. 2.12 can be reduced to yield

$$\begin{aligned} P_{e_n}^{(n)}(t) &= \int_0^\infty d\tau_n \int_0^\infty d\tau_{n-1} \dots \int_0^\infty d\tau_1 R_{e_1, e_2, \dots, e_n}^{(n)}(\tau_n, \tau_{n-1}, \dots, \tau_1) \\ &\quad \times E_n(t - \tau_n) E_{n-1}(t - \tau_n - \tau_{n-1}) \dots E_1(t - \tau_n - \tau_{n-1} - \dots - \tau_1), \end{aligned} \quad (2.13)$$

where the optical polarizations of the input beams, $\hat{\mathbf{e}}_n$, have selected a specific element of the response function tensor, $R_{e_1, e_2, \dots, e_n}^{(n)}$. It is in this manner that the response functions (or susceptibilities) can couple fields in one spatial direction to another spatial direction. Input signal fields with particular wave vectors can generate signal

fields in new directions. The response function tensors are macroscopic quantities whose elements contain all of the measurable properties of the sample, including crystal symmetry, dipole strengths, and resonance frequencies. As the order increases, the rank of the tensor increases, and the number of elements in the tensor increases dramatically. Fortunately many elements have a value of zero, and for samples with inversion symmetry, such as gases and liquids, the even-ordered susceptibilities ($\chi^{(2)}$, $\chi^{(4)}$, ...) vanish entirely.

Energy and momentum conservation of the input fields, the *phase matching* conditions, must be satisfied for signal fields to propagate in new directions. The physical interpretation of this is that the polarization waves in the sample are interfering constructively in only certain directions. The two conservation laws for n field interactions can be expressed as

$$\mathbf{k}_{sig} = \sum_n \pm \mathbf{k}_n, \text{ and} \quad (2.14)$$

$$\omega_{sig} = \sum_n \pm \omega_n. \quad (2.15)$$

For example, consider the situation if the sample has nonzero $\chi^{(3)}$ tensor elements. A third-order polarization can then be produced in the following manner

$$\mathbf{P}_{ed}^{(3)}(\mathbf{r}, \omega_{sig}) = \chi_{e_a e_b e_c e_d}^{(3)} [\tilde{E}_a(\omega) \tilde{E}_b(\omega) \tilde{E}_c(\omega) e^{i((-\mathbf{k}_a + \mathbf{k}_b + \mathbf{k}_c)\mathbf{r} - (\omega_a + \omega_b + \omega_c)t} + c.c.], \quad (2.16)$$

where the optical polarizations of the three input beams have selected the $\chi_{e_a, e_b, e_c, e_d}^{(3)}$ element of the $\chi^{(3)}$ tensor, or equivalently in the time domain as

$$\begin{aligned} \mathbf{P}_{ed}^{(3)}(\mathbf{r}, t) = & \int_0^\infty d\tau_c \int_0^\infty d\tau_b \int_0^\infty d\tau_a R_{e_a e_b e_c e_d}^{(3)}(\tau_c, \tau_b, \tau_a) [\tilde{E}_a(t - \tau_c) \tilde{E}_b(t - \tau_b) \\ & \times \tilde{E}_c(t - \tau_a) e^{i((-\mathbf{k}_a + \mathbf{k}_b + \mathbf{k}_c)\mathbf{r} - (\omega_a + \omega_b + \omega_c)t} + c.c.]. \end{aligned} \quad (2.17)$$

In this example, fields \mathbf{E}_b and \mathbf{E}_c contribute forward-propagating components ($+\mathbf{k}$); they are called *nonconjugate* fields. Field \mathbf{E}_a contributes a backward-propagating component ($-\mathbf{k}$) and is called a *conjugate* field. The resulting signal field will propagate in a direction $\mathbf{k}_{sig} = -\mathbf{k}_a + \mathbf{k}_b + \mathbf{k}_c$ with a frequency $\omega_{sig} = -\omega_a + \omega_b + \omega_c$. If the frequencies of the three input fields are the same—a common situation—this is called degenerate four-wave-mixing (DFWM). We use this type of signal in many experiments presented in Chapters 4 and 5. Similar phase-matching analyses are used throughout the thesis to calculate the directions in which signal fields will propagate, and how many input field interactions were involved in producing those signal fields.

This is as complete a general description as possible in the macroscopic-only do-

main, the top two steps of Fig. 2-1. This level of treatment is sufficient to predict in what directions and with what frequencies signals will emerge given that the response function tensor has nonzero elements.

2.1.2 Microscopic origins

We now consider the microscopic nature of the material—the quantum mechanics of the system—so that we can calculate the time dependence of the signal field, $E_{out}(t)$. Most derivations of the equations of motion work in an ‘interaction picture’ and use the density matrix, ρ —rather than wavefunctions—to describe the system. The wavefunction and density matrix approaches are equivalent, but the density matrix approach has several advantages for nonlinear spectroscopy. A macroscopic observable in the form of the expectation value of any operator, \hat{A} , can be found from quantum mechanics [179] by taking the trace over the density matrix

$$\langle A \rangle = \text{Tr}[\hat{A} \cdot \rho]. \quad (2.18)$$

We learned in the preceding section that the induced polarization, $P(t)$, is connected to the dipole moment. Thus, macroscopic polarizations can be computed from the density matrix using the quantum mechanical dipole moment operator, $\hat{\mu}$, as given by

$$P(t) \propto \langle \hat{\mu}(t) \rangle = \text{Tr}[\hat{\mu}(t) \cdot \rho(t)]. \quad (2.19)$$

Each microscopic dipole results from a coherent superposition of system eigenstates, $|\Psi\rangle = \sum_i c_i \phi_i$, as described in Sec. 1.5. The frequency, orientation, and phase of each dipole is defined by the excitation fields and the spatial location in the sample. The microscopic dipoles act like a phased array to generate a macroscopic signal field in a direction determined by phase matching of the excitation fields. The emergent signal field is the result of interfering signals from many individual chromophores. In this manner, the phase of the generated signal field depends on the phase of each microscopic excitation.

In Eqn. 2.19, time dependence was made explicit. The time dependence of the density matrix is governed by the quantum-Liouville equation

$$\frac{\partial}{\partial t} \rho(t) = -\frac{i}{\hbar} [\hat{H}(t), \rho(t)], \quad (2.20)$$

where the Hamiltonian is often separated into two parts, a system Hamiltonian, \hat{H}_0 , and the perturbative interaction(s) with the electric field(s). This can be expressed

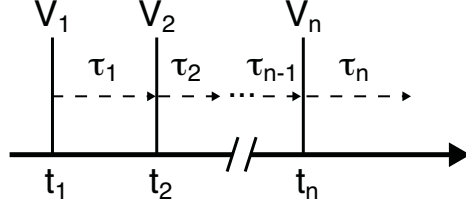


Figure 2-2: Sequential operations on the density matrix. Fields interactions V_n occur at times t_n and are separated by time periods τ_n .

as

$$\hat{H}(t) = \hat{H}_0 + \hat{V}(t), \quad (2.21)$$

where $\hat{V}(t) = -\vec{\mu}(\mathbf{r}) \cdot \mathbf{E}(\mathbf{r}, t)$.

Often, \hat{H}_0 is known well enough to define the eigenstates of interest and several field interactions occur sequentially. These sequential events are depicted in Fig. 2-2. The density matrix is calculated in a stepwise fashion, where each field interaction introduces a perturbation at time t_n , and during time interval τ_n , the system evolves according to the quantum-Liouville equation. In some computations, the differential forms of the equations of motion are integrated numerically. In other computations, the equations are transformed from differentials to integrals. This results in a nested set of commutators,

$$\rho^{(n)}(t) = \left(-\frac{i}{\hbar}\right)^n \int_{-\infty}^t dt_n \int_{-\infty}^{t_n} dt_{n-1} \dots \int_{-\infty}^{t_2} dt_1 \left[V(t_n), \left[V(t_{n-1}), \left[\dots, \left[V(t_1), \rho_0 \right] \dots \right] \right] \right]. \quad (2.22)$$

To calculate the system polarization using the density matrix, we switch from interaction times, t_n , to time intervals, τ_n , and take its trace, $P^{(n)}(t) = \text{Tr}\{\mu(t) \cdot \rho^{(n)}(t)\}$. This transformation results in an equation of the form

$$\begin{aligned} P^{(n)}(t) = & \left(-\frac{i}{\hbar}\right)^n \int_0^\infty d\tau_n \int_0^\infty d\tau_{n-1} \dots \int_0^\infty d\tau_1 \theta(\tau_1) \theta(\tau_2) \dots \theta(\tau_n) \\ & \times E_n(t - \tau_n) E_{n-1}(t - \tau_n - \tau_{n-1}) \dots E_1(t - \tau_n - \tau_{n-1} - \dots - \tau_1) \\ & \times \text{Tr} \left\{ \left[\left[\dots \left[\mu(\tau_n + \tau_{n-1} + \dots + \tau_1), \mu(\tau_{n-1} + \tau_{n-2} + \dots + \tau_1) \right], \dots \right], \mu(0) \right] \rho_0 \right\}, \end{aligned} \quad (2.23)$$

where the step functions, $\theta(\tau)$, enforce causality. At this point, derivations often mix the macroscopic and microscopic terminologies by comparing Eqn. 2.23 to Eqn. 2.13

and concluding that the macroscopic response function is given microscopically by

$$\begin{aligned}
 R_{e_1 e_2 \dots e_n}^{(n)}(\tau_1, \tau_2, \dots, \tau_n) &= \left(-\frac{i}{\hbar}\right)^n \theta(\tau_1)\theta(\tau_2)\dots\theta(\tau_n) \\
 &\times \text{Tr} \left\{ \left[\dots \left[\mu(\tau_n + \tau_{n-1} + \dots + \tau_1), \right. \right. \right. \\
 &\left. \left. \left. \mu(\tau_{n-1} + \tau_{n-2} + \dots + \tau_1) \right] \dots \right], \mu(0) \right] \rho_0 \right\}.
 \end{aligned}
 \tag{2.24}$$

The nested commutators can be expanded into a sum of sequences of dipole operators. This sum contains terms with different orderings of the dipole operators, and usually each distinct time ordering is labeled by an individual response function, $R_m^{(n)}$. The complete nonlinear signal field detected in the phase-matched direction includes all possible energy and momentum conserving sequences of interactions that link the eigenstates. Often, there are many possible pathways through Liouville space that can contribute to the total signal field, and they can interfere with each other. This will be discussed more in the next section for the specific example of third-order response functions.

In this section we showed that signal fields, E_{out} , are generated by sample polarizations, P , through the Maxwell equation, Eqn. 2.5. The macroscopic polarization is connected to quantum mechanical chromophores using the expectation value of the dipole operator, $\hat{\mu}$, through Eqn. 2.19. The time-dependent density matrix, $\rho(t)$, is calculated using the quantum-Liouville equation, Eqn. 2.20. This resulted in a series of nested commutators that is convolved with the electric fields in a sometimes intractable fashion.

The three methods described in the rest of this chapter will allow us to compute the nonlinear polarization through the density matrix under different approximations, leading to different ranges of applicability. For instance, the sum-over-states model is purely perturbative, while the other two methods can be used to model non-perturbative effects as well, such as Rabi oscillations [180]. Another distinguishing characteristic of any model is the basis set chosen for the computation. A systematic many-body analysis treats the electron and holes separately, and includes Coulomb potentials explicitly to describe multi-particle correlations. Such an analysis may match an experimental result very well, but it may be computationally prohibitive. On the other hand, models that work in an exciton basis can provide significant physical insights with minimal computational effort.

The most commonly used method is the sum-over-states model, where the fields are assumed to be perturbatively-small impulse functions, and the individual response

functions can be understood using a diagrammatic method because the field convolutions become trivial. The Bloch equations—the second method—are also widely used and are not limited to the perturbative limit. As the name suggests, they work well in the context of spatially homogeneous extended samples such as semiconductors. Both methods use exciton states as the fundamental unit of excitation. In the third approach—the nonlinear exciton equations—electrons and holes are considered separately and the Coulomb correlations are explicit. In the chapters that follow, we use all three approaches when appropriate.

2.2 Sum-over-states model

The sum-over-states model is an intuitive tool for analyzing multidimensional spectra, and the model is the subject of review articles [126, 181, 182], textbooks [16, 178], and online class notes [183, 184]. Using a few—often accurate—approximations, the nonlinear polarization induced by the excitation fields can be reduced to a sum of terms. Each term is a specific time ordering of dipole operators that traces one path through Liouville space. Each path can be represented by an easily understood Feynman diagram. The diagrams provide insights into the origin of peaks and features associated with system eigenstates.

In this model, the nonlinear polarization is calculated in the impulsive limit, where the electric fields retain their frequency and wave vector, but the temporal dependence is assumed to be a δ -function,

$$\tilde{E}_n(t) = \delta(t) |\tilde{E}_n|. \quad (2.25)$$

The model requires the energy levels of all eigenstates and their transition dipoles to be input manually, often in the form of matrices. It cannot include exciton-exciton interactions. These conditions generally hold when studying molecular vibrations, Frenkel excitons, or atomic and molecular excited states using femtosecond pulses, but the model often fails to predict signals due to many-body interactions among Wannier excitons because of the long-range Coulomb interactions. These assumption reduce Eqn. 2.23 to

$$P^{(n)}(t) = R^{(n)}(\tau_1, \tau_2, \dots, \tau_n) |E_1(t - \tau_n - \dots - \tau_1)| \dots |E_n(t - \tau_n)|, \quad (2.26)$$

where $R^{(n)}$ can be written in terms of individual response functions, $R_m^{(n)}$, as

$$R^{(n)}(\tau_1, \dots, \tau_n) = \left(-\frac{i}{\hbar}\right)^n \theta(\tau_n) \dots \theta(\tau_1) \times \sum_m \left[R_m^{(n)}(\tau_1, \dots, \tau_n) - R_m^{*(n)}(\tau_1, \dots, \tau_n) \right]. \quad (2.27)$$

At third order for a two-level system, there are eight total terms, one of which is given by

$$R_1^{(3)}(\tau_3, \tau_2, \tau_1) = \sum_{a,b,c,d} p \langle \hat{\mu}_{ad}(\tau_3 + \tau_2 + \tau_1) \hat{\mu}_{dc}(\tau_2 + \tau_1) \hat{\mu}_{cb}(\tau_1) \hat{\mu}_{ba}(0) \rangle. \quad (2.28)$$

The individual response functions provide minimal physical insight when written explicitly as a sequence of dipole operators. However, each term can be depicted using a diagrammatic perturbation method to keep track of the states and the light-matter interactions. If desired, the Feynman diagrams can be converted easily to a mathematical expression for the resulting nonlinear polarization [16] and this can be used to compute a spectrum. Usually, however, the diagrams are used merely to predict at what frequency coordinates pathways will appear. These expressions include such parameters as the energy levels, dephasing times, lifetimes, dipole transitions, and even coherence transfer rates [185].

Although resonant third-order responses (four-wave-mixing) are the most-often described signals using Feynman diagrams, a wide variety of nonlinear optical phenomena can be depicted through these diagrams. Fig. 2-3 shows a few examples. In part (a), the typical three-pulse four-wave-mixing rephasing experiment is depicted. The first field interaction induces a coherence between the ground state $|0\rangle$ and an excited state $|1\rangle$. The second field interaction completes the photon absorption process to the excited state. The third field induces new coherences between the ground and excited states. These coherence emit signal in the phase-matched direction. A nonresonant four-wave-mixing process is illustrated in (b), where a difference-frequency process between the first two input fields creates a coherence involving a nonresonant state—for example, a Raman-active vibration—and the third field stimulates the emission; fifth-order nonresonant signals (2D Raman) have now been observed even though they necessarily involve a formally forbidden transition [186–192]. Part (c) is a similar nonresonant signal although it is a fifth-order process requiring four field interactions to induce a hyperpolarizability [188]. Finally, a pathway for a third-order pump-probe signal is illustrated in part (d). This process is similar to (a) except the first two field interactions occur simultaneously. *Single-shot* pump-probe measurements can be used to study lattice vibrations during irreversible phase transitions

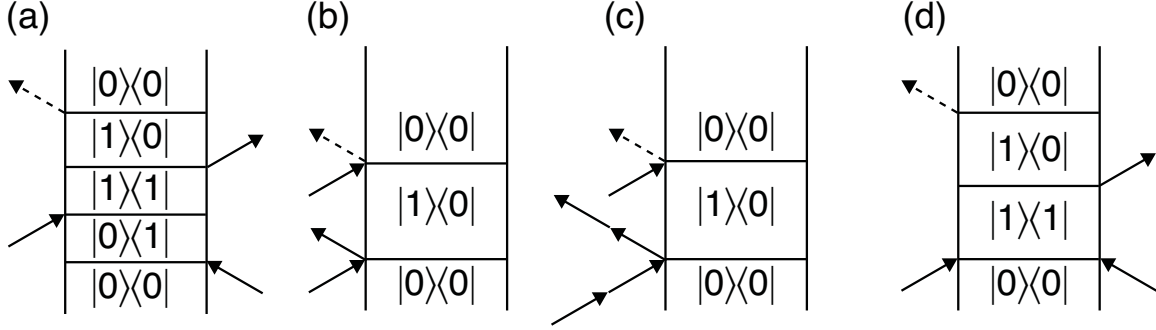


Figure 2-3: Feynman diagrams for a variety of nonlinear signals. (a) Three-pulse four-wave-mixing photon echo (b) Third-order Raman (c) Fifth-order Raman due to a hyperpolarizability (d) Third-order pump-probe.

[193]. Most nonlinear optical techniques—those discussed above and others, such as pathways involving coherence and population transfers [185], RaPTORS [194], FSRS [195], and more—can be described using Feynman diagrams.

As an example of how Feynman diagrams can be used to interpret a 2D spectrum to learn about the system Hamiltonian and its transition dipoles, we consider a third-order rephasing experiment in the self-diffraction geometry for the two materials that were mentioned in Sec. 1.6, systems X and Y. The momentum-conserving direction is $\mathbf{k}_{sig} = 2\mathbf{k}_b - \mathbf{k}_a$. In a rephasing experiment, the conjugate field, field E_a , interacts first with the sample. In both systems, the sample has two excited states with energy levels ϵ_1 and ϵ_2 , but in system X the two transitions are not coupled through a common ground state. As shown in Fig. 2-4, signals due to pathways $i - iv$ will emerge from both system X and system Y. However, system Y will also have signals due to the four pathways that appear as cross peaks, diagrams $v - viii$.

The spectra can be used to construct the Hamiltonian for each systems. In fact, this is the purpose of nonlinear spectroscopy: to use the emitted signal field to learn about the system Hamiltonian. System Y is the case of two coupled transitions,

$$\hat{H}_0 = \begin{pmatrix} 0 & 0 & 0 \\ 0 & \epsilon_1 & 0 \\ 0 & 0 & \epsilon_2 \end{pmatrix} \quad \hat{V} = \begin{pmatrix} 0 & \mu_1 & \mu_2 \\ \mu_1^* & 0 & 0 \\ \mu_2^* & 0 & 0 \end{pmatrix}. \quad (2.29)$$

Dipole operators will be able to induce transitions between eigenstates $|1\rangle$ and $|2\rangle$ through the perturbatively small elements μ_i in the off-diagonal components of V . Meanwhile, the second system also has two transitions, but they are not coupled through the ground state. This system has a Hamiltonian and a dipole matrix given

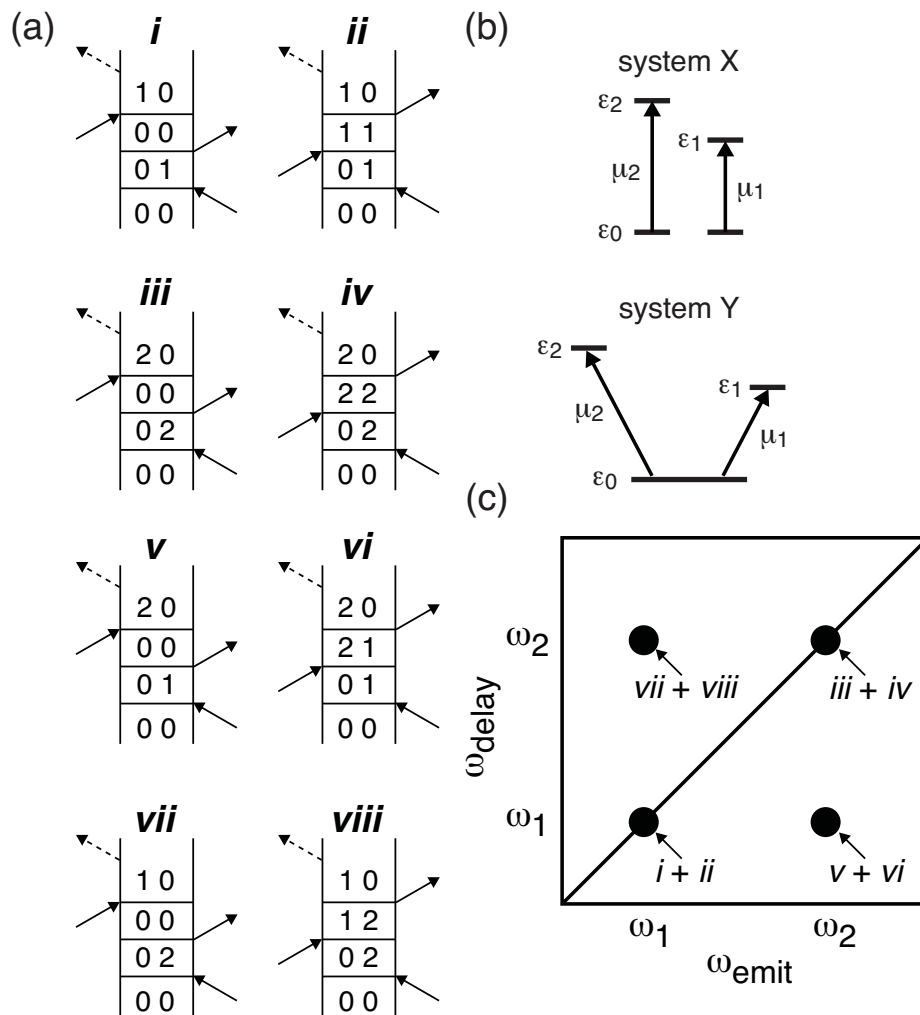


Figure 2-4: Feynman diagram contributions to a two-dimensional spectrum. (a) Possible signal pathways for a self-diffraction measurement in which field E_a interacts first. As a conjugate field, it interacts with an arrow pointing to the left. (b) States of the uncoupled (X) and coupled (Y) systems. (c) A schematic 2D spectrum for the rephasing self-diffraction experiment. If both transitions are coupled through a common ground state—system Y—then cross peaks due to pathways *v*, *vi*, *vii*, and *viii* will appear.

by

$$\hat{H}_0 = \begin{pmatrix} 0 & 0 & 0 & 0 \\ 0 & \epsilon_1 & 0 & 0 \\ 0 & 0 & 0 & 0 \\ 0 & 0 & 0 & \epsilon_2 \end{pmatrix} \quad \hat{V} = \begin{pmatrix} 0 & \mu_1 & 0 & 0 \\ \mu_1^* & 0 & 0 & 0 \\ 0 & 0 & 0 & \mu_2 \\ 0 & 0 & \mu_2^* & 0 \end{pmatrix}. \quad (2.30)$$

The block-diagonal nature of this matrix prevents states $|1\rangle$ and $|2\rangle$ from evolving with the same phase. This system will have a spectrum without cross peaks, and any temporal beatings in the signal oscillations that occur are due to macroscopic polarization interference [71].

The sum-over-states model provides a glimpse into the expected signal contributions for non-interacting particles. This model allows us to interpret the information present in the spectrum quickly. It can reveal insights into the energy levels, dephasing times, lifetimes, inhomogeneities, and dipole transitions. Deviations from this model indicate that interactions are both present in the material and strong enough to manifest themselves in the signal.

2.3 Bloch equations

The sum-over-states model can successfully reproduce spectra when exciton-exciton interactions are not present. The Bloch equations can incorporate exciton-exciton interactions phenomenologically in the coherent optical response, and they reduce to an equivalent form of the sum-over-states model when the fields are perturbatively small. This model uses the differential form of the quantum-Liouville equation, and its solutions require numerical integration of a system of coupled equations.

The complete derivation of these equations is presented in many textbooks [16, 38, 100, 196–198]; here, we outline the derivation and show how various interactions are incorporated to support the experiments presented in future chapters². The derivation can either begin in an electron-hole space that includes the Coulomb correlation and the dispersion relations explicitly—this leads to an equivalent form of the nonlinear exciton equations called the semiconductor Bloch equations developed in the next section—or it can begin in the exciton basis. The exciton basis, which we use here, incorporates the Coulomb correlations implicitly. This leads to a phenomenological treatment of the many-body interactions. The equations derived in the phenomenological approach are called the modified optical Bloch equations.

²I gratefully acknowledge contributions by Patrick Wen. He simulated the spectra in Chapter 5 through tedious algebraic derivations and careful computer programming. My role was basically limited to suggesting what signals should be simulated using this model.

In the exciton basis, the density matrix and the Hamiltonian describe the ground state and each exciton or multiexciton state just as in the sum-over-states model. An n -level system has a Hamiltonian with n diagonal matrix elements containing the energy of each state and its lifetime. The off-diagonal elements contain the electric field interactions and the dephasing parameters. For example, the four-level Hamiltonian given in Eqn. 2.31 is used to represent the ground (g), H exciton (X), HH biexciton (B), and HHH triexciton (T) states. We use this Hamiltonian in the simulations in Ch. 5. Optical transitions are allowed between states with ± 1 number of electron-hole pairs composing the states such that

$$\hat{H}(t) = -i \begin{bmatrix} 0 & \Delta_l(t) - i\gamma_{Xg} & 0 & 0 \\ \Delta_l^*(t) + i\gamma_{Xg} & \epsilon_X - i\Gamma_X & \Delta_l(t) - i\gamma_{BX} & 0 \\ 0 & \Delta_l^*(t) + i\gamma_{BX} & \epsilon_B - i\Gamma_B & \Delta_l(t) - i\gamma_{TB} \\ 0 & 0 & \Delta_l^*(t) + i\gamma_{TB} & \epsilon_T - i\Gamma_T \end{bmatrix}, \quad (2.31)$$

where ϵ_n and Γ_n represent the energy and lifetime of state n , respectively, and γ_{mn} represents the dephasing of the off-diagonal matrix elements, where n and $m \in \{X, B, T\}$, and $\Delta_l(t)$ represents the electric field provided by a laser pulse. The density matrix and Hamiltonian are inserted into the quantum-Liouville equation, and a set of coupled differential equations are derived. The density matrix for the example four-level system is given by

$$\rho = \begin{bmatrix} \rho_{gg} & \rho_{gX} & \rho_{gB} & \rho_{gT} \\ \rho_{Xg} & \rho_{XX} & \rho_{XB} & \rho_{XT} \\ \rho_{Bg} & \rho_{BX} & \rho_{BB} & \rho_{BT} \\ \rho_{Tg} & \rho_{TX} & \rho_{TB} & \rho_{TT} \end{bmatrix}, \quad (2.32)$$

where time dependence has been suppressed. Generalized diagonal density matrix elements derived from the quantum-Liouville equation describe the population dynamics,

$$\frac{d}{dt}\rho_{aa} = -\Gamma_{aa}\rho_{aa} + i[(\rho_{a,a-1} - \rho_{a+1,a})\Delta_l(t) - (\rho_{a-1,a} + \rho_{a,a+1})\Delta_l^*(t)], \quad (2.33)$$

and off-diagonal elements describe the coherence terms,

$$\begin{aligned} \frac{d}{dt}\rho_{ab} = & -\gamma_{ab} + i[\omega_{ab}\rho_{ab} + (\rho_{aa} - \rho_{bb} + \rho_{a,b-1} - \rho_{a+1,b})\Delta_l(t) \\ & + (-\rho_{bb} + \rho_{aa} - \rho_{a-1,b} + \rho_{a,b+1})\Delta_l^*(t)], \end{aligned} \quad (2.34)$$

where $\omega_{ab} = \epsilon_a - \epsilon_b$. These coupled equations are not transformed to integrals. Instead, realistic electric field interactions—rather than impulse functions—can be

included, and the equations can be solved through numerical integration techniques. Eqns. 2.33 and 2.34 are the optical Bloch equations.

The wave vector dependence is incorporated using a spatial Fourier expansion of the matrix elements to determine which components contribute to signals in a particular direction (the phase-matched direction) [199–202]. Since the equations are not perturbative, in this discussion ‘order’ refers to the spatial direction, not the susceptibility. In principle, the wave vector expansion of the density matrix elements can result in a large number of coupled equations. For example, if two fields were used, the interaction with the system could be written as

$$\Delta_l(t) = \mu \cdot E_-(t)e^{-i(\mathbf{K}-\mathbf{k})\cdot\mathbf{r}} + \mu \cdot E_+(t)e^{-i(\mathbf{K}+\mathbf{k})\cdot\mathbf{r}}, \quad (2.35)$$

where μ is the dipole moment of the transition and $E_+(t)$ and $E_-(t)$ are the electric fields in the $\mathbf{K} + \mathbf{k}$ and $\mathbf{K} - \mathbf{k}$ directions, respectively. Describing the wave vectors of the two fields in this manner allows one to count spatial expansion orders easily. The density matrix elements are then expanded in terms of these wave vectors,

$$\rho_{aa} = \sum_{A=-m}^{+m} \rho_{aa,A} e^{iA\mathbf{k}\cdot\mathbf{r}} \quad (2.36)$$

and

$$\rho_{ab} = \sum_{A=-m}^{+m} \rho_{ab,A} e^{i(|b-a|A\mathbf{k}+\mathbf{k})\cdot\mathbf{r}}. \quad (2.37)$$

In our approach, we truncate A at $\pm m$ using the desired spatial expansion order. For example, in the fifth-order expansion, any term with $|A| > 5$ is set to zero.

The standard approach is to assume the system begins in only the ground state: initially only $\rho_{gg,0}$ is nonzero. At first order, the fields will couple $\rho_{gg,0}$ to $\rho_{Xg,\pm 1}$, and so forth for higher orders. This hierarchy of equations is organized with respect to the order of the field, and lower-order elements act as sources for the higher-order density matrix elements. Additional field interactions can cause higher-order elements to act as sources for lower-order elements. A portion of the set of equations for the four-level system example is shown in Fig. 2-5. This hierarchy represents signals in positive- \mathbf{k} directions where lower-order terms are sources for higher-order terms. The set of differential equations for signal in negative- \mathbf{k} directions is represented by the same hierarchy except solid (dashed) lines represent multiplication by $\mu \cdot E_-(t)$ ($\mu \cdot E_+(t)$) and all elements have negative- \mathbf{k} indices (for example, $\rho_{gX,-1}$ instead of $\rho_{gX,1}$). Not shown in Fig. 2-5 are transitions for which higher-order terms are sources

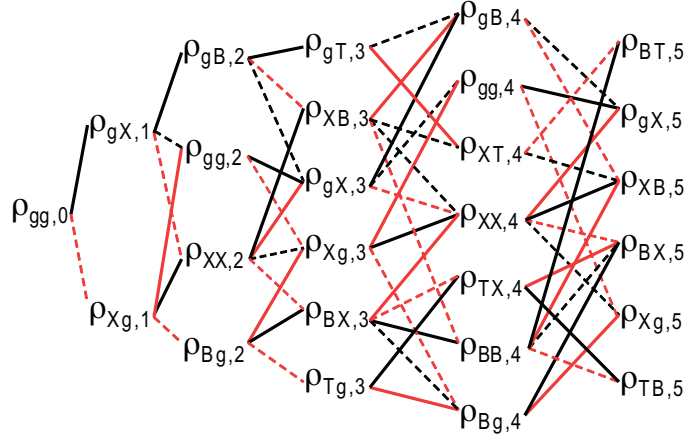


Figure 2-5: Hierarchy of differential equations for a portion of the fifth-order signal in Ch. 5. Lower-order terms act as source terms for higher-order terms. Solid (dashed) lines represent multiplication of lower order terms with $\mu \cdot E_+(t)$ ($\mu \cdot E_-(t)$) before addition (black lines) or subtraction (red lines) to differential equation of higher order terms. Some transitions—higher-order terms leading to lower-order terms—are not shown. For example, $\rho_{Xg,1}$ can lead to terms $\rho_{XX,2}$ (shown) and $\rho_{XX,0}$ (not shown).

for lower-order terms. Representative equations for the fifth-order example include

$$\frac{d}{dt}\rho_{Xg,5} = [-\gamma_{Xg} + i\omega_{Xg}]\rho_{Xg,5} + i\mu \cdot [-E_-(t) \cdot \rho_{Bg,4} - E_+^*(t) \cdot \rho_{gg,4} + E_+^*(t) \cdot \rho_{XX,4}], \quad (2.38)$$

$$\begin{aligned} \frac{d}{dt}\rho_{BX,5} &= [-\gamma_{BX} + i\omega_{BX}]\rho_{BX,5} + i\mu \cdot [E_-^*(t) \cdot \rho_{Bg,4} \\ &\quad - E_-(t) \cdot \rho_{TX,4} - E_+^*(t) \cdot \rho_{XX,4} + E_+^*(t) \cdot \rho_{BB,4}], \end{aligned} \quad (2.39)$$

$$\begin{aligned} \frac{d}{dt}\rho_{Xg,3} &= [-\gamma_{Xg} + i\omega_{Xg}]\rho_{Xg,3} + i\mu \cdot [E_+(t) \cdot \rho_{Bg,4} - E_-(t) \cdot \rho_{Bg,2} \\ &\quad + E_-^*(t) \cdot (\rho_{XX,4} - \rho_{gg,4}) + E_+^*(t) \cdot (\rho_{XX,2} - \rho_{gg,2})], \end{aligned} \quad (2.40)$$

$$\begin{aligned} \frac{d}{dt}\rho_{gX,1} &= [-\gamma_{gX} + i\omega_{gX}]\rho_{gX,1} + i\mu \cdot [-E_+(t) \cdot \rho_{Bg,2} - E_-(t) \cdot \rho_{Bg,0} \\ &\quad + E_-^*(t) \cdot (\rho_{XX,2} - \rho_{gg,2}) + E_+^*(t) \cdot (\rho_{XX,0} - \rho_{gg,0})], \end{aligned} \quad (2.41)$$

and

$$\frac{d}{dt}\rho_{TB,5} = [-\gamma_{TB} + i\omega_{TB}]\rho_{TB,5} + i\mu \cdot [E_-^*(t) \cdot \rho_{TX,4} - \mu \cdot E_+^*(t) \cdot \rho_{BB,4}]. \quad (2.42)$$

The terms $\rho_{Bg,0}$ and $\rho_{XX,0}$ in Eqn. 2.41 are not illustrated in Fig. 2-5.

Many-body interactions such LFE, EID, and EIS can be incorporated by inserting phenomenological terms. Although we do not use the ubiquitous but nebulous term, the signals these terms produced were often called *interaction-induced* effects [38, 203]. Local fields act as density-dependent source terms that modify the field interaction, and they are included by introducing a new electric field, $\Delta(t)$, that includes the original electric field, $\Delta_l(t)$, and the LFE, as given by

$$\Delta(t) = \Delta_l(t) + \Delta^{LFE}(t), \quad (2.43)$$

where

$$\Delta^{LFE}(t) = \mu N l [\mu \rho_{Xg,-1}(t) e^{-i(\mathbf{K}-\mathbf{k})\cdot\mathbf{r}} + \mu \rho_{Xg,+1}(t) e^{-i(\mathbf{K}+\mathbf{k})\cdot\mathbf{r}}]. \quad (2.44)$$

We neglect terms such as $\rho_{BX,\pm 1}$, which, although they have the appropriate spatial order to be included in the total LFE source, they are generated by multiple field interactions. The density of excitons in the system is given by N . The excitation-induced effects are modifications to the dephasing rate, γ' , and frequency, ω' . Including all three effects results in equations of motion with the following forms. Coherence terms have the form

$$\begin{aligned} \frac{d}{dt} \sum_A \rho_{ab,A} = & [-(\gamma_{ab} + \gamma'_{ab} N \sum_A \rho_{aa,A}) + i(\omega_{ab} + \omega'_{ab} N \sum_A \rho_{aa,A})] \sum_A \rho_{ab,A} \\ & + i(\sum_A \rho_{aa,A} + \sum_A \rho_{ab,A}) \Delta(t), \end{aligned} \quad (2.45)$$

and population terms have the form

$$\frac{d}{dt} \sum_A \rho_{aa,A} = - \sum_A \Gamma_{aa} \rho_{aa,A} + i \sum_A \rho_{ab,A} \Delta(t), \quad (2.46)$$

where we can collect terms having the same spatial expansion order (given by the value of A) and equate them. Two elements from our fifth-order example are the complete equations for $\rho_{Xg,5}$ and $\rho_{gX,1}$,

$$\begin{aligned} \frac{d}{dt} \rho_{Xg,5} = & [-\gamma_{Xg} + i\omega_{Xg}] \rho_{Xg,5} + i\mu \cdot [-E_-(t) \cdot \rho_{Bg,4} - E_+^*(t) \cdot \rho_{gg,4} \\ & + E_+^*(t) \cdot \rho_{XX,4}] + (\gamma' + i\omega') N [\rho_{Xg,1} (\rho_{XX,4} + \rho_{BB,4} + \rho_{TT,4}) \\ & + \rho_{Xg,3} (\rho_{XX,2} + \rho_{BB,2} + \rho_{TT,2}) \\ & + \rho_{Xg,5} (\rho_{XX,0} + \rho_{BB,0} + \rho_{TT,0})], \end{aligned} \quad (2.47)$$

and

$$\begin{aligned}
\frac{d}{dt}\rho_{gX,1} = & [-\gamma_{gX} + i\omega_{gX}]\rho_{gX,1} + i\mu \cdot [-E_+(t) \cdot \rho_{Bg,2} - E_-(t) \cdot \rho_{Bg,0} \\
& + E_-^*(t) \cdot (\rho_{XX,2} - \rho_{gg,2}) + E_+^*(t) \cdot (\rho_{XX,0} - \rho_{gg,0})] \\
& + (\gamma' + i\omega')N[\rho_{gX,-3}(\rho_{XX,4} + \rho_{BB,4} + \rho_{TT,4}) \\
& + \rho_{gX,-1}(\rho_{XX,2} + \rho_{BB,2} + \rho_{TT,2}) \\
& + \rho_{gX,1}(\rho_{XX,0} + \rho_{BB,0} + \rho_{TT,0}) \\
& + \rho_{gX,3}(\rho_{XX,-2} + \rho_{BB,-2} + \rho_{TT,-2}) \\
& + \rho_{gX,5}(\rho_{XX,-4} + \rho_{BB,-4} + \rho_{TT,-4})]. \tag{2.48}
\end{aligned}$$

In the equation for $\rho_{gX,1}$, Eqn. 2.48, there are no terms in the $\rho_{gX,-5}$ direction because—even though the resulting signal is fifth-order—such terms would require sixth-order populations, $\rho_{XX,6}$ for example, which are excluded from our spatial expansion. Similarly, there are no terms due to $\rho_{Xg,-1}$ in Eqn. 2.47.

The simplified equations, Eqns. 2.45 and 2.46, show that the EID and EIS terms provide density-dependent modifications to the real and imaginary parts, respectively, of coherences.

2.4 Nonlinear exciton equations

The nonlinear exciton equations [204–208]—identical to the dynamics controlled truncation formalism [200, 201] and related to the semiconductor Bloch equations [197]—have been extended recently to simulate 2D FTOPT experiments of excitonic many-body interactions in semiconductor nanostructures [147, 198, 209–211].

This model does not re-diagonalize the Hamiltonian into exciton states like the previous two models. Instead, it assumes the sample is a linear chain of oscillators, and each oscillator can couple to its neighbors, as illustrated in Fig. 2-6. No additional levels or phenomenological many-body terms are assumed. The model uses a multi-band, one-dimensional tight-binding Hamiltonian that captures the possible electron and hole combinations of the system, and the linear chain has a finite number of sites with periodic boundary conditions. Because calculating a 2D FTOPT spectrum requires significant computation time using this model, the number of sites is reduced to the minimum number required to maintain the convergence of the exciton energies; current simulations of three-band systems (electrons, heavy-holes, and light-holes) use ten sites.

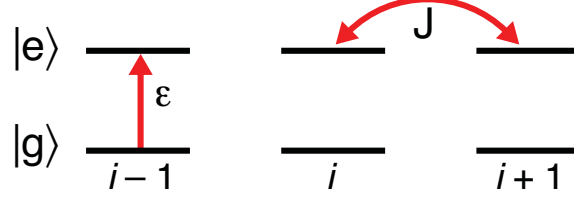


Figure 2-6: In the nonlinear exciton equations, a photon can excite an electron-hole pair on each site, i , and sites can couple to nearest neighbors, $i \pm 1$, with a strength J .

The total Hamiltonian is composed of three terms

$$\hat{H} = \hat{H}_0 + \hat{H}_C + \hat{H}_L. \quad (2.49)$$

The light-matter interaction is given by

$$\hat{H}_L = -\mathbf{E}(t) \cdot \hat{\mathbf{P}}, \quad (2.50)$$

where the electric field is time-dependent, not a δ -function, and the interband polarization operator, $\hat{\mathbf{P}}$, has a familiar form. It depends on the dipole moment connecting the conduction band, e , to the valence band, h , through excitation on sites i and j , as given by

$$\hat{\mathbf{P}} = \sum_{ijeh} [\mu_{ij}^{he} p_{ij}^{he} + H.C.]. \quad (2.51)$$

The polarization operator is given by

$$p_{ij}^{he} = \langle d_i^h c_j^e \rangle. \quad (2.52)$$

The interband transition dipoles μ_{ij}^{he} are governed by two rules. The first is the set of selection rules of the system. The second is that light can only create or destroy an electron and hole that share a site, so, for an allowed transition between valence band h and conduction band e ,

$$\mu_{ij}^{he} \propto \delta_{ij}. \quad (2.53)$$

The free-band Hamiltonian and the coupling between different sites is given by

$$H_0 = \sum_{ije} T_{ij}^e c_i^{e\dagger} c_j^e + \sum_{ijh} T_{ij}^h d_i^{h\dagger} d_j^h, \quad (2.54)$$

where $c_i^{e\dagger}$ (c_i^e) represents the creation (destruction) operators of electrons in site i from the conduction band e , and $d_i^{h\dagger}$ (d_i^h) represent the same operators for the holes in the valence band h . The diagonal elements $T_{i=j}^{eh}$ correspond to site energies for each

electron (in the conduction band) or hole (in the valence band). The off-diagonal elements $T_{i \neq j}^{eh}$ represent couplings between the different sites, labeled J in Fig. 2-6. The nearest-neighbor tight-binding approximation for electronic coupling is typically used: $T_{ij}^{eh} = 0$ for $|i - j| > 1$. The Coulomb interaction term is given by

$$\hat{H}_C = \frac{1}{2} \sum_{ij} \left(\sum_{e'} c_i^{e'\dagger} c_i^{e'} - \sum_{h'} d_i^{h'\dagger} d_i^{h'} \right) V_{ij} \left(\sum_e c_j^{e\dagger} c_j^e - \sum_h d_j^{h\dagger} d_j^h \right), \quad (2.55)$$

where the matrix element V_{ij} of the Coulomb potential energy has its $\frac{1}{r}$ form. In the model, this is given by

$$V_{ij} = U_0 \frac{d}{d|i - j| + a_0}, \quad (2.56)$$

where U_0 is an interaction strength, a_0 is a spatial cutoff, and d is the lattice constant for the material. The interaction term V_{ij} describes the Coulombic attraction and repulsion between particles at sites i and j . Alternatively, if the derivation were performed in a momentum basis to derive the related semiconductor Bloch equations, this term would describe the Coulomb forces between particles in different momentum states. Regardless, the Coulomb term has two primary effects: it renormalizes the electron and hole energies—it makes excitons!—and it can change the interaction strength of the field.

Inserting only the site energy (\hat{H}_0) and light-matter interaction (\hat{H}_L) portions of the Hamiltonian into the equations of motion, we obtain an equation involving only interband quantities,

$$-i\hbar \frac{d}{dt} p_{ij}^{he} = - \sum_n T_{jn}^e p_{in}^{he} - \sum_m T_{mi}^h p_{mj}^{he} + \mathbf{E}(t) \cdot \left[(\mu_{ij}^{he})^* \right] \quad (2.57)$$

$$- \sum_{abh'e'} \left[(\mu_{ib}^{he'})^* (p_{ab}^{h'e'})^* p_{aj}^{h'e} + (\mu_{bj}^{h'e})^* (p_{ba}^{h'e'})^* p_{ia}^{he'} \right], \quad (2.58)$$

that can be written in an abbreviated manner

$$-i\hbar \frac{d}{dt} p = -\hbar\omega p + \mu^* E - \mu^* E p^* p. \quad (2.59)$$

This equation has the same structure as the optical Bloch equations, Eqn. 2.34. The $\hbar\omega p$ term represents the single-particle energies, and the other two terms are the source, $\mu^* E$, and its phase-space filling correction, $(1 - p^* p)$. In this limit, the sum-over-states model parallels the nonlinear exciton equations [212].

Unfortunately, including the Coulomb portion of the Hamiltonian (\hat{H}_C) to capture all of the electron-hole interactions results in an infinite hierarchy of coupled equations

of motion. This set of equations is truncated based on the same spatial Fourier expansion as was done for the Bloch equations [200–202, 213]. To first order in the field E_a with wave vector \mathbf{k}_a and an exciton dephasing constant τ_X , the polarization is given by

$$-\left(i\hbar + \frac{i}{\tau_X}\right) \frac{d}{dt} p_{ij}^{he[\mathbf{k}_a]} = -\sum_n T_{jn}^e p_{in}^{he[\mathbf{k}_a]} - \sum_m T_{mi}^h p_{mj}^{he[\mathbf{k}_a]} + V_{ij} p_{ij}^{he[\mathbf{k}_a]} + \mathbf{E}_a(t) \cdot (\mu_{ij}^{he})^*. \quad (2.60)$$

The trace of the density matrix is the polarization,

$$\mathbf{P}^{[\mathbf{k}_a]}(t) = \sum_{ijhe} \mu_{ij}^{he} p_{ij}^{he[\mathbf{k}_a]}(t), \quad (2.61)$$

and the computation and its result are presented in Appendix B. The signal is computed using an adaptive Runge-Kutta algorithm that estimates the error to adjust the step size as needed.

The equations can also be truncated at third order. In a simulation of the ‘self-diffraction’ measurement, there would be two beams, one with wave vector \mathbf{k}_a and the other with wave vector \mathbf{k}_b . The first-order polarizations for the two input beams given by Eqn. 2.60 are source terms for the higher-order polarizations. Here, the correlated two-exciton amplitudes are defined by

$$B_{lkij}^{h'e'he} \equiv \langle d_l^{h'} c_k^{e'} d_i^h c_j^e \rangle + \langle p_{lj}^{h'e} \rangle \langle p_{ik}^{he} \rangle - \langle p_{lk}^{h'e'} \rangle \langle p_{ij}^{he} \rangle. \quad (2.62)$$

The following equations of motion govern the time-dependence of the polarization, where the exciton and two-exciton dephasing times are described by τ_X and τ_{XX} , respectively,

$$\begin{aligned} -\left(i\hbar + \frac{i}{\tau_X}\right) \frac{d}{dt} p_{ij}^{he[\mathbf{k}_{sig}]} &= -\sum_n T_{jn}^e p_{in}^{he[\mathbf{k}_{sig}]} - \sum_m T_{mi}^h p_{mj}^{he[\mathbf{k}_{sig}]} + V_{ij} p_{ij}^{he[\mathbf{k}_{sig}]} \\ &+ \sum_{klh'e'} (V_{kj} - V_{ki} - V_{lj} + V_{li}) \left[(p_{lk}^{h'e'[\mathbf{k}_a]})^* p_{lj}^{h'e[\mathbf{k}_b]} p_{ik}^{he'[\mathbf{k}_b]} \right. \\ &- (p_{lk}^{h'e'[\mathbf{k}_a]})^* p_{lk}^{h'e'[\mathbf{k}_b]} p_{ij}^{he[\mathbf{k}_b]} - (p_{lk}^{h'e'[\mathbf{k}_a]})^* B_{lkij}^{h'e'he} \left. \right] \\ &+ \mathbf{E}(t) \cdot \left[(\mu_{ij}^{he})^* - \sum_{klh'e'} \left[(\mu_{il}^{he'})^* (p_{kl}^{h'e'[\mathbf{k}_a]})^* p_{kj}^{h'e[\mathbf{k}_b]} \right. \right. \\ &\left. \left. - (\mu_{lj}^{h'e})^* (p_{lk}^{h'e'[\mathbf{k}_a]})^* p_{ik}^{he'[\mathbf{k}_b]} \right] \right], \end{aligned} \quad (2.63)$$

and

$$\begin{aligned}
-\left(i\hbar + \frac{i}{\tau_{XX}}\right) \frac{d}{dt} B_{lki j}^{h'e'he} &= -\sum_m \left(T_{jm}^e B_{lkim}^{h'e'he} + T_{mi}^h B_{lkmj}^{h'e'he} + T_{km}^e B_{lmi j}^{h'e'he} + T_{ml}^h B_{mki j}^{h'e'he} \right) \\
&+ (V_{lk} + V_{lj} + V_{ik} + V_{ij} - V_{li} - V_{kj}) B_{lki j}^{h'e'he} \\
&- (V_{lk} + V_{ij} - V_{li} - V_{kj}) p_{ik}^{he[\mathbf{k}_b]} p_{lj}^{h'e[\mathbf{k}_b]} \\
&+ (V_{ik} + V_{lj} - V_{li} - V_{kj}) p_{lk}^{h'e'[\mathbf{k}_b]} p_{ij}^{he[\mathbf{k}_b]},
\end{aligned} \tag{2.64}$$

The meaning of conjugate and nonconjugate fields is clear in the above equations. As the conjugate field in the self-diffraction measurement, polarizations due to field E_a are conjugated, $(p_{ij}^{he[\mathbf{k}_a]})^*$, whereas polarizations due to field E_b are not, $p_{ij}^{he[\mathbf{k}_b]}$. Calculating third-order spectra incorporating the full equations presented here for a three-band model with co-linear polarization including the full Coulomb coupling using ten sites takes approximately one month of computation time on a 64 bit Opteron processor [210]. Fifth-order expressions involving full six-particle correlations would take much longer because the computations would scale as the sixth power of the number of sites.

The third-order equations above can be written in abbreviated form as

$$-i\hbar \frac{d}{dt} p = -\hbar\omega_x p + V p^* p p + V p^* B + \mu^* E - \mu^* E p^* p, \tag{2.65}$$

and

$$-i\hbar \frac{d}{dt} B = -\hbar\omega_{2x} B + V p p p. \tag{2.66}$$

The abbreviated form of the emitted field equation has exciton energies $\hbar\omega_x$, two-exciton energies $\hbar\omega_{2x}$, phase-space filling (also called Pauli blocking) term $\mu^* E p^* p$, first-order many-body Coulomb contribution $V p^* p p$, and many-body Coulomb correlation $V p^* B$.

The above equations are rather complicated. Nevertheless, we can understand some of the underlying physics qualitatively by examining their forms. First we discuss the consequences of beam polarization. In our sample, which we discuss at length in the next section, circularly polarized light allows only specific transitions between the conduction and valence bands. The consequence of the selection rules is that some transitions μ_{ij}^{he} are zero even when $i = j$. If this is the case, the value of $p_{ij}^{he[\mathbf{k}_a, \mathbf{b}]}(t)$ will be zero for all time. If the third-order signal is desired, this first-order polarization is inserted into the equation for B , causing either the third or fourth lines of Eqn. 2.64 to be zero. Since the equation governing B is a differential equation, this changes the frequency of the two-quantum oscillation. In this manner,

cross-polarized fields that cause biexciton–ground-state coherences reduce the rate at which B changes, reducing the value of the two-quantum frequency.

We can extract at least one more important physical insight from the equations. The Vp^*B term results in two-exciton correlations that are weighted by the value of Vp^* . Similarly, in Eqn. 2.63, the two-exciton dynamics are weighted in the sum by a conjugate first-order polarization, $-(p_{lk}^{h'e'[ka]})^*$ and the Coulomb coupling factors V_{ab} . As we will see, 2D FTOPT S_{III} scans measure the B dynamics along the two-quantum dimension and the Vp^*B dynamics along the emission dimension, and the value of the biexciton binding energy can be altered in the emission dimension.

One approximation method used to decrease the computation time is the Hartree-Fock approximation. This method supposes that the Coulomb correlation terms (any term involving B) is small. Mathematically, the four-particle correlation function is reduced to a product of two two-particle correlation functions,

$$\langle d_l^{h'} c_k^{e'} d_i^h c_j^e \rangle \approx p_{lk}^{h'e'} p_{ij}^{he} - p_{lj}^{h'e} p_{ik}^{he'} = \langle d_l^{h'} c_k^{e'} \rangle \langle d_i^h c_j^e \rangle - \langle d_l^{h'} c_j^e \rangle \langle d_i^h c_k^{e'} \rangle. \quad (2.67)$$

This approximation eliminates the B term and doing so decreases computation times dramatically. Unfortunately, simulations under this approximation reproduce 2D FTOPT experiments poorly [41, 143, 209].

The Pauli-blocking approximation removes both the four-particle correlations, B , and the first-order Coulomb terms, Vp^*pp . This approximation only incorporates the μEp^*p term, which describes how the number of allowed transitions to the excited states decreases as the excited states become populated. This term is important in discrete systems where the Pauli exclusion principle plays a large role in the system energetics, and in extended systems at high densities where absorption saturation may occur.

2.5 Material properties of GaAs

The nonlinear spectroscopy methodology described in this chapter can be—and has been—used to study a wide variety of samples in which electronic correlations are present. This thesis applies these techniques to GaAs. Therefore, in this section we detail background information about the electronic properties of our sample, the GaAs quantum well.

Although coherent exciton dynamics and correlations have been studied in a many materials—ZnO [214, 215], ZnSe [216], CuCl [217], and more—GaAs remains favored because the interactions are strong enough to induce exciton-exciton correlations

Table 2.2: Properties of GaAs

electron effective mass (m_e^*)	$0.06 m_e^a$
heavy hole effective mass (m_H^*)	$0.5 m_e$
light hole effective mass (m_L^*)	$0.08 m_e$
dielectric constant	12
lattice constant	5.5 \AA
exciton Bohr radius	10 nm
crystal structure	zinc blende
coordination geometry	tetrahedral

^aThe mass of a free electron (m_e) is 9.1×10^{-31} Kg.

but weak enough to allow long coherence times. For example, biexciton coherences in GaAs remain coherent for about 2 ps, whereas biexciton coherences in ZnO dephase in about 100 fs. Many semiconductor nanostructures, including GaAs quantum wells, are grown using molecular beam epitaxy, a deposition technique developed in the 1960s [218]. Commercial devices often incorporate GaAs because it is a direct-gap semiconductor (unlike silicon) with excellent optoelectronic properties, and it can be nanofabricated. It is used in a range of applications including photovoltaics, high-performance transistors, LEDs, and solid state lasers [219]. Thus, many of its properties have been measured [220, 221]; several are listed in Table 2.2. Notably, GaAs has a high dielectric constant and a large exciton Bohr radius. The effective masses of the light-holes and conduction-band electrons are nearly equal, indicating that their spatial distributions are roughly equivalent. On the other hand, the heavy-hole effective mass is much larger. Its wavefunction is more strongly modulated by the nuclei.

The electrons and holes that compose the excitons originate in the underlying atomic orbitals of the Ga and As atoms. Isolated Ga atoms have three valence electrons; isolated As atoms have five valence electrons. Fig. 2-7(a) illustrates the relative energy levels of the atomic orbitals for each atom and hypothetical ‘molecular’ orbitals created when viewing GaAs as a diatomic molecule. This representation is useful for determining the selection rules of the solid because the valence band wave functions in GaAs have angular momentum properties similar to p -orbital wave functions, and similarly the conduction band wave functions have angular momentum properties similar to s -orbital wave functions³. The eight valence electrons fill the lowest molecular orbitals, and the incident light promotes an electron from a π orbital

³For more details, see Sec. 6.1.3 in Ref. [38], Sec. 2.6.2 in Ref. [25], and Ch. 19 in Ref. [17].

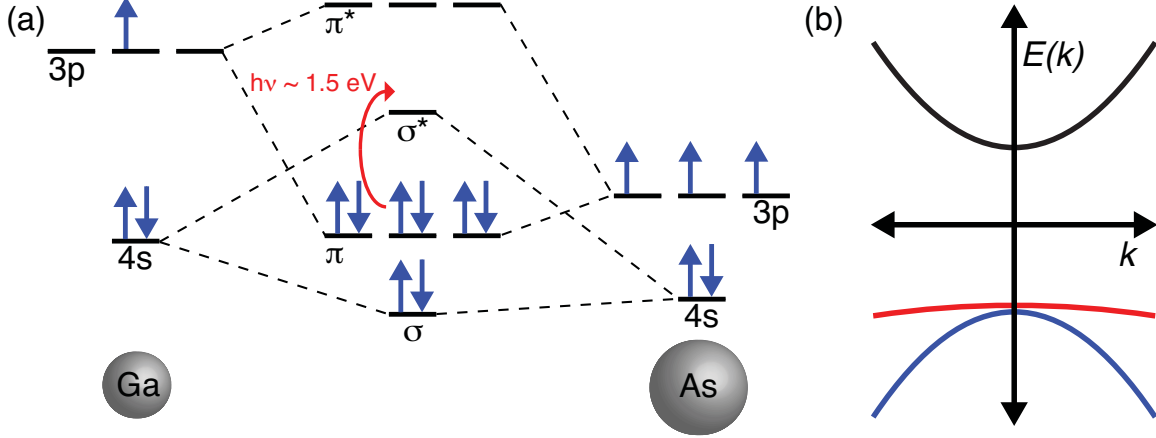


Figure 2-7: The III-V semiconductor GaAs. (a) Underlying atomic orbitals of the solid. Ga atoms have three valence electrons and As atoms have five. The eight electrons fill the lowest-occupied s -like (σ) and p -like (π) ‘molecular’ orbitals. The incident light promotes the electron from a π orbital to a σ^* orbital. These orbitals are used to understand the selection rules of the valence and conduction bands of the semiconductor. (b) Relevant bands of GaAs. The electrons reside in the conduction band (black) and the holes (H and L) reside in the valence bands (red and blue, respectively).

to a σ^* orbital. These molecular orbitals become related the dispersion curves in the band diagram shown in Fig. 2-7(b) when many atoms form a solid.

To determine the optical selection rules, we must consider the total angular momentum of each particle. The total angular momentum (\mathbf{J}) is the sum of the particle spin (\mathbf{S}) and the orbital angular momentum (\mathbf{L}) vectors,

$$\mathbf{J} = \mathbf{L} + \mathbf{S}. \quad (2.68)$$

Electrons are spin one-half particles with $|\mathbf{S}| = \frac{1}{2}$. Holes can be viewed as particles with spin $|\mathbf{S}| = \frac{1}{2}$. The orbital angular momentum is less straightforward. An excited electron resides in a conduction band that has angular momentum properties similar to a σ molecular orbital with $|\mathbf{L}_\sigma| = 0$. Thus the total angular momentum of the electron is one-half, $|\mathbf{J}_e| = \frac{1}{2}$. A hole resides in a valence band that has angular momentum properties similar to a π molecular orbital with $|\mathbf{L}_\pi| \in \{0, 1\}$, and thus the total angular momentum of a hole can have two values, $|\mathbf{J}_h| \in \{\frac{1}{2}, \frac{3}{2}\}$. Holes with $|\mathbf{J}_h| = \frac{1}{2}$ reside in the so-called ‘split-off’ band. At the band edge ($\mathbf{k} = 0$), they are split by about 0.5 eV from holes with $|\mathbf{J}_h| = \frac{3}{2}$. This band is not depicted in Fig. 2-7(b) and it will not be considered further because excitations from it to the conduction band are not resonant with the laser spectrum. This leaves two possible total angular momentum values for an electron, $m_j^e \in \{\pm\frac{1}{2}\}$, and four possible values for a hole, $m_j^h \in \{\pm\frac{1}{2}, \pm\frac{3}{2}\}$. In our quantum well sample, the confinement stress

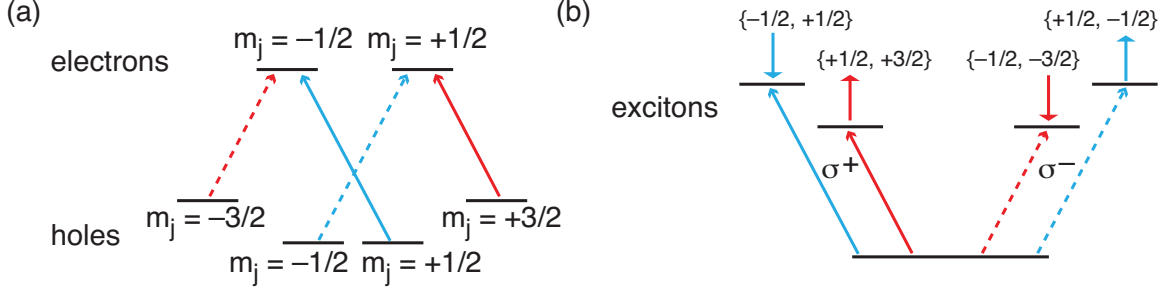


Figure 2-8: Optical selection rules for electron excitation. Quantum confinement splits the two valence bands by about 6 meV. Solid (dashed) lines indicate left (right) polarized light. (a) In the band representation, a photon can promote an electron from one of the four (two pairs of degenerate) valence bands to one of the two (degenerate) conduction bands. This is often called the electron-hole representation because after optical excitation, electrons reside in the conduction band and holes reside in the valence band with the given angular momentum values. (b) In this frequently used ‘excitonic’ representation, optical fields couple the four exciton states to the ground state.

separates the $m_j^h = \pm\frac{1}{2}$ band about 6 meV from the $m_j^h = \pm\frac{3}{2}$ band.

The allowed optical transitions between the bands are shown in Fig. 2-8(a), where each particle is denoted by its angular momentum value. Photons promote electrons from the valence bands to the conduction bands. Thus this is called the ‘electron-hole’ representation. Spectroscopists often change the representation to the ‘quasi-particle’ or ‘excitonic’ view, illustrated in Fig. 2-8(b). In this representation, light can cause excitation from the ground state to any of the four exciton states as illustrated: spin-up heavy-hole, $|\uparrow\rangle$, spin-down heavy-hole, $|\downarrow\rangle$, spin-up light-hole, $|\uparrow\rangle$, and spin-down light-hole, $|\downarrow\rangle$. Each type of exciton is denoted in Fig. 2-8(b) by the {electron, hole} angular momentum values. There are two H excitons, $\{\pm\frac{1}{2}, \pm\frac{3}{2}\}$ and two L excitons, $\{\mp\frac{1}{2}, \pm\frac{1}{2}\}$. The polarization and energy of the light can be used to excite specific electron-hole combinations. Crucially, circularly polarized light excites H and L excitons of different spin. For example, a σ^+ photon will create a spin-up H exciton, $|\uparrow\rangle$, but a spin-down L exciton, $|\downarrow\rangle$. The electron-hole representation is important because it illustrates that co-circular polarized fields create excitons that are *not* coupled through a common ground state; the excitons are independent two-level systems. Strong exciton-exciton interactions couple the two independent systems [77, 78, 143, 144]. Thus, although we use the excitonic representation throughout the thesis, it is important to note that a better representation would be to have two ground states: one for right-circular excitation and the other for left-circular excitation. We return to this discussion in Sec. 4.4.

The spectra presented in the following chapters will allow us to extract the properties of excitons and multiexcitons. Fig. 2-9 shows the relative energy levels of each

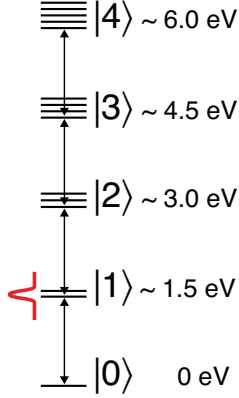


Figure 2-9: GaAs exciton and multiexciton states sought or observed in this work. The ladder of exciton states illustrates the ground state, $|0\rangle$, the two single exciton states, $|1\rangle$, the three biexciton states, $|2\rangle$, the four triexciton states, $|3\rangle$, and in principle the five quadexciton states, $|4\rangle$. The approximate energy of each set of levels is listed. The binding energies of the excitons are about 10 meV [222], and the binding energies of the multiexcitons will be shown to be about 1–2 meV. A typical spectrum of our laser field is indicated by the red line.

rung of the multiexciton ladder that was explored in our measurements. At each rung of the ladder, there are more possible bound multiexciton correlations formed by any combination of H and L exciton constituents; there are three possible biexcitons, four possible triexcitons, and five possible quadexcitons.

2.6 Summary

This chapter described how intense input electric fields provided by laser beams can interact with a sample to induce a nonlinear polarization which emits as the signal field. The nonlinear polarization was cast in the density matrix formalism where time evolution is governed by the quantum-Liouville equation.

Three treatments of the density matrix were described. Two methods—the sum-over-states and the Bloch equations—involved re-diagonalizing the Hamiltonian into a set of levels that implicitly include the Coulomb interactions as excitons and multiexcitons. The sum-over-states model includes an additional approximation about the form of the electric field so that the two-dimensional spectrum can be calculated with ease by drawing a set of easily interpretable Feynman diagrams. The nonlinear exciton equation approach requires time-consuming computations, but it can incorporate the Coulomb couplings between the charged particles in the system explicitly without re-diagonalizing the Hamiltonian. This method has resulted in calculated spectra that fit the experimental results well.

Chapter 3

Experimental Methods

This chapter begins with an orientation to femtosecond pulse shaping and its use in multidimensional spectroscopy. We then describe the construction, alignment, and calibration of the instrument used to make the measurements, the Coherent Optical Laser BEam Recombination Technique (COLBERT) spectrometer. We discuss the basic principles of beam shaping and pulse shaping. The measurement procedure is then outlined, and we conclude by showing how to extract a complex spectrum from the measured data.

3.1 Shaping femtosecond pulses

While the initial goal in the late 1980s in the field of femtochemistry was to monitor the transition states involved in chemical reactions [223, 224], it was soon recognized that the products of a reaction could be influenced by using carefully constructed laser pulses to direct the flow of electronic or vibrational energy. Early coherent control experiments were performed in the early 1990s [225–228], and the field has been reviewed many times [229–233]. One ultimate goal in this field is to control a chemical reaction to such an extent that one target product is produced above all other possible products; polarization, amplitude, and phase profiles of ultrafast pulses can be manipulated to reach the target product. Unfortunately, it is often hopeless to predict the optical waveform required to enhance or suppress a particular chemical product because intramolecular vibrational redistribution processes make the Hamiltonian completely intractable to theoretical analysis. Thus, instead of attempting to compute the desired waveform, iterative algorithms are often used in feedback-controlled loops in the laboratory [234, 235]. There are at least fifty demonstrations of coherent control in this fashion. These experiments often involve spatial light modulators (SLMs) to adjust the waveform characteristics.

Pulse shaping work in the Nelson group had focused on using a two-dimensional liquid crystal SLM to control collective lattice vibrations that travel at light-like speeds, or phonon-polaritons [236]. Recently, however, the group showed that pulse shaping with this device could be used to measure multidimensional FTOPT spectra [129, 140]. Pulse shapers have also been used in 2D IR measurements [237–242]. Basic pulse shaping involves separating the frequency components of an ultrafast pulse; manipulating the phase or amplitude, or both, of each frequency using an SLM; and then recombining the separated frequency components to form the modified ultrafast pulse. Canonical pulse shapes include time delays, phase shifts, pulse trains, and chirps.

Multidimensional FTOPT measurements involve nonlinear signals generated by a series of femtosecond pulses. During the time periods between field interactions, coherent superpositions of system eigenstates can evolve. Measuring coherent oscillations requires optical phase stability among most or all of the pulses. This requires careful instrumentation at optical wavelengths when the pulses are in different laser beams. Unlike the relatively standardized equipment of 2D NMR, multidimensional FTOPT measurements have been performed using a variety of approaches to stabilize the relative optical phases between pulses [128, 133–135, 137, 156, 157]. Most have involved a subset of the following optics: beam splitters, diffractive optics, wedges, and translation stages. Some use phase cancellation approaches to stabilize the device passively for a subset of possible scans [128, 133, 137, 156, 157]. Others can measure a variety of third-order signals using actively stabilized translation stages [135] or passively stabilized movable wedges [134]. In general, a major challenge arises from the randomization of the optical phase of a pulse each time it is delayed through movement of a mechanical delay stage or insertion of a variable thickness wedge in its path.

Our device [150–152] is distinct from the others in that it is versatile, has full passive phase stability, and has no moving parts. As we will see, it can also accommodate higher-order measurements with little additional effort, unlike other devices. At the heart of the instrument are twin 2D SLMs, one for 2D spatial beam shaping and the other for spatiotemporal pulse shaping. The COLBERT spectrometer makes the diverse array of 2D FTOPT measurements presented in the following chapters possible.

The number of possible nonlinear optical measurements is large. There are four essential parameters that can be used to organize most nonlinear optical experiments: the beam geometry, the pulse timing sequence, the spectral content of each pulse, and the optical polarization of each beam. The beam geometry sets the phase-matching

conditions, the number of field interactions per beam, and which are the conjugate and nonconjugate beams. The pulse time ordering determines whether a scan is rephasing or nonrephasing, and how many quanta are involved. The spectral content and polarization scheme describe which resonances are excited and in what ways the excitations can couple. In the COLBERT spectrometer, a spatial beam shaper sets the pulse geometry, a spatiotemporal pulse shaper changes the time orderings, individual waveplates set the beam polarizations, and the laser can be adjusted to vary the spectral content.

3.2 COLBERT construction

A Ti:sapphire oscillator was adjusted to produce a collimated beam that was 2 mm in diameter containing near-transform-limited 90 fs pulses (intensity FWHM, measured with FROG). The pulse spectra were centered at 806 nm, each pulse had an energy of about 5 nJ, and the laser repetition rate was 92.5 MHz. The pulse duration and center wavelength vary from measurement to measurement as we isolate specific interactions. We indicate the values of the parameters for each experiment.

A block diagram of the apparatus is illustrated in Fig. 3-1(a). The laser beam is first converted to a set of beams in a user-defined geometric pattern by the spatial beam shaper. The temporal waveform of the femtosecond pulse in each beam is set by the spatiotemporal pulse shaper. The pulses in all the beams are then focused into the sample and the radiated signal is measured by a spectrometer.

A more detailed schematic is presented in Fig. 3-1(b). The spatial beam shaper, illustrated in the blue box, is composed of three optics: a 150 cm focal length spherical lens (L1), a 2D spatial light modulator (SLM 1), and a second 150 cm spherical lens (L2). Both the beam shaper and the pulse shaper used SLMs (Hamamatsu X8267) with 768 by 768 pixels; the size of each pixel was 24 by 24 microns. The long focal length of lens L1 creates a focused spot with a large beam waist (~ 1 mm) at the SLM 1 surface which illuminates many pixels. This reduces the likelihood of damage, keeps the SLM in its linear operating range [243], and defines the specified phase pattern—which includes multiple periodic features to create the desired beams by diffraction of the incident beam—over many periods for each feature. The pattern encoded into SLM 1 is a pixelated version of the Fourier transform of the desired output geometry. In Sec. 3.5 we detail the consequences of pixelation. Any extra diffraction orders are blocked, and lens L2 collimates the beams into the desired arrangement.

The spatiotemporal pulse shaper is illustrated in the green box of Fig. 3-1(b). It is improved from previous designs [99, 140, 145, 148] for a fourfold increase in efficiency

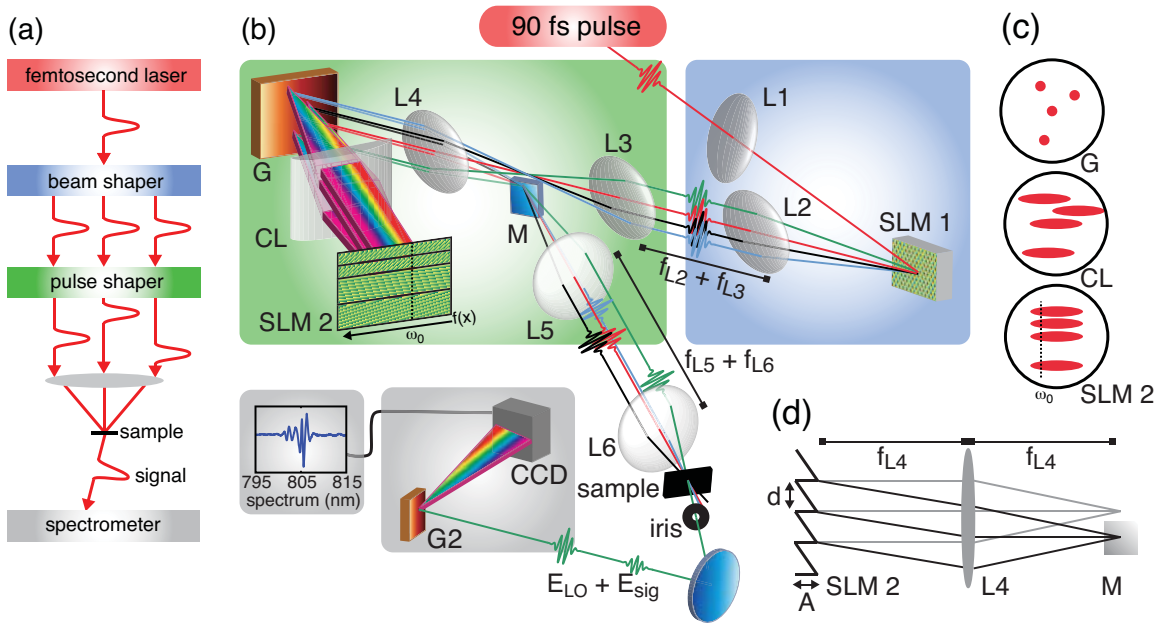


Figure 3-1: Experimental apparatus for coherent multidimensional spectroscopy. (a) The apparatus contains four essential components: a laser producing femtosecond pulses (red box), a spatial beam shaper producing a user-defined 2D geometrical arrangement of beams (blue box), a spatiotemporal pulse shaper capable of independently delaying each pulse in the set of beams (green box), and finally a signal detector which in this case is a spectrometer with a CCD array (grey box). The three-beam geometry is shown for clarity. For additional clarity, the final lens which collimates the signal and LO and the waveplates used to control the polarization of each beam are not shown. (b) A more detailed depiction of the apparatus following the same color-coding scheme as above but illustrating a four-beam, Y-shaped geometry. The spatial beam shaper is composed of two lenses and a 2D spatial light modulator (SLM 1). The spatiotemporal pulse shaper imparts delays and phase shifts to the pulses in the beams by constructing sawtooth phase grating patterns on the second 2D SLM (SLM 2). After lens L5, the beams have the geometry defined by SLM 1 with relative pulse timings and phases (or more general specified amplitude and phase profiles) defined by SLM 2. The signal is generated in the same direction as the LO; this beam is isolated by the iris. Their interference fringes are read by a CCD detector after diffraction by the grating in the spectrometer (G2). (c) The beam geometry at three points in the pulse shaper. The top arrangement illustrates propagation throughout most of the device. The middle is the beam arrangement at the plane of the cylindrical lens (CL) in the pulse shaper. The bottom arrangement shows how the beams are refocused on the SLM 2 surface so that a single frequency encounters one vertical column of pixels, regardless of which beam is considered. (d) The SLM 2 plane is focused by lens L4 to the plane of the pick-off mirror (M), which is adjusted to send only the desired first-order diffraction toward the sample.

by eliminating a dual-use beam splitter. The beams produced by the beam shaper are first focused and then recollimated by a pair of 75 cm focal length spherical lenses (L3 and L4). After recollimation, each beam reaches a vertically distinct region of a 1400 groove/mm diffraction grating (G). The frequency components are dispersed horizontally by the grating and focused by a cylindrical lens (CL) to vertically distinct bands across the surface of SLM 2, placed at the Fourier plane of the grating. The focal length of the CL depends on the pulse bandwidth. In normal operation, it ranges between 10 cm and 25 cm, and we often use a 12.5 cm focal length lens; in that case the distance between L4 and G is 50 cm. The beam geometry at three locations in the apparatus is shown in Fig. 3-1(c). The pulse shaper operates in diffraction mode [244, 245], which is shown in Fig 3-1(d) and detailed in Sec. 3.6. The shaped frequency components are recombined at the grating to produce the temporally shaped fields. The small vertical wave vector shifts—about 0.016° —imparted by the vertical sawtooth phase pattern of SLM 2 are converted by lens L4 to vertical spatial shifts—about 2 mm—as shown in Fig. 3-1(d). All orders of diffraction from SLM 2 are blocked except zero-order, which reflects back through the setup, and first-order, which is the desired order. The shaped pulses in the first-order diffraction are separated from the reflected input beams by a pick-off mirror (M), which redirects the diffracted beams towards a 100 cm focal length lens (L5). Lenses L3, L4, and L5 all share a common focal plane in which M is placed.

An optical isolator (Optics For Research O-5BB-800-HP) placed at the output of the laser before lens L1 prevents the zero-order diffraction that reflects back through the setup from disturbing the laser. The longer focal length of lens L5 increases the size of the geometry, allowing quarter-wave plates (Tower Optical AO12.7DZ 1/4 0800) to be placed in each beam without blocking the other beams. A large-diameter quarter-wave plate common to all of the beams was also used (Tower Optical AO25DZ 1/4 0800). This wave plate combination allowed us to select any required polarization configuration without inserting or removing any optics. We often place reflective neutral density filters between lenses L5 and L6 to attenuate the beams. Between these lenses, the pulses have the beam geometry defined by SLM 1 with relative timings and phases defined by SLM 2. The local oscillator beam—whose purpose is to superpose with the signal field generated by the other beams—is attenuated by a factor of 10^{-4} with a reflective neutral density filter (Thorlabs ND40A). The filter was etched carefully using a strong acid so that all beams propagate through the glass but only the LO is attenuated by the reflective coating. The beams are then focused by a 15 cm focal length spherical lens (L6) to a spot size with a radius of 40 microns to generate the phase-matched signal. The focused area was about 5×10^{-5} cm².

The sample consisted of ten periods of 10 nm thick GaAs separated by 10 nm $\text{Al}_{0.3}\text{Ga}_{0.7}\text{As}$ barriers, mounted on a sapphire plate, which was held in a cold-finger cryostat (Janis ST100, LakeShore 331 temperature controller) below 10 K. Not shown in Fig. 3-1(b) are a 15 cm focal length lens to collimate the signal and several extra routing mirrors. The signal is routed to the CCD camera (Princeton Instruments PIXIS 100) attached to an imaging spectrometer (Acton SpectraPro 300i). The spectrometer was calibrated using the sharp emission lines of an Ar lamp (Thorlabs). All eight lenses are two inches in diameter and were anti-reflective coated at 800 nm for greater efficiency. In conjunction with the optical isolator, the anti-reflective coatings prevented reflections from destabilizing the oscillator.

The device operates on the principle of relay imaging; any pulse-front tilt (spatial chirp) imparted to the optical pulses by SLM 1 is eliminated at the sample if the beams are imaged properly from their point of generation to the sample [246]. This means that the distance between each lens pair is such that the phase pattern applied by SLM 1 is reconstructed at the sample where the beams overlap spatially and temporally. Since higher-order diffractions from the beam shaper are blocked, it will not be an identical reconstruction but instead will only include the fundamental wave vector components encoded into SLM 1. For proper imaging, the distance between the last lens of the beam shaper (L2) and the first lens of the pulse shaper (L3) is the sum of their focal lengths, which in this case is 225 cm. Similarly, the distance between L5 and L6 is 115 cm. The total distance traveled by the pulses from lens L1 to the sample is 11.3 m. Including the distance from the sample to the spectrometer, the total path length is about 12.5 m. Although the distance is long, the relay imaging nature of the setup allows the beam pointing stability to remain high. Using different imaging ratios throughout the setup, particularly different lenses L2 and L3, could allow the path length to be reduced.

Because all the beam traverse the same set of optics, the optical phase stability is high. It was measured to be $\lambda/147$ over twelve minutes and $\lambda/88$ over fourteen hours, as depicted by the black line in Fig. 3-2. These times roughly correspond to the amount of time needed to acquire 2D and 3D spectra, respectively. We increased the phase stability (to $\lambda/219$ short-term and $\lambda/157$ long-term) by placing the laser on the same optical table as the spectrometer; they were previously on separate, uncoupled optical tables [99, 129, 140, 145, 148, 150, 151]. This phase stability is noteworthy because no special precautions—such as floating the tables or placing boxes around the device to minimize air currents, much less using interferometric feedback loops [135, 138]—were taken to minimize the phase fluctuations.

The efficiency of the setup, as measured from the laser output to the sample,

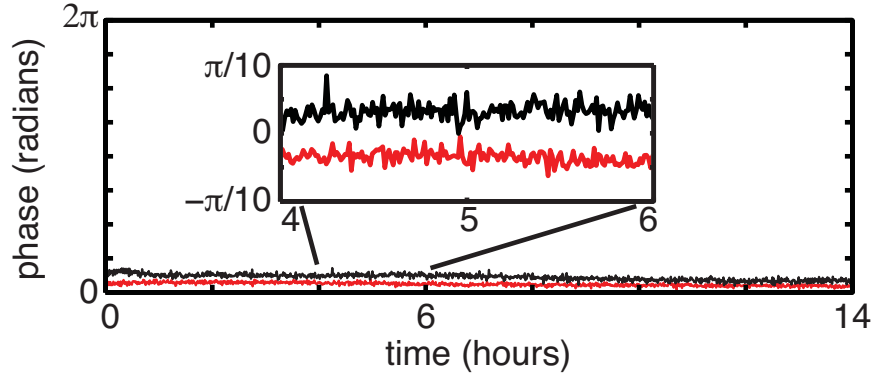


Figure 3-2: Phase stability of the COLBERT spectrometer. The spectra presented here were measured on a device with a phase stability of $\lambda/88$ over fourteen hours (black line). A recent improvement increased the phase stability to $\lambda/157$ (red line). The two traces are offset from each other for clarity. The inset shows an enhanced view of two hours of the measurement.

depends on the chosen geometry. For the geometries used in these experiments, it ranges from 40% to 75%. All of the losses are from unwanted diffractions: once from SLM 1, twice from G, and once from the vertical sawtooth pattern on SLM 2. Not only is the setup efficient, it is versatile. The only changes needed to perform a new spectroscopic measurement that may have a different number of beams as well as a completely different beam pattern are: to update the phase pattern applied to SLM 1, to rearrange the spatial filters that block unwanted diffraction orders, to update the phase patterns applied to SLM 2 during the experiment, to insert or rearrange any waveplates needed to define the polarizations, to move the iris that isolates the signal after the sample, and to reroute the signal beam into the detector. Since the beam geometry and all time delays and optical phase changes are controlled by the computer, there are no moving delay stages, interferometers, or wedges that would normally need realignment after changes in the experimental geometry. Nor would the phase need readjustment after each increment in the time delay of any pulse.

3.3 Extended-cavity oscillator

To generate measureable seventh-order signals and to have a small range over which to vary the power, we required input pulse energies greater than our femtosecond laser oscillator could normally produce. The typical pulse energy is about 5 nJ per pulse, which—after propagating through the COLBERT apparatus—is not enough to generate stable seventh-order signals. Since we required only a modest amount of additional energy per pulse, we extended the distance between the two end mirrors

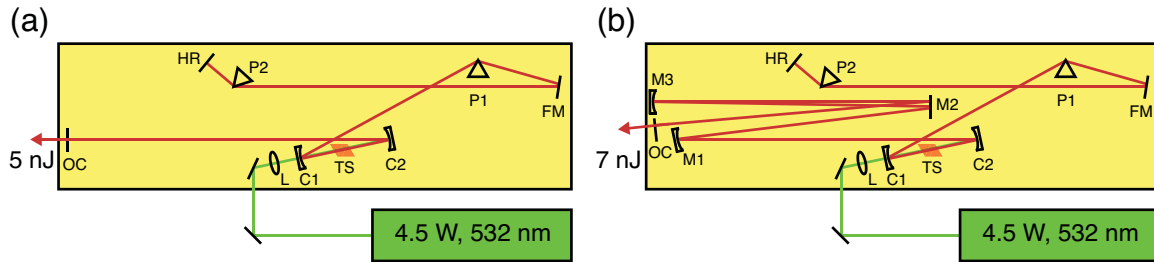


Figure 3-3: Femtosecond oscillator. (a) Standard operational configuration. The pump laser is focused by a spherical lens (L) to the Brewster-cut Ti:sapphire crystal (TS), which causes gain and fluorescence. Some of the fluorescence is reflected by the first cavity mirror (C1) toward a prism (P1). The prism refracts the light toward the folding mirror (FM), which sends the light towards a second prism (P2). After refraction by P2, the light is directed toward the high reflector (HR), which retroreflects the light through the optics back toward the crystal. In the opposite direction, the fluorescence is captured by the second cavity mirror (C2), and is directed toward the output coupler (OC), a 95% reflective mirror. When the two passes overlap each other and the pump beam in the crystal, lasing occurs. The pulse repetition rate is 92.5 MHz and each output pulse has an energy of 5 nJ. (b) Extended cavity configuration. Three mirrors (M1–M3) are placed between the crystal and the OC. Mirrors M1 and M3 are curved mirrors with 50 cm focal lengths. The pulse repetition rate is 41.6 MHz and each output pulse has an energy of 7 nJ.

of the laser cavity—the high-reflector and the output coupler—to increase the round-trip time of each pulse in the cavity. This additional time allows the pump laser to add more gain in the Ti:sapphire crystal. When the pulse arrives, the extra excited electrons result in additional stimulated emission. The increased pathlength lowered the repetition rate from 92.5 MHz to 41.6 MHz, and the energy per pulse increased to about 7 nJ. Since the intensity of the signal, superposed with the LO, varies as the fourth power of the pulse energy, the small increase in energy yielded a notably stronger seventh-order signal. If the power of the pump laser (Coherent V5 Verdi) could have been increased to the expected 5 W, the increase in output pulse energy would have been higher, about 10 nJ.

The path length was increased by 200 cm by placing three extra mirrors between the Ti:sapphire crystal and the output coupler. The normal and extended-cavity configurations are illustrated in Fig. 3-3. Two of the mirrors (M1 and M3) are spherically curved with focal lengths of 50 cm. The curved mirrors image the beam, adding stability to the system. Without imaging, the natural beam pointing fluctuations prevent the laser from mode-locking stably. The extended cavity configuration was used only for the seventh-order measurements.

3.4 COLBERT alignment

The device requires geometric and temporal alignments. Geometric alignment refers to the positioning and tilt variables which primarily affect the optical imaging. Temporal alignment refers to those variables which primarily change the temporal profile of the pulses.

The geometry alignment is surprisingly simple. We use a single beam by applying a flat phase pattern to SLM 1. This single beam is aligned to the center of all the optics and into the spectrometer after applying no waveform changes to SLM 2 except the sawtooth pattern which is uniform for all the dispersed frequency components. The pulse shaper is aligned using the standard procedure [247]. This nearly completes the geometric alignment of the device except the ‘z’ position of SLM 2, which controls the distance between CL and SLM 2. This is aligned after the temporal procedure. To align this, we create a symmetric geometry—the BOXCARS geometry, for example—using SLM 1 and then adjust the positioning until the visible astigmatism of the beam geometry at M disappears.

Temporal alignment involves adjusting the ‘z’ positioning of the CL—changing the distance between G and CL—by repeated FROG measurements until the single pulse is transform-limited. We also adjust the ‘x’ tilt of the CL (the tilt that cannot be aligned using a back-reflection) to reduce pulse-front tilt. This is performed using the symmetric beam geometry and placing a BBO crystal at the sample position. The CL tilt is adjusted carefully until the pulse cross-correlation beams are maximized at the sample. The adjustment is extremely sensitive.

3.5 Two-dimensional Fourier beam shaping

The versatility of this device enables the spectroscopist to tailor all the key features of a measurement to reveal the desired information. As an example using exciton correlations, the biexciton binding energy can be extracted from biexciton–ground-state coherences measured in a third-order two-quantum 2D FTOPT measurement with cross-linear polarization [99]. However, if biexciton inhomogeneity information is desired, fifth-order two-quantum rephasing scans are required [150, 151]. Both of these cases are presented in future chapters. More generally, the information extracted from an experiment depends on the number of beams, their geometrical arrangement and polarizations, the time ordering, and the time delay variable(s) scanned. Thus, these parameters must all be considered when designing an experiment.

Of particular importance is the beam geometry because this determines the phase-

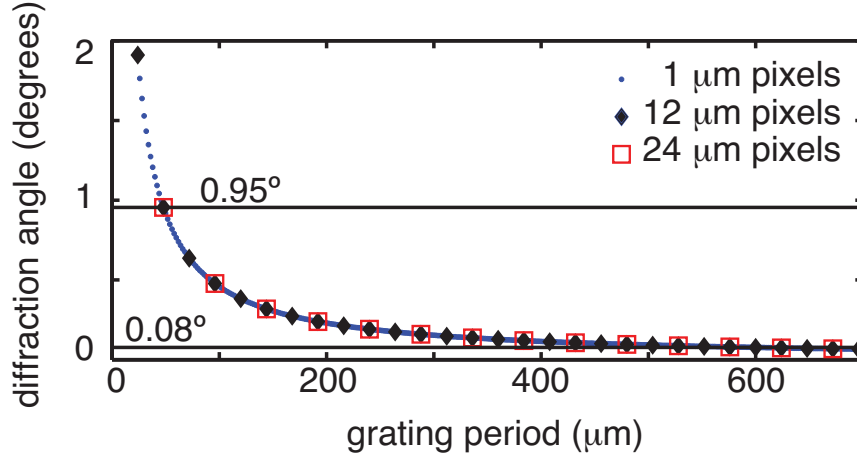


Figure 3-4: The SLM pixel size restricts the possible grating periods, which in turn restricts the available diffraction angles. Smaller pixels allow more accurate placement of the beams. The available grating periods—up to $700\ \mu\text{m}$ —and their associated diffraction angles for one dimension of the 2D SLM are shown for $1\ \mu\text{m}$ (blue dots), $12\ \mu\text{m}$ (black diamonds), and $24\ \mu\text{m}$ (open red squares) pixel sizes. Their respective largest diffraction angles are about 24° , 2° , and 1° . For the $150\ \text{cm}$ focal length lens used here, the minimum angle needed to clear the input beam is 0.08° ; the maximum angle, 0.95° , is governed by the radius of the output lens ($2.5\ \text{cm}$). As the pixel size decreases toward $1\ \mu\text{m}$, the available angles approach a continuum.

matching conditions of the measurement. Phase-matching, also called wave vector matching, is the process by which energy and momentum conservation of the input fields determine the direction in which signal is generated [16, 177]. Momentum conservation of the input field wave vectors links the beam geometry to the measurable information. Once the desired beam geometry is determined, the correct phase pattern must be created and encoded into SLM 1. This phase pattern is essentially the Fourier transform of the desired real-space beam pattern, where the size of the features depend on the focal length of the input lens.

The pixelation of the device complicates the otherwise simple Fourier transform and display processes because pixelation limits the available grating spacings. This is most easily understood using a one-dimensional example. As shown in Fig. 3-4, the pixel size determines both the largest diffraction angle and the density of diffraction angles. The smallest diffraction angle is governed by the number of illuminated pixels. To show the effects of pixel size, we calculated diffraction angles for pixels of three commercially available SLMs using the grating equation $n\lambda = d \sin(\theta)$. The smallest value of d available along one dimension of our SLM is $48\ \mu\text{m}$, and thus it has at most a 1° diffraction for the $150\ \text{cm}$ focal length lens. This translates to about 1 inch, which is at the edge of lens L2.

A 2D phase pattern is computed in the following manner. The set of beam coordinates and amplitudes is converted from Cartesian coordinates (b_i) to spherical polar coordinates (c_i), Eqn. 3.1. Then, transformations in beam angles due to refractive index changes or rotations in the beam geometry yield a modified set of polar coordinates, \tilde{c}_i , Eqn. 3.2. These angles are then transformed back to Cartesian coordinates (\tilde{b}_i), Eqn. 3.3, taking care to account for the quadrant ambiguity of the arctan function,

$$\{b_i(x, y, a)\} \rightarrow \{c_i(\theta, \phi, a)\} \quad (3.1)$$

$$\{c_i(\theta, \phi, a)\} \rightarrow \{\tilde{c}_i(\theta, \phi, a)\} \quad (3.2)$$

$$\{\tilde{c}_i(\theta, \phi, a)\} \rightarrow \{\tilde{b}_i(x, y, a)\}. \quad (3.3)$$

A matrix describing the size of the SLM surface, \underline{S} , is created in wave vector coordinates with every element initially having a value of zero. This is Fourier transformed as described by Eqn. 3.4 to the real-space domain, \underline{T} , where again all matrix elements are equal to zero. Seemingly unnecessary, this process ensures that the real-space pixelation is correct so that its inverse Fourier transform back to wave vector space has the desired pixelation. The values of those specific matrix elements in \underline{T} found to be nearest the desired beam coordinates, $\tilde{b}_i(x, y)$, are replaced with values equal to the desired beam amplitudes, $0 \leq \tilde{b}_i(a) \leq 1$. This matrix is then inverse Fourier-transformed to the wave vector domain as described by Eqn. 3.6, and its angle (the imaginary part of the natural logarithm, Eqn. 3.7) is calculated to yield the resulting phase pattern. Software converts the phase value of each matrix element to a grayscale value, Eqn. 3.8. The conversion requires the calibration relating greyscale to phase described in Sec. 3.9.1. The grayscale matrix, $\tilde{\underline{S}}$, is encoded into the device. Fig. 3-5 captures this procedure.

$$\mathcal{F}[\underline{S}(q_x, q_y, 0)] = \underline{T}(x, y, 0) \quad (3.4)$$

$$\underline{T}(x, y, 0) \rightarrow \underline{T}(x, y, a) \quad (3.5)$$

$$\mathcal{F}^{-1}[\underline{T}(x, y, a)] = \underline{S}(q_x, q_y, a) \quad (3.6)$$

$$\text{Im}[\ln[\underline{S}(q_x, q_y, a)]] = \underline{S}(q_x, q_y, \phi) \quad (3.7)$$

$$\underline{S}(q_x, q_y, \phi) \rightarrow \tilde{\underline{S}}(q_x, q_y, g). \quad (3.8)$$

Spatiotemporal pulse shaping was first used in 2D FTOPT spectroscopy without a diffractive optic to shape the beams spatially [129]. That method of spatial filtering blocked most of the light, and light scattered by the edges of the holes in the spatial mask added to experimental noise. Beam shaping by diffraction—a concept

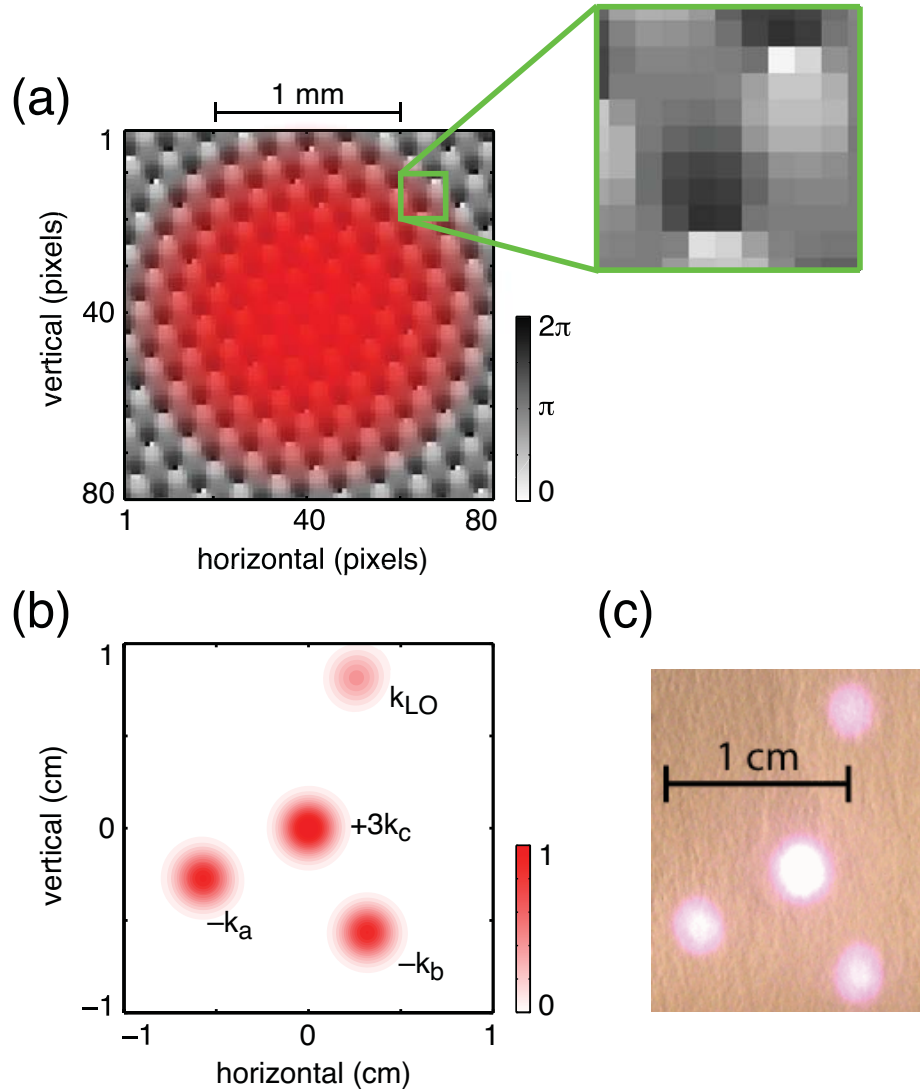


Figure 3-5: Two-dimensional Fourier beam shaping. (a) An 80 pixel by 80 pixel portion of the phase pattern encoded in the beam shaping SLM; each pixel is $24 \mu\text{m} \times 24 \mu\text{m}$. This specific pattern is used to generate a Y-shaped beam geometry [151], and the red area illustrates the focused input beam. The beam waist diameter is about 1 mm, corresponding to 40 pixels. The geometry is rotated by about 15° so that each beam encounters a different vertical region of the spatiotemporal pulse shaper. The green box is a 10 pixel by 10 pixel portion which clearly shows the pixelation of the pattern. (b) The calculated real space beam pattern after recollimation by the output lens. The position and intensity of each beam can be controlled. (c) Photograph of scatter from an index card of the experimental beam geometry with clearly visible relative intensity differences. Unwanted, low-intensity diffraction orders were blocked.

used in other spectroscopic implementations [187, 192, 246, 248, 249]—in our beam shaper increases the efficiency of the apparatus, produces outputs with Gaussian spatial profiles, and minimizes cross-talk between pulses. Moreover, beam shaping by diffraction using an SLM simplifies the procedure of changing the beam geometry. Instead of creating a spatial mask by etching a diffractive optic for each geometry, only a calculated phase pattern is updated.

3.6 Diffraction-based spatiotemporal pulse shaping

Pulse shaping of ultrafast optical fields is a robust method of performing many ultrafast spectroscopy measurements [129]. In general, the temporal profile of a femtosecond laser pulse is modulated by filtering the amplitudes and phases of its frequency components. This requires optical components that can separate and control the pulse frequencies. Temporal pulse shaping setups typically use a diffraction grating to disperse the broadband laser pulse spectrally and a focusing element such as a lens to focus the frequency components to different spatial locations. The filtering device—the SLM—is placed at the Fourier plane of the focusing element [247, 250, 251].

One benefit to measuring multidimensional FTOPT spectra using spatiotemporal pulse shaping is that since the phase profile is user-defined, in principle the user has complete control over the temporal waveform of each field. Delays, chirps, pulse trains, and more complicated temporal profiles can be introduced by merely updating the phase pattern on the SLM. Hence, as mentioned in the introduction, pulse shapers are often used in coherent control experiments [235, 252–255].

Unfortunately, liquid crystal SLMs are pixelated; this means that the pulse shaper does not have complete freedom to define phase profiles because the phase changes are not continuous across the spectrum [247]. The discontinuous sampling of the applied phase profile affects the output waveform, except in the rare case when line-by-line shaping can be used [256]. One of the most significant consequences of pixelated phase profiles is that the output pulse cannot be delayed beyond a certain maximum value in time; in the current system this time is about 10 picoseconds. To understand how this happens, and how to calculate minimum and maximum delay times, we consider the following situations.

Pulse delays are related to the phase profile through the Fourier shift theorem. A time delay of the pulse envelope, τ_{del} , corresponds to a linear change in the phase with respect to frequency such that the slope is τ_{del} and the user-defined carrier frequency

is ω_0 ,

$$\phi(\omega) = \tau_{del}(\omega - \omega_0). \quad (3.9)$$

Effectively, since the maximum of a femtosecond pulse envelope occurs when all of the frequencies are in phase, at times before and after the maximum the phases are shifted linearly as a function of frequency. Thus, a linear phase sweep imposed by the pulse shaper simply moves the time of the envelope maximum. Stated another way, the slope of the phase function is a constant, and this constant is the pulse envelope delay,

$$\frac{\delta}{\delta\omega}\phi(\omega) = \frac{\Delta\phi}{\Delta\omega} = \tau_{del}. \quad (3.10)$$

For the moment we do not consider pixel binning, and we first want to find the minimum delay possible, τ_{min} . To do this we need two values: the minimum phase change from one pixel to the next, $\frac{\Delta\phi_{min}}{1 \text{ pixel}}$, and the frequency difference from one pixel to the next, $\frac{\Delta\omega}{1 \text{ pixel}}$. The minimum time delay is

$$\tau_{min} = \frac{\frac{\Delta\phi_{min}}{1 \text{ pixel}}}{\frac{\Delta\omega}{1 \text{ pixel}}} = \frac{\Delta\phi_{min}}{\Delta\omega}. \quad (3.11)$$

For reflection-based pulse shaping, the numerator is related to the number of greyscale settings of the device and the total phase change possible, see Sec. 3.9.1. Our device has 256 greyscale settings encompassing about 2.5π phase modulation, thus $\Delta\phi_{min} = 0.03$ radians. Meanwhile, if the pixels are small enough and if there are enough pixels to cover the spectral bandwidth, the denominator is determined by the frequency resolution of the grating/lens pair, see Sec. 3.7. Our grating/lens combination gives a linear frequency resolution ($\frac{\Delta\nu}{1 \text{ pixel}}$) of 0.02 THz. Thus,

$$\tau_{min} = \frac{0.03}{2\pi * 0.02 \text{ THz}} \approx 240 \text{ fs}. \quad (3.12)$$

The SLM is ordinarily a phase-only device; the liquid crystal rotation at any pixel is used to shift the phase of light that arrives there. In diffraction mode [244], each of the separated frequency components of each pulse is diffracted by a vertical sawtooth grating pixel pattern within the horizontal stripe of SLM 2 that shapes that pulse. This allows some degree of control over the amplitude while retaining control of the phase. The phase and amplitude of the first-order diffracted frequency components are controlled by the spatial phase, $\phi(\omega)$, and amplitude, $A(\omega)$, of a sawtooth grating pattern with periodicity d_s , see Fig. 3-1(c). The spectral component of the diffracted

light, $E(\omega)$, is controlled by the pattern such that

$$E(\omega) = e^{i2\pi\Delta/d_s} \text{sinc}(\pi(1 - A(\omega))), \quad (3.13)$$

where Δ is the vertical displacement of the sawtooth grating pattern.

In diffraction-based shaping, the minimum delay situation is exactly the same as was the case for reflection-based shaping, except the definition of $\Delta\phi_{min}$ is no longer related to the number of greyscale settings of the device. It is instead related to d_s , the number of pixels used to define one sawtooth period. In our case, we use twelve pixels to define one sawtooth period, and so $\Delta\phi_{min} = 2\pi\frac{1}{12}$, yielding $\tau_{min} = 4.2$ ps. This value and the one found for reflection-based shaping are too large for 2D FTOPT measurements, which often involve sub-femtosecond time delays. However, these minimum delays correspond to the situation where the minimum phase step is taken from one vertical column of pixels to the next across the SLM surface.

In practice the linear phase profile is oversampled in the frequency domain; several columns of pixels are binned together to have the same phase shift. For example, in diffraction-based shaping, if the columns of pixels are binned into four groups of 192 pixels each, then

$$\frac{\Delta\phi_{min}}{pixel} = \frac{2\pi/12}{192} = 0.003, \quad (3.14)$$

and the minimum time delay is reduced to about 25 fs. As we see below, this is adequate for many 2D FTOPT measurements.

In principle, we could use the same analysis to find a maximum pulse delay. In that case, we would take the maximum possible phase step from one pixel to the next, remembering the modulus 2π . In the limit where $\Delta\phi_{max}$ approaches 2π , τ_{max} approaches 50 ps for our given spectral resolution. For the diffraction-based example, $\Delta\phi_{max} = 2\pi\frac{11}{12}$ and $\tau_{max} = 45.8$ ps, and for the reflection-based example, $\Delta\phi_{max} = 2\pi\frac{255}{256}$ and $\tau_{max} = 49.8$ ps. Thus, τ_{max} depends weakly on the number of phase steps, but instead strongly depends on the spectral resolution.

In practice, however, we are limited by a Gaussian-sinc window governing the amplitude modulation of the pulse as it is delayed. Derived elsewhere [257], this window is given by

$$E_{out}(\tau_{del}) \propto \exp(-\pi^2\delta\nu^2\tau_{del}^2) \text{sinc}(\pi\Delta\nu\tau_{del}), \quad (3.15)$$

where

$$\delta\nu = \frac{\delta x \Delta\nu}{h}, \quad (3.16)$$

h is the width of one pixel, and $\delta x = \frac{4F\lambda}{\pi D}$ is the spot size with the CL focal length

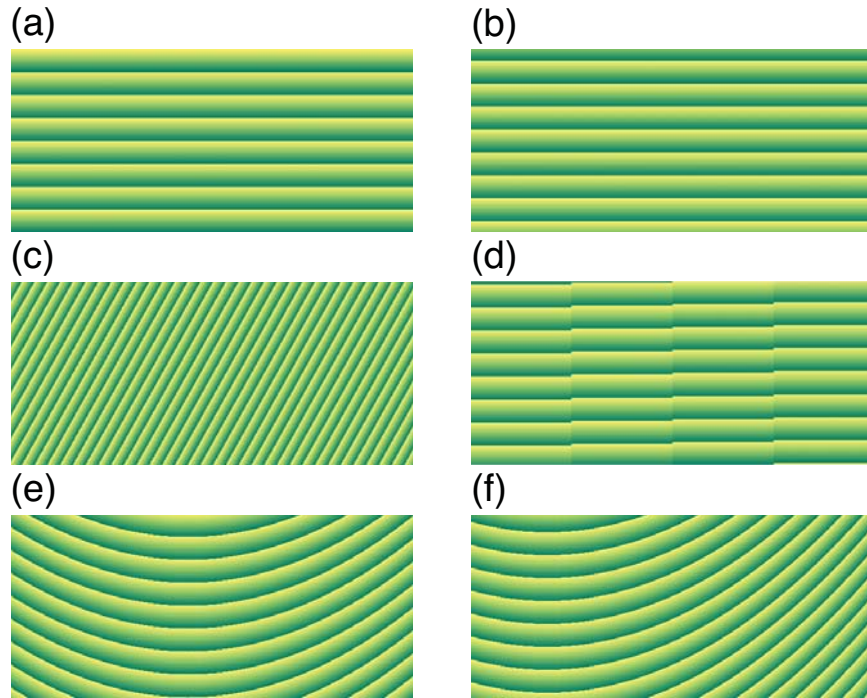


Figure 3-6: Calculated two-dimensional diffraction-based pulse shaping patterns. The broadband pulse is dispersed across the horizontal dimension spectrally. (a) Stripe with all phase parameters set to zero. (b) A π phase offset was applied, shifting the entire saw-tooth pattern up by half a period. (c) The pulse had no phase offset, but was delayed by 500 fs. (d) Same as previous but a delay using four groups of binned pixels. (e) The pulse has no phase offset or time delay, but was given a small amount of quadratic chirp. (f) The pulse was given a time delay of 100 fs and the same chirp as in (e).

F , beam diameter D and wavelength λ . In our usual configuration¹ where $\Delta\nu = 0.02$ THz, $\delta x = 60 \mu\text{m}$, and $h = 24 \mu\text{m}$, then $\delta\nu = 0.05$ THz, and the resulting FWHM of this function is about 10.5 ps. This function imposes a minimum linewidth that will be convolved with the linewidth of the measured spectral features along any scanned time coordinate. In Sec. 3.9.5 we discuss how to decouple this delay-dependent amplitude modulation from the measurement when an accurate linewidth is required.

In diffraction-based shaping, the applied phase profiles create stripes across the SLM surface. The phase patterns illustrated in Fig. 3-6 show the algebraically intuitive sawtooth grating patterns for different phase profiles: an unaltered pulse, a phase shifted pulse, a time-delayed pulse, a time-delayed pulse requiring binning, a chirped pulse, and pulse with a chirp and a delay. This process is multiplexed for several pulses across the vertical dimension of the 2D SLM [258] as shown in Fig. 3-1(b).

Diffraction-based pulse shaping also discriminates against the pulse replica which appear in the shaped waveforms of reflection-based pulse shaping using pixelated phase patterns [247, 259]. Present only in the zero-order diffraction beam, replica are eliminated by spatially filtering the beams using the pick-off mirror (M) illustrated in Fig. 3-1.

3.7 Pulse shaper resolution

The resolution of the pulse shaper—frequency per pixel ($\frac{\Delta\nu}{\text{pixel}}$)—is a difficult quantity to calculate exactly, and we do so only approximately. We use the standard notation where angular frequency (ω) is related to linear frequency (ν) via $\omega = 2\pi\nu$. We first relate $\frac{\Delta\nu}{\text{pixel}}$ to the spatial distance $\Delta x = x_2 - x_1$ between two frequencies $\Delta\nu = \nu_2 - \nu_1$,

$$\frac{\Delta\nu}{\text{pixel}} = \frac{(\nu_2 - \nu_1)h}{(x_2 - x_1)}, \quad (3.17)$$

where h is the width of one pixel. We typically pick ν_2 and ν_1 using the width of the pulse spectrum: $\nu_2 = \nu_0 + \sigma$ and $\nu_1 = \nu_0 - \sigma$, where ν_0 is the center frequency of the pulse and σ is the standard deviation. The approximation lies in our ability to calculate the coordinates at which these two frequencies are focused, x_2 and x_1 .

¹In this configuration each frequency is focused to a line with a width that is greater than one column of pixels.

Using the Taylor expansion result of Ref. [250],

$$x_i = \frac{mcF}{d\nu_0^2 \cos(\theta_i)}(\nu_i - \nu_0), \quad (3.18)$$

where F is the focal length of CL, c is the speed of light, m is diffraction order (usually $m = 1$), d is the grating spacing of G, and θ_i is the angle at which frequency ν_i diffracts from G. The grating spacing d is the inverse of the groove density. The diffraction angle of frequency ν_i is given by the grating equation,

$$\theta_i = \sin^{-1} \left(\frac{m\lambda_i}{d} - \sin(a) \right), \quad (3.19)$$

where a is the angle at which the beam is incident on G.

In our standard configuration, $d = 0.714 \mu\text{m}$, $a = 10^\circ$, $\lambda_0 = 800 \text{ nm}$, $\sigma = 5 \text{ nm}$, $F = 12.5 \text{ cm}$, and $h = 24 \mu\text{m}$. Using these values, $\nu_2 = 377.1 \text{ THz}$ and $\nu_1 = 372.4 \text{ THz}$, $\theta_2 = 70.0^\circ$ and $\theta_1 = 72.4^\circ$, $x_2 = -2.56 \text{ mm}$ and $x_1 = +2.88 \text{ mm}$, and $\frac{\Delta\nu}{\text{pixel}} = 0.02 \text{ THz}$. This value is accurate in the linear dispersion approximation; had we chosen a different frequency range, this value could have varied by as much as 50%.

3.8 Rotating frame detection

The method used to delay excitation pulses in an FTOPT experiment profoundly affects the phase behavior of the signal [260]. When a pulse is delayed by a translation stage or a wedge—a ‘path-length’ delay—its arrival time is given by

$$E(t) = \tilde{A}(t - \tau)(e^{-i\omega_c(t-\tau)} + c.c.), \quad (3.20)$$

where $\tilde{A}(t-\tau)$ is the amplitude envelope and ω_c is the center frequency of the Gaussian pulse. Its Fourier transform to the frequency domain is

$$E(\omega) = A(\omega - \omega_c)(e^{-i\omega\tau} + c.c.). \quad (3.21)$$

Over the delay time τ , a frequency ω_a accumulates a phase of $\omega_a\tau$; the optical phase of the signal field is swept through a complete cycle each time an excitation pulse is delayed by just one optical period. Therefore, data must be recorded at many delay points within a single optical period in order to elucidate the signal phase behavior.

If pulses are delayed using a pulse shaper, however, the phase at a user-defined carrier frequency, ω_0 , can be held constant while the relative phases of other frequen-

cies, such as a resonance frequency ω_a , shift in proportion to the frequency difference $\omega_a - \omega_0$. This is analogous to rotating frame detection in NMR [100]. The phase of the excitation and signal fields oscillate gradually as functions of excitation pulse delay, and the signal phase behavior can be sampled using large time steps.

To delay a pulse using this method, ω_0 is selected—usually but not necessarily within the pulse bandwidth—and the slope of the linear phase sweep is varied in the SLM pixel pattern. This advances the pulse envelope but keeps the phase of the carrier frequency constant. Thus, the waveform generated by the SLM can be written in the time domain as

$$E(t) = \tilde{A}(t - \tau)(e^{-i\omega_0 t} + c.c.), \quad (3.22)$$

whose Fourier transform to the frequency domain is

$$E(\omega) = A(\omega - \omega_0)(e^{-i(\omega - \omega_0)\tau} + c.c.). \quad (3.23)$$

The phase of a frequency component ω_a still advances as the pulse envelope is delayed, but at a relatively slow rate. A full 2π cycle for the phase at frequency ω_a occurs only when the time delay increases by the beat period, $2\pi/(\omega_a - \omega_0)$. This period can correspond to roughly 100 optical periods, in contrast to signal oscillations that occur at the much faster optical frequency when pulses are delayed using ‘path-length’ changes. Slowing the coherent oscillations in this manner allows large step sizes to be taken without undersampling.

In practice the selected carrier frequency has its phase held constant in all the beams by keeping their sawtooth grating patterns at that frequency identical to each other. We often select 368 THz (1522 meV) as the carrier frequency. Referencing coherent oscillations to this frequency slows them as much as possible to allow for large step sizes, but without completely removing the oscillatory behavior. The oscillations are useful when eliminating scatter. At this carrier frequency, the H and L excitons oscillate at about 4 and 7 THz, respectively. Considering only H excitons, this means that two-quantum, three-quantum, and four-quantum coherences respectively oscillate at about 8 THz, 12 THz, and 16 THz. Step sizes need to be taken considering these frequencies, not the optical frequencies which correspond to 4–6 eV. Specifically, in the two-quantum rephasing measurement, the $-2\mathbf{k}_a$ field was scanned from 0 to 2.5 ps in 256 steps, giving a maximum frequency of 51 THz. The $+3\mathbf{k}_b$ field was scanned in three-quantum nonrephasing measurements from 0 to 1.5 ps in 256 steps, resulting in a maximum frequency of 85 THz. The $-3\mathbf{k}_b$ field in three-quantum rephasing measurements and the $+4\mathbf{k}_b$ field in the four-quantum nonrephasing measurement were scanned from 0 to 1 in 128 steps, resulting in a maximum frequency of over

60 THz. The step sizes taken in these scans are sufficient to observe the multiple-quantum coherent oscillations.

In the present work, we shift all frequency axes which result from delayed pulses out of the rotating frame frequencies to true optical frequencies by first accurately measuring the carrier frequency and then adding the carrier frequency value(s) to the axis values. Multiple ω_0 values might be needed if more than one beam is delayed. In Sec. 3.9.4 below, we discuss how to determine the carrier frequency with high accuracy.

3.9 Calibrating COLBERT

The device requires several calibration procedures for optimal performance, some of which were suggested above. The amount of phase shift imparted by each greyscale setting of the SLMs must be measured. This calibration depends only minimally on the wavelength and needs to be performed only once per device; the calibration curves of our SLMs have been reproducible over a period of years. The five remaining calibrations are less forgiving. Each time the spectrum of the pulse changes or the COLBERT is realigned, three calibrations must be performed. The frequencies of light controlled by each vertical stripe of pixels must be determined for proper delay calculations; the carrier frequency of each delayed pulse must be determined for proper rotating frame delay relations; and the beam distortions from the cylindrical lens of the pulse shaper must be reversed. If accurate linewidths or dephasing times are required, the delay-dependent amplitude modulation must be determined. Finally, each measurement in which the complex signal, rather than simply the amplitude, is desired requires a measurement of the global phase offset. These six calibrations are detailed below.

3.9.1 Greyscale to phase shift calibration

A basic calibration required of any SLM is to determine the phase change imparted by each greyscale value setting. Our 8-bit SLMs have 256 greyscale settings encompassing about 2.5π radians of phase modulation for 800 nm light. The optical setup for this calibration procedure, depicted in Fig. 3-7(a), involves vertically splitting the SLM into two regions; the left side remains at a greyscale value of zero while the greyscale value of the right side will be varied. A cylindrical lens focuses the two first-order diffractions from the phase mask onto the plane of the SLM surface. A beam splitter is placed before the phase mask, and one interference fringe of the recombined

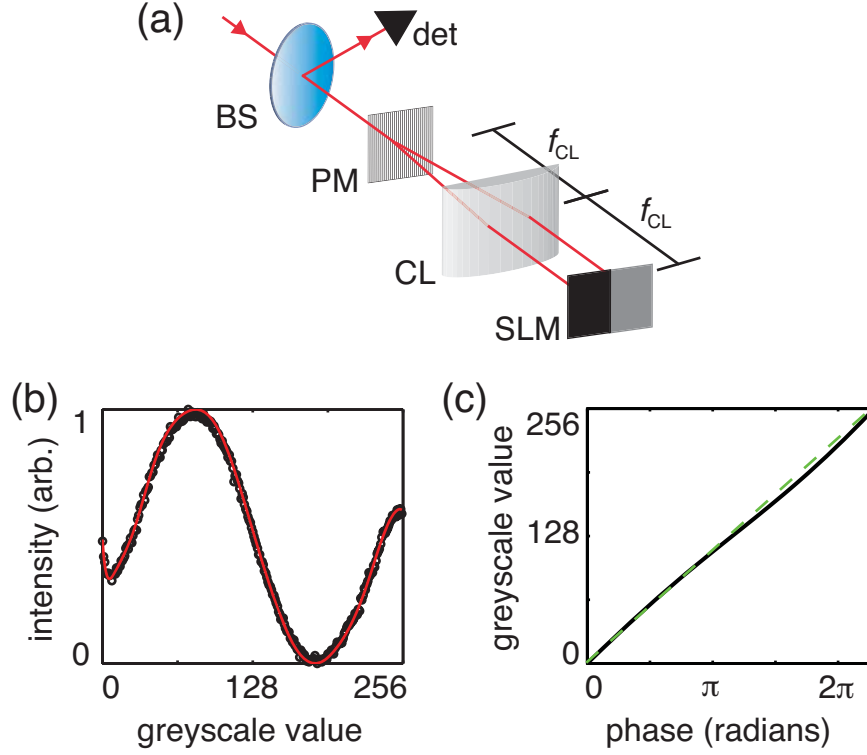


Figure 3-7: Greyscale to phase calibration of the spatial light modulator (SLM). (a) The input beam transmits through a beam splitter (BS), and the two first-order diffractions from the phase mask (PM) are focused by the cylindrical lens (CL) onto the surface of the SLM. One half of the SLM surface remains at a greyscale value of zero while the other half is scanned. At each of the 256 values, an isolated fringe of the beam reflected by the BS is measured by the detector (det). (b) Measured greyscale to phase change function (black dots) and its fit to a fifteenth order polynomial (solid red line). (b) From the polynomial fit, the function relating greyscale to phase, $g(\phi)$, is calculated and plotted. This specific SLM is capable of about 2.5π phase modulation for 800 nm light. The green dashed line is a linear reference to show the slight nonlinearity of the function. The two SLMs have different responses and so must be calibrated individually.

beam is isolated with an iris and used to measure the phase change. We chop one arm (Thorlabs MC1000) at 500 Hz as it passes between the CL and the SLM. The signal is detected in a silicon photodiode (Thorlabs DET10A) and transmitted to the computer by a lock-in amplifier (Stanford Research Instruments SR830 DSP).

Following Refs. [259, 261], we fit the measured profile shown in Fig. 3-7(b) to a fifteenth-order polynomial function, take its inverse cosine, and then patch the sections together to form a continuous greyscale-to-phase function, $\phi(g)$. This function is inverted, and the resulting phase-to-greyscale function, $g(\phi)$, is fit to a fifth-order polynomial; this is shown in Fig. 3-7(c). This is used by the software to convert a desired phase shift to a greyscale value.

This calibration procedure assumes that the device response is not wavelength dependent. This assumption is valid for low bandwidths, and phase changes do not measurably differ for our 100 fs pulses. For higher-bandwidth pulses, this deviation introduces significant phase errors [262]. In that case, the phase calibration for each frequency should be measured independently.

3.9.2 Wavelength to pixel calibration

Proper operation of the spatiotemporal pulse shaper requires knowing which frequencies are controlled by each pixel [259]. The calibration procedure is shown schematically in Fig. 3-8(a) and requires an accurate alignment of the rotation of the SLM face. A three-pixel-wide vertical stripe is displayed, and the spectral components are measured in the spectrometer. The wavelength of maximum intensity (λ_n) is the wavelength of the center pixel in the stripe (x_n). The stripe is three pixels wide because a minimum of three pixels is required to have a full phase shift of the center pixel [259]. This stripe is scanned across the surface, usually every five pixels. Measureable light intensity fills about half the width of the SLM surface, thus about 80 measurements are made. An example data set is shown in Fig. 3-8(b). It is fit to a polynomial, and this function— $\lambda(x)$ —is inverted and interpolated to the frequency-to-pixel function, $x(\nu)$. This function, shown in Fig. 3-8(c), is used when encoding waveforms. The calibration is performed before sample insertion.

3.9.3 Aberration-induced temporal modulation correction

One drawback to the current spatiotemporal pulse shaping component of the COLBERT spectrometer is the cylindrical focusing lens. This optical element causes spherical and chromatic aberrations that are difficult or impossible to correct optically [251]. These aberrations cause the pulses in the beams to experience different amounts of dispersion because the beams traverse different horizontal locations of the cylindrical lens, as shown in Fig. 3-1(d). The varying amounts of dispersion make the pulses arrive at the sample location at different times with various amounts of chirp.

To compensate for these distortions, we correct one beam optically by adjusting the ‘z’ position of the cylindrical lens while monitoring the duration of the pulse in the chosen beam using a frequency-resolved optical gating (FROG) apparatus [263]. We are unable to correct all of the beams simultaneously in this fashion because, depending on the horizontal distance from the center of the cylindrical lens, the optimal ‘z’ position differs. After correcting the one—usually the center—beam, we

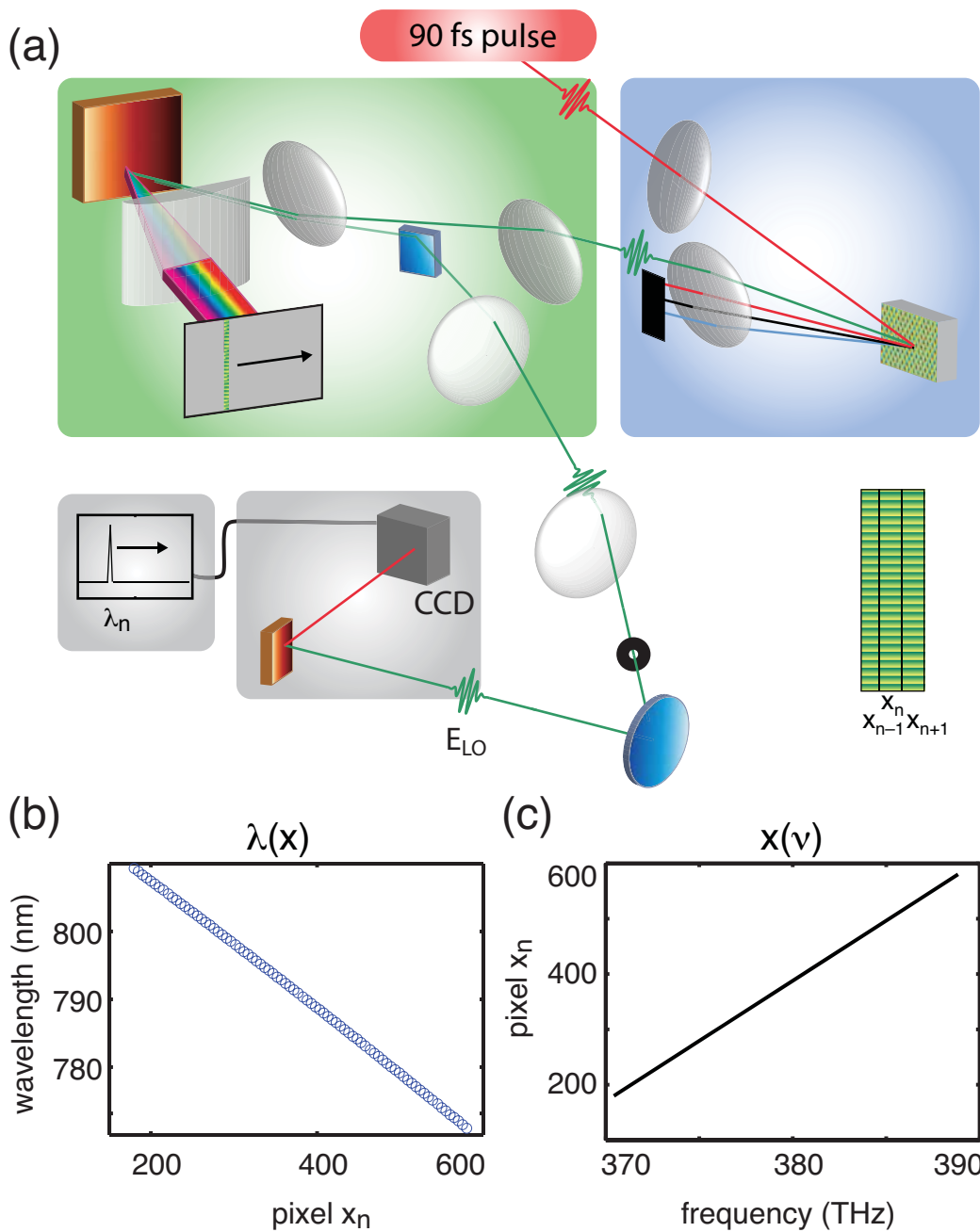


Figure 3-8: The wavelength to pixel calibration is performed with the sample removed and all beams except the LO blocked. (a) The position of a three-pixel-wide stripe, centered at pixel x_n , is scanned across the SLM surface, usually every five pixels. At each position, the wavelength corresponding to the maximum of the sharp spectral peak, λ_n , is measured. (b) Maximum wavelength values are collected across the SLM surface. (c) The wavelength values are interpolated to a frequency coordinate and fit to a fifth-order polynomial. This function is then inverted to the desired frequency-to-pixel function: $\lambda(x) \rightarrow x(\nu)$.

place a 100 μm thick BBO crystal at the sample location, and, one at a time, the pulses in the beams are cross-correlated with this transform-limited pulse. We detect the doubled, 400 nm, signal in a photodiode and use lock-in detection with a beam chopper placed in the transform-limited beam. Typically the only compensation needed to return the deformed beams to a transform-limited state are first-order and second-order phase modulations, corresponding to temporal delays and quadratic chirp, respectively. These compensation parameters are then incorporated in the subsequent coherent measurements. Typical correction factors are delays of about 0.200 ps and chirps of about 0.010 ps². If the cross-correlations are performed with the waveplates in place, waveplates thickness delays are corrected at the same time.

3.9.4 Carrier frequency calibration

As discussed above, one selected spectral component is selected as the carrier frequency ω_0 ; its phase in all the fields is kept constant as the envelopes of pulses are time delayed. We calibrate the carrier frequency using one-quantum measurements in which a diagonal peak location is determined by emission from an exciton coherence at frequency—determined with ± 0.01 meV accuracy in the spectrometer—and the beat frequency at which the signal oscillates as a function of the time delay between the first two pulses. To calibrate the carrier frequency of beam \mathbf{k}_i , we measure a one-quantum co-circular polarization signal by delaying pulse E_i . Co-circular one-quantum signals generate a strong H exciton peak which should be symmetric about the diagonal because the H excitons should absorb and emit at the same frequency [146]. Accurate calibration of the carrier frequency yields accurate determination of multiple-quantum coherence frequencies from which multiexciton binding energies are determined. Our calibrations gave an uncertainty of ± 0.1 meV for each quantum involved in the multiple-quantum energies, limited by the precision of beat frequency measurements due to signal-to-noise limitations, not by calibration accuracy.

3.9.5 Delay-dependent amplitude modulation correction

As mentioned in Sec. 3.6, the intensity of a pulse delayed using a spatiotemporal pulse shaper is modulated with respect to its delay, $I(\tau_{del})$ by a Gaussian-sinc window. The Fourier transform of this decay is a spectral linewidth,

$$\mathcal{F}[I(\tau_{del})] = I(\omega_{del}). \quad (3.24)$$

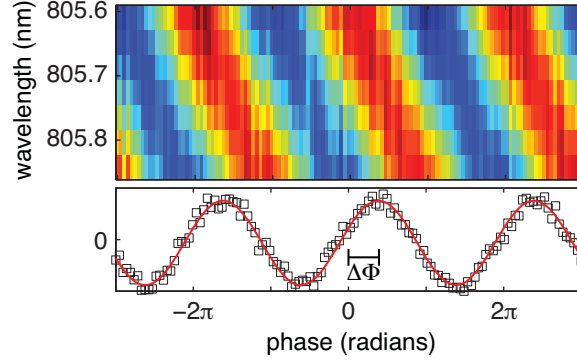


Figure 3-9: Measuring the global phase offset ($\Delta\Phi$) of the emitted signal to phase a 2D spectrum. (top) Spectra around the H exciton wavelength measured for varying values of the phase of one excitation pulse. (bottom) Measured (black squares) and cosine fit (red line) to the integrated phase profile. The fit to several cycles of the cosine function indicates that $\Delta\Phi = 1.2$ radians.

Unless they are compensated, FTOPT signals measured during a delayed time period will be convolved with $I(\omega_{del})$ in the frequency domain. We can compensate for this modulation by designating an upper bound on the amplitude of the output waveform. The amplitude of the output waveform is then modulated to change the overall amplitude of the sawtooth phase profile— $A(\omega)$ in Fig. 3-1(c)—as the pulse is delayed. The correction procedure involves first measuring $I(\tau_{del})$ by blocking all fields except the LO and measuring the pulse spectrum while delaying the LO over a ± 8 ps range without phase cycling. We then integrate spectrally and fit the resulting data set to a polynomial. If a desired pulse delay is within the designated temporal range, the amplitude of the sawtooth phase pattern is decreased according to the fit function. In this manner, the pulse energy is maintained constant while the delay is swept. Unfortunately, much of the pulse energy is lost by this method. Another way to compensate for the modulation is to deconvolve it from the resulting signal trace. This method is acceptable if the time-dependent signal profile is not affected substantially by the changes in pulse energy—and exciton density—at different delays.

3.9.6 Global phase calibration

Although the timings of the excitation pulses are calibrated at the sample using the procedure above, uncertainty remains about the relative optical phase of each pulse. Since the optical phase of the signal field depends on the optical phase of each excitation field, uncertainty remains about the global phase offset of the signal. Determining the value of the global phase offset is critical if the complex field—not merely the amplitude—is to be reported. The emitted third-order signal field can be

written in the frequency domain as the product of an amplitude function $A(\omega)$, and, for $\tau_1 = \tau_2 = 0$, the global phase offset given by the phase offsets of the excitation pulses ($\delta\phi_i$),

$$E_{sig}(\omega) \propto A(\omega)e^{-i(-\delta\phi_a + \delta\phi_b + \delta\phi_c)}. \quad (3.25)$$

The measured interference pattern between the signal field and the LO is then

$$\begin{aligned} I(\omega) &\propto \cos(\delta\phi_{LO} - \delta\phi_a + \delta\phi_b + \delta\phi_c) \\ &= \cos(\Delta\Phi), \end{aligned} \quad (3.26)$$

where $\Delta\Phi$ is the global phase offset. Note that Eqn. 3.26 holds only for third-order measurements in the BOXCARS geometry. $\Delta\Phi$ must be calculated for any specific geometry.

Several methods have been developed to determine this global phase offset [110, 132, 264]. Here, we use the pulse shaper itself to both measure and correct the phase offset between the LO and the emitted signal. ‘Phasing’ in this manner does not require independent pump-probe measurements [110] or an external imaging apparatus [132, 264]. We measure the global phase offset by varying the phase of one of the pulses and measuring the interferogram at each phase value as illustrated in Fig. 3-9. We then integrate the interferogram over the H exciton emission energy and fit the resulting traces to a cosine function to determine the phase offset. By applying a phase value that makes the global phase offset to be zero, we have ‘phased’ our signal.

The determined phase offset value can either be added as a phase factor to one of the pulses during the experiment, or it can be used as a multiplier for the entire data set after the measurement. Although a single measurement is sufficient, the phase offset can be determined with greater accuracy if this procedure is performed for every excitation field to calculate an average phase offset. This procedure must be performed each time the polarizations of the excitation fields are changed.

3.10 Spectral interferometry

When sent alone into the spectrometer, all phase information about the signal field,

$$E_{sig}(\omega) = A_{sig}(\omega)(e^{-i\phi_{sig}(\omega)} + e^{+i\phi_{sig}(\omega)}), \quad (3.27)$$

is lost by square-law detection,

$$|E_{sig}(\omega)|^2 = A_{sig}(\omega)^2. \quad (3.28)$$

The most common method used to retrieve this phase information is a heterodyne detection method in which the signal is superposed with the LO field and the resulting spectral fringes are measured by a spectrometer [265]. A cross-term which depends on both the signal and local oscillator phases can be measured, and if calculated properly, the phase of the signal, $\phi_{sig}(\omega)$, can be isolated by applying a filter in the Fourier domain.

This is performed by first measuring the interference spectrum between the emitted signal and the LO,

$$I(\lambda) = |E_{sig}(\lambda) + E_{LO}(\lambda)|^2. \quad (3.29)$$

The temporal delay between the two fields (τ_{LO}) causes a fringe pattern to appear in the spectrometer, as shown in Fig. 3-10(a). The fringe width is the inverse of τ_{LO} —we typically use 1 ps. The location of the fringe relative to a stationary frequency index gives the relative phase of the signal field. The next step is to subtract the two homodyne portions obtained in separate measurements and interpolate from wavelength to frequency coordinates to leave only the cross term,

$$E_{XT} = I(\omega) - I_{LO}(\omega) - I_{sig}(\omega) \quad (3.30)$$

$$= 2A_{sig}(\omega)A_{LO}(\omega) \cos(\phi_{sig}(\omega) - \phi_{LO}(\omega)). \quad (3.31)$$

This process is depicted in Fig. 3-10(a), where the signal spectrum (with all fields at $\tau = 0$), the LO spectrum (which shows a dip at the resonances because the LO propagates through the sample), and their interference spectrum are depicted. Also shown is the difference spectrum, $E_{XT}(\lambda)$, which is interpolated to a linear frequency coordinate, $E_{XT}(\omega)$, in Fig. 3-10(b). In the COLBERT spectrometer, phase cycling procedures (discussed in Sec. 3.11) accomplish the homodyne subtraction indicated by Eqn. 3.30, and the interpolation is performed on the computer.

The cross term is real (with no imaginary components), and it can therefore be written as the sum of two complex conjugate signals,

$$E_{XT} = 2A_{sig}(\omega)A_{LO}(\omega)(e^{-i(\phi_{sig}(\omega)-\phi_{LO}(\omega))} + c.c.) \quad (3.32)$$

We isolate one of the two phase terms by first inverse Fourier transforming to the

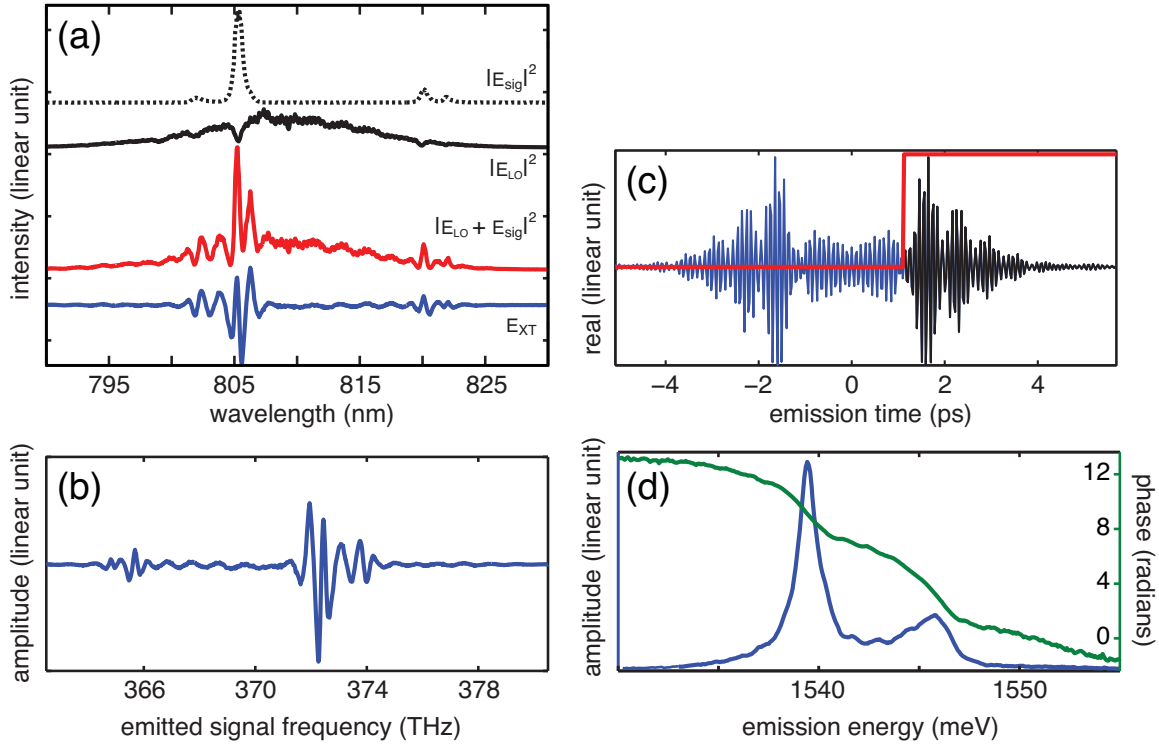


Figure 3-10: Spectral interferometry algorithm. (a) Spectral fringes caused by interfering the signal with the LO in the spectrometer. The $\tau_1 = \tau_2 = 0$ spectrum of the emitted signal (black dashed line) and the LO spectrum (black solid line) are subtracted from their interference spectrum (red solid line) to leave only the cross term (blue solid line). While the H exciton is the strong feature at 806 nm, the L exciton feature—which is barely visible at 802 nm in the signal spectrum—is enhanced in the interference and cross term spectra. Signals from the substrate are visible near 820 nm. (b) The cross term is interpolated to a frequency axis. (c) The cross term is then Fourier transformed to the time domain (blue and black lines), and a filter (red line) is applied to select only the positive-time component of the signal (black line). Only the real part of the complex signal is displayed. (d) The remaining signal is Fourier transformed back to the frequency domain and converted to an energy unit. The amplitude (blue line) and phase (green line) of the resulting complex-valued signal are displayed.

time domain to yield signals at both positive and negative times,

$$\begin{aligned} & \mathcal{F}^{-1}[A_{sig}(\omega)A_{LO}(\omega)\cos(\phi_{sig}(\omega) - \phi_{LO}(\omega))] \\ & = B^+(t) + B^-(t). \end{aligned} \quad (3.33)$$

Because the signal is not emitted before all the excitation pulses have interacted, a step function can be applied to remove the portion of the signal that appears at negative times, $B^-(t)$. The remaining portion, $B^+(t)$, is Fourier transformed back to the frequency domain to yield a complex signal,

$$\mathcal{F}[B^+(t)] = A_{sig}(\omega)A_{LO}(\omega)e^{i\phi_{sig}(\omega)-i\phi_{LO}(\omega)}. \quad (3.34)$$

To isolate $\phi_{sig}(\omega)$, we use the key spectral interferometry step to remove $\phi_{LO}(\omega)$ with the relation

$$\phi_{LO}(\omega) = (\omega - \omega_0)\tau_{LO}, \quad (3.35)$$

and the amplitude of the LO spectrum such that

$$\frac{A_{sig}(\omega)A_{LO}(\omega)e^{i\phi_{sig}(\omega)-i\phi_{LO}(\omega)} * e^{+i(\omega-\omega_0)\tau_{LO}}}{A_{LO}(\omega)} = A_{sig}(\omega)e^{i\phi_{sig}(\omega)}. \quad (3.36)$$

Computationally, spectral interferometry is performed by first interpolating the initial real-valued 2D data set, $S(\tau_{scan}, \lambda_{emit})$, to a similar real-valued data set with frequency values, $S(\tau_{scan}, \omega_{emit})$. The emission dimension is inverse Fourier transformed to yield a temporal data set, $S(\tau_{scan}, \tau_{emit})$, whose matrix elements are complex. The negative-time side of the emission dimension is zeroed, $S(\tau_{scan}, \tau_{emit} < 0) = 0$. The emission dimension is Fourier transformed back to the frequency domain, but now the matrix elements of $S(\tau_{scan}, \omega_{emit})$ are complex. The spectral interferometry algorithm—removing the phase accumulated during τ_{LO} and the amplitude of LO spectrum—is then applied to yield $\tilde{S}(\tau_{scan}, \omega_{emit})$. At this point any global phase offset can be removed using the inverse of the measured global phase shift. The amplitude and phase of the emitted field for any value of the scanned time dimension can now be retrieved from $\tilde{S}(\tau_{scan}, \omega_{emit})$.

The general process for performing spectral interferometry is described in this section. Several studies have focused on the accuracy of the extracted information. Specifically, the role that the detector calibration plays on the extracted phase profile has been studied [266, 267]. Other work has focused on extracting information using a second-order diffraction from the grating in the spectrometer [268].

3.11 Phase cycling procedures

Phase cycling [129] reduces undesired signals due to scattered light from both the sample and the SLM surface. This is accomplished by summing measurements with different phases of the input fields to eliminate all terms that do not have the desired dependence on the phases of all the inputs. Phase cycling is commonly used in NMR spectroscopy [100] to reduce unwanted signal contributions, and it has been used previously in FTOPT measurements [99, 129, 140, 145, 148]. Wave vector selectivity significantly reduces the number of possible contaminating signals in FTOPT compared to NMR, so instead of tens or hundreds of steps, we often use just eight. As an example of how phase-matching can reduce the number of signal contributions, in a co-linear beam geometry, sixteen steps were required for the same scan in which we use eight steps because of overlapping rephasing and nonrephasing signals [106, 127]. In this instance, this drawback could be an advantage for collecting correlation spectra, as we will see in Sec. 4.4.

In the phase cycling procedure of third-order measurements using the BOXCAR geometry, the phase of each input beam was varied by π since each beam contributed one field interaction. In high-order measurements, a single beam often contributes more than one field interaction, and thus the phase variation is a corresponding fraction of π , such that the overall signal phase is varied by π and the appropriate terms will be eliminated when the signals are subtracted. As an example, consider scatter from both beams in a fifth-order $3\mathbf{k}_b - 2\mathbf{k}_a$ measurement. The intensity recorded by the spectrometer is

$$I(\omega) = \left| \begin{array}{l} E_{LO}(\omega)e^{i\phi_{LO}(\omega)} + E_{sig}(\omega)e^{i\phi_{sig}(\omega)} \\ + E_a(\omega)e^{i\phi_a(\omega)} + E_b(\omega)e^{i\phi_b(\omega)} \end{array} \right|^2, \quad (3.37)$$

where

$$\phi_{sig}(\omega) = -2\phi_a(\omega) + 3\phi_b(\omega). \quad (3.38)$$

Suppressing the frequency dependence, a complete expansion of this equation,

$$\begin{aligned} I &= I_{LO} + I_{sig} + I_a + I_b \\ &+ 2E_{LO}E_{sig} \cos(-2\phi_a + 3\phi_b - \phi_{LO}) \\ &+ 2E_{LO}E_a \cos(\phi_a - \phi_{LO}) + 2E_{LO}E_b \cos(\phi_b - \phi_{LO}) \\ &+ 2E_{sig}E_a \cos(3\phi_a - 3\phi_b) + 2E_{sig}E_b \cos(2\phi_a - 2\phi_b) \\ &+ 2E_aE_b \cos(\phi_b - \phi_a), \end{aligned} \quad (3.39)$$

includes four intensity terms and six cross terms. Only one is the desired term, the local oscillator crossed with the signal,

$$2E_{LO}E_{sig} \cos(-2\phi_a + 3\phi_b - \phi_{LO}). \quad (3.40)$$

An eight-step procedure can isolate the desired cross term; beam \mathbf{k}_a is incremented in steps of $\pi/2$, beam \mathbf{k}_b is incremented in steps of either π or $\pi/3$, and beam \mathbf{k}_{LO} is cycled in steps of π . After cycling \mathbf{k}_b in the first step,

$$\begin{aligned} I_{\text{two-step}} &= I(\phi_a, \phi_b, \phi_{LO}) - I(\phi_a, \phi_b + \pi, \phi_{LO}) \\ &= 4E_{LO}E_{sig} \cos(-2\phi_a + 3\phi_b - \phi_{LO}) \\ &\quad + 4E_{LO}E_b \cos(\phi_b - \phi_{LO}) \\ &\quad + 4E_{sig}E_a \cos(3\phi_a - 3\phi_b) \\ &\quad + 4E_{sig}E_b \cos(2\phi_a - 2\phi_b) \\ &\quad + 4E_aE_b \cos(\phi_b - \phi_a), \end{aligned} \quad (3.41)$$

only five terms remain. Cycling beam \mathbf{k}_{LO} in addition to beam \mathbf{k}_b requires two more measurements. This eliminates all but two terms,

$$\begin{aligned} I_{\text{four-step}} &= I(\phi_a, \phi_b, \phi_{LO}) \\ &\quad - I(\phi_a, \phi_b + \pi, \phi_{LO}) \\ &\quad - I(\phi_a, \phi_b, \phi_{LO} + \pi) \\ &\quad + I(\phi_a, \phi_b + \pi, \phi_{LO} + \pi) \\ &= 8E_{LO}E_{sig} \cos(-2\phi_a + 3\phi_b - \phi_{LO}) \\ &\quad + 8E_{LO}E_b \cos(\phi_b - \phi_{LO}). \end{aligned} \quad (3.42)$$

The eight step cycle,

$$\begin{aligned} I_{\text{eight-step}} &= I(\phi_a, \phi_b, \phi_{LO}) \\ &\quad - I(\phi_a + \pi/2, \phi_b, \phi_{LO}) \\ &\quad - I(\phi_a, \phi_b + \pi, \phi_{LO}) \\ &\quad - I(\phi_a, \phi_b, \phi_{LO} + \pi) \\ &\quad + I(\phi_a + \pi/2, \phi_b + \pi, \phi_{LO}) \\ &\quad + I(\phi_a + \pi/2, \phi_b, \phi_{LO} + \pi) \\ &\quad + I(\phi_a, \phi_b + \pi, \phi_{LO} + \pi) \end{aligned}$$

$$\begin{aligned}
& - I(\phi_a + \pi/2, \phi_b + \pi, \phi_{LO} + \pi) \\
= & 16E_{LO}E_{sig} \cos(\phi_{sig} - \phi_{LO}), \tag{3.43}
\end{aligned}$$

isolates and amplifies the desired cross term.

Each measurement requires a unique phase cycling scheme where, as shown above, the phase increment is simply the inverse of the number of field interactions by that beam. Finally, the more beams involved in a measurement, the more cycle steps are needed. Although this increases data acquisition times, it amplifies the signal further. For cycling procedures involving many steps, it may be advantageous to incorporate non-integer-fraction cycling procedures, such as a COGWHEEL, to reduce the number of overall steps [269].

3.12 Operation COLBERT: Performing a measurement

Once the preceding calibrations are in place, the device is ready to perform a measurement. The software can convert desired phase shifts into the correct greyscale values on the SLM using the calibration curve. The apparatus was built in an all-imaging arrangement. The pulse shaper was set so that one beam was measured to be near-transform-limited by an external FROG. The calibration procedure relating frequency to pixel location was then performed so that pulse delays and phase shifts can be properly encoded. The aberration-induced modulations were fixed by performing cross correlations at the sample plane using the near-transform-limited pulse as a reference. One-quantum two-dimensional co-circular measurements, using the proper phase cycling procedure, were then performed to calibrate the carrier frequency in each scanned beam. A final calibration measurement using the polarization conditions of interest was then performed, but instead of time-delaying the field(s), the phase of one field was varied to calibrate the global phase offset. The delay-dependent amplitude modulation was also corrected. Finally, a two-dimensional scan was performed and analyzed using the data acquisition and spectral interferometry procedures depicted in Fig. 3-11. The scanned time dimension of the resulting data set—using the notation of Sec. 3.10, $\tilde{S}(\tau_{scan}, \omega_{emit})$ —was zero padded if needed and then Fourier transformed to yield $\tilde{S}(\omega_{scan}, \omega_{emit})$. The carrier frequency², was added to the scanned frequency axis values to yield $\tilde{S}(\omega_{scan} + \omega_0, \omega_{emit})$. The resulting complex-valued spectrum was then transformed to $\tilde{S}(E_{scan}, E_{emit})$ by multiplying the

²Or frequencies if two or more different beams were scanned.

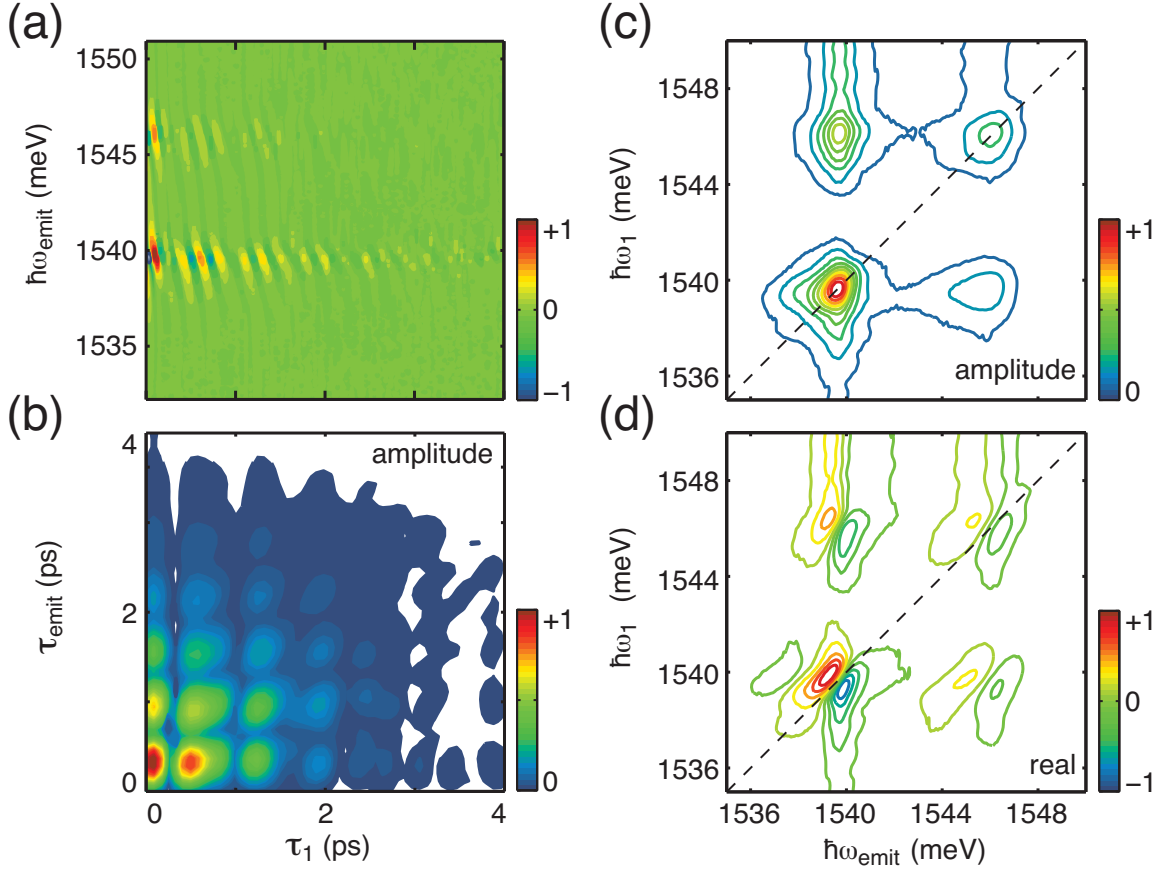


Figure 3-11: Result of a third-order rephasing experiment ($\tau_2 = 0$) using co-linearly polarized pulses in the BOXCAR geometry. (a) The unprocessed data shows coherent oscillations at the H and L exciton emission energies of 1540 and 1546 meV, respectively. Phase cycling reduced signals due to scattered light, eliminated homodyne contributions, and amplified the signal. (b) One step in the spectral interferometry procedure is to Fourier transform the emission frequency dimension to the time domain. At this point in the procedure, we plot the amplitude of the complex-valued time domain signal. (c) The final amplitude spectrum after finishing the spectral interferometry procedure along the emission dimension and Fourier transforming the scanned time dimension. Cross peaks between the H and L excitons indicate their coupling. (d) The real part of the spectrum provides additional information about many-body interactions [139].

axis values by the Planck constant. Often the amplitude of this spectrum or only its real part are displayed. A 2D spectrum can be acquired in about ten minutes for eight-step phase cycling whereas a 3D spectral solid data set requires about ten hours to acquire. The current laboratory procedure for measuring a signal involves at least six—and up to ten—steps:

1. Adjust the laser to have the desired bandwidth and central wavelength.
2. Perform the geometric alignment.
3. Insert waveplates, if needed.
4. Perform the temporal alignment of the center beam.
5. Perform the wavelength-to-pixel calibration.
6. Correct the temporal modulations using cross-correlation measurements.
7. Calibrate the carrier frequency, if needed.
8. Calibrate the global phase, if needed.
9. Calibrate the amplitude modulation, if needed.
10. Acquire the desired spectrum using spectral interferometry and phase cycling.

The raw phase-cycled data for a third-order co-linear polarized scan are shown in Fig. 3-11(a). Coherent oscillations with positive and negative amplitudes are observed at the H and L exciton energies—1540 and 1546 meV, respectively—during time period τ_1 . The tilt of the peaks is related to the difference between the exciton frequency and the carrier frequency, $\omega_e - \omega_0$. Increasing this frequency difference makes the phase, $(\omega_e - \omega_0)\tau_{del}$, accumulate faster as the pulse is delayed. This results in faster-moving fringes that must be sampled using smaller time steps. While applying the spectral interferometry algorithm—performed across ω_{emit} for each τ_1 value—the two-dimensional temporal signal can be retrieved. The amplitude of this signal is displayed in Fig. 3-11(b). After the spectral interferometry algorithm is finished and the scanned time dimension, τ_1 , has been Fourier transformed, the resulting spectrum can be displayed. Its amplitude is displayed in Fig. 3-11(c), and its real part is displayed in Fig. 3-11(d). The values along the vertical axis—which Fourier transform to negative values because of the frequency-accounting scheme used to illustrate which field(s) contribute a negative wave vector to the emitted signal—were converted to positive values. Several many-body interactions are observed in this spectrum as discussed in future chapters and in Ref. [139].

3.13 Limitations of the COLBERT spectrometer

Although the COLBERT spectrometer is versatile and efficient, it also has limitations. In principle, all of the problems have solutions. The most hindering limitation is the delay-dependent amplitude modulation. Line-by-line shaping [256] can overcome this problem, but it requires a carrier-envelope phase-stabilized oscillator [270], and—for our pulse bandwidth—this technique requires an SLM with about an order of magnitude more pixels in the horizontal dimension than the one used here. Furthermore, the oscillator would need to be at a high repetition rate so that the frequency separation between each line in the comb is large. The pulse spectra would also need to have a small bandwidth to minimize the number of lines in the comb. The ensuing long pulse duration is acceptable for GaAs quantum wells but could prohibit studies of systems with faster dephasing times. On the other hand, if the coherences dephase quickly, the amplitude modulation will have less of an influence.

The aberration-induced temporal modulations caused by the cylindrical lens present another challenge. These modulations can be eliminated by replacing the lens with a cylindrically curved mirror and changing to a reflective geometry [251]. This change will eliminate the off-axis cylindrical aberrations so that all of the beams will have the same dispersion. Thus all of the beams can be optically corrected without additional phase compensations through cross correlations. However, this introduces a vertically dependent temporal delay problem because the top beams and the bottom beams will traverse slightly different pathlengths.

The long path length may hinder commercial acceptance. The length can be reduced by using shorter focal length lenses throughout the device, but this requires a beam shaping SLM with a higher damage threshold and smaller pixels. Another approach is to replace some lenses to use non-unitary imaging ratios. For example, lenses L2 and L3 could be smaller focal lengths as long as the distances were simultaneously changed so that the focal planes remain unchanged: L2 must recollimate the outputs of the beam shaper and L3 must have a focal plane at M. If waveplates were not needed, the focal length of lens L5 could be significantly shortened.

Although our SLMs have a damage threshold of 2 W/cm^2 , the coatings used to do this limit the bandwidth to $800 \pm 50 \text{ nm}$. In general, however, COLBERT is not limited to this particular region of the spectrum. Liquid crystal on silicon (LCOS) SLMs which cover most of the visible and near-IR parts of the spectrum are available. MEMS-based SLMs capable of working in the visible and UV regions are also available, and 2D infrared SLMs are in development.

Finally, the data acquisition time could be reduced if the SLM refresh rate, currently 3 Hz, were increased. Since this depends on the rise time of the liquid crystals,

MEMS-based devices would be more appropriate [172]. Unfortunately, such devices are less efficient because the large gaps between pixels cause additional unwanted diffractions.

3.14 Summary

In this chapter we described a versatile and efficient device, the COLBERT spectrometer, capable of performing multidimensional coherent spectroscopic measurements at optical wavelengths. The device requires relatively few optics and, once constructed, requires relatively little reconfiguration to perform measurements at varying nonlinear orders under varying conditions. The biggest limitation of the device is its limited delay range. Several calibration procedures are required for optimal operation. We also discussed areas for future improvements to the spectrometer.

In the following chapters, we show numerous multidimensional spectra. The spectra demonstrate the sophisticated and wide-ranging experiments possible using the COLBERT spectrometer.

Chapter 4

Two-particle correlations: excitons

This chapter describes several experiments designed to measure the properties of the single excitons in our system. The linear absorption spectrum of the material has two resonances due to the H and L excitons. We can extract resonance energies, absorption coefficients, and dephasing times from the locations, amplitudes, and widths of the peaks, respectively. We use the absorption coefficients to estimate the carrier density. The transient grating experiment reveals an unusual initial nonexponential decay in addition to the lifetime of the H excitons. After these one-dimensional measurements are presented, discussion proceeds to multidimensional spectra.

The presence of cross peaks in the 2D FTOPT spectra indicate that the H and L excitons are coupled. The 2D FTOPT spectrum changes as polarization conditions are varied, and many of the changes are not merely due to pathway selectivity differences. Correlation spectra at different waiting times reveal additional features not predicted by the sum-over-states model. Two-dimensional projections of a 3D spectral solid contain features due to strong excitonic quantum beats even in the co-circular polarization configuration. Throughout the measurements, we discuss features that indicate the presence of exciton-exciton correlations.

4.1 Exciton resonance energies and strengths

One of the simplest and most important spectroscopic experiments is an absorption measurement. Absorption coefficients—effectively a fractional absorption per unit length at each frequency—can be extracted from absorption spectra. The absorption spectrum shown in Fig. 4-1(b) was calculated from the two measurements in Fig.

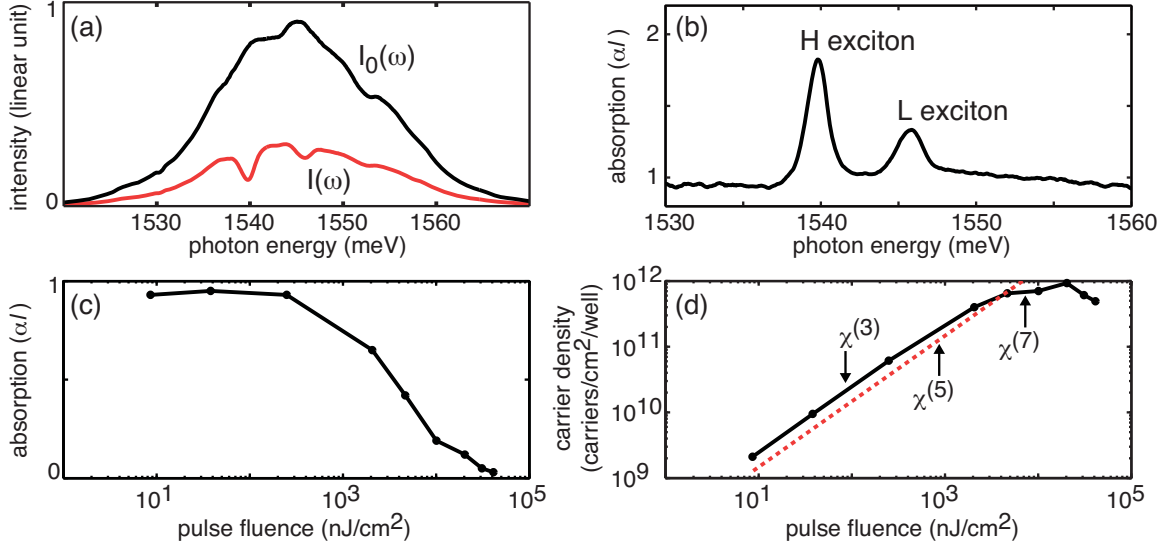


Figure 4-1: Absorption spectrum of GaAs sample. (a) Spectral intensity measured by the spectrometer without (black line) and with (red line) the sample inserted. (b) The unetched, residual substrate has an absorption of $\alpha l \sim 1$ across the spectrum. The measured exciton absorption coefficients are about $\alpha_H = 5 \times 10^5 \text{ cm}^{-1}$ at 1540 meV and $\alpha_L = 1.5 \times 10^5 \text{ cm}^{-1}$ at 1546 meV. (c) Measurements of the H exciton absorption at varying pulse fluences. Saturation begins to occur at about 10^3 nJ/cm^2 . (d) Converting the absorption to an upper bound for carrier density as described in the text. The minimum fluences at which nonlinear signals were observed are indicated. The red dashed line reflects a linear relationship between carrier density and fluence.

4-1(a) as given by the Beer-Lambert law,

$$\alpha(\omega)l = -\ln\left(\frac{I(\omega)}{I_0(\omega)}\right). \quad (4.1)$$

The energies of the excitons are $E_H = 1540 \text{ meV}$ and $E_L = 1546 \text{ meV}$. Since the pathlength is 100 nm, the exciton absorption coefficients are about $\alpha_H = 5 \times 10^5 \text{ cm}^{-1}$ and $\alpha_L = 1.5 \times 10^5 \text{ cm}^{-1}$, where we included an estimate that the reflection losses due to index mismatches at the surface and between layers are about fifty percent. These values are somewhat higher than previous reports of 10^4 cm^{-1} for bulk GaAs [271, 272] but in agreement with a previous measurement of this sample [273]. The background absorption is due to excitations in the unetched substrate that do not interact with the excitons in the wells because the substrate is separated from the wells by a thick (hundreds of nanometers) $\text{Al}_{0.3}\text{Ga}_{0.7}\text{As}$ barrier. The linewidths of the features in the absorption spectrum are about 1.5 meV, which corresponds to a total dephasing time of about 1.5 ps.

The absorption spectrum can be used to estimate the density of carriers excited

in the sample. As we will see, carrier density estimates using the pulse fluence have uncertainty. The energy in each laser pulse, E_{pulse} , can be found by measuring the power of the laser beam and the pulse repetition rate. Using a pinhole at the focus of the beam where the sample is placed, we can measure the illuminated area, A . (These values yield the fluence, F . The spectra in Fig. 4-1(a) were measured at a fluence of ~ 30 nJ/cm².) We estimate the number of photons per pulse, N , by assuming that each photon has the energy of the heavy-hole exciton, $E_{photon} = 2.47 \times 10^{-10}$ nJ. Then the number of photons can be computed by $N = \frac{E_{pulse}}{E_{photon}}$. The photon density, p , is given by $p = \frac{N}{A} = \frac{F}{E_{photon}}$. Finally, the carrier density, c_d , can be estimated from the absorption by

$$c_d = p \times (1 - e^{-\alpha l}) / N_{wells}, \quad (4.2)$$

where N_{wells} is the number of quantum wells, ten for our sample. Panels (c) and (d) in Fig. 4-1 reveal absorption saturation at fluences above 10^3 nJ/cm². This effect will have consequences in several of the higher-order measurements that were performed at high fluences. The carrier density saturates at just below 10^{12} excitons/cm²/well. This value corresponds to the number of excitons with a Bohr radius of 10 nm that can fit in 1 cm².

Three variables make this an upper bound on the carrier density. First—although we assumed it above—not all of the pulse energy was converted to excitons because not all of the photons in the pulse were resonant with the H or L excitons. Clearly this is the case for Fig. 4-1(a) where the pulse bandwidth is about 20 meV. However, some measurements in the following chapters used pulses with bandwidths less than 10 meV. As an added complication, exciton–free-carrier scattering can cause photons with energy greater than the exciton energy to be converted from free carriers to excitons. Therefore, including a spectral density function in Eqn. 4.2 to account for the overlap between the excitation spectrum and the absorption spectrum may or may not be accurate. Second, although we did not measure it, the sample reflects a portion of the input light. We estimated this loss mechanism using index mismatch values. The third variable is intrinsic to the time-dependent nature of the measurement: the time at which we define the carrier density. In this work we use the total power of all the beams that interact the sample. At least one study estimated the carrier density only using the sum of powers of those beams that were scanned [99]. For example, the carrier density of a third-order (one-quantum) rephasing measurement would incorporate only the power in the one beam that was scanned, not all three excitation beams. This would cause a difference of a factor of three from the densities reported in this thesis. Unfortunately, most studies simply report a value of the carrier density; they did not indicate how these three variables were incorporated. The carrier

density values reported in this thesis did not incorporate a spectral density function, accounted for reflections using an estimate, and used the total power of all beams.

Careful measurement and analysis of the sample absorption is required to estimate the carrier density accurately. Our indicated values are upper bounds, perhaps by as much as one order of magnitude, depending on the pulse bandwidth and number of fields scanned. The carrier density is an important parameter used to anchor the experiments because spectral features can change dramatically as the carrier density changes. We will note some of these changes throughout our results.

4.2 Exciton lifetimes

Transient grating measurements [274–276] are four-wave-mixing measurements in which the first two fields, E_a and E_b , overlap at the sample to create a spatially periodic exciton population grating, and, after a variable time delay (τ_2), beam E_c is diffracted by this interference pattern into the background-free signal direction. The beam geometry is depicted in Fig. 4-2. The scanned time period—which typically contains only incoherent signals—contains information about the decay of the eigenstate populations, and by measuring the time-integrated intensity of the emitted signal as function of delay time, one can extract the lifetimes of the states. The data set presented in Fig. 4-2 was measured using pulses whose spectral FWHM were less than 10 meV with a fluence just below 10^3 nJ/cm² to generate strong, clean signals from only H excitons. We constructed a traditional beam splitter and delay stage apparatus instead of using the COLBERT spectrometer to scan beyond 10 ps. This is the only measurement in which we did not use the COLBERT spectrometer. A bandpass filter prevented contributions from the substrate at 820 nm from contributing to the signal. The lifetime of L excitons can be measured in exactly the same fashion but with the pulse spectra centered on the L resonance.

The data show an initial nonexponential decay followed by a decay that is fit with a time constant of 420 ps. The beams had co-circular polarization to prevent biexciton-exciton emission contributions discussed in the next section. The initial nonexponential decay was observed previously in studies of quantum dots and was attributed to surface defects, exciton recombination, and passivation [277]. This nonexponential decay can be simulated as an overdamped Fano system with two discrete states and a continuum [198]. In work on quantum dots, the authors also described a fitting procedure to extract the biexciton lifetime from a fifth-order version of a transient grating measurement. We have taken preliminary fifth-order measurements to extract the HH biexciton lifetime, and we observed rapid signal decays similar to

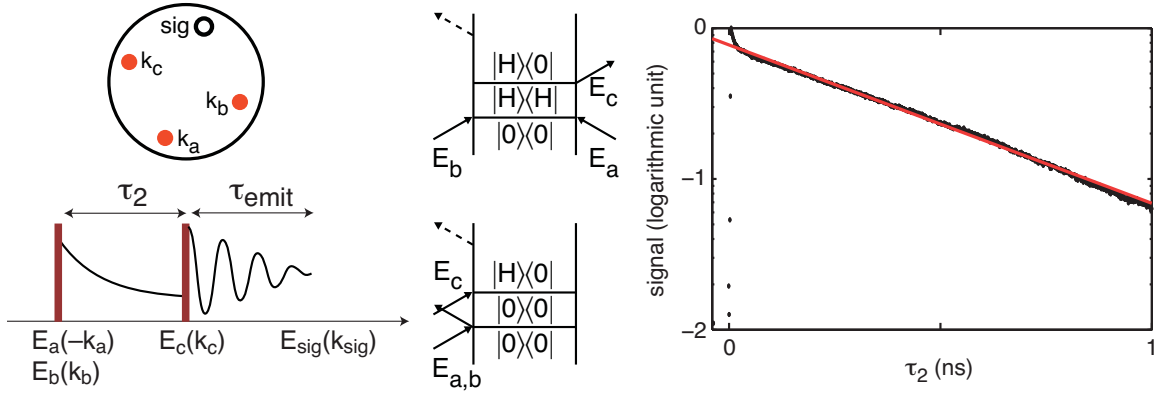


Figure 4-2: Third-order transient grating measurement of H excitons in the BOXCARS geometry using co-circular polarization. Time period τ_2 was scanned for one nanosecond using a delay stage. At each delay, the emitted signal was time-integrated with a photodiode. The pulse spectra were resonant with only the H exciton. After a brief nonexponential decay, the signal decays with a time constant of 420 ps. In addition to the exciton interactions that cause the initial nonexponential decay, two Feynman pathways which decay with the exciton lifetime contribute to this signal.

those observed in Ref. [277].

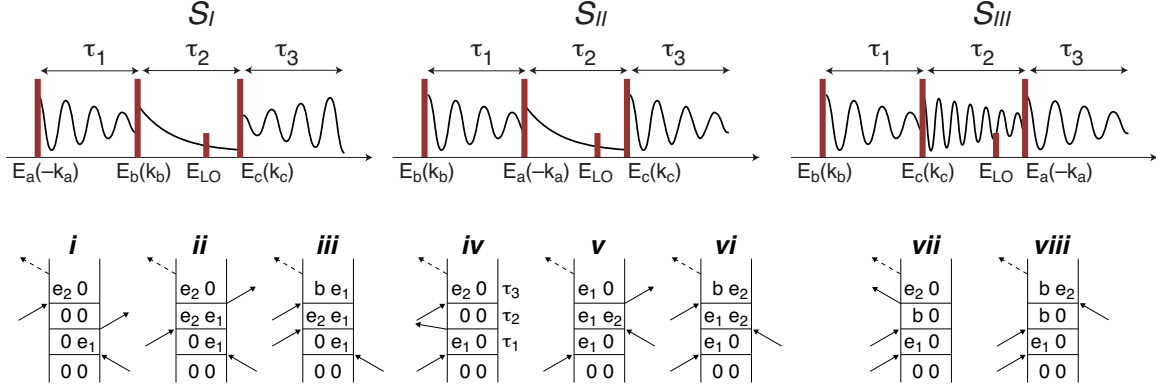


Figure 4-3: The three possible pulse timing sequences in third-order measurements and generalized Feynman diagrams for each sequence. The local oscillator always interacts 1 ps before the third field interaction and propagates in the signal direction. (left) S_I measurements are used to rephase exciton coherences. (middle) S_{II} measurements have population decays during τ_2 and free-polarization decays during τ_3 . (right) S_{III} measurements have two-quantum coherences during τ_2 which can be correlated to the emitted frequencies. (diagrams) The labels 0, e_1 , e_2 , and b represent the ground state, one exciton state, another exciton state, and biexciton states. When $e_1 = e_2$, the diagrams contribute to diagonal peaks; when $e_1 \neq e_2$, the diagrams contribute to cross peaks. The biexciton state b can include pure biexcitons, HH and LL , and mixed biexcitons, HL , depending on the polarization conditions.

4.3 Cross peaks between excitons

We next measure coherent 2D FTOPT spectra using a third-order four-wave-mixing signal. There are three types of third-order 2D FTOPT scans, and they are distinguishable by the time ordering of the conjugate field. As depicted in Fig. 4-3, rephasing scans are those in which the conjugate field interacts first; they are abbreviated as S_I measurements. Similarly, transient grating (also called virtual echo) measurements are those in which the conjugate field interacts second, and they are abbreviated as S_{II} . The third type of scan is different than the first two in regards to the dynamics during the second time period. When the conjugate field interacts third in these S_{III} scans, the first two fields create two-quantum coherences that evolve during time period τ_2 and which are then projected onto one-quantum coherences that radiate signal. As we will see in the next chapter, these two-quantum coherences will allow us to measure two-exciton interactions directly. Representative Feynman diagrams are shown for each pulse sequence.

The 2D FTOPT measurement shown in Fig. 4-4 is the result of an S_I scan in the BOXCAR geometry when all four fields had horizontal polarization and the spectrum covered both the H and L resonances. The pulse fluence was about 10^2 nJ/cm². The conjugate field interacted first with the sample, and the exciton coherences it in-

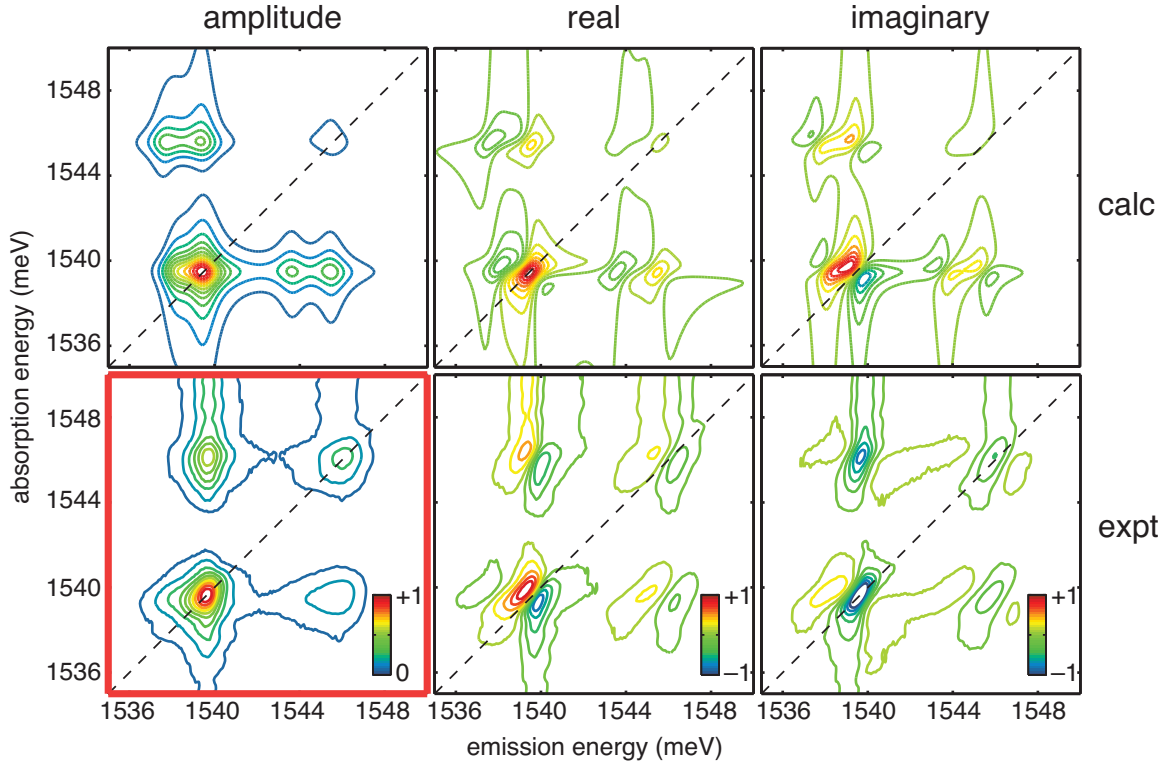


Figure 4-4: Rephasing measurements of H and L excitons under co-linear polarization. The top are the amplitude, real, and imaginary parts of the spectrum from a simulation using the sum-over-states model incorporating the exciton energies and transition dipole values found using the linear absorption measurement. The bottom are the amplitude, real, and imaginary parts of the experimentally measured spectrum. The bold red box surrounds the amplitude of the experimental spectrum in which we observe the cross peaks between the H and L excitons. The simulation deviates significantly from the experiment. The most striking deviations are the phase offset that swaps the real and imaginary parts, the lack of HL biexciton features in the experiment, the strong vertical stripes present in the experiment, and the inequality in the experimental cross-peak amplitudes.

duced during the scanned time period, τ_1 , were rephased during the emission time, τ_3 . The second time period was not swept but had a constant value of $\tau_2 = 0$. As discussed in Ch. 3, the first time period was swept from 0 to 6 ps in 128 steps and the carrier frequency was set so that exciton coherences oscillated at slow, rotating-frame frequencies of less than 10 THz during τ_1 . The scanned time dimension was subsequently Fourier transformed to yield the absorption energies. The emission energies were detected directly in the spectrometer via spectral interferometry.

For the moment we focus on the amplitude of the measured spectrum outlined in the bold red box. It shows two diagonal peaks and two cross peaks, reminiscent of the ‘V’-shaped example system shown in Fig. 2-4 in which two excited states were coupled through a common ground state. The full field was measured, so in addition to the amplitude of the spectrum, we can display its real and imaginary parts.

We simulated the spectrum using a set of Feynman diagrams similar to the generalized diagrams *i*, *ii*, and *iii* in Fig. 4-3. The top row of Fig. 4-4 contains the amplitude, real, and imaginary parts of the simulated spectrum. Several discrepancies exist between the simulation and the experiment. The most significant is the phase shift which causes the real part of the peaks to have dispersive lineshapes rather than absorptive lineshapes. Phenomenological simulations using the modified optical Bloch equations incorporating EID were able to reproduce this phase shift [139]. A second deviation is the presence of large vertical stripes on the two high-energy absorption features. The stripes are due to free carriers that initially absorbed, but then—through exciton–free-carrier coupling—scattered coherently into excitons that radiated signal. A third difference between the simulation and the experiment is that the mixed-biexciton–exciton emission features, which are prominent as red-shifted shoulders in the simulation cross peaks, are almost nonexistent in the experimental spectrum. Interactions in the sample cause the transition dipoles to these states to be less than expected. Finally, the cross peaks have equal amplitudes in the simulation but unequal in the experiment; this difference is due to many-body interactions and will be discussed more in the next section.

Both the measurement and its simulation were performed under co-linear polarization; this polarization scheme contains all possible signal contributions. It is not optimal for isolating specific many-body interactions. In the next section we present results for two polarization conditions in which we excite specific many-body interactions.

4.4 Exciton correlation spectra

In this section we present the 2D FTOPT measurements and simulations using cross-linear and co-circular polarization schemes as correlation spectra: the S_I and S_{II} signals are summed to eliminate phase twist and sharpen the features [109, 110, 122, 125, 128, 278]. As with most concepts in multidimensional optical spectroscopy, this is borrowed from multidimensional NMR spectroscopy [100, 279]. The phase-twisted shape in the rephasing and nonrephasing signals is due to Fourier transformation of a signal that evolves with a complex phase in two time periods; this mixes the absorptive (a) and dispersive (d) components of a spectral peak. Roughly, $\text{Re}[S_I] = a(\tau_1)a(\tau_3) - d(\tau_1)d(\tau_3)$ and $\text{Re}[S_{II}] = a(\tau_1)a(\tau_3) + d(\tau_1)d(\tau_3)$, see Sec. 6.5 in Ref. [100]. If the rephasing and nonrephasing signals contribute equally to the signal, their sum will eliminate the dispersive contributions¹, $\text{Re}[S_I + S_{II}] = 2a(\tau_1)a(\tau_3)$. For this reason, correlation spectra have also been called *purely absorptive* spectra. Correlation spectra can also be created in a single scan, where one beam contains a variably delayed pulse pair. Only one signal is then measured; this decreases the data acquisition time and increases the signal-to-noise ratio [237, 240, 280].

Cross-linear polarized (VH VH) signals do not contain contributions from exciton population effects such as EIS and EID because the first two fields create two spatially periodic exciton population gratings that are π phase shifted [281, 282]. It is worthwhile to note that the two exciton gratings are due to a single resonance, for example the H excitons alone. For simultaneous H and L excitation, there are effectively four gratings, two for each exciton. Each pair would have a π phase shift between the constituents. The net result is that there is no exciton population grating, and therefore signals are weak in this polarization configuration [146]. This polarization scheme isolates signals due to single excitons H and L , and pure biexcitons HH and LL . The sum-over-states model did not include signal pathways that lead to mixed biexcitons, HL , and since exciton-exciton interactions cannot be incorporated, they were already excluded.

Co-circular polarized ($\sigma^+\sigma^+\sigma^+\sigma^+$) signals will contain contributions due to EID, EIS, exciton-free-carrier scattering, and mixed biexcitons. However, contributions due to pure biexcitons will be eliminated, and this scheme is simulated by eliminating signal pathways due to pure biexcitons. We expect the simulation and experiments to differ significantly because the strong exciton-exciton interactions cannot be repro-

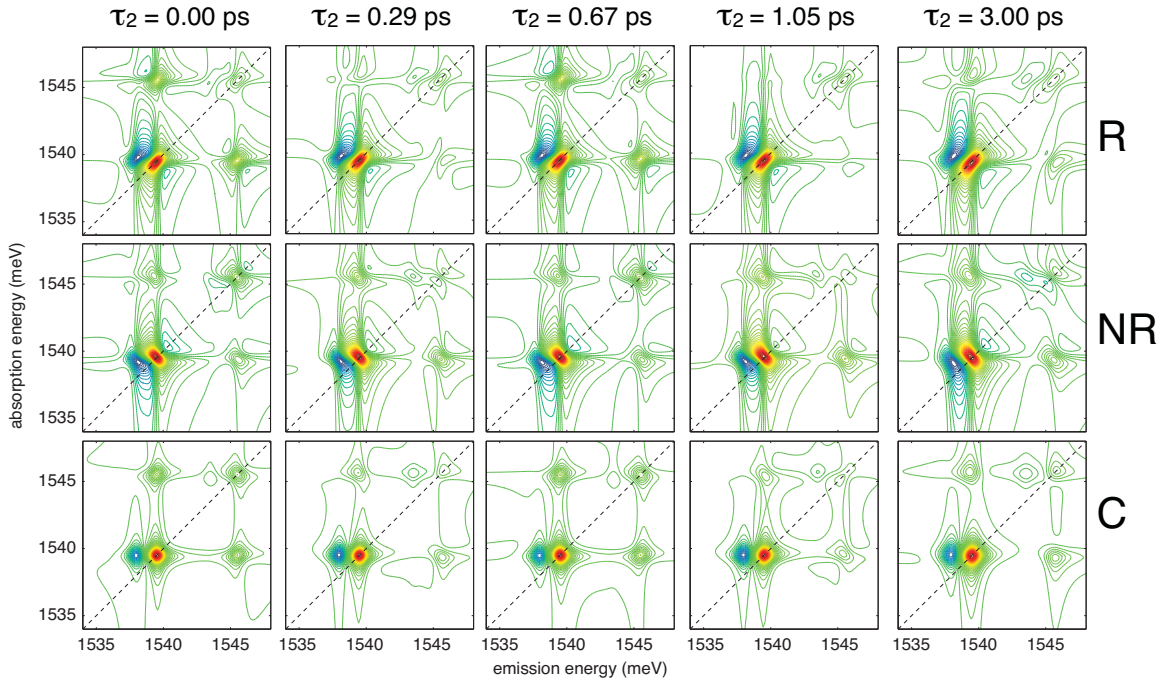
¹Similarly, their difference would eliminate the absorptive contributions, although to our knowledge this has not been explored. Such a ‘purely dispersive’ 2D spectrum could also be created by summing the imaginary components of the S_I and S_{II} signals. In most nonlinear optical measurements, the imaginary (dispersive) component of a resonance feature corresponds to ϵ .

duced using the sum-over-states model. The simulations implicitly incorporate strong Coulomb coupling between the H and L excitons in a manner similar to quantum coupling through a common ground state, as discussed in Sec. 2.5.

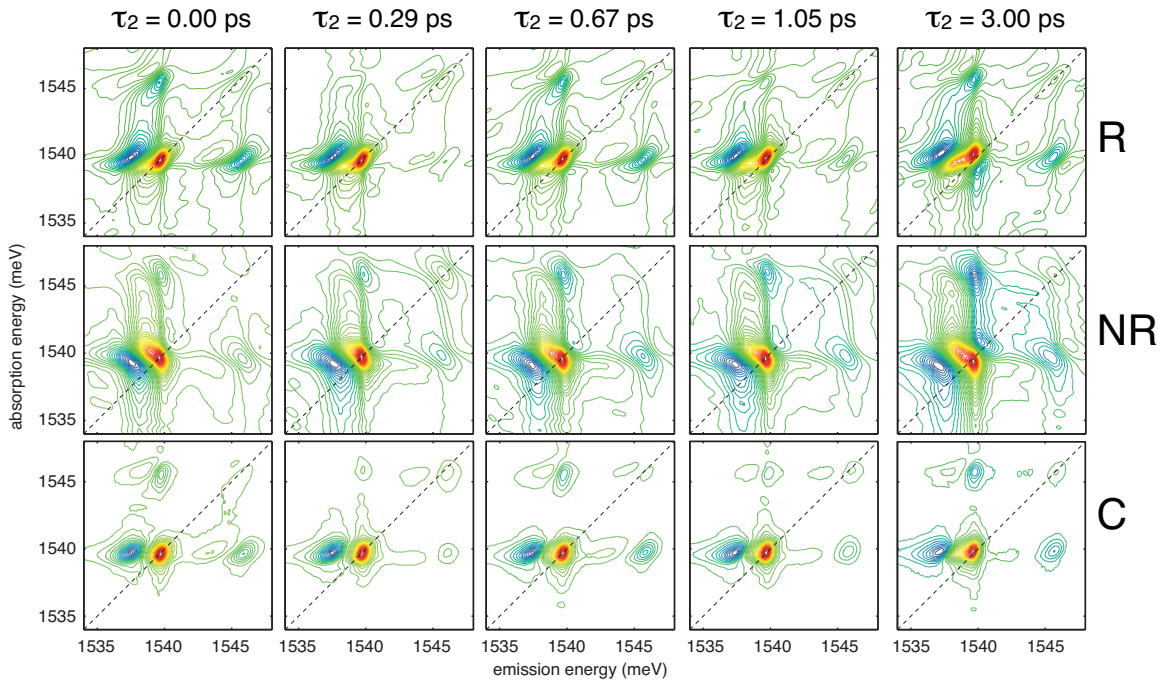
Fig. 4-5(a) shows the simulated spectra for cross-linear polarized fields. Rephasing spectra, nonrephasing spectra, and their sum—the correlation spectra—are shown for five τ_2 values. These times were chosen because they correspond to peaks and valleys in the H - L quantum-beat frequency of about 6 meV, or about 1.5 THz. The advantage of the correlation spectrum is clear; peaks are sharper and the phase twist is eliminated. Moreover, the HH biexciton-exciton emission pathway in the correlation spectrum appears as a separate peak rather than as a shoulder. As a testament to how well this polarization configuration can suppress many-body interactions, our simulations in Fig. 4-5(a) and experiments in Fig. 4-5(b) agree in almost every detail. The strongest peak—the H diagonal peak—has an absorptive lineshape in both cases. The HH biexciton-exciton shoulder to the H diagonal peak has the opposite sign because it is an excited-state-emission pathway, diagram *iii* in Fig. 4-3. The node between these two features remains at a constant angle as τ_2 evolves. The L diagonal peak and the shoulder due to LL biexciton-exciton emission are much weaker than their H counterparts because the transition dipoles are smaller. The two cross peaks have similar amplitudes.

The two cross peaks have interesting oscillatory dynamics during τ_2 in both amplitude and phase. These oscillations are due to pathways—of type *ii* and *v* listed in Fig. 4-3, where $e_1 \neq e_2$ —that involve quantum beats between the H and L excitons during the second time period: an $|H\rangle\langle L|$ or $|L\rangle\langle H|$ coherence. Crucially, quantum beat pathways contribute to the cross peaks of a rephasing scan (diagram *ii* in Fig. 4-3) but contribute to the diagonal peaks in a nonrephasing scan (diagram *v* in Fig. 4-3). Thus, at $\tau_2 = 0.29$ ps, the rephasing pathway that contributes to each cross peak is near a minimum, reducing the rephasing signal at the cross peak coordinates, and therefore the correlation spectrum has less rephasing character. In both the simulation and the experiment, at these τ_2 valleys the nonrephasing and rephasing pathways are nearly equal. The opposite situation happens at $\tau_2 = 0.67$ ps when the rephasing quantum beat pathways are at maxima. The rephasing signal contributes more strongly than the nonrephasing signal because inhomogeneous dephasing—which reduces the coherent amplitude—is reversed (meaning rephased) in the former but not in the latter. The correlation spectrum has strong rephasing character at these τ_2 values, and therefore the nodes in the cross peaks are parallel to the diagonal and the cross peak amplitudes are strengthened.

All of these effects appear in the experimental spectra in Fig 4-5(b) as well. The



(a) The real part of the simulated rephasing (R), nonrephasing (NR), and correlation (C) spectra.



(b) The real part of the experimental rephasing (R), nonrephasing (NR), and correlation (C) spectra.

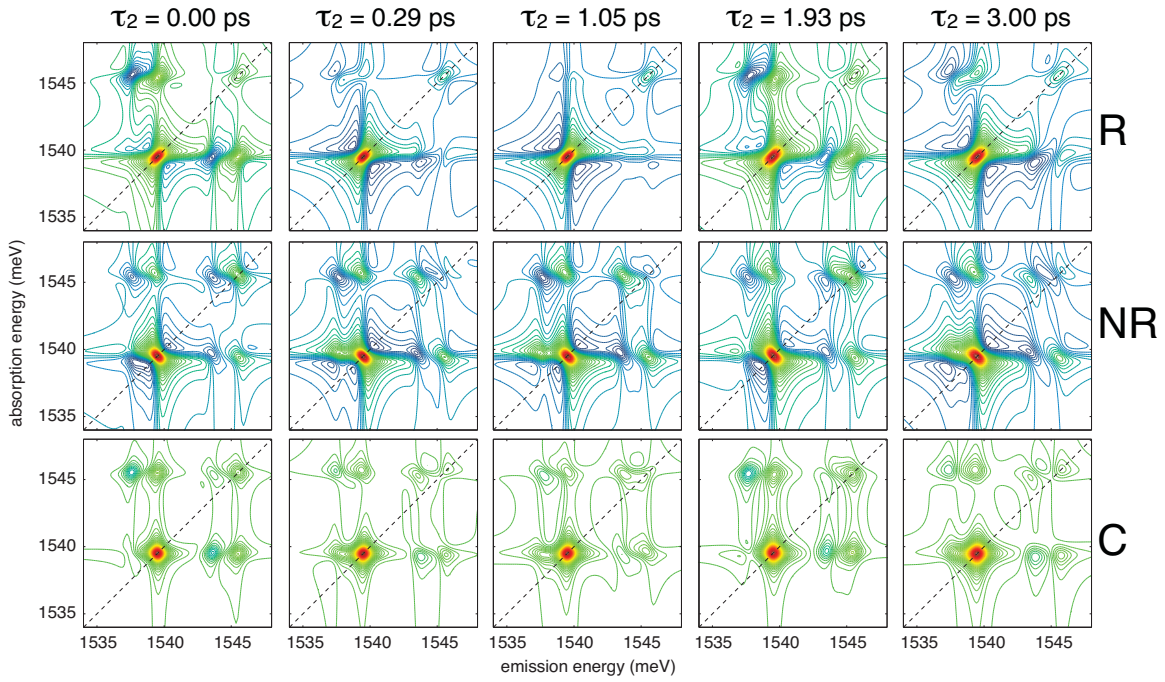
Figure 4-5: Simulation and experiment of correlation spectra at various τ_2 times for cross-linear polarized excitation fields.

biexciton-exciton emission signal appears as a peak rather than as a shoulder in the correlation spectrum. The nodal angle and amplitude of the cross peaks oscillate, and they do so because the rephasing pathways oscillate. Another experimental feature that is replicated by the model is the equal amplitude of the two cross peaks.

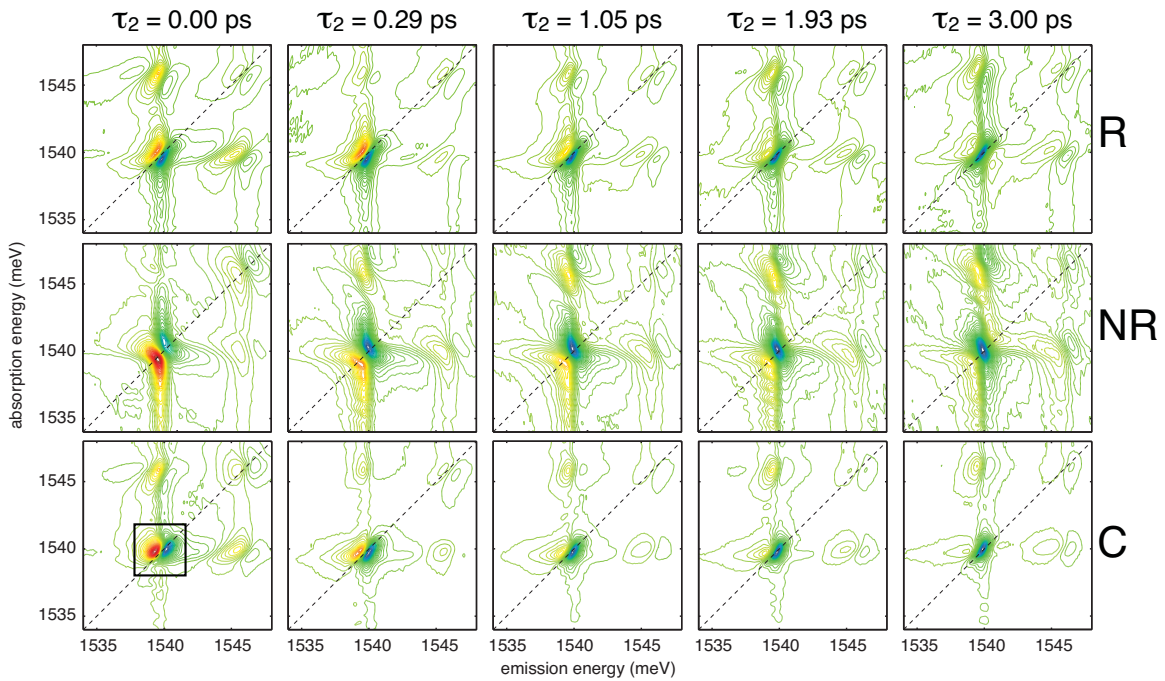
Nevertheless, we can note at least two deviations from the simulation. First, the cross peak oscillations (amplitude and phase) weaken as τ_2 evolves in the experiment; the time during which the excitons can remain coherent is the same exciton dephasing time—1.5 ps—extracted from the linear absorption experiment. Exciton dephasing during τ_2 was not included in the simulation. Second, the H diagonal peak and its biexciton shoulder are elongated along the diagonal slightly in the experiment. This is due to the small amount of inhomogeneous broadening present in our sample due to well-width fluctuations. This broadening mechanism was not incorporated in the simulation. On the whole, however, the sum-over-states model describes the cross-polarization scheme accurately since most many-body interactions, including exciton-free-carrier scattering and excitation-induced effects, were eliminated.

We now display the same rephasing, nonrephasing, and correlation spectra as above but for co-circular polarized fields. Simulated spectra are presented in Fig. 4-6(a) and experimental spectra are presented in Fig. 4-6(b). Cross peaks exist in this polarization configuration, even though the exciton selection rules presented in Sec. 2.5 indicate that the excitons should be independent two-level systems, similar to System X in Fig. 2-4. Instead, the existence of the cross peaks indicates that the two exciton states are coupled, similar to System Y in Fig. 2-4. In this case the coupling is not due to a common ground state, but is instead due to many-body interactions. Therefore we included pathways leading to cross peaks in the simulation. Additionally, since pathways involving HH biexcitons have been suppressed, the H exciton diagonal features in the rephasing spectra are predicted to have absorptive lineshapes. However, in the nonrephasing pathway, HL biexciton-exciton emission can appear as a shoulder on the H exciton diagonal peak. Since the transition dipole of the HL biexciton is much smaller than that of the HH biexciton, biexciton-exciton features are much weaker than those in the cross-linear polarization scheme. In the correlation spectrum, rephasing quantum beat pathways cause the nodal angles and amplitudes of the cross peaks to oscillate. Here we display spectra with $\tau_2 = 1.95$ ps instead of $\tau_2 = 0.67$ ps so that we have spectra measured close to 1 ps intervals.

The experimental co-circular spectra show many deviations from the simulations. Most striking at $\tau_2 = 0$ is the phase shift in the H diagonal feature due to EID [139]. By taking spectra at varying τ_2 times, we see the phase shift diminish. The H exciton diagonal feature loses most of its dispersive character by $\tau_2 = 3$ ps, suggesting a decay



(a) The real part of the simulated rephasing (R), nonrephasing (NR), and correlation (C) spectra.



(b) The real part of the experimental rephasing (R), nonrephasing (NR), and correlation (C) spectra.

Figure 4-6: Simulation and experiment of correlation spectra at various τ_2 times for co-circular polarized excitation fields.

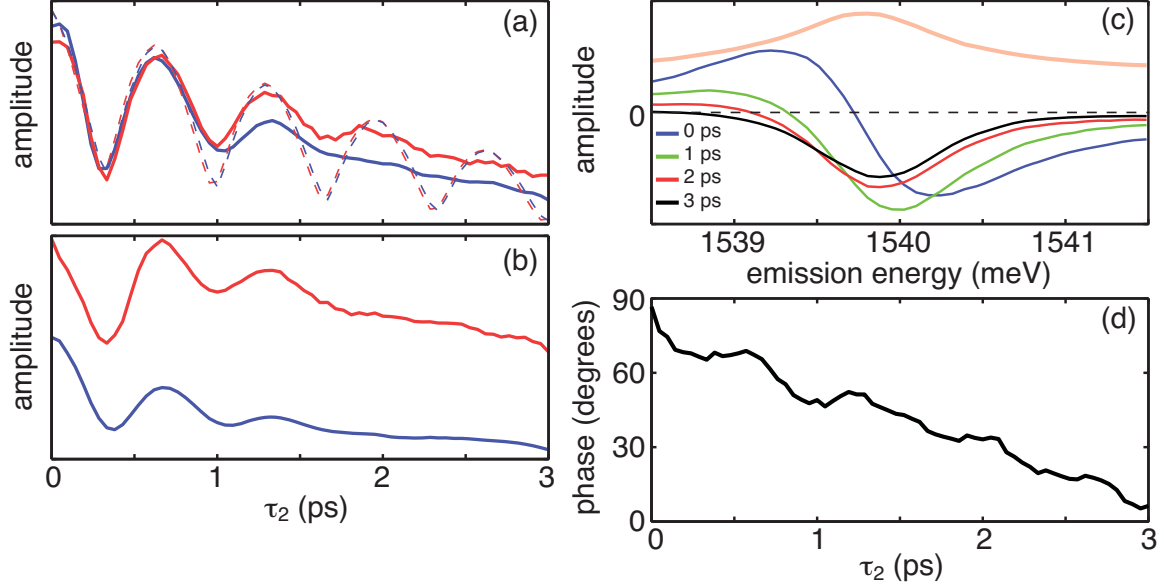


Figure 4-7: Extracted cross peak amplitudes for cross-linear (a) and co-circular (b) polarization configurations as a function of τ_2 . Red (blue) is H (L) emission feature. The dashed lines in (a) are extracted from the cross-linear simulation (c) Projection onto the emission axis of the real part of the H diagonal peak for co-circular polarization at the indicated τ_2 values. The thick orange curve is the amplitude of the projection at $\tau_2 = 0$. (d) Extracted phase of same peak at all values of τ_2 indicating decay of the EID contribution.

in the EID effect. Simulated features due to HL biexcitons do not appear at all in the experiment. The cross peaks have different amplitudes in the experiment but equal amplitudes in the simulation. The nodal angle oscillations in the cross peaks in the experiment are much weaker than in the simulation. The ratio of the diagonal and antidiagonal linewidths in the H diagonal feature again reflects the amount of inhomogeneous broadening present in the sample.

We now analyze many-body interaction dynamics for both polarization conditions. We extract spectral features due to many-body interactions as functions of time period τ_2 and display the results in Fig. 4-7. The cross peak amplitudes evolve for cross-linear (a) and co-circular (b) polarization configurations similarly. The traces are almost identical, indicating that Coulombic coupling in the co-circular polarization experiment has nearly the same effect as true quantum coupling in the cross-linear polarization experiment. Moreover, the dashed lines in (a) are extracted from the cross-linear simulation. They match well, although the quantum beat dephasing was not incorporated into the simulation. The delay-dependent amplitude modulation was incorporated, causing the observed decay in the envelope but not damping of the oscillations. There is one significant difference between the cross-linear (a) and co-circular (b) cross-peak amplitude data. In the co-circular experiment, the cross

peak which emits as L is much weaker than the cross peak which emits as H . This suggests a coherent Coulomb-assisted decay channel from the L exciton to the H exciton. Nevertheless, the same number of oscillation periods are observed in all four cross peaks, indicating that although their amplitudes are different, their dephasing rates are not. This equality in timescales for the quantum beat oscillations indicates that the Coulomb coupling is strong enough that the decay time is not limited by the strength of the many-body interaction, but rather is limited by general dephasing processes.

We also extracted the dynamics of the phase of the H diagonal peak in the co-circular polarization configuration. Fig. 4-7 parts (c) and (d) describe the dynamics; these data can only be extracted from correlation spectra. Rephasing or nonrephasing spectra alone would have additional dispersive wings due to phase twist. The four traces shown in (c) were produced by projecting a neighborhood around the H diagonal peak of real part of the correlation spectrum onto the emission axis as indicated by the box in Fig. 4-6(b). At $\tau_2 = 0$, the blue line in Fig. 4-7(c) indicates the dispersive lineshape. As τ_2 evolves, the lineshape becomes increasingly absorptive as shown by the green, red, and black lines at $\tau_2 = 1, 2,$ and 3 ps, respectively. We also display, using the thick orange curve, the amplitude of the projection of the peak at $\tau_2 = 0$. We averaged the phase of the same neighborhood around the H diagonal peak. This radial phase was converted to an angle, and this angle was monitored as a function of delay time τ_2 and is displayed in part (d). An angle of 90° indicates a completely dispersive peak and an angle of 0° indicates a completely absorptive peak. Interestingly, the transition from dispersive to absorptive does not appear to be an exponential decay. Since the EID effect is responsible for the dispersive character, we conclude that this decay corresponds to the duration of the EID effect. The short timescale may be surprising because the EID effect is seemingly due to exciton populations, which are long-lived. The rationale for the short timescale is that this is still manifest in a coherent signal, and in fact, in the nonlinear exciton equations this effect is a four-particle correlation [143]. Finally, we should comment on the co-circular spectra at $\tau_2 = 3$ ps. Although both the simulation and the experiment are absorptive in character, the former indicates that the peak should be positive going (red) while the latter shows a negative-going peak (blue). This indicates that an additional π phase shift is present, possibly due to incomplete decay of the many-body interaction.

We can attempt to understand the EID decay using the modified optical Bloch equations, Eqn. 2.45. Advanced simulations could reveal if either γ' or N is time-dependent, or both. A previous experiment suggests the answer. From the transient grating experiment described earlier in this chapter, we observed a rapid signal decay

at early τ_2 times. Thus N in the equations is in fact time dependent: $N(\tau_2)$. It is possible that $N(\tau_2 = 3 \text{ ps})$ corresponds to the time when the product $\gamma'N(\tau_2 = 3 \text{ ps})$ contributes the small residual (5°) phase and the additional π phase to the emitted signal. Another possibility, which we intimate here, is that the EID term itself is time dependent, $\gamma'(\tau_2)$. An experiment could distinguish between the two situations in the following manner. Because the τ_2 time period does not contain oscillations at optical frequencies for either the S_I or S_{II} pulse sequence—and thus does not require interferometric stability—we can construct a new apparatus that incorporates a mechanical delay stage. It would then be feasible to measure 2D FTOPT correlation spectra like those shown in Fig. 4-6(b) for τ_2 delays up to one nanosecond, as was done in the transient grating experiment. One added advantage to using a delay stage for the τ_2 delay is that there will not be a delay-dependent amplitude modulation decay during this time period. If the phase decay follows the transient grating decay, this would suggest that γ' is not time dependent.

4.5 Exciton quantum beats in a 3D spectrum

The COLBERT spectrometer is capable of scanning multiple time dimensions. In this experiment, we perform scans similar to those presented in the previous section except we Fourier transform the oscillations during time period τ_2 to yield a 3D spectral solid². To investigate the quantum beats between the excitons, in Fig. 4-8(a) we present three projections of the S_I co-circular measurement. This measurement was performed by stepping the second time period in 40 steps from 0 to 2 ps, and at each step scanning the first time period in 128 steps over 4 ps. All possible Feynman pathways are illustrated; the four pathways involving biexciton–exciton emission, diagrams *ix* – *xii* again contribute minimally.

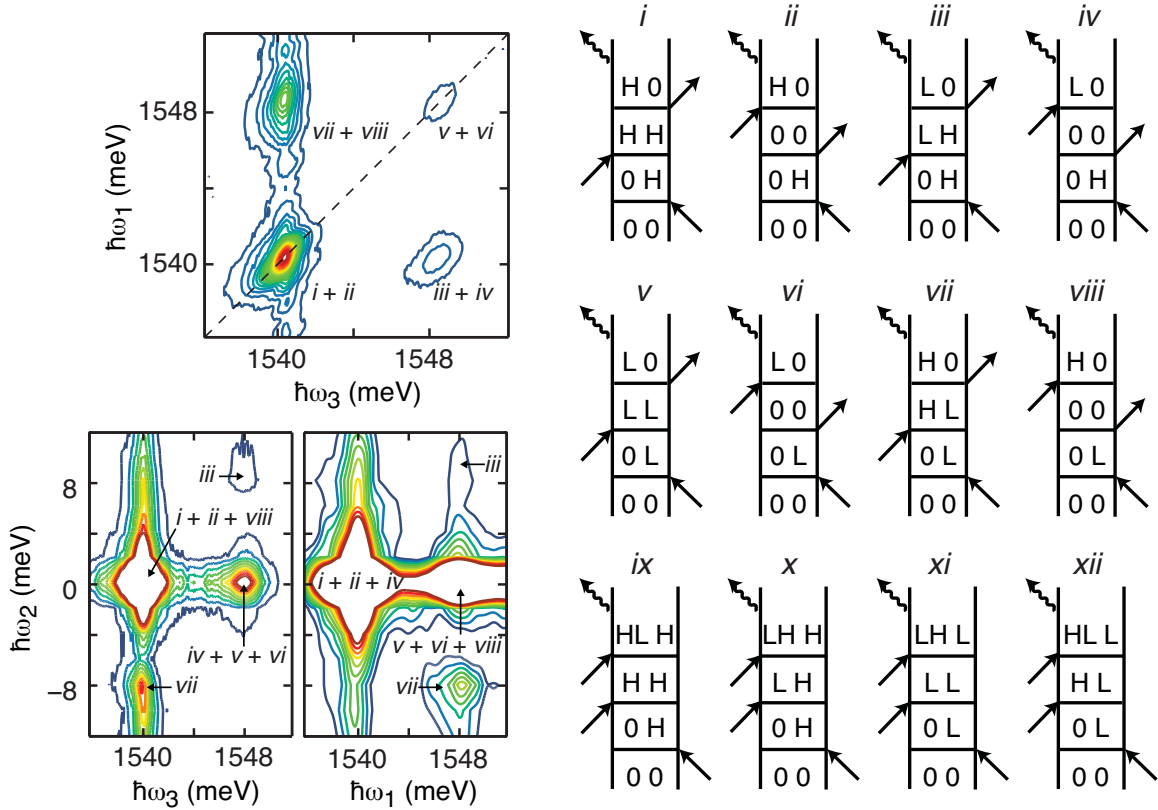
The first projection—the projection onto the $(\hbar\omega_1, \hbar\omega_3)$ plane—is similar to a typical S_I scan and shows two diagonal peaks (described by pathways *i*, *ii*, *v*, and *vi*) and two cross peaks (described by pathways *iii*, *iv*, *vii*, and *viii*). It is not exactly equivalent to a 2D S_I measurement because the 2D experiment was performed at one specific value of τ_2 ; this projection of the 3D solid is integrated across the $\hbar\omega_2$ axis. The stretching of the two diagonal peaks reflects the inhomogeneous broadening; the diagonal linewidth FWHM for the strong feature from the H exciton is $2.2 \pm 0.1 \text{ meV}$

²In this section and the 3D measurements in the next chapter, quantum beats appear at about 8 meV rather than 6 meV because the 3D data was acquired two years before most of the other measurements presented in this thesis. In the ensuing time, the sample was removed, cleaned, and remounted in the cryostat several times, meaning that a variety of experimental conditions—such as thermal contact and pressure from the bolts holding the sample in place—changed.

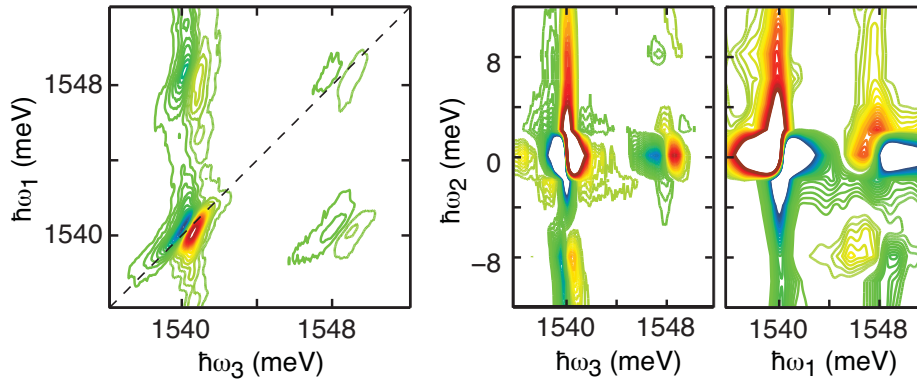
and its antidiagonal (homogeneous) linewidth FWHM is 1.1 ± 0.1 meV. The other diagonal feature is far weaker because the L exciton transition dipole is one-third that of the H exciton as measured in the linear absorption. Many of the features in this projection, such as the relative brightness of the cross peaks and the vertical stripe, were described in detail previously in this chapter and elsewhere [143].

Since S_I scans are usually void of coherent oscillations during the second time period, most of the peaks on the corresponding energy axis, $\hbar\omega_2$, are at zero frequency. However, because two Feynman paths contain quantum beats [56, 144, 145, 283] during τ_2 , a small peak is seen at the difference frequency. The $(\hbar\omega_2, \hbar\omega_3)$ projection created by integrating through the absorption $(\hbar\omega_1)$ axis shows H and L oscillations at their expected energies on the $\hbar\omega_3$ axis. All of the diagrams except *iii* and *vii* indicate features that do not oscillate during τ_2 . Indeed this is seen in the $(\hbar\omega_2, \hbar\omega_3)$ projection, as the most intense peaks appear at the zero value of the $\hbar\omega_2$ axis. The small peaks near ± 8 meV along the $\hbar\omega_2$ axis are due to pathways *iii* and *vii*, where the oscillations are quantum beats between the two coupled exciton states. It is worth reiterating that in the co-circular polarization configuration, the cross peaks are due to pure Coulomb correlations. The $(\hbar\omega_1, \hbar\omega_2)$ projection is inaccessible in standard 2D FTOPT measurements. The most intense portions at zero frequency on the $\hbar\omega_2$ axis are due to the majority of the pathways. The weak peak at -7.9 ± 0.1 meV is due to pathway *vii* and the shoulder with a positive energy value is due to pathway *iii*. The difference in relative intensities of these quantum beat peaks is due to exciton interactions in the system.

In addition to the amplitude spectra presented in Fig. 4-8(a), the real parts are presented in Fig. 4-8(b). All of the features—even quantum-beat pathways—are dispersive, even though the spectra are a result of summing several experiments in which the dispersive nature was decaying, as was observed in the previous section. This should perhaps not be surprising because we have observed that Coulomb correlations can cause phase shifts, and this peak is due to a pure Coulomb correlation. A cross-linear 3D S_I measurement, which we have not performed due to low signal levels, would be interesting because in that case the cross peaks are due to quantum coupling, not Coulomb correlations. Regardless, simulations using any method—all three methods will require extensive computation time—would provide a valuable reference point.



(a) Projections and Feynman diagrams for a 3D S_I co-circular polarization measurement. The $(\hbar\omega_1, \hbar\omega_3)$ projection is obtained by integrating over the full range of $\hbar\omega_2$ energies. It is similar to a standard 2D FTOPT rephasing scan. All pathways except iii and vii appear at a value of zero along axis $\hbar\omega_2$ in either projection. The full set of contributing double-sided Feynman diagrams is presented; as illustrated, each peak in the three projections is due to a specific subset of diagrams. Some pairs, for example i and ii , are not separable even in 3D FTOPT, while other pairs such as iii and iv are now separable. Quantum beats appear as peaks and shoulders along $\hbar\omega_2$ up to ± 8 meV, due to pathways described by diagrams iii and vii . The four pathways involving biexcitons, ix – xii , contribute minimally and are therefore not labeled.



(b) The real parts of the projections of the co-circular S_I 3D spectral solid. All of the features, even the quantum beat features due to pathways iii and iv , have dispersive lineshapes.

Figure 4-8: The amplitudes and real parts of the projections of the co-circular S_I 3D spectral solid.

4.6 Hints of higher-order correlations

The spectra presented in this chapter revealed many important parameters of the excitons in this system, and several many-body interactions were manifest in the signals. We extracted the exciton energies, their absorption coefficients, and total dephasing times from the linear absorption spectrum. Absorption measurements at increasing fluences revealed a saturation effect that occurs at a carrier density corresponding to the point at which excitons have completely filled the quantum wells. The transient grating measurement—which should have shown a strictly monoexponential decay with the H exciton lifetime—showed a sharp initial drop followed by the monoexponential decay.

Many one-quantum 2D FTOPT measurements were performed. We observed that cross peaks were present in co-linear spectra, indicating that the H and L excitons are coupled. The spectra also showed several unexpected features that were investigated further using cross-linear and co-circular polarization schemes. The cross-linear measurements showed cross peaks with rocking nodal-plane angles and oscillating amplitudes in the correlation spectrum, and these were shown to be due to quantum beats. In the co-circular correlation spectra measured at varying τ_2 times, the H exciton diagonal feature initially had a dispersive character that evolved into an absorptive character after about 3 ps, revealing a decay in the EID contribution. Simulations using the modified optical Bloch equations or the nonlinear exciton equations may be able to reproduce this decay. Finally, the 3D spectral solid measured using co-circular polarization revealed features that are Fourier transforms of quantum beats during τ_2 . These peaks, which appear at $\hbar\omega_2 = \pm 8$ meV, also have dispersive character.

Chapter 5

Four-particle correlations

In this chapter we investigate two-exciton correlations using a variety of two-quantum scans, some of which use the S_{III} pulse sequence described in the previous chapter. The spectra show features due to both bound biexcitons and unbound-but-correlated exciton pairs. At third order we measure the binding energies and dephasing rates of bound biexcitons, and we confirm the suggestion from Sec. 2.4 that the value of the binding energy depends on how it is measured. We also measure the dephasing time of unbound two-excitons, which are present in two-quantum signals unless polarization control is used to suppress them. We selectively integrate a 3D FTOPT spectral solid around the mixed biexciton features to reveal a peak that had been obscured, and this peak reveals a many-body interaction manifest in its amplitude. At fifth order, we investigate inhomogeneity and dephasing using two-quantum rephasing pulse sequences. The unbound two-exciton feature changes with the laser fluence, indicating the presence of still higher-order correlations.

5.1 Third-order two-quantum coherences

Four-wave-mixing measurements in which two-quantum coherences are correlated to radiative one-quantum coherences using the S_{III} pulse sequence were demonstrated first in 2D IR [284] to extract vibrational anharmonicities. This sequence has now been used in the visible to investigate properties of two-exciton correlations and molecular excited states [99, 145, 148, 156, 157]. One kind of two-exciton correlation is a biexciton. Biexcitons in GaAs quantum wells were first observed in 1982 [90], and the biexciton binding energy—measured as the difference between single exciton emission and biexciton-exciton emission—was 1.5 meV. Here we use the S_{III} sequence to isolate biexciton coherences spectrally so that their properties can be measured directly. Other peaks appear along the two-quantum axis due to unbound-

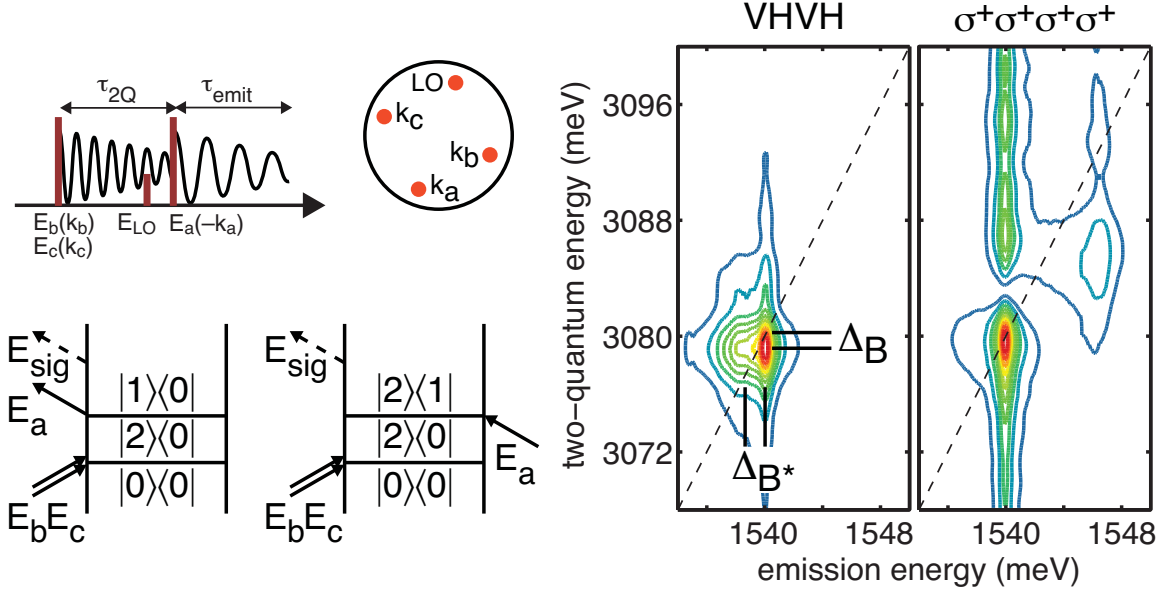


Figure 5-1: Third-order two-quantum 2D spectra measured in the BOXCAR beam geometry. The two diagrams that contribute to the pure biexciton peaks are depicted. The LO interacts 1 ps before the final excitation pulse. Spectra measured for cross-linear and co-circular polarization configurations are in contrast. The two binding energies for the HH biexciton extracted from the cross-linear measurement are $\Delta_B = 1.0$ meV and $\Delta_{B^*} = 1.5$ meV.

but-correlated two-excitons and due to exciton–free-carrier scattering. Polarization control and unconventional pulse timing sequences allow us to isolate specific signals.

Two-quantum spectra were measured using cross-linear, cross-circular, co-linear, and co-circular polarized input fields. In co-circular (co-linear) measurements, all four fields were given the same circular (linear) polarization while in cross-circular (cross-linear) measurements the first two fields (the two nonconjugates) had opposite circular (linear) polarization and the final two fields (the conjugate and the LO) were also oppositely circularly (linearly) polarized. 2D FTOPT measurements were performed by stepping τ_2 in 128 steps from 0 to 2 ps, and 3D FTOPT measurements were performed by stepping τ_2 in 64 steps from 0 to 2 ps and at each step scanning the first time period in 64 steps over 4 ps.

In Fig. 5-1, the spectra were measured using the BOXCARS geometry with an S_{III} pulse timing sequence. Two amplitude spectra are presented. The first was measured using cross-linear polarization, VHVH, with a pulse spectrum set to excite only the H exciton. Signals due to exciton–free-carrier scattering and unbound-but-correlated exciton pairs are suppressed in this polarization configuration. Thus, only two pathways contribute to this signal. In the first pathway, fields E_b and E_c create the two-quantum coherence, $|2\rangle\langle 0|$, and field E_a projects that coherence onto a radiative

single-quantum coherence between the exciton and ground states, $|1\rangle\langle 0|$. The second pathway involves a radiative biexciton-exciton coherence, $|2\rangle\langle 1|$, during the last step because the final field interaction acts on the right side of the diagram. Thus, the cross-linear amplitude spectrum shows a strong peak due to the first pathway and a weaker peak with the same two-quantum energy but with a red-shifted emission. The HH biexciton dephasing time is about 2.5 ps, and we have shown that this dephasing time depends slightly on the pulse fluence [99], indicating the presence of higher-order correlations.

From this spectrum we can measure the HH biexciton binding energy in two ways. For noninteracting systems, such as an anharmonic oscillator, the two methods should yield identical values. The first method is the difference between the measured two-quantum energy and twice the measured single quantum energy, Δ_B in Fig. 5-1. This value is 1.0 ± 0.1 meV. The second method uses the difference between the single exciton emission and the biexciton-exciton emission as shown by Δ_{B^*} . This is the manner in which the biexciton binding energy was first measured in photoluminescence experiments [90], and we also measure a value of 1.5 ± 0.1 meV. Remarkably, the Coulomb interactions cause the two values to differ because the second is weighted by the transition dipole between subsets of exciton and biexciton correlations as was shown in Eqn. 2.63.

The second spectrum displayed in Fig. 5-1 was measured using co-circular polarization. Two-quantum signals due to pure biexcitons were suppressed in this polarization configuration. The pulse excitation spectrum was resonant with both the H and L exciton energies so that pathways involving mixed biexcitons, HL , were not suppressed. The polarization scheme also allows unbound-but-correlated exciton pairs and exciton-free-carrier scattering to contribute to the signal. The unbound-but-correlated exciton pair signal is the result of Coulomb interactions between excitons that can be phenomenologically modeled as EIS [148, 273], and the exciton-free-carrier scattering signal is due to Coulomb interactions between excitons and free carriers that can be phenomenologically modeled as EID. The mixed biexciton has a binding energy, Δ_B^{HL} of 1.4 ± 0.2 meV and a dephasing time of about 1.5 ps.

To investigate these two-quantum coherences further, in Fig. 5-2 we display the real part of the two-quantum signal for all four polarization conditions. From left to right, the polarization conditions increase the contributions due to many-body interactions and decrease contributions due to pure biexcitons. The cross-linear polarization spectrum shows one main feature with positive and negative lobes due to interference and overlap between the two pathways involving HH biexcitons shown in Fig. 5-1. The cross-circular polarization spectrum shows those two features but

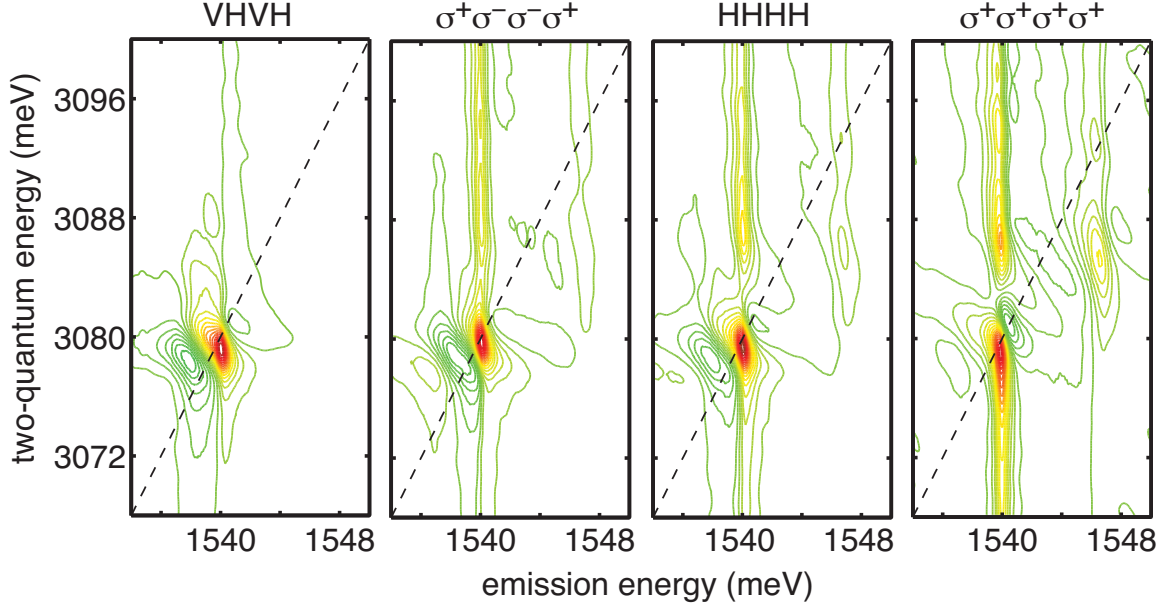


Figure 5-2: Real parts of third-order two-quantum 2D spectra. Four polarization conditions are presented: cross-linear (VHVH), cross-circular ($\sigma^+\sigma^-\sigma^-\sigma^+$), co-linear (HHHH), and co-circular ($\sigma^+\sigma^+\sigma^+\sigma^+$). The positive and negative lobes in each feature reveal the phases of the peaks, and these phases reveal information about the many-body interactions which result in the unbound-but-correlated and exciton-free-carrier scattering signals.

with an additional phase factor that moves the peaks slightly and causes a third lobe to appear. This additional phase factor is due to interference by a small amount of unbound-but-correlated exciton pair (HH^*) signal, which does appear in the cross-circular polarization configuration [147]. The cross-circular spectrum also shows significant signal due to exciton-free-carrier scattering at two-quantum energies above 3085 meV. The co-linear spectrum has the same interference at the HH biexciton feature, and it has a significant node between the HH biexciton feature and the features at higher two-quantum energies. This is due to the presence of several signals that are out of phase with each other but that overlap in two-quantum energy. Unbound-but-correlated exciton pairs, mixed biexcitons, and exciton-continuum scattering are three effects that appear in this part of the spectrum. As we will see later in this chapter, projections of the two-quantum 3D FTOPT spectral solid can isolate some of these overlapping signal pathways. The co-circular spectrum has no signal due to pure biexcitons, and the peaks appearing on the two-quantum diagonal are due to HH^* and LL^* . Since mixed biexcitons have weak biexciton-exciton emission signals, in the co-circular scan the feature due to the mixed biexcitons has an absorptive line-shape, unlike the HH biexciton peak whose biexciton-exciton shoulder contributes strongly, causing the peak to appear to be dispersive. We will return to a discussion

of this lineshape in Sec. 5.3.

A three-dimensional spectral solid for a cross-circular S_{III} measurement is shown in Fig. 5-3, where each energy axis is labeled by its corresponding time period. While it is clear that the peak is around 1540 meV for both the $\hbar\omega_1$ and $\hbar\omega_3$ axes and near 3080 meV for the $\hbar\omega_2$ axis, this plot is not convenient for extracting detailed information because it is difficult to view. The three projections created by integrating along specified ranges of particular axes are more useful.

The projection onto the $(\hbar\omega_1, \hbar\omega_3)$ plane shows the expected two peaks that are slightly separated due to the biexciton-exciton emission red shift. The projection onto the $(\hbar\omega_2, \hbar\omega_3)$ plane is similar to the normal 2D S_{III} plot [99, 285]. The peak just below the diagonal line of slope two appears at coordinates that give a binding energy of 1.1 ± 0.1 meV. The same value for the HH biexciton binding energy is extracted from the location of the peak in the $(\hbar\omega_2, \hbar\omega_1)$ projection shown, only now the two pathways are part of a single peak. Thus it is clear that projections of the spectral solid can be utilized to separate peaks that overlap in two-quantum 2D FTOPT measurements. Spectral solids can be further exploited by slicing or projecting along axes other than the three frequency axes. For example—although we do not demonstrate it here—an S_{III} scan can be sliced through the diagonal of the $(\hbar\omega_1, \hbar\omega_3)$ plane and displayed against $\hbar\omega_2$. This projection would show the subset of excitons which both absorbed and emitted at the same frequency, and would correlate them to the two-quantum axis, potentially enhancing spectral resolution.

We present projections of an S_{III} co-circular spectral solid in Fig. 5-4 to show how overlapping Feynman pathways can be separated using 3D spectroscopy. In doing so, we reveal a mixed biexciton peak that was obscured. The two pathways we wish to separate are indicated by the different time-orderings in pathways i and ii . Both create mixed biexcitons in the second time period and then emit at L , but pathway i has initial absorption in H while pathway ii has initial absorption in L . Figure 5-4(a) is the projection of the 3D S_{III} co-circular spectral solid onto the $(\hbar\omega_1, \hbar\omega_3)$ plane. The four pathways are visible as separate peaks, although many-body interactions such as exciton-free-carrier scattering are also present in these features. The $(\hbar\omega_2, \hbar\omega_3)$ projection is shown in Fig. 5-4(b), and it is similar to a 2D S_{III} measurement. The most prominent feature due to HH^* is located at exactly twice the H exciton frequency on the two-quantum axis and at the H exciton frequency on the emission axis. The peak appears shifted below the diagonal because of interference with the mixed biexcitons. The analogous feature involving L excitons, LL^* , is weaker because of the lower L exciton transition dipole.

The mixed biexciton features appear between the two unbound features on the

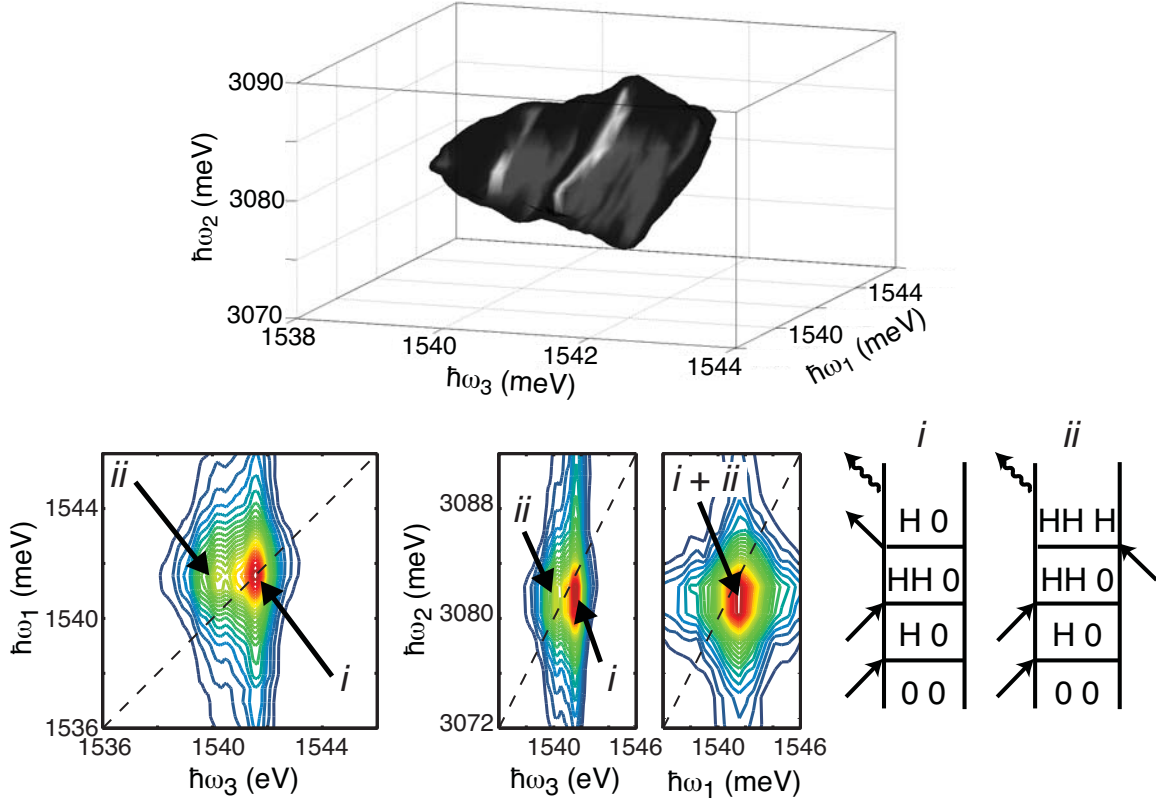


Figure 5-3: The 3D spectral solid (top) is shown for a cross-circular S_{III} measurement where each energy axis is labeled according to its corresponding time period. The one-quantum axes $\hbar\omega_1$ and $\hbar\omega_3$ have been cropped to include only the H feature, and the two-quantum axis $\hbar\omega_2$ has been cropped around the HH biexciton feature. (bottom) Projections of the cropped spectral solid. The two contributing double-sided Feynman diagrams are depicted. Diagram i contains the biexciton–ground-state coherence during τ_2 and an exciton–ground state coherence during τ_3 while diagram ii contains the same biexciton–ground-state coherence during τ_2 but a biexciton–exciton coherence during τ_3 . These two diagrams are separated in the $(\hbar\omega_1, \hbar\omega_3)$ and $(\hbar\omega_2, \hbar\omega_3)$ projections, and they overlap in the $(\hbar\omega_2, \hbar\omega_1)$ projection.

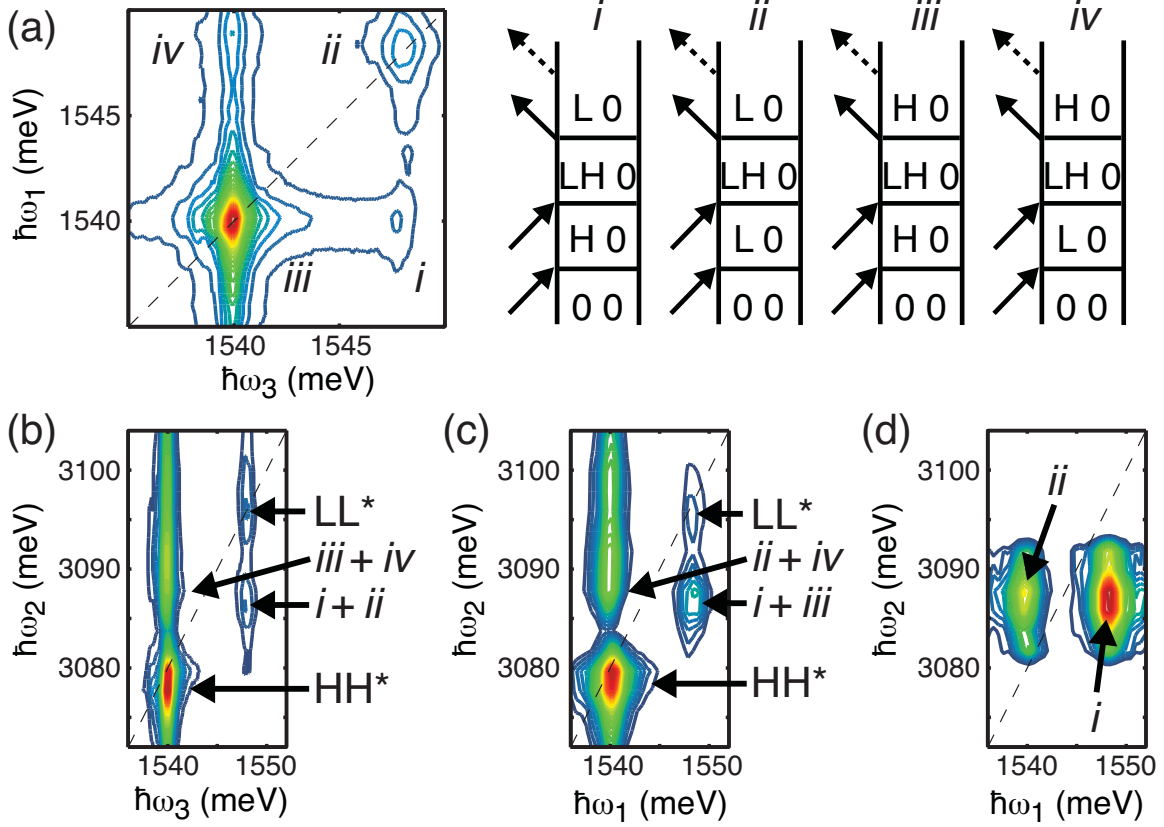


Figure 5-4: Projections of the 3D S_{III} co-circular spectral solid. The projection shown in (a) is onto the $(\hbar\omega_1, \hbar\omega_3)$ plane. The four listed pathways are separable, although interaction-induced features also contribute to the peaks. Part (b) is the projection onto the $(\hbar\omega_2, \hbar\omega_3)$ plane showing that diagrams *i* and *ii* are not distinguishable and that diagrams *iii* and *iv*, also indistinguishable, are masked by the interaction-induced feature. The spectrum shown in part (c) is the projection onto the $(\hbar\omega_2, \hbar\omega_1)$ plane, integrated over the entire $\hbar\omega_3$ axis. Pathways *ii* and *iv* now form a single peak, and pathways *i* and *iii*, which do the same, are largely obscured. (d) The spectral solid is again projected onto the $(\hbar\omega_2, \hbar\omega_1)$ plane but integration was limited to $\hbar\omega_3$ energies around L and $\hbar\omega_2$ energies around the mixed biexciton. Diagrams *i* and *ii* are now separated from each other without interference from the other pathways or the strong interaction-induced feature.

$\hbar\omega_2$ axis at slightly less than the sum of the H and L exciton energies, and at the L or H emission energy depending on whether the final process is L or H exciton emission (pathways i and ii or iii and iv , respectively). The spectrum in part (c) is the projection onto the $(\hbar\omega_2, \hbar\omega_1)$ plane showing that the mixed biexcitons that absorbed the first field at H destructively interfere with the stronger HH^* feature, and are obscured by the resulting node. Similar interference may occur between the mixed biexcitons that absorb the first field at L and the LL^* feature, but since this feature is weak, the biexciton feature is largely unaffected. As an added difficulty in isolating pathway i from ii , the features from pathways iii and iv superpose with them in this projection.

Therefore in part (d) we hone in on the two pathways of interest by viewing the projection in the same $(\hbar\omega_2, \hbar\omega_1)$ plane, but instead of integrating over all emission energies, we integrated over only the L exciton emission energy. This separates pathway i from iii and pathway ii from iv since i and ii emit at L while iii and iv emit at H . It also largely removes the strongest unbound feature, HH^* , which also emits at H . A projection in the same plane with $\hbar\omega_3$ integrated only over energies around H would similarly isolate mixed biexciton pathways iii and iv , although the feature from pathway iv would still be as obscured by the interference with the HH^* feature as it is in part (b). The plot in (d) is also cropped in the $\hbar\omega_2$ dimension to include only the energies within the range of mixed biexciton features to eliminate the tail of the strong HH^* feature. In part (d), pathways i and ii are clearly distinguishable now that the unbound features and pathways iii and iv are suppressed. The peak corresponding to pathway ii is roughly 60% brighter than the peak corresponding to pathway i and their $\hbar\omega_1$ linewidths are equal, with FWHMs of 2.6 ± 0.1 meV. The $\hbar\omega_2$ linewidths are also similar: pathways i and ii have FWHMs of 9.0 ± 0.2 meV and 8.9 ± 0.1 meV, respectively, giving the mixed biexciton dephasing rate.

In this section we isolated and measured features due to biexcitons and unbound-but-correlated exciton pairs in several third-order S_{III} 2D FTOPT spectra. Although the signals reveal significant insights, additional information can be learned by using phase-windows to enhance two-quantum features [254, 255]. In these measurements, selectively removing or phase-shifting bands of the spectra can increase the absorption rate into desired two-quantum states. In this manner, mixed biexciton features—which are difficult to observe even in 3D measurements—can be enhanced.

5.2 Fifth-order two-quantum rephasing spectra

The above results from third-order two-quantum spectroscopy revealed information about four-particle many-body interactions. We extracted the binding energies and dephasing times for various biexcitons. We also observed unbound-but-correlated exciton pairs. However, more information can be gained about the two-quantum phenomena using additional fields to generate higher-order signals. In this section, we show how fifth-order signals¹ created through a two-quantum rephasing pulse sequence allow us to investigate inhomogeneity and dephasing in more detail. Notably, the HH^* feature exhibits strong inhomogeneity that varies with the pulse fluence.

We measure the fifth-order signals using the Y-shaped beam geometry illustrated in Fig. 5-5. Although five fields interact with the sample and many field parameters could be varied, in the present measurements only the time period (τ_{2Q}) between the conjugate fields (\mathbf{E}_a and \mathbf{E}_b) and the final field (\mathbf{E}_c) is scanned. The final three field interactions—all due to one laser beam, \mathbf{E}_c —convert the two-quantum coherences created by beams \mathbf{E}_a and \mathbf{E}_b to radiative one-quantum coherences. The laser was adjusted to create near-transform-limited pulses of 150 fs in duration, centered at 1534 meV, with a FWHM of about 11 meV. The pulse spectra are set so that only resonances involving H excitons appear; resonances involving L excitons, such as mixed biexcitons, are suppressed. This unconventional beam geometry, detailed in Fig. 3-5, would be difficult to generate using standard approaches involving static diffractive optics. The COLBERT spectrometer—with its reconfigurable beam shaper—can generate the geometry with ease.

We show spectra measured using three different polarization configurations. The first spectrum, measured with co-linear polarized pulses, shows peaks due to both types of two-quantum coherences. The second spectrum, measured with cross-linear polarized pulses, suppresses the unbound-but-correlated feature to reveal only biexciton coherences. The third spectrum, measured with co-circular polarized pulses to suppress biexciton coherences, allows us to explore the dynamics of the unbound-but-correlated two-exciton coherences. Finally, we use two different theoretical models to simulate the signals and to help us determine which many-body interactions produce the observed spectral features.

The first spectrum is measured using co-linear polarized pulses. The fluence was 10^3 nJ/cm² for the co-linear and cross-linear measurements, and varied for the co-circular measurements. Both biexciton (HH) and unbound-but-correlated two-

¹As we will see, the signals are *at least* fifth-order in the electric field because of spectral features that change with increasing fluence. Since spectral features not limited to the signal amplitude vary with the pulse fluence, this indicates the presence of higher-order signals.

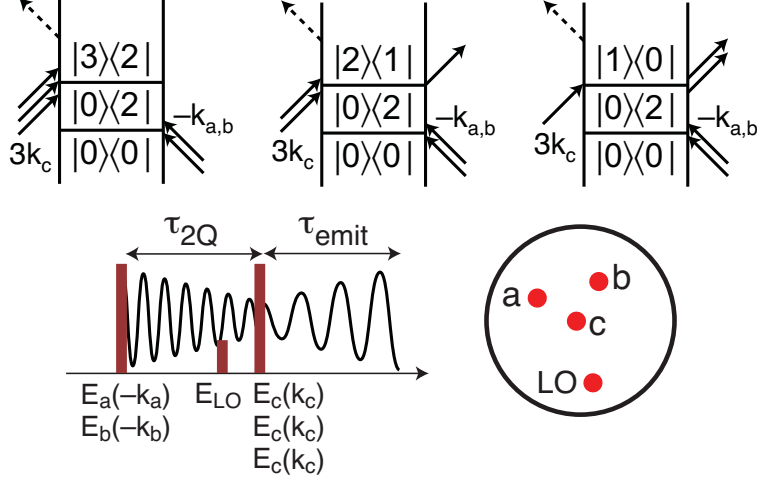


Figure 5-5: The fifth-order Y-shaped measurement. Fields \mathbf{E}_a and \mathbf{E}_b interact first, followed—after a variable delay (τ_{2Q})—by field \mathbf{E}_c to generate a phase-matched signal in the $3\mathbf{k}_c - \mathbf{k}_a - \mathbf{k}_b$ direction. The Feynman diagrams illustrate the three possible emissive coherences.

exciton (HH^*) coherent oscillations are measured during time interval τ_{2Q} in the co-linear polarization configuration. The amplitude of the spectrum, Fig. 5-6(a), has a node between the two features, distorting them such that their peaks are farther apart than their energy separation. Multiexciton emission is visible as a red-shifted shoulder on the biexciton peak. The real part of the spectrum, Fig. 5-6(b), shows that the biexciton feature has an absorptive lineshape and the unbound feature has a dispersive lineshape. The interference between the two signals results in an entwined lineshape and makes analysis difficult.

In the cross-linear polarization measurement, all of the fields have horizontal polarization except field \mathbf{E}_a , which has vertical polarization; we measure identical spectra if only field \mathbf{E}_b is vertically polarized or if only field \mathbf{E}_c is vertically polarized. The main feature due to biexciton coherences in the amplitude of the spectrum, Fig. 5-6(c), is shifted below the diagonal (a red-shift) by an amount equal to the biexciton–ground-state binding energy (Δ_B), which we measure to be 1.2 ± 0.2 meV. The two-quantum linewidth appears to have increased relative to the co-linear polarized spectrum. We show below that this elongation is due to local field effect (LFE). The red-shifted shoulder on the biexciton peak is due to the energy difference between the radiative exciton–ground-state coherence and the multiexciton radiative emission coherences. Because the three pathways overlap, we cannot separate the different emission energies. Unlike in third-order rephasing spectra of single excitons where the nodes are parallel to the diagonal [146], the nodes in Fig. 5-6(d) are slightly tilted. Finally, we note that the peak is not elongated along the diagonal, indicating a lack of biexciton

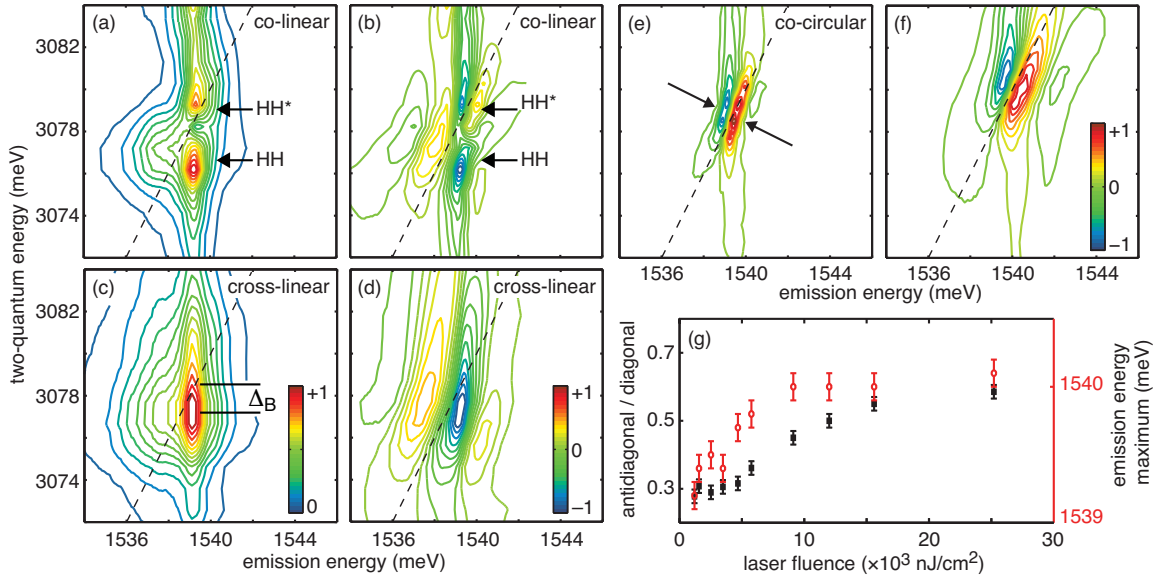


Figure 5-6: Experimental 2D spectra measured using the pulse sequence and geometry shown in Fig. 5-5 for three polarization configurations. Dashed lines are two-quantum diagonals, $E_{2Q} = 2E_{emit}$. Amplitude (a) and real (b) parts of the spectrum for co-linear polarized fields show both HH coherences and HH^* coherences. Cross-linear polarized fields suppress the unbound-but-correlated two-exciton coherences to isolate biexciton coherences in the amplitude (c) and real (d) parts of the spectrum. Real parts of the spectra for co-circular polarized fields at low (e) and high (f) pulse fluences. The arrows indicate the anti-diagonal. (g) Result of ten co-circular measurements with varying fluences. The peak broadens—mostly homogeneously—(filled black squares) and blue-shifts (open red circles) as the fluence increases.

inhomogeneity.

Fig. 5-6(e) and (f) are the real parts of the spectra, displaying only the HH^* feature, measured using co-circular polarization at low (1×10^3 nJ/cm²) and high (2.5×10^4 nJ/cm²) pulse fluences. In both spectra, the lineshapes are dispersive and the nodes are again not parallel to the diagonal. The peak has elongated diagonally by a small amount and has elongated antidiagonally by a large amount. The peak blue-shifts by about 1 meV along the two-quantum diagonal at higher powers, indicating the presence of EIS. To investigate these changes further, we measured co-circular spectra at ten different pulse fluences. Fig. 5-6(g) shows how the linewidth ratio (antidiagonal/diagonal) and the position of the emission energy maximum change with pulse fluence. As the fluence increases, the diagonal linewidth increases 14% from 3.6 to 4.1 meV and the antidiagonal linewidth increases 140% from 1.0 to 2.4 meV. At higher fluences, the carrier density increases and then saturates according to Fig. 4-1(d). As the density increases, more scattering occurs and therefore the coherence dephases more quickly; the antidiagonal linewidth measures this dephasing. This variation indicates the presence of many-body interactions that can be viewed as an EID effect. The increase in inhomogeneous dephasing could be due to Pauli blocking [213]. It may be possible to investigate this unexpected increase by selectively eliminating the appropriate term in the nonlinear exciton equations.

The tilts, elongations, and energy shifts in the spectra all indicate the presence of many-body interactions. We use two theoretical models to help understand these subtle spectral features. As described in Sec. 2.3, the sum-over-states model treats the excitons and multiexcitons as isolated states. This simplified approach reproduces only the features due to non-interacting particles. The phenomenological model starts with the isolated states and can incorporate interactions due to EID, EIS, and LFE. Here the modified optical Bloch equations have been extended to fifth-order. The purpose of these calculations is not to simulate the signal rigorously using the nonlinear exciton equations, but to extract physical insights by identifying which phenomenological many-body interactions contribute to the experimental spectra.

Calculations using the sum-over-states method result in the spectrum in Fig. 5-7(a). Exciton-ground-state pathways and both biexciton-exciton and triexciton-biexciton emission pathways—all three are shown in Fig. 5-5—are included in this cross-linear spectrum. The pathways are weighted by the number of field permutations: three exciton-ground-state, three biexciton-exciton, and one triexciton-biexciton pathways contribute to the signal. Triexcitons will be discussed in the next chapter, but for now, it is sufficient to state that the nodes do not appear in the correct locations and the lobes do not have the correct relative intensities if this pathway is

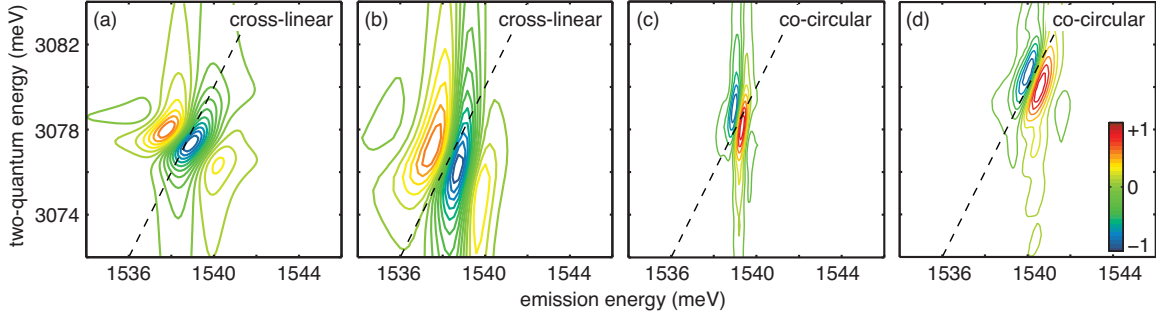


Figure 5-7: Fifth-order Y-shaped simulations. (a) Result of a calculation using the sum-over-states model for cross-linear polarized fields. This model produces no peak for the co-circular polarization configuration. (b) Result of calculations using the phenomenological model for cross-linear polarized fields. This model captures subtle tilts and vertical elongations by including LFE. (c) and (d) Result of calculations using the phenomenological model for co-circular polarized fields at low and high fluence, respectively. The model incorporated EIS to generate the features; only states g and X were included.

not included. Although this model qualitatively reproduces the number of nodes, their locations, and their relative intensities, there are several deviations from the experimental spectrum. The multiexciton emission feature is blue-shifted along the two-quantum axis from its experimental location; the slight tilt of the nodes is not captured; and the distinct vertical elongation is not present. A co-circular spectrum is even more problematic: Because the unbound feature is not a state, no peak appears at all!

The modified optical Bloch equations reproduce the experiment more accurately by including terms to represent the many-body interactions. The energies of the states are still input manually into the Hamiltonian, unlike in first-principles calculations where the Coulomb coupling matrix directs the exciton and multiexciton binding energies as described in Sec. 2.4. The cross-linear simulation used the four-level Hamiltonian, Eqn. 2.31, while the co-circular Hamiltonian included only two states: g and X . Here, we derive explicit equations of motion for density matrix elements using the quantum-Liouville equation as described in Sec. 2.3. Briefly, the coupled differential equations, up to the fifth-order field interaction, are truncated and selected for the appropriate signal propagation direction according to spatial Fourier expansion of the density matrix elements [199]. We then include terms to represent EID, EIS, LFE, and the binding energies. We include inhomogenous broadening by summing spectra calculated with a range of exciton energies. The cross-linear spectrum, Fig. 5-7(b), does not include EID or EIS because they are suppressed in this polarization scheme. However, LFE can still contribute to the signal, and their inclusion stretches the peak vertically and tilts the nodes, yielding a better match to the experiment.

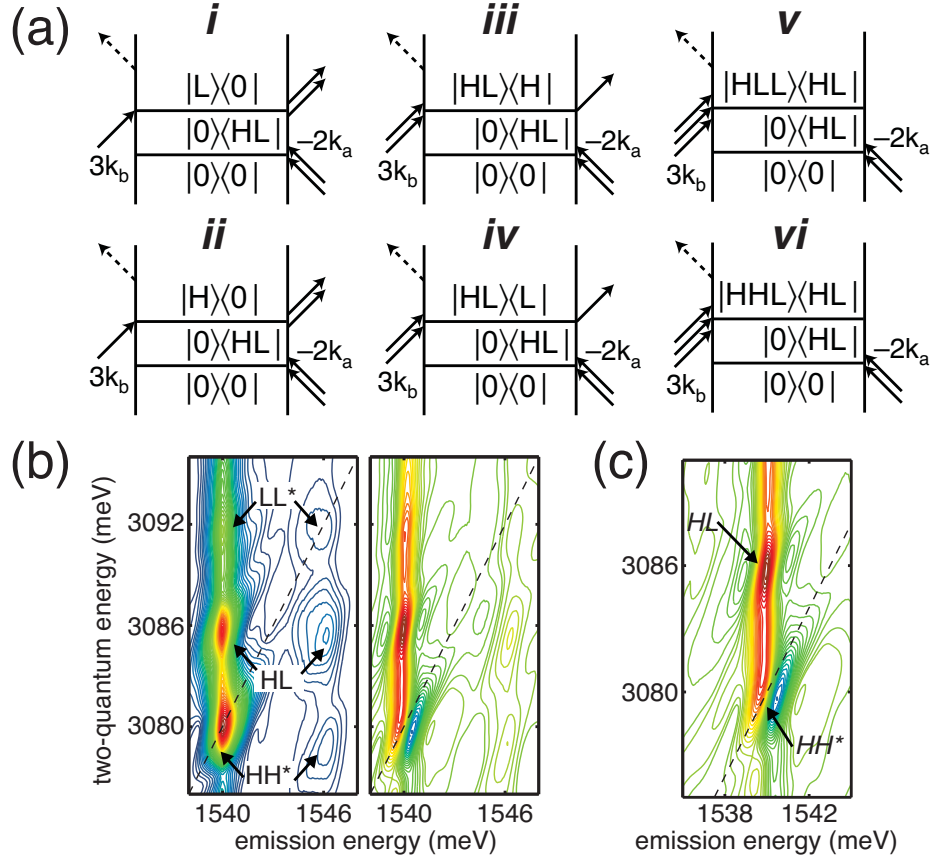


Figure 5-8: Fifth-order two-quantum rephasing measurements for co-circular polarization. (a) Feynman diagrams that contribute to the two HL peaks. (b) The excitation fields were resonant with both the H and L excitons, and six features are observed. Two of the features are due to unbound L exciton pairs, LL^* , two are due to unbound H excitons pairs, HH^* , and two are due to mixed biexcitons, HL . (c) Magnified view of two features showing the absorptive nature of the HL peak and the dispersive nature of the HH^* peak.

Features in the spectrum measured in the co-circular polarization configuration, Fig. 5-7(c) and (d), are largely reproduced with an EIS term, although adding small amounts of EID and LFE cause the vertical stretching. The fluence in (c) was 2×10^3 nJ/cm² and the fluence in (d) was 1.6×10^4 nJ/cm². The simulations show that the fifth-order measurements provide sensitive indicators of distinct many-body interactions, and they add to the insights offered by third-order spectroscopic features.

5.3 Fifth-order two-quantum rephasing of mixed biexcitons

In the next measurement, we adjusted the laser so that the pulse spectrum covered both the L and H transitions to investigate the mixed biexciton rephasing; the fluence was about 10^3 nJ/cm². A co-circular polarization measurement is presented in Fig. 5-8. There are six main features in the amplitude of the spectrum and its real part in part (b). The two features at about 3080 meV are due to HH^* , the two features at two-quantum energies near 3086 meV are due to mixed biexcitons—specifically pathways i and ii —and the two features at about 3092 meV along the two-quantum axis are due to LL^* . The real part of the spectrum is magnified in part (c) around the HH^* and HL features in the two-quantum axis and around the H exciton emission energy. The absorptive lineshape of the HL feature is in stark contrast to the dispersive character of the HH^* feature. This phase shift indicates that the two features have different microscopic origins, which can be related to the four-particle correlation term in the nonlinear exciton equations, Eqn. 2.63. Different Coulomb matrix values, V_{ab} , will weight the polarization terms that drive the two-quantum coherence, $p_{ab}^{he[\mathbf{k}_b]}$, differently to cause the different energies and phases of the two types of four-particle correlations. The mixed biexcitons report this phase shift nicely since multiexciton emission is limited due to low transition dipole values (as compared to the HH biexcitons in the previous section). In other words, pathways i and ii dominate the HL features in Fig. 5-8(b) and (c) while pathways $iii - vi$ contribute minimally.

5.4 Simulated fifth-order two-quantum correlation spectra

The five fields used in fifth-order measurements make it possible—using a suitable geometry and correct pulse timing schemes—to perform two-quantum rephasing and two-quantum nonrephasing measurements and sum them to create a two-quantum correlation spectrum just as was done at third order. In the simplest case of scanning a pair of field interactions relative to the three time-coincident field interactions, there are more pathways leading to nonrephasing signals than those that lead to rephasing signals. Thus a time delay beyond the pulse duration between the fourth and fifth pulses is introduced; in this simulation the time delay, τ_4 , was 250 fs. This time delay is needed in both the rephasing and nonrephasing measurements so that the signals are weighted equally in terms of the number of diagrams which contribute

in the sum-over-states model. In both signals, one pathway leads to $|3\rangle\langle 2|$ emission, three pathways lead to $|2\rangle\langle 1|$ emission, and three pathways lead to $|1\rangle\langle 0|$ emission. In either case, there are two time orderings for the pathways involving $|1\rangle\langle 1|$ population decays during τ_4 .

In Fig. 5-9, we present simulations of a cross-linear polarization measurement of two-quantum rephasing, two-quantum nonrephasing, and their sum, the two-quantum correlation spectrum using the sum-over-states model. Here cross-linear means that only pure HH biexcitons are measured. This requires restricting the spectrum to only the H exciton resonance. One acceptable polarization configuration is that field E_a is perpendicular to field E_b , field E_c is perpendicular to field E_d , and field E_a is perpendicular to field E_{LO} .

Fig. 5-9(d) incorporates the triexciton-biexciton emission pathways. The inserted binding energies resulted in a value of 1.5 meV as the biexciton-exciton red-shift and a value of 0.7 meV as the triexciton-biexciton red shift. There are seven total diagrams for each spectrum. In both cases, three have exciton-ground-state emission, three have biexciton-exciton emission (which, because of the odd number of field interactions on the right-hand side of the Feynman diagram, will be of opposite sign), and one pathway has triexciton-biexciton emission. This final pathway will have the same sign as the exciton-ground-state emission. Fig. 5-9(e) shows a simulation using the same model but excludes the triexciton-biexciton emission pathway. In this case there is no asymmetry in the correlation spectrum, and the two peaks have equal intensity but opposite sign.

The advantage of the correlation spectrum is that removing the phase twist sharpens the features, allowing us to extract the relevant information about triexciton-biexciton emission more easily. Two-quantum correlation scans using co-circular polarization could give additional insights into the unbound-but-correlated exciton-pair dynamics.

5.5 Hints of even higher-order correlations

In this chapter we used third-order and fifth-order signals to measure many properties of biexcitons including binding energies and dephasing times. The cross-linear fifth-order measurements showed that triexciton-biexciton emission had to be included in order to make the simulations match the experiment. We also observed and isolated features due to unbound-but-correlated exciton pairs. These peaks can be modeled using an EIS term in the phenomenological equations. The two-quantum rephasing spectra showed that the biexciton feature has little inhomogeneity, but the shape and

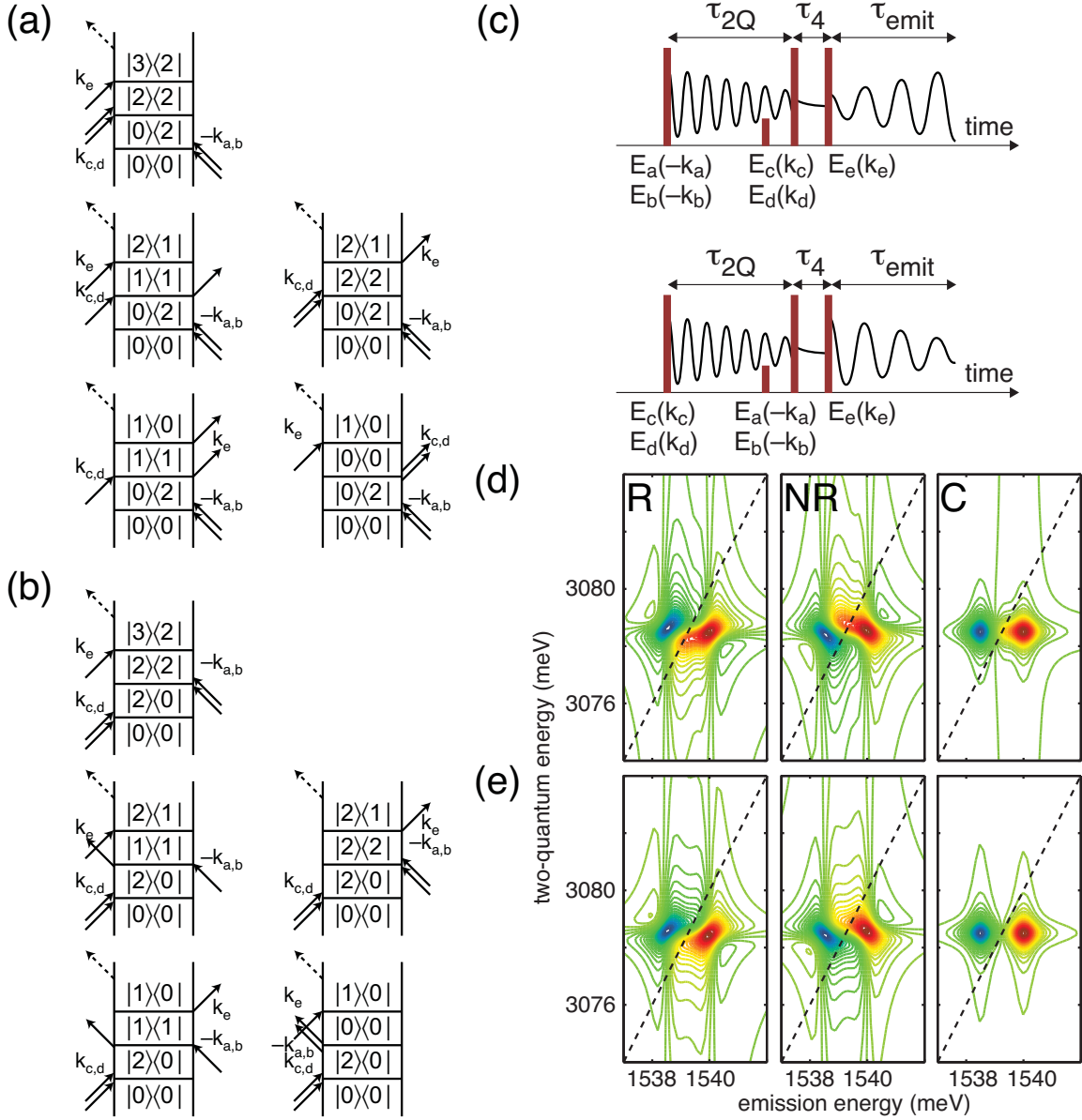


Figure 5-9: Fifth-order two-quantum rephasing (R), nonrephasing (NR), and correlation (C) spectra for cross-linear polarization. Feynman diagrams contributing to the (a) rephasing and (b) nonrephasing signals. (c) The two pulse timing sequences. The LO is indicated but not labeled. (d) The triexciton-biexciton emission pathway is included, and the binding energy difference leads to a red-shift of 0.7 meV. The slight shifts present in the R and NR spectra result in an asymmetry in the correlation spectrum. (e) The triexciton-biexciton emission pathway is not included, and the correlation spectrum is symmetric.

location of the HH^* feature depends on pulse fluence. This indicated the presence of still higher-order correlations, and this led to the conclusion that although we were measuring a signal in a phase-matched direction that is most easily described using five field interactions, there must be higher-order signals present in that direction. In the future, a three-dimensional seventh-order measurement could be used to correlate two-quantum coherences, $|0\rangle\langle 2|$, to other two-quantum coherences, $|2\rangle\langle 0|$, before signal is radiated, a fully two-quantum rephasing technique.

Chapter 6

Six-particle correlations

In the previous two chapters, we observed correlations of up to four particles directly. However, we also observed subtle features that could only be replicated if additional levels were included. Correlations involving more than four particles have been predicted theoretically [286] and have been observed indirectly through their influence on various one-dimensional time-resolved signals [287–292]. In this chapter we measure coherent six-particle correlations directly. At fifth order, we use a three-quantum non-rephasing pulse sequence to observe features due to four types of triexcitons. And, at seventh order, we measure three-quantum rephasing signals whose spectra have features due to two of the triexcitons, but the signal is dominated by exciton–free-carrier scattering.

Three-quantum, fifth-order signals were measured in the two-beam ‘self-diffraction’ geometry shown in Fig. 6-1(e) and (f). Signal is measured in the phase-matched direction, $\mathbf{k}_{sig}^{(5)} = 3\mathbf{k}_b - 2\mathbf{k}_a$ with co-linear polarization. The \mathbf{k}_b beam is delayed, and its field interactions create three-quantum coherences that are then projected onto one-quantum coherences by the two conjugate field interactions. In this manner, three-quantum oscillations are Fourier transformed and their phases are correlated to the radiative one-quantum coherences. Feynman diagrams representing typical signal contributions and the measured spectrum are presented in Fig. 6-1(a). The spectrum shows four main features that appear at coordinates which indicate they are bound correlations of three excitons. The HHH triexciton coherence is the most intense feature near 4618.2 ± 0.2 meV. We use its peak location just below the diagonal to measure its binding energy, Δ_{HHH} , to be 1.7 ± 0.2 meV. The other three features are due to HHL (4625.6 ± 0.2 meV, $\Delta_{HHL} = 1.8 \pm 0.2$ meV), HLL (4632.5 ± 0.3 meV, $\Delta_{HLL} = 2.4 \pm 0.3$ meV), and LLL (4640.0 ± 0.3 meV, $\Delta_{LLL} = 2.4 \pm 0.4$ meV) triexciton coherences. The three-quantum linewidths give dephasing times of about 1.3 ± 0.3 ps. Unlike the two-quantum coherence measurements that showed strong signals from

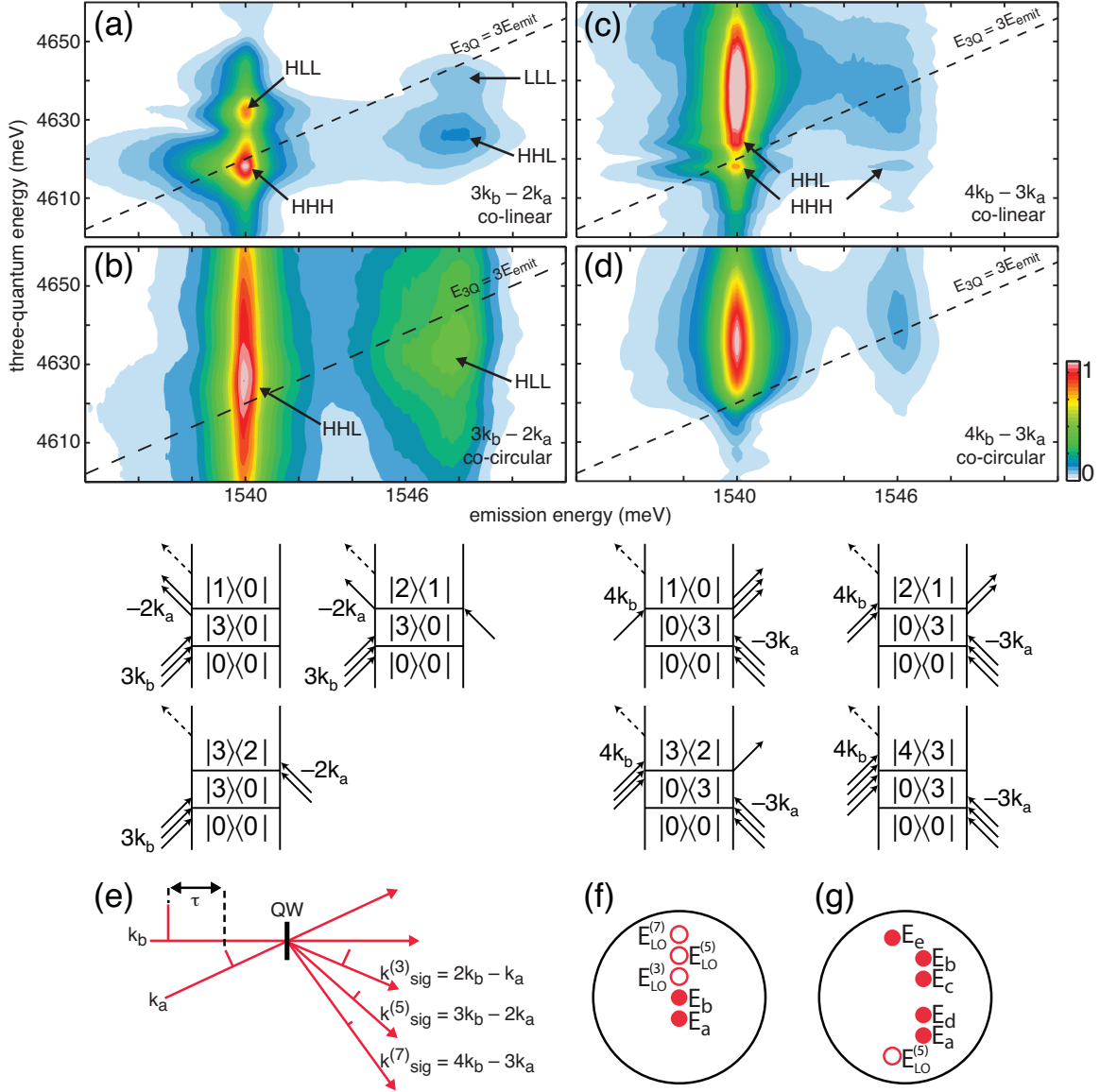


Figure 6-1: Three-quantum spectra of triexciton coherences. (a) Fifth-order signal measured in the $3\mathbf{k}_b - 2\mathbf{k}_a$ direction using co-linear polarization showing four main features due to triexciton-ground-state coherences. (b) Fifth-order co-circular polarization spectrum has significant exciton-free-carrier scattering, but both HHL and HLL triexciton features are visible. (c) Seventh-order rephasing spectrum measured in the $4\mathbf{k}_b - 3\mathbf{k}_a$ direction using co-linear polarization is dominated by exciton-free-carrier scattering but HHH and perhaps HHL features are visible. (d) Seventh-order co-circular polarization spectrum shows only exciton-free-carrier scattering. In any of the four measurements, there are no features indicating signals due to unbound-but-correlated three-exciton complexes, HHH^* . (e) Three-beam (\mathbf{k}_a , \mathbf{k}_b , and \mathbf{k}_{LO}) geometry used in the fifth-order and seventh-order measurements. (f) Confocal view of the beams in the three-beam geometries. (g) Confocal view of the beams in the six-beam geometry.

both bound (biexciton) and unbound-but-correlated two-exciton correlations, in this case there are no measurable signals from unbound three-exciton correlations even though the strongest triexciton signal/noise ratios are on the order of 10^3 . This result suggests that there are no significant unbound six-particle correlations in this system under the present conditions.

We used the six-beam geometry¹ shown in Fig. 6-1(g) to validate our fifth-order signals in three ways. First, we verified that the generated fifth-order signal depends on all five input beams; blocking any one beam caused the signal to disappear. Second, we confirmed that the fifth-order spectra were identical to those collected in the $3\mathbf{k}_b - 2\mathbf{k}_a$ geometry. Third, by placing wave plates in the beams to control the polarizations of the fields independently, we verified that bound HHH triexcitons were created by any combination of polarizations except co-circular, which could not create identical exciton constituents with different spins. In this geometry, it is possible to generate 3D and 4D spectra correlating multiple events in multiple time periods, which could lead to new insights.

We performed the same experiment under co-circular polarization; the spectrum is presented in Fig. 6-1(b). This spectrum shows the two peaks due to mixed triexciton-ground-state coherences that are expected from the dipole selection rules. The large stripes beneath the two peaks are due to exciton-free-carrier scattering, which is not suppressed in this polarization configuration. As in the co-linear configuration, no unbound-but-correlated three-quantum features are visible along the diagonal.

We then performed a co-linear polarized $\mathbf{k}_{sig}^{(7)} = 4\mathbf{k}_b - 3\mathbf{k}_a$ seventh-order rephasing measurement in which the three-quantum coherences produced by the first three ($-\mathbf{k}_a$) field interactions are projected by the four variably delayed (\mathbf{k}_b) field interactions onto radiative one-quantum coherences as shown by the Feynman diagrams; rephasing now occurs at one-third the three-quantum dephasing rate. The spectrum shown in Fig. 6-1(c) used a co-linear polarization configuration. Exciton-free-carrier scattering dominates the spectrum at three-quantum energies above 4630 meV. Nevertheless, rephased triexciton coherences are visible, most notably the HHH triexciton at 4618 meV, and perhaps the HHL at 4626 meV. We performed the same scan with co-circular polarization (which excludes HHH triexcitons since all of the exciton constituents would have parallel spins) as another attempt to observe any six-particle unbound-but-correlated features. These features do not appear along the diagonal in Fig. 6-1(d), however, and only exciton-free-carrier scattering features are visible.

¹Generating this geometry to produce signal in the $\mathbf{k}_{sig}^{(5)} = \mathbf{k}_a - \mathbf{k}_b - \mathbf{k}_c + \mathbf{k}_d + \mathbf{k}_e$ direction with the spatial beam shaper in the COLBERT spectrometer is straightforward; had we not used this apparatus, a new static diffractive optic would have been needed.

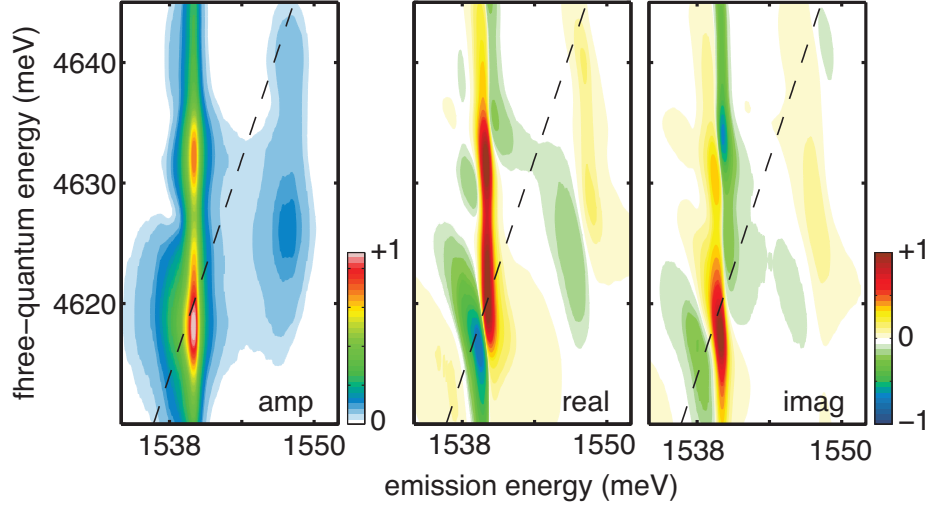


Figure 6-2: Fifth-order three-quantum nonrephasing spectrum. The amplitude of the spectrum (left) is identical to Fig. 6-1(a) except it is presented with equal energy increments for both axes. Triexciton coherences decay rapidly, within about 1 ps. The real (middle) and imaginary (right) portions of the spectrum are also presented. The lineshapes of the peaks indicate that unbound-but-correlated three-exciton coherences are not present.

This result further indicates an absence of unbound six-particle correlations.

The spectra displayed in Fig. 6-1 were stretched horizontally to make the features easier to view. To indicate the true consequences of the rapid dephasing times of these signals, the fifth-order three-quantum spectrum for co-linear polarization is presented again in Fig. 6-2, but with equal energy increments along both axes. The features are elongated vertically, and the rapid dephasing is manifest in this elongation. We also present the real and imaginary parts of the spectrum. The clean character of the peaks indicates that they are not influenced by unbound six-particle correlations as the biexciton coherences were influenced by the HH^* correlation in the S_{III} scan at third-order under the same polarization conditions.

These measurements suggest our multi-exciton level scheme can be described by the transition hierarchy depicted in Fig. 6-3. Fields can couple the common ground state to four exciton states. The single exciton states can couple to two-exciton states, both bound and unbound, which in turn can couple to triexciton states. Patterns emerge in the coupling scheme. The ground and exciton states have four transitions, biexcitons states have six transitions, unbound-but-correlated levels have three transitions, and triexciton states have two transitions.

Although the numerical solutions would require extensive computation time, the three-quantum results—especially the spectrum shown in Fig. 6-2—should be simulated by expanding the nonlinear exciton equations to fifth-order. A partial deriva-

Chapter 7

Eight-particle correlations

Based on the observation of exciton, biexciton, and triexciton coherences, it is tempting to surmise that the ladder of multiexciton states should continue. Therefore, we performed a nonrephasing seventh-order experiment to measure eight-particle coherences due to either bound quadexcitons or unbound-but-correlated four-exciton coherences. The pulse spectra covered both the H and L exciton resonances. As can be seen in Fig. 7-1, however, no peak is observed below or along the diagonal in this $\mathbf{k}_{sig}^{(7)} = 4\mathbf{k}_b - 3\mathbf{k}_a$ measurement. The two pulses had co-linear polarization and the fluence was about 10^4 nJ/cm². Fluences this high result in absorption saturation, see Fig. 4-1. Exciton-free-carrier scattering completely dominates the signal, indicating that at these carrier densities, correlations of more than six particles are not significant. The exciton-free-carrier scattering signal can be due to either one excited electron that has a large nonzero momentum— $\mathbf{k} \gg 0$ —or it could be due to several correlated excited carriers, all with smaller nonzero momenta— $\mathbf{k} > 0$. The reduction of correlation as the number of electron-hole pairs increases, accentuated

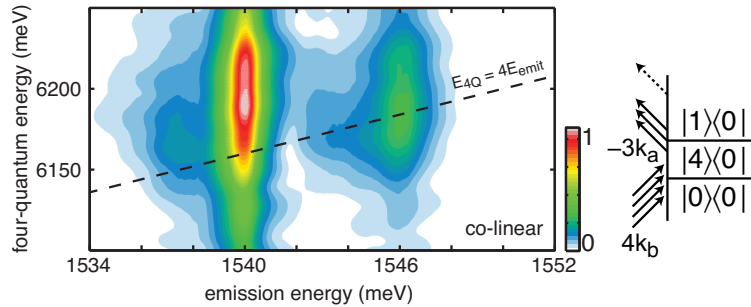


Figure 7-1: A four-quantum seventh-order co-linear polarization measurement indicates the absence of eight-particle correlations. If $HHHH$ quadexciton coherences were produced as indicated by the pathway shown, then a peak would appear below the diagonal line drawn along $E_{4Q} = 4E_{emit}$. The large vertical features are due to exciton-free-carrier scattering.

in the absence of a binding energy, results from the fluctuating forces exerted by all the nearby electrons and holes. The measured binding energies of 1.7–2.4 meV are sufficient to sustain triexciton correlations against some fluctuations at the sample temperature.

Additional measurements could be used to determine if the absence of eight-particle correlations in the above measurement is because the measurement was not sensitive enough to detect the correlations, or because the correlations do not exist. Separating one or more of the four initial field interactions into a distinct beam so that at least one of the fields could be time separated from the others before the four-quantum coherence time will allow the initial excited carrier(s) to decay, and thus the background signal would have less exciton–free-carrier scattering. Another future experiment is to use a cross-linear polarization scheme to eliminate much of the exciton–free-carrier scattering¹. These two measurements would be more sensitive to eight-particle correlations and could reveal their signatures hidden in the above 2D spectrum.

Regardless, a pattern is beginning to emerge. We have now measured several spectra at fluences above 10^3 nJ/cm². In each measurement, unexpected effects were observed as the fluence exceeded this value. The linear spectra described in Sec. 4.1 showed absorption saturation. The two-quantum rephasing fifth-order measurements with co-circular polarization presented in Sec. 5.2 indicated that the EIS and EID effects cause energy and broadening shifts, respectively, of the unbound-but-correlated feature, with a clear transition in this fluence range. In this chapter, we observed that significant exciton-exciton correlations other than exciton–free-carrier scattering were not observable in four-quantum measurements. These effects likely originate in the fact that at these fluence levels, the carrier density suggests that the excitons essentially fill the volume of the sample. Undoubtedly, the strong Coulomb interactions between charged particles in GaAs quantum wells lead to interesting effects as the carrier density increases.

¹A preliminary measurement showed no signal for this polarization configuration.

Chapter 8

Conclusions

We will first understand how simple the universe is when we recognize how strange it is.

It is my opinion that everything must be based on a simple idea. And it is my opinion that this idea, once we have finally discovered it, will be so compelling, so beautiful, that we will say to one another, yes, how could it have been any different.

— Quotable American physicist John Archibald Wheeler (1911–2008), doctoral advisor to Richard Feynman and colleague of Albert Einstein [294].

8.1 Summary

These quotes—and the one in the introductory chapter—suggest that science and science fiction agree: the universe should be explainable in simple terms. This is understandable because both the physics of the very small and the very large can be described by rather simple equations [295]. Nevertheless, it is particle interactions that cause the complexities of life, whether those particles are electrons, proteins, fish, birds, humans, or planets. This raises many philosophical issues, some of which—decoherence and entanglement—are topics at the heart of quantum mechanics [296–299].

Are the quotes correct, at least for GaAs? That is, is there a complete yet simple equation that describes the ‘universe’ of many-body interactions in the quantum well? We should consider whether any of the three models listed in Chapter 2 satisfies these two characteristics. The sum-over-states model used the excitons as an organizing principle to describe the energies of the correlations, their transition dipoles, and

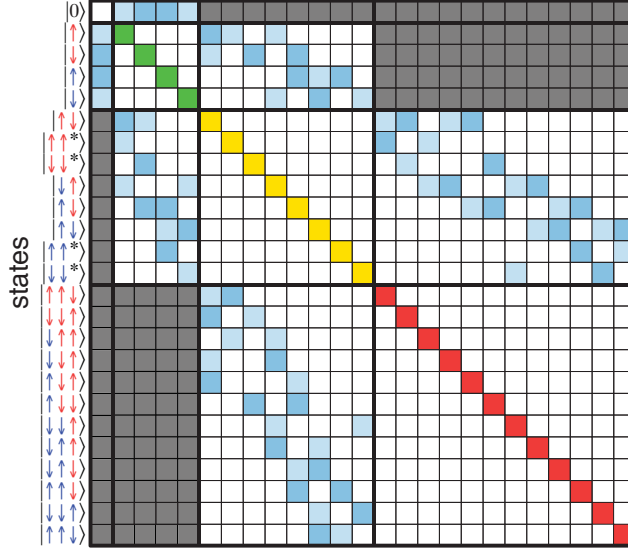


Figure 8-1: Graphical representation of the system Hamiltonian in the sum-over-states model. The upper left corner is the ground state. The green, yellow, and red squares represent the single exciton levels, the two-exciton levels, and the three-exciton levels, respectively. The light blue and dark blue squares represent perturbatively small right-circular and left-circular polarized transitions; the excitons and multiexciton states listed on the left are a diagonal basis for the system. The dark grey squares are multiple-photon transitions that were not explored in our experiments.

their decoherence times and lifetimes. In a sense, the rich spectra are distilled into just a few key pieces of information. We present the energy levels and the nonzero transitions dipoles in a graphical form of the Hamiltonian matrix in Fig. 8-1. This is an illustration of a more advanced form of the example matrices shown in Eqn. 2.29. The colored diagonal elements represent the energy levels of the correlations listed to the left, which indicate the ground $|0\rangle$, single-exciton (one arrow), two-exciton (two arrows), and three-exciton (three arrow) states. Red arrows represent H excitons and their spin, while blue arrows represent L excitons and their spin. The blue, off-diagonal squares in the matrix represent the allowed transitions of the system, and the grey areas are multiple-photon transitions that we did not investigate. Moreover, our results from Chapter 7 suggest that the Hamiltonian matrix is no larger. This satisfies the simplicity requirement. Unfortunately the sum-over-states model is a poor way to understand the complex many-body interactions in this system because the correlations cannot be predicted. Instead they are included in a haphazard manner after they are observed. The Bloch equations suffer from the same problem; although the many-body correlations can be inserted phenomenologically, correlations are included only after they have been observed. Thus, although these two models are simple, they are not complete because they cannot predict the observed

correlations. On the other hand, the nonlinear exciton equations model also fails to satisfy both characteristics. Although thus far they have predicted the two-particle and four-particle interactions manifest in the measured spectra, they are anything but simple. The lack of simplicity has prevented theoretical investigations of direct coherent six-particle correlations.

The experiments contained in this thesis illustrate the difficulty of this philosophical question. As described, we studied the fundamental physical problem of many-body interactions using the technologically important material GaAs [300]. Such studies began in the 1980s; recent advances using two-dimensional optical spectroscopy suggested that complete elaboration of the many-body interactions was both possible and necessary. The experimental apparatus we designed and built—the COLBERT spectrometer—performed these measurements with ease, even though the measurement conditions were performed under varying geometries, pulse timing schemes, and polarization conditions. The measured spectra revealed several many-body interactions that give scientists a better understanding of ‘many’. We observed that correlations involving two particles, four particles, and six particles can contribute to the signal, but correlations involving more than six particles do not contribute under the conditions used here. Additionally, the spectra contained detailed information, such as energetics and dephasing dynamics, about each correlation. Thus our work described the properties as well as the limits of many-body correlations in this system. Although our knowledge of perturbation theory led us to suspect that eight-particle correlations should exist, their unexpected absence here brings to mind another Wheeler quote,

No phenomenon is a real phenomenon until it is an observed phenomenon.

8.2 Outlook

The femtosecond pulse shaping methods devised in the Nelson group over the past decade are now robust enough to be used for many scientific investigations beyond pulse shaping development. Most of the technical challenges inherent to measuring 2D FTOPT spectra using the COLBERT spectrometer have been overcome, meaning attention can focus on scientific questions. Since spectroscopic measurements can reveal insights about electronic excitations and their interactions, important excitonic and molecular systems can be investigated.

First, more can be learned about the GaAs sample. Several straightforward experiments were mentioned in the text. In addition, tailored pulses can be used to select desired correlations. One type of tailoring technique is a double-pulse technique

in which emission pathways can be suppressed or enhanced [301]. A second technique involves phase-windows [254, 255] to enhance or suppress desired two-exciton coherences. We have performed preliminary measurements using both coherent-control techniques to attempt to isolate multiexciton coherence even further. Another ultimate goal would be to characterize the exciton wavefunction completely through quantum-state tomography. Our measurements begin that journey. In a similar manner, these ideas and measurements may be valuable for understanding and implementing nonlinear wave packet interferometry experiments [302], where detection and knowledge of the correlations among events in all time periods could be useful. Further knowledge of the many-body interactions could be gained if magnetic [303–305] or THz [306] fields were introduced to modulate or to enhance the Coulomb interactions. Multidimensional studies of the exciton and multiexciton fine structure [38] and exchange interactions [307] would be valuable.

Measurements on other systems are also underway. Two-dimensional measurements on exciton-polaritons in semiconductor microcavities will lead to a better understanding of parametric scattering processes [308–311]. Similar interactions involving strong coupling between J -aggregates and light in microcavities can be investigated [312–314] and hopefully incorporated into optical switches. In both the inorganic and organic systems, the strong coupling between light and matter in microcavities will make it easier to manipulate and control the excitations. It may also be possible to measure or control exciton-polariton propagation. Exciton and exciton-polariton propagation are important topics because excitonic systems can transport energy without transporting charge; a number of technological applications may exploit this property. The capabilities of the COLBERT device could also be used to perform multiple transient grating measurements at varying wave vectors between the pump beams—all under computer control—to study exciton diffusion in J -aggregates and other systems.

Two-dimensional correlation spectra and S_{III} measurements on quantum dots will extend state-resolved pump-probe measurements [315, 316] to reveal additional insights into the electronic structure of the biexcitons. In photosynthetic light-harvesting complexes, fifth-order measurements of the two-exciton–exciton coherence can expose additional quantum correlations beyond those already measured [165, 168]. Energy transfer mechanisms in coupled quantum-dot/ J -aggregate systems can also be investigated [317, 318]. Theoretical investigations of all of the above systems will be crucial. As we have seen, however, simulations quickly become nontrivial; new simulation techniques must be developed.

The topic of quantum entanglement is ripe for investigation, both theoretical and

experimental. Examples have been demonstrated: decoherence—a topic distinct from dephasing [319]—has been controlled [320], entanglement measures for photosynthetic complexes have been suggested [321] and created [322], and entangled images have been generated through four-wave-mixing measurements [323], yet the impact on nonlinear spectroscopy has been limited [324, 325]. Although they have only begun to emerge, the subtle but powerful methods of quantum entanglement are anticipated to bring about significant advances and profound insights into the field of nonlinear spectroscopy.

Appendix A

Analysis of cascade contamination

Each time a new high-order spectroscopy is developed, the issue of cascaded lower-order contributions needs to be addressed because their presence greatly affected the development of 2D Raman spectroscopy [186, 326–328]. Cascaded signals can be misinterpreted as true high-order signals because they satisfy the same phase-matching and power-law conditions. The prototypical cascade is the third-order/third-order cascade—where the field emitted by one third-order process is reabsorbed in a second third-order process—which can contaminate a fifth-order signal. At higher orders other sets of cascades are possible [329].

Few experimental tests are available to identify the cascades and to estimate the degree of contamination. A linear dependence on concentration is the most common piece of evidence used to confirm the absence of cascades. We have a solid sample and are unable to change the carrier concentration (in GaAs this is the carrier density) independently from the input power. A cascade-free fifth-order signal will also depend linearly on sample path length. We cannot vary the sample path length because the width of the quantum well determines the exciton energies. Changing the number of quantum wells would be the correct approach, but this is technologically impractical, and would provide at most only one order of magnitude variation (one to ten quantum wells [41]). Furthermore, in nonresonant fifth-order measurements, phase-sensitive heterodyne detection was used to discriminate against cascades because they were $\frac{\pi}{2}$ phase-shifted from the true signal [330]. In resonant fifth-order measurements, the phase of the cascades and the true signal are π phase-shifted because the response functions are imaginary, meaning heterodyne detection cannot be used to discriminate against the cascades [331]. Any contributions from cascades in a resonant measurement simply interfere destructively with the true high-order signal, causing an overall loss of amplitude. Resonant seventh-order measurements suffer from an analogous lack of phase discrimination; the fifth-order/third-order cascades

will by π phase-shifted from the true signal, while the third-order/third-order/third-order cascades will have the same phase as the true signal. These phase shifts result from additional Maxwell equation events that are not part of a true high-order process.

Instead, we rely on two pieces of information. The first is that cascaded contributions have typically dominated only nonresonant measurements in which the high-order signal involved a formally forbidden transition. All transitions in resonant measurements like those performed here involve formally allowed transitions. Previous fifth-order 2D IR resonant spectroscopies had at most minimal ($<2\%$) contamination by cascades [111]. Accounting for wavelength (800 nm), path length (10 nm), concentration (10^{24} m^{-3}), and transition dipole moment differences (the present transition moments are ~ 15 Debye), we estimate the amount of cascade contamination should be one-tenth that of the IR, giving a contamination degree of $<0.2\%$.

The second piece of evidence is that we can draw the Feynman pathways for the cascaded contributions and determine the frequency coordinates at which the cascades should appear. This analysis relies on the fact that in our fifth-order three-quantum measurements, only the true fifth-order signal can arise from coherences involving triexcitons. Cascades would appear either on the diagonal or shifted below it by the biexciton binding energy ($\sim 1 \text{ meV}$), due to polarization interferences in parallel cascades; the measured peak is shifted even lower ($\sim 1.8 \text{ meV}$). This suggests that the coherence is due to a true triexciton-ground-state coherence. Furthermore, the triexciton-biexciton emission observed in fifth order two-quantum rephasing is not possible in a cascaded signal, indicating that the two-quantum rephasing signal shown is also not contaminated significantly. This is even clearer from the real part of the rephasing spectrum, Fig. 5-6(d). Similar arguments hold for the rephased triexcitons observed at seventh order. Additionally, the seventh-order, three-quantum rephasing, co-circular signal—were it due to cascades—should have contained a peak arising from a parallel cascade between a two-quantum unbound-but-correlated coherence and a single exciton coherence. But since this signal does not appear exactly along the diagonal, this indicates that the previous observation was also not a cascade. Phase-cycling procedures will eliminate some cascade contributions, but only those cascades which do not remain coherent. By subtracting signals that are not strictly dependent on the phase of all five fields in a deterministic manner, phase cycling eliminates cascades that involve random scattering events during the intermediate-emission and reabsorption processes. Thus, although we cannot perform concentration, pathlength variation, or phase-discrimination tests, the evidence strongly suggests that cascades do not contaminate our signals substantially.

Appendix B

Spectrum from the nonlinear exciton equations

In this appendix, we show how to calculate a one-dimensional spectrum using an adaptive Runge-Kutta algorithm to integrate the nonlinear exciton equation, Eqn. 2.60, numerically. The algorithm we use is known as RKF45. The computation uses a three-band model that includes the one conduction and two valence bands of GaAs.

The bulk of the code—everything until line 72—involves constructing the matrices that describe the site energies, dephasing, Coulomb interactions, and RKF45 implementation. The algorithm itself occurs on lines 73–83, and it incorporates a subfunction, `np1`, to propagate the system from an initial time point, `t(aa)`, to a desired time point, `t(aa+1)`. The `while` loop repeats until time, `t`, reaches the final time, `tf`, regardless of the number of steps required. Variable `aa` counts the steps. The time and the total polarization vectors, `t` and `totp`, respectively, are then interpolated to evenly spaced vectors and Fourier transformed to yield frequency and spectral data sets.

The elements of Eqns. 2.60 and 2.61 are present in the code: dephasing t_X , `deph`; density matrices ρ_{ij}^{he} , `pH`, and `pL`; sites i and j , `Ndim`; conduction band T^c , `tc`; H valence band T^H , `tH`; L valence band T^L , `tL`; Coulomb interactions V_{ij} , `coul`; electric field \mathbf{E}_a , `fld`; dipoles μ_{ij}^{he} , `muH` and `muL`, and polarizations $\mathbf{P}(t)$, `tpHH`, `tpLH`, and their sum, `totp`. The tolerance is given by `tol`. All of the parameters are inserted into the subfunction `np1` at each time point. The algorithm contained in this subfunction then computes the new polarization, the new density matrix, and a suggested new time step, `h`. The summation in lines 50 and 52 are not allowed in a two-dimensional simulation, slowing computations.

```

1 %% Parameters
2 Ndim = 10; % number of sites
3 h = 0.10; % initial time step (ps)
4 tol = 1e-2; % error tolerance
5 deph = 6; % exciton dephasing (ps)
6 hbar = 0.241798977*2*pi; % convert meV to angular THz
7
8 %% Free-band matrices
9 blnk = diag(ones(1,Ndim-1),1) + diag(ones(1,Ndim-1),-1);
10 blnk(Ndim,1) = 1; blnk(1,Ndim) = 1;
11 tc = blnk.*8*hbar; tH = blnk.*4.75*hbar; tL = blnk.*2.52*hbar;
12 tc = tc'; tH = tH'; tL = tL';
13 clear blnk;
14
15 %% Coulomb matrix
16 % constants for coupling matrix
17 U0 = 10*hbar;
18 a0_d = 0.5;
19 v = zeros(1,Ndim);
20 for ii=1:Ndim
21     v(ii) = U0/((ii-1)+a0_d);
22 end
23
24 coul = zeros(Ndim,Ndim);
25 for ii = 1:Ndim
26     for jj = 1:Ndim
27         if abs(ii-jj)<round(Ndim/2)
28             coul(ii,jj) = v(1+abs(ii-jj));
29         else
30             % account for periodic boundary conditions
31             coul(ii,jj) = v(1+Ndim-abs(ii-jj));
32         end
33     end
34 end
35 clear ii jj v U0 a0_d;
36
37 %% Dipole matrix
38 muH = eye(Ndim); % heavy-hole
39 muL = 0.75.*muH; % light-hole
40
41 %% Time
42 tf = 50; % propagate polarizations until (ps)
43 t1 = 0.7; % pulse delay (ps)
44 dt = 0.3; % pulse width (ps)

```

```

45
46 %% Prepare empty matrices
47 pH = zeros(Ndim,Ndim); pL = pH;
48 coul = li*coul; tc = -li*tc;
49 tH = -li*tH; tL = -li*tL;
50 tmatH = tc + tH; tmatL = tc + tL;
51 % pre-add these outside the 'for' loop
52 deph = -1/deph; dcm = deph + coul;
53
54 %% Create Runge-Kutta-Fehlberg matrices
55 % time changes for each of six steps
56 rkt      = [0,1/4,3/8,12/13,1,1/2];
57 % multipliers
58 rkv(1,:) = [0,0,0,0,0];
59 rkv(2,:) = [1/4,0,0,0,0];
60 rkv(3,:) = [3/32,9/32,0,0,0];
61 rkv(4,:) = [1932/2197,-7200/2197,7296/2197,0,0];
62 rkv(5,:) = [439/216,-8,3680/513,-845/4104,0];
63 rkv(6,:) = [-8/27,2,-3544/2565,1859/4104,-11/40];
64 % final multiplicative factors of sums
65 rkm(1,:) = [25/216,0,1408/2565,2197/4104,-1/5,0];
66 rkm(2,:) = [16/135,0,6656/12825,28561/56430,-9/50,2/55];
67
68 %% Numerical integration
69 aa = 1; % time points counter
70 t(1) = 0; % time starts at t=0 (ps)
71 tpHH = zeros(1,10000); tpLH = zeros(1,10000);
72
73 while t(aa) < tf
74     % first propose a new time step: 'h'
75     t(aa+1) = t(aa) + h;
76     [pH,spH,hH] = np1(pH,h,t(aa),tol,tmatH,dcm,rkt,rkv,rkm,t1,dt,muH);
77     [pL,spL,hL] = np1(pL,h,t(aa),tol,tmatL,dcm,rkt,rkv,rkm,t1,dt,muL);
78     h = min(hH,hL);
79     % find the total polarization at this time point
80     tpHH(aa) = spH; tpLH(aa) = spL;
81     % increment to the next point
82     aa = aa + 1;
83 end

```

The subfunction `np1` implements the RKF45 algorithm by calculating the fourth-order and fifth-order slopes, `pa` and `pb`; the difference between the slopes is the numerical error, `er`. This is the advantage of the RKF45 algorithm.

Several elements in this subfunction are worth noting. For example, line 51 is the trace operation given by Eqn. 2.19; the density matrices at different orders—`pa` and `pb`—are projected by the dipole matrix, `mu`, and the traces are taken using the `sum` functions. Lines 53-62 compare the error to the tolerance. If the error is less than the tolerance, the step is accepted and line 56 calculates the time increment, `hn`, to be used in the next iteration. If the step is rejected, the time step is reduced by half in line 61 and the loop executes again. In this subfunction, the variable `aa` is the stop mechanism. If the step is within the error tolerance and is accepted, `aa` changes from a zero to a one on line 59, and the `while` loop stops. This subfunction uses a second subfunction, `f1d` for the electric field. The mathematics of Eqn. 2.60 occur on lines 29-47. In the two-dimensional simulation, the matrix mathematics performed on line 39 must be done element-by-element, slowing computations dramatically.

```

1 function [npt,sp1,hn] = np1(p,h,t,tol,tmat,dcm,rkt,rkv,rkm,t1,delt,mu)
2
3 % INPUTS
4 %     p:      initial p_i-j(t_n)
5 %     h:      desired time step
6 %     t:      time of previous pij (tn)
7 %     tol:    desired error tolerance
8 %     tmat:   Tc and Tv matrices
9 %     dcm:    dephasing and coulomb matrices
10 %    rkt:    RKF45 time elements
11 %    rkv:    RKF45 vector elements
12 %    rkm:    RKF45 multiply elements
13 %    t1:     pulse delay (ps)
14 %    delt:   width of pulse
15 %    mu:     dipole matrix
16 %
17 % OUTPUTS
18 %    npt:    new p_i-j(t_n+1)
19 %    sp1:    new p(t_n+1) (*mu & sum(_i-j) )
20 %    hn:     next guess for 'h'
21 %
22 Ndim = length(p);
23 aa = 0;
24 while lt(aa,1)
25     % erase the RKF45 storage matrix after a complete step

```



```

26 p2t = zeros(Ndim,Ndim,6);
27 % clear the sub-sums at each time point
28 p2_1 = zeros(Ndim,Ndim); p2_2 = p2_1;
29 for rk = 1:6
30     % 'rk' counts the Runge-Kutta steps
31     % find k1-k6
32     sba = zeros(Ndim,Ndim);
33     for cc = 1:(rk-1)
34         % 'cc' counts the sub-sum of the RK method
35         sba = sba + rkv(rk,cc)*p2t(:, :, cc);
36     end
37     sb = p + h*sba;
38     % the T & V matrices
39     m1 = dcm.*sb + tmat*sb;
40     % the source term: the electric field
41     m2 = fld(t+rkt(rk)*h,t1,delt).*mu;
42     p2t(:, :, rk) = m1 + m2;
43     % the sub-sum for the 4th-order sum
44     p2_1 = p2_1 + rkm(1,rk)*(m1 + m2);
45     % the sub-sum for the 5th-order sum
46     p2_2 = p2_2 + rkm(2,rk)*(m1 + m2);
47 end
48 % the 4th-order & 5th-order sums
49 pa = p + h*p2_1; pb = p + h*p2_2;
50 % calculate the 4th-order & 5th-order polarizations
51 sp1 = sum(sum(mu.*pa)); sp2 = sum(sum(mu.*pb));
52 er = abs(sp2-sp1);
53 if le(er,tol)
54     % if the calculated error is less than the tolerance
55     % the new 'h'
56     hn = h*(tol*h/(2*er))^(1/4);
57     % save and increment
58     npt = pa;
59     aa = 1;
60 else
61     h = h/2;
62 end
63 end

```

The subfunction below, `fld`, is used in line 41 of `np1`. This function defines the electric field that drives the system polarization. The value of the function at time `tp` is calculated using a Gaussian function whose standard deviation is given by `delt` (300 fs), whose envelope delay is given by `t1` (700 fs), and whose carrier frequency is set to the induced heavy-hole oscillation frequency, -35.165 meV.

```

1 function fldpt = fld(tp,t1,delt)
2
3 %% carrier freq (meV to angular THz)
4 % freq = -35.165*(2*pi*0.241798977);
5
6 %% field envelope for a delay 't1' and width 'delt'
7 env = exp(-(tp-t1).^2/(delt)^2);
8
9 %% include carrier freq, calculate field at time 'tp'
10 fldpt = 1i*env.*exp(1i*53.42505*tp);

```

The results are shown in Fig. B-1. Part (a) reports the progress of the adaptive algorithm. The initial time increment of 100 fs is diminished in about four steps until a fairly steady time increment of about 5 fs is reached. Then the time increment begins to increase slowly to about 20 fs because the amplitude of the oscillations decreases as time evolves. About 3300 time steps were required to reach the end time of 50 ps; the average time step was about 15 fs. The electric field that drives the sample polarization is illustrated in part (b), and the first 10 ps of the resulting signal are shown in part (c). Polarization interference between the H and L excitons is visible as beats in the signal. Finally, the field and the polarization are Fourier transformed and their amplitudes are displayed in part (d). The field is resonant with the H exciton frequency. The L exciton has a reduced oscillator strength because it has a smaller dipole moment value and because it is not resonant with the brightest part of the driving field. The energy axis has been shifted so that the H exciton energy has a value of zero.

If hundreds of sites are used and if the carrier frequency of the incident field is tuned above the L exciton, a higher-energy continuum will appear in addition to the two exciton absorption features. This continuum is due to absorption by free carriers. The computation time scales as N_{dim}^2 , so it increases to about one hour on a modern PC.

Two-dimensional computations are significantly more challenging than the one-dimensional computation performed here. The mathematics become more complicated because the equations are larger, the computations cannot be reduced to matrix

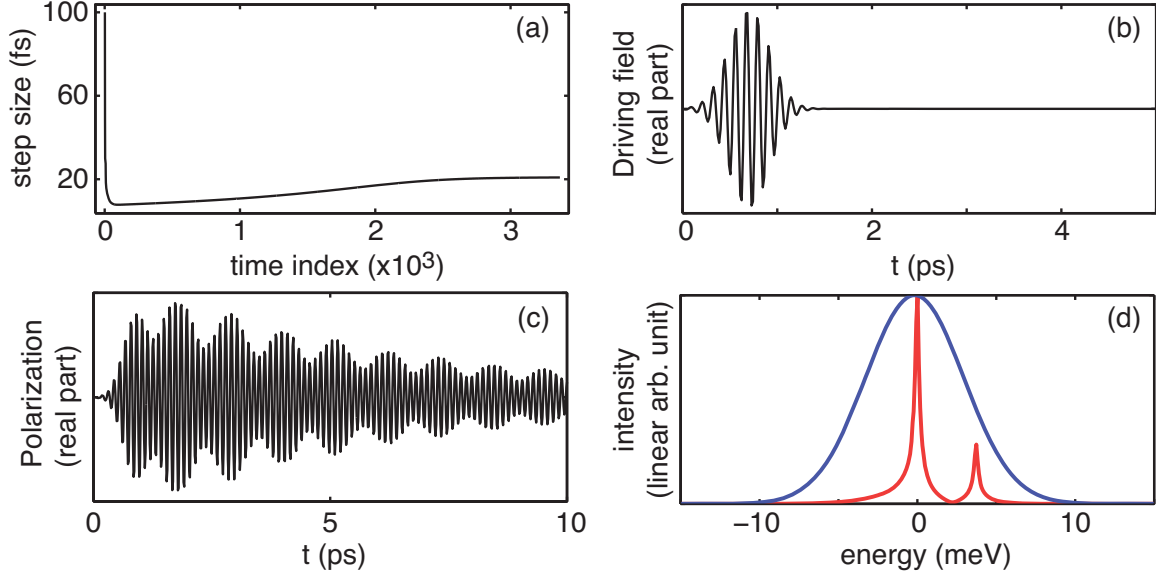


Figure B-1: Nonlinear exciton equation numerical integration. (a) The adaptive algorithm takes steps as large as possible within the defined tolerance. (b) The electric field that drives the sample polarization. (c) The sample polarization induced by the electric field. (d) Fourier transform of the sample polarization (red) and of the resonant driving field (blue). There are two peaks due to H and L excitons.

multiplication and instead must be performed element-by-element, and more fields and polarizations must be tracked. In addition, the lengthy computation times complicate debugging tasks, especially for scientists without formal training in computer programming.

Bibliography

- [1] S. E. Pollack, D. Dries, and R. G. Hulet, *Science*, **326**, 1683 (2009).
- [2] P. B. Lissaman and C. A. Shollenberger, *Science*, **168**, 1003 (1970).
- [3] I. L. Bajec and F. H. Heppner, *Animal Behaviour*, **78**, 777 (2009).
- [4] H. Chate, F. Ginelli, G. Gregoire, F. Peruani, and F. Raynaud, *Eur. Phys. J. B*, **64**, 451 (2008).
- [5] A. Tero et al., *Science*, **327**, 439 (2010).
- [6] D. Peak, J. D. West, S. M. Messinger, and K. A. Mott, *Proc. Natl. Acad. Sci. U.S.A.*, **101**, 918 (2004).
- [7] J. E. Balzer, W. G. Proud, S. M. Walley, and J. E. Field, *Combustion and Flame*, **135**, 547 (2003).
- [8] G. Hayafus, *Stopping Time: The Photographs of Harold Edgerton*, Harry N. Abrams, Inc., New York, 1987.
- [9] R. R. Bruce, *Seeing the Unseen: Dr. Harold E. Edgerton and the Wonders of Strobe Alley*, The MIT Press, 1994.
- [10] A. P. French, *Vibrations and Waves*, W. W. Norton and Company Inc, New York, 1971.
- [11] S. T. Cundiff, *J. Phys. D: Appl. Phys.*, **35**, R43 (2002).
- [12] D. J. Ulness and A. C. Albrecht, *Phys. Rev. A*, **53**, 1081 (1996).
- [13] M. J. Stimson, D. J. Ulness, and A. C. Albrecht, *Chem. Phys. Lett.*, **263**, 185 (1996).
- [14] D. J. Ulness, J. C. Kirkwood, M. J. Stimson, and A. C. Albrecht, *J. Chem. Phys.*, **107**, 7127 (1997).
- [15] D. J. Ulness, *J. Phys. Chem. A*, **107**, 8111 (2003).
- [16] S. Mukamel, *Principles of Nonlinear Optical Spectroscopy*, Oxford University Press, New York, 1995.
- [17] N. W. Ashcroft and N. D. Mermin, *Solid State Physics*, Brooks Cole, 1976.
- [18] R. Uno, T. Okano, and K. Yukino, *J. Phys. Soc. Jap.*, **28**, 437 (1970).
- [19] R. Colella, *Phys. Rev. B*, **3**, 4308 (1971).
- [20] I. Fujimoto, *Jap. J. Appl. Phys.*, **19**, L345 (1980).

- [21] U. Pietsch, V. G. Tsirelson, and R. P. Ozerov, *phys. stat. sol. (b)*, **138**, 47 (1986).
- [22] P. M. Levalois and G. Allais, *Acta. Cryst.*, **B42**, 443 (1986).
- [23] R. Uno, J. Ishigaki, H. Ozawa, and K. Yukino, *Jap. J. Appl. Phys.*, **28**, 573 (1989).
- [24] U. Pietsch and N. K. Hansen, *Acta. Cryst.*, **B52**, 596 (1996).
- [25] P. Y. Yu and M. Cardona, *Fundamentals of Semiconductors: Physics and Materials Properties*, Springer-Verlag, Berlin Heidelberg New York, 2005.
- [26] R. J. Elliott, *Phys. Rev.*, **108**, 1384 (1957).
- [27] D. S. Chemla and J. Shah, *Nature*, **411**, 549 (2001).
- [28] G. D. Scholes and G. Rumbles, *Nature Materials*, **5**, 683 (2006).
- [29] R. Rossetti, S. Nakahara, and L. E. Brus, *J. Chem. Phys.*, **79**, 1086 (1983).
- [30] D. J. Norris, A. Sacra, C. B. Murray, and M. G. Bawendi, *Phys. Rev. Lett.*, **72**, 2612 (1994).
- [31] B. E. Brinson, J. B. Lassiter, C. S. Levin, R. Bardhan, M. Mirin, and N. J. Halas, *Langmuir*, **24**, 14166 (2008).
- [32] Y. Sun, B. Wiley, Z.-Y. Li, and Y. Xia, *J. Am. Chem. Soc.*, **126**, 9399 (2004).
- [33] Y. Khalavka, J. Becker, and C. Sönnichsen, *J. Am. Chem. Soc.*, **131**, 1871 (2009).
- [34] A. Wijaya, S. B. Schaffer, I. G. Pallares, and K. Hamad-Schifferli, *ACS Nano*, **3**, 80 (2009).
- [35] D. Peer, J. M. Karp, S. Hong, O. C. Farokhzad, R. Margalit, and R. Langer, *Nature Nanotechnology*, **2**, 751 (2007).
- [36] A. d. I. Zerda and S. S. Gambhir, *Nature Nanotechnology*, **2**, 745 (2007).
- [37] B. J. McCall et al., *Phys. Rev. A*, **70**, 052716 (2004).
- [38] J. Shah, *Ultrafast Spectroscopy of Semiconductors and Semiconductor Nanostructures*, Springer Verlag, Berlin, 1999.
- [39] S. W. Koch, M. Kira, and T. Meier, *J. Opt. B: Quant. Semiclass. Opt.*, **3**, R29 (2001).
- [40] V. M. Axt and T. Kuhn, *Rep. Prog. Phys.*, **67**, 433 (2004).
- [41] S. T. Cundiff, *Opt. Express*, **16**, 4639 (2008).
- [42] S. Schmitt-Rink, D. S. Chemla, and D. A. B. Miller, *Phys. Rev. B*, **32**, 6601 (1985).
- [43] M. Lindberg and S. W. Koch, *Phys. Rev. B*, **38**, 3342 (1988).
- [44] D. A. B. Miller, D. S. Chemla, P. W. Smith, A. C. Gossard, and W. Wiegmann, *Opt. Lett.*, **8**, 477 (1983).
- [45] J. Hegarty, M. D. Sturge, A. C. Gossard, and W. Wiegmann, *Appl. Phys. Lett.*, **40**, 132 (1982).
- [46] D. A. B. Miller, D. S. Chemla, D. J. Eilenberger, P. W. Smith, A. C. Gossard, and W. Wiegmann, *Appl. Phys. Lett.*, **42**, 925 (1983).

- [47] L. Schultheis, M. D. Sturge, and J. Hegarty, *Appl. Phys. Lett.*, **47**, 995 (1985).
- [48] D. S. Chemla and D. A. B. Miller, *J. Opt. Soc. Am. B*, **2**, 1155 (1985).
- [49] L. Schultheis, J. Kuhl, A. Honold, and C. W. Tu, *Phys. Rev. Lett.*, **57** (1986).
- [50] L. Schultheis, A. Honold, J. Kuhl, K. Köhler, and C. W. Tu, *Phys. Rev. B*, **34**, 9027 (1986).
- [51] M. Koch, J. Feldmann, E. O. Göbel, P. Thomas, and K. Köhler, *Phys. Rev. Lett.*, **69**, 3631 (1992).
- [52] V. G. Lyssenko, J. Erland, I. Balslev, K. H. Pantke, B. S. Razbirin, and J. H. Hvam, *Phys. Rev. B*, **48**, 5720 (1993).
- [53] S. T. Cundiff, *Phys. Rev. A*, **49**, 3114 (1994).
- [54] X. Zhu, M. S. Hybertsen, and P. B. Littlewood, *Phys. Rev. Lett.*, **73**, 209 (1994).
- [55] M. Koch, J. Feldmann, G. von Plessen, S. T. Cundiff, E. O. Göbel, P. Thomas, and K. Köhler, *Phys. Rev. Lett.*, **73**, 210 (1994).
- [56] K. Leo, T. C. Damen, J. Shah, E. O. Göbel, and K. Kohler, *Appl. Phys. Lett.*, **57**, 19 (1990).
- [57] B. Feuerbacher, J. Kuhl, R. Eccleston, and K. Ploog, *Solid State Comm.*, **74**, 1279 (1990).
- [58] T. F. Albrecht, J. H. H. Sandmann, S. T. Cundiff, J. Feldmann, W. Stolz, and E. O. Göbel, *Solid State Elec.*, **37**, 1327 (1994).
- [59] T. Yajima, K. Yoshihara, C. B. Harris, and S. Hionoya, editors, *Ultrafast Phenomena VI*, volume 48, Berling Heidelberg New York, 1989, Springer-Verlag.
- [60] A. Honold, L. Schultheis, J. Kuhl, and C. W. Tu, *Phys. Rev. B*, **40**, 6442 (1989).
- [61] M. Koch, R. Hellmann, G. Bastian, J. Feldmann, E. O. Göbel, and P. Dawson, *Phys. Rev. B*, **51**, 13887 (1995).
- [62] A. Lohner, K. Rick, P. Leisching, A. Leitenstorfer, T. Elsaesser, T. Kuhn, F. Rossi, and W. Stolz, *Phys. Rev. Lett.*, **71**, 77 (1993).
- [63] A. Leitenstorfer et al., *Phys. Rev. B*, **49**, 16372 (1994).
- [64] J. Feldmann et al., *Phys. Rev. Lett.*, **70**, 3027 (1993).
- [65] T. Meier, A. Schulze, P. Thomas, H. Vaupel, and K. Maschke, *Phys. Rev. B*, **51**, 13977 (1995).
- [66] J. Lee, E. S. Koteles, and M. O. Vassell, *Phys. Rev. B*, **33**, 5512 (1986).
- [67] J. Hegarty, L. Goldner, and M. D. Sturge, *Phys. Rev. B*, **30**, 7346 (1984).
- [68] A. Mysyrowicz, D. Hulin, A. Antonetti, A. Migus, W. T. Masselink, and H. Morkoc, *Phys. Rev. Lett.*, **56**, 2748 (1986).
- [69] A. Von Lehmen, D. S. Chemla, J. E. Zucker, and J. P. Heritage, *Opt. Lett.*, **11**, 609 (1986).
- [70] U. Siegner, M. A. Mycek, S. Glutsch, and D. S. Chemla, *Phys. Rev. Lett.*, **74**, 470 (1995).
- [71] E. O. Göbel, K. Leo, T. Damen, J. Shah, S. Schmitt-Rink, W. Schafer, J. Muller, and K. Köhler, *Phys. Rev. Lett.*, **64**, 1801 (1990).

- [72] A. V. Durrant, J. Manners, and P. M. Clark, *Eur. J. Phys.*, **10**, 291 (1989).
- [73] D.-S. Kim, J. Shah, J. E. Cunningham, T. C. Damen, W. Schäfer, M. Hartmann, and S. Schmitt-Rink, *Phys. Rev. Lett.*, **68**, 1006 (1992).
- [74] K. Leo, M. Wegener, J. Shah, D. Chemla, E. Gobel, T. Damen, S. Schmitt-Rink, and W. Schafer, *Phys. Rev. Lett.*, **65**, 1340 (1990).
- [75] M. Wegener, D. S. Chemla, S. Schmitt-Rink, and W. Schäfer, *Phys. Rev. A*, **42**, 5675 (1990).
- [76] X. Chen, W. Walecki, O. Buccafusca, D. Fittinghoff, and A. Smirl, *Phys. Rev. B*, **56**, 9738 (1997).
- [77] M. Phillips and H. Wang, *Solid State Comm.*, **111**, 317 (1999).
- [78] A. Smirl, M. J. Stevens, X. Chen, and O. Buccafusca, *Phys. Rev. B*, **60**, 8267 (1999).
- [79] S. T. Cundiff, H. Wang, and D. G. Steel, *Phys. Rev. B*, **46**, 7248 (1992).
- [80] D. Bennhardt, P. Thomas, R. Eccleston, E. J. Mayer, and J. Kuhl, *Phys. Rev. B*, **47**, 13485 (1993).
- [81] R. Eccleston, J. Kuhl, D. Bennhardt, and P. Thomas, *Solid State Comm.*, **86**, 93 (1993).
- [82] H. Wang, K. Ferrio, D. Steel, Y. Hu, R. Binder, and S. Koch, *Phys. Rev. Lett.*, **71**, 1261 (1993).
- [83] H. Wang, K. Ferrio, D. Steel, P. Berman, Y. Hu, R. Binder, and S. Koch, *Phys. Rev. A*, **49**, R1551 (1994).
- [84] D. S. Chemla, W. H. Knox, D. A. B. Miller, S. Schmitt-Rink, J. B. Stark, and R. Zimmermann, *J. Lumin.*, **44**, 233 (1989).
- [85] G. Manzke, Q. Y. Peng, K. Henneberger, U. Neukirch, K. Hauke, K. Wundke, J. Gutowski, and D. Hommel, *Phys. Rev. Lett.*, **80**, 4943 (1998).
- [86] J. M. Shacklette and S. T. Cundiff, *Phys. Rev. B*, **66**, 045309 (2002).
- [87] C. N. Borca, T. Zhang, X. Li, and S. T. Cundiff, *Chem. Phys. Lett.*, **416**, 311 (2005).
- [88] B. F. Feuerbacher, J. Kuhl, and K. Ploog, *Phys. Rev. B*, **43**, 2439 (1991).
- [89] D. J. Lovering, R. T. Phillips, G. J. Denton, and G. W. Smith, *Phys. Rev. Lett.*, **68**, 1880 (1992).
- [90] R. C. Miller, D. A. Kleinman, A. C. Gossard, and O. Munteanu, *Phys. Rev. B*, **25**, 6545 (1982).
- [91] D. A. Kleinman, *Phys. Rev. B*, **28**, 871 (1983).
- [92] V. I. Klimov, A. A. Mikhailovsky, S. Xu, A. Malko, J. A. Hollingsworth, C. A. Leatherdale, H.-J. Eisler, and M. G. Bawendi, *Science*, **290**, 314 (2000).
- [93] X. Li et al., *Science*, **301**, 809 (2003).
- [94] D. Abramavicius, D. V. Voronine, and S. Mukamel, *Proc. Natl. Acad. Sci. U.S.A.*, **105**, 8525 (2008).

- [95] M. Kirm et al., *Phys. Rev. B*, **79**, 233103 (2009).
- [96] S. Sukiasyan, C. McDonald, C. Destefani, M. Y. Ivanov, and T. Brabec, *Phys. Rev. Lett.*, **102**, 223002 (2009).
- [97] R. M. Stevenson, R. J. Young, P. Atkinson, K. Cooper, D. A. Ritchie, and A. J. Shields, *Nature*, **439**, 179 (2006).
- [98] S. Utsunomiya et al., *Nat. Phys.*, **4**, 700 (2008).
- [99] K. W. Stone, K. Gundogdu, D. B. Turner, X. Li, S. T. Cundiff, and K. A. Nelson, *Science*, **324**, 1169 (2009).
- [100] R. R. Ernst, G. Bodenhausen, and A. Wokaun, *Principles of Nuclear Magnetic Resonance in One and Two Dimensions*, Clarendon Press, Oxford, 1987.
- [101] C. Griesinger, O. Sorensen, and R. Ernst, *J. Mag. Res.*, **73**, 574 (1987).
- [102] C. Griesinger, O. Sorensen, and R. R. Ernst, *J. Am. Chem. Soc.*, **109**, 7227 (1987).
- [103] H. Oschkinat, C. Griesinger, P. J. Kraulis, O. W. Sørensen, R. R. Ernst, A. M. Gronenborn, and G. M. Clore, *Nature*, **332**, 374 (1988).
- [104] H. Oschkinat, C. Cieslar, T. Holak, G. Clore, and A. Gronenborn, *J. Mag. Res.*, **83**, 450 (1989).
- [105] R. M. Silverstein, F. X. Webster, and D. Kiemle, *Spectrometric Identification of Organic Compounds*, Wiley, 7th edition, 2005.
- [106] D. Keusters, H.-S. Tan, and W. S. Warren, *J. Phys. Chem. A*, **103**, 10369 (1999).
- [107] O. Golonzka, M. Khalil, N. Demirdöven, and A. Tokmakoff, *Phys. Rev. Lett.*, **86**, 2154 (2001).
- [108] M. T. Zanni and R. M. Hochstrasser, *Curr. Opin. Struct. Biol.*, **11**, 516 (2001).
- [109] N. Demirdöven, M. Khalil, and A. Tokmakoff, *Phys. Rev. Lett.*, **89**, 237401 (2002).
- [110] M. Khalil, N. Demirdöven, and A. Tokmakoff, *Phys. Rev. Lett.*, **90**, 047401 (2003).
- [111] E. C. Fulmer, F. Ding, P. Mukherjee, and M. T. Zanni, *Phys. Rev. Lett.*, **94**, 067402 (2005).
- [112] C. J. Fecko, J. D. Eaves, J. J. Loparo, A. Tokmakoff, and P. L. Geissler, *Science*, **301**, 1698 (2003).
- [113] J. D. Eaves, J. J. Loparo, C. J. Fecko, S. T. Roberts, A. Tokmakoff, and P. L. Geissler, *Proc. Natl. Acad. Sci. U.S.A.*, **120**, 13019 (2005).
- [114] S. T. Roberts, P. B. Petersen, K. Ramasesha, A. Tokmakoff, I. S. Ufimtsev, and T. J. Martinez, *Proc. Natl. Acad. Sci. U.S.A.*, **106**, 15154 (2009).
- [115] S. T. Roberts, K. Ramasesha, and A. Tokmakoff, *Acc. Chem. Res.*, **42**, 1239 (2009).
- [116] M. D. Fayer, *Ann. Rev. Phys. Chem.*, **60**, 21 (2009).
- [117] H. S. Chung, M. Khalil, A. W. Smith, Z. Ganim, and A. Tokmakoff, *Proc. Natl. Acad. Sci. U.S.A.*, **102**, 612 (2005).
- [118] P. Hamm, J. Helbing, and J. Bredenbeck, *Ann. Rev. Phys. Chem.*, **59**, 291 (2008).

- [119] Y. S. Kim and R. M. Hochstrasser, *J. Phys. Chem. B*, **113**, 8231 (2009).
- [120] W. Xiong, J. E. Laaser, P. Paoprasert, R. A. Franking, R. J. Hamers, P. Gopalan, and M. T. Zanni, *J. Am. Chem. Soc.*, **131**, 18040 (2009).
- [121] S.-H. Shim, R. Gupta, Y. L. Ling, D. B. Strasfeld, D. P. Raleigh, and M. T. Zanni, *Proc. Natl. Acad. Sci. U.S.A.*, **106**, 6614 (2009).
- [122] J. D. Hybl, A. W. Albrecht, S. M. Gallagher Faeder, and D. M. Jonas, *Chem. Phys. Lett.*, **297**, 307 (1998).
- [123] K. Okumura, A. Tokmakoff, and Y. Tanimura, *Chem. Phys. Lett.*, **314**, 488 (1999).
- [124] A. Tokmakoff, *J. Phys. Chem. A*, **104**, 4247 (2000).
- [125] J. D. Hybl, A. Albrecht Ferro, and D. M. Jonas, *J. Chem. Phys.*, **115**, 6606 (2001).
- [126] D. M. Jonas, *Ann. Rev. Phys. Chem.*, **54**, 425 (2003).
- [127] P. Tian, D. Keusters, Y. Suzaki, and W. S. Warren, *Science*, **300**, 1553 (2003).
- [128] T. Brixner, T. Mancal, I. V. Stiopkin, and G. R. Fleming, *J. Chem. Phys.*, **121**, 4221 (2004).
- [129] J. C. Vaughan, T. Hornung, K. W. Stone, and K. A. Nelson, *J. Phys. Chem. A*, **111**, 4873 (2007).
- [130] E. L. Read, G. S. Engel, T. R. Calhoun, T. Mancal, T. K. Ahn, R. E. Blankenship, and G. R. Fleming, *Proc. Natl. Acad. Sci. U.S.A.*, **104**, 14203 (2007).
- [131] J. A. Myers, K. L. M. Lewis, P. F. Tekavec, and J. P. Ogilvie, *Opt. Express*, **16**, 17420 (2008).
- [132] A. D. Bristow, D. Karaiskaj, X. Dai, and S. T. Cundiff, *Opt. Express*, **16**, 18017 (2008).
- [133] U. Selig, F. Langhojer, F. Dimler, T. Löhri, C. Schwarz, B. Gieseck, and T. Brixner, *Opt. Lett.*, **33**, 2851 (2008).
- [134] A. Nemeth, J. Sperling, J. Hauer, H. F. Kauffmann, and F. Milota, *Opt. Lett.*, **34**, 3301 (2009).
- [135] A. D. Bristow, D. Karaiskaj, X. Dai, T. Zhang, C. Carlsson, K. R. Hagen, R. Jimenez, and S. T. Cundiff, *Rev. Sci. Instrum.*, **80**, 073108 (2009).
- [136] P. F. Tekavec, J. A. Myers, K. L. M. Lewis, and J. P. Ogilvie, *Opt. Lett.*, **34**, 1390 (2009).
- [137] V. I. Prokhorenko, A. Halpin, and R. J. D. Miller, *Opt. Express*, **17**, 9764 (2009).
- [138] T. Zhang, C. Borca, X. Li, and S. Cundiff, *Opt. Express*, **13**, 7432 (2005).
- [139] X. Li, T. Zhang, C. N. Borca, and S. T. Cundiff, *Phys. Rev. Lett.*, **96**, 057406 (2006).
- [140] K. Gundogdu, K. W. Stone, D. B. Turner, and K. A. Nelson, *Chem. Phys.*, **341**, 89 (2007).
- [141] M. Erementchouk, M. N. Leuenberger, and L. J. Sham, *Phys. Rev. B*, **76**, 115307 (2007).
- [142] I. Kuznetsova, T. Meier, S. T. Cundiff, and P. Thomas, *Phys. Rev. B*, **76**, 153301 (2007).
- [143] T. Zhang, I. Kuznetsova, T. Meier, X. Li, R. P. Mirin, P. Thomas, and S. T. Cundiff, *Proc. Natl. Acad. Sci. U.S.A.*, **104**, 14227 (2007).

- [144] L. Yang, T. Zhang, A. D. Bristow, S. T. Cundiff, and S. Mukamel, *J. Chem. Phys.*, **129**, 234711 (2008).
- [145] D. B. Turner, K. W. Stone, K. Gundogdu, and K. A. Nelson, *J. Chem. Phys.*, **131**, 144510 (2009).
- [146] A. D. Bristow, D. Karaiskaj, X. Dai, R. P. Mirin, and S. T. Cundiff, *Phys. Rev. B*, **79**, 161305(R) (2009).
- [147] D. Karaiskaj, A. D. Bristow, L. Yang, X. Dai, R. P. Mirin, S. Mukamel, and S. T. Cundiff, *Phys. Rev. Lett.*, **104**, 117401 (2010).
- [148] K. W. Stone, D. B. Turner, K. Gundogdu, S. T. Cundiff, and K. A. Nelson, *Acc. Chem. Res.*, **42**, 1452 (2009).
- [149] S. Cundiff, T. Zhang, A. Bristow, D. Karaiskaj, and X. Dai, *Acc. Chem. Res.*, (2009).
- [150] D. B. Turner and K. A. Nelson, (*submitted*), (2010).
- [151] D. B. Turner, P. Wen, D. H. Arias, and K. A. Nelson, (*manuscript in preparation*), (2010).
- [152] D. B. Turner, P. Wen, D. H. Arias, and K. A. Nelson, (*manuscript in preparation*), (2010).
- [153] X. Li, T. Zhang, S. Mukamel, R. P. Mirin, and S. T. Cundiff, *Solid State Comm.*, **149**, 361 (2009).
- [154] E. Collini and G. D. Scholes, *Science*, **323**, 369 (2009).
- [155] E. Collini and G. D. Scholes, *J. Phys. Chem. A*, **113**, 4223 (2009).
- [156] J. Kim, S. Mukamel, and G. D. Scholes, *Acc. Chem. Res.*, **42**, 1375 (2009).
- [157] J. Kim, V. M. Huxter, C. Curutchet, and G. D. Scholes, *J. Phys. Chem. A*, **113**, 12122 (2009).
- [158] N. Christensson, F. Milota, A. Nemeth, J. Sperling, H. F. Kauffmann, T. Pullerits, and J. Hauer, *J. Phys. Chem. B*, (2009).
- [159] I. Stiopkin, T. Brixner, M. Yang, and G. R. Fleming, *J. Phys. Chem. B*, **110**, 20032 (2006).
- [160] A. Nemeth, F. Milota, J. Sperling, D. Abramavicius, S. Mukamel, and H. F. Kauffmann, *Chem. Phys. Lett.*, **469**, 130 (2009).
- [161] F. Milota, J. Sperling, A. Nemeth, D. Abramavicius, S. Mukamel, and H. F. Kauffmann, *J. Chem. Phys.*, **131**, 054510 (2009).
- [162] F. Milota, J. Sperling, A. Nemeth, T. Mancal, and H. F. Kauffmann, *Acc. Chem. Res.*, **42**, 1364 (2009).
- [163] J. M. Womick, S. A. Miller, and A. M. Moran, *J. Phys. Chem. B*, **113**, 6630 (2009).
- [164] T. Brixner, J. Stenger, H. M. Vaswani, M. Cho, R. E. Blankenship, and G. R. Fleming, *Nature*, **434**, 625 (2005).
- [165] G. S. Engel, T. R. Calhoun, E. L. Read, T.-K. Ahn, T. Mancal, Y.-C. Cheng, R. E. Blankenship, and G. R. Fleming, *Nature*, **446**, 782 (2007).
- [166] H. Lee, Y.-C. Cheng, and G. R. Fleming, *Science*, **316**, 1462 (2007).

- [167] J. M. Womick and A. M. Moran, *J. Phys. Chem. B*, **113**, 15771 (2009).
- [168] E. Collini, C. Y. Wong, K. E. Wilk, P. M. G. Curmi, P. Brumer, and G. D. Scholes, *Nature*, **463**, 644 (2010).
- [169] G. Panitchayangkoon, D. Hayes, K. A. Fransted, J. R. Caram, E. Harel, J. Wen, R. E. Blankenship, and G. S. Engel, *arXiv*, **1001.5108** (2010).
- [170] M. C. Hoffmann, J. Hebling, H. Y. Hwang, K.-L. Yeh, and K. A. Nelson, *J. Opt. Soc. Am. B*, **26**, A29 (2009).
- [171] M. C. Hoffmann, J. Hebling, H. Y. Hwang, K.-L. Yeh, and K. A. Nelson, *Phys. Rev. B*, **79**, 161201(R) (2009).
- [172] A. Rondi, J. Extermann, L. Bonacina, S. M. Weber, and J.-P. Wolf, *Appl. Phys. B*, **96**, 757 (2009).
- [173] S. Mukamel, D. Abramavicius, L. Yang, W. Zhuang, I. V. Schweigert, and D. V. Voronine, *Acc. Chem. Res.*, **42**, 553 (2009).
- [174] P. A. Franken, A. E. Hill, C. W. Peters, and G. Weinreich, *Phys. Rev. Lett.*, **7**, 118 (1961).
- [175] T. H. Maiman, *Nature*, **187**, 493 (1960).
- [176] K. J. Kubarych, C. J. Milne, S. Lin, V. Astinov, and R. J. D. Miller, *J. Chem. Phys.*, **116**, 2016 (2002).
- [177] R. W. Boyd, *Nonlinear Optics*, Academic Press, San Diego, CA, 2003.
- [178] Y. R. Shen, *The Principles of Nonlinear Optics*, Wiley, 2003.
- [179] C. Cohen-Tannoudji, B. Diu, and F. Laloë, *Quantum Mechanics*, Wiley, New York, 2005.
- [180] S. T. Cundiff, A. Knorr, J. Feldmann, S. W. Koch, E. O. Göbel, and H. Nickel, *Phys. Rev. Lett.*, **73**, 1178 (1994).
- [181] S. Mukamel, *Annu. Rev. Phys. Chem.*, **41**, 647 (1990).
- [182] S. Mukamel, *Annu. Rev. Phys. Chem.*, **51**, 691 (2000).
- [183] A. Tokmakoff, (5.74) time-dependent quantum mechanics and spectroscopy, (MIT OpenCourseWare: Massachusetts Institute of Technology) License: Creative commons BY-NC-SA <http://www.mit.edu/~tokmakof/TDQMS/>, 2010.
- [184] P. Hamm, Principles of nonlinear optical spectroscopy: A practical approach, <http://www.mitr.p.lodz.pl/evu/lectures/Hamm.pdf>, 2010.
- [185] M. Khalil, N. Demirdöven, and A. Tokmakoff, *J. Chem. Phys.*, **121**, 362 (2004).
- [186] D. A. Blank, L. J. Kaufman, and G. R. Fleming, *J. Chem. Phys.*, **113**, 771 (2000).
- [187] V. Astinov, K. J. Kubarych, C. J. Milne, and R. J. D. Miller, *Opt. Lett.*, **25**, 853 (2000).
- [188] L. J. Kaufman, D. A. Blank, and G. R. Fleming, *J. Chem. Phys.*, **114**, 2312 (2001).
- [189] L. J. Kaufman, J. Heo, L. D. Ziegler, and G. R. Fleming, *Phys. Rev. Lett.*, **88**, 207402 (2002).
- [190] K. J. Kubarych, C. J. Milne, S. Lin, and R. J. D. Miller, *Appl. Phys. B*, **74**, S107 (2002).

- [191] K. J. Kubarych, C. J. Milne, and R. J. D. Miller, *Chem. Phys. Lett.*, **369**, 635 (2003).
- [192] C. J. Milne, Y. L. Li, T. I. C. Jansen, L. Huang, and R. J. D. Miller, *J. Phys. Chem. B*, **110**, 19867 (2006).
- [193] P. R. Poulin and K. A. Nelson, *Science*, **313** (2006).
- [194] D. F. Underwood and D. A. Blank, *J. Phys. Chem. A*, **107**, 956 (2003).
- [195] P. Kukura, D. W. McCamant, and R. A. Mathies, *Ann. Rev. Phys. Chem.*, **58** (2007).
- [196] G. C. Schatz and M. A. Ratner, *Quantum Mechanics in Chemistry*, Dover Publications, Inc., Mineola, New York, 2002.
- [197] H. Haug and S. W. Koch, *Quantum Theory of the Optical and Electronic Properties of Semiconductors*, World Scientific, New Jersey, 2009.
- [198] T. Meier, P. Thomas, and S. Koch, *Coherent Semiconductor Optics: From Basic Concepts to Nanostructure Applications*, Springer-Verlag, Berlin, 2007.
- [199] Lindberg, Binder, and Koch, *Phys. Rev. A*, **45**, 1865 (1992).
- [200] V. M. Axt and A. Stahl, *Zeit. für Phys. B*, **93**, 195 (1994).
- [201] V. M. Axt and A. Stahl, *Zeit. für Phys. B*, **93**, 205 (1994).
- [202] M. Lindberg, Y. Hu, R. Binder, and S. W. Koch, *Phys. Rev. B*, **50**, 18060 (1994).
- [203] H. P. Wagner, A. Schätz, W. Langbein, J. M. Hvam, and A. Smirl, *Phys. Rev. B*, **60**, 4454 (1999).
- [204] J. A. Leegwater and S. Mukamel, *Phys. Rev. A*, **46**, 452 (1992).
- [205] V. Chernyak, N. Wang, and S. Mukamel, *Physical Reports*, **263**, 213 (1995).
- [206] V. M. Axt and S. Mukamel, *Rev. Mod. Phys.*, **70**, 145 (1998).
- [207] V. Chernyak, W. M. Zhang, and S. Mukamel, *J. Chem. Phys.*, **109**, 9587 (1998).
- [208] S. Mukamel and D. Abramavicius, *Chem. Rev.*, **104**, 2073 (2004).
- [209] I. Kuznetsova, P. Thomas, T. Meier, T. Zhang, X. Li, R. P. Mirin, and S. T. Cundiff, *Solid State Comm.*, **142**, 154 (2007).
- [210] L. Yang, I. V. Schweigert, S. T. Cundiff, and S. Mukamel, *Phys. Rev. B*, **75**, 125302 (2007).
- [211] L. Yang and S. Mukamel, *Phys. Rev. B*, **77**, 075335 (2008).
- [212] K. Victor, V. M. Axt, G. Bartels, A. Stahl, K. Bott, and P. Thomas, *Zeit. für Phys. B*, **99**, 197 (1996).
- [213] S. Schumacher, N. H. Kwong, R. Binder, and A. Smirl, *phys. stat. sol. (b)*, **246**, 307 (2009).
- [214] J. A. Davis et al., *Appl. Phys. Lett.*, **89**, 182109 (2006).
- [215] K. Hazu et al., *Phys. Rev. B*, **68**, 033205 (2003).
- [216] T. Kuroda, K. Inoue, R. Kuribayashi, F. Minami, A. Mysyrowicz, and I. Suemune, *J. Lumin.*, **66-67**, 429 (1996).

- [217] K. Miyajima, M. Ashida, and T. Itoh, *J. Phys.: Condens. Matter*, **19**, 445006 (2007).
- [218] A. Y. Cho and J. R. Arthur, *Prog. Solid-State Chem.*, **10**, 157 (1975).
- [219] R. N. Hall, G. E. Fenner, J. D. Kingsley, T. J. Soltys, and R. O. Carlson, *Phys. Rev. Lett.*, **9**, 366 (1962).
- [220] S. Adachi, *J. Appl. Phys.*, **58**, R1 (1985).
- [221] J. Singh, *Physics of Semiconductors and their Heterostructures*, McGraw-Hill, Inc., New York, 1992.
- [222] M. H. Degani and O. Hipólito, *Semicond. Sci. Technol.*, **2**, 578 (1987).
- [223] M. Dantus, M. J. Rosker, and A. H. Zewail, *J. Chem. Phys.*, **87**, 2395 (1987).
- [224] M. J. Rosker, M. Dantus, and A. H. Zewail, *Science*, **241**, 1200 (1988).
- [225] A. Sinha, M. C. Hsiao, and F. F. Crim, *J. Chem. Phys.*, **92**, 6333 (1990).
- [226] A. Sinha, M. C. Hsiao, and F. F. Crim, *J. Chem. Phys.*, **94**, 4928 (1991).
- [227] A. Sinha, J. D. Thoemke, and F. F. Crim, *J. Chem. Phys.*, **96**, 372 (1992).
- [228] M. J. Bronikowski, W. R. Simpson, B. Girard, and R. N. Zare, *J. Chem. Phys.*, **95**, 8647 (1991).
- [229] F. F. Crim, *Ann. Rev. Phys. Chem.*, **44**, 397 (1993).
- [230] R. J. Gordon and S. A. Rice, *Ann. Rev. Phys. Chem.*, **48**, 601 (1997).
- [231] R. N. Zare, *Science*, **279**, 1875 (1998).
- [232] R. J. Gordon, L. Zhu, and T. Seideman, *Acc. Chem. Res.*, **32**, 1007 (1999).
- [233] M. Shapiro and P. Brumer, *Principles of the Quantum Control of Molecular Processes*, Wiley, New York, 2003.
- [234] A. Assion, T. Baumert, M. Bergt, T. Brixner, B. Kiefer, V. Seyfried, M. Strehle, and G. Gerber, *Science*, **282**, 919 (1998).
- [235] J. L. Herek, W. Wohlleben, R. J. Cogdell, D. Zeidler, and M. Motzkus, *Nature*, **417**, 533 (2002).
- [236] T. Feurer, J. C. Vaughan, and K. A. Nelson, *Science*, **299**, 374 (2003).
- [237] S.-H. Shim, D. B. Strasfeld, Y. L. Ling, and M. T. Zanni, *Proc. Natl. Acad. Sci. U.S.A.*, **104**, 14197 (2007).
- [238] D. B. Strasfeld, S.-H. Shim, and M. T. Zanni, *Phys. Rev. Lett.*, **99**, 038102 (2007).
- [239] D. B. Strasfeld, Y. L. Ling, S.-H. Shim, and M. T. Zanni, *J. Am. Chem. Soc.*, **130**, 6698 (2008).
- [240] S.-H. Shim and M. T. Zanni, *Phys. Chem. Chem. Phys.*, **11**, 748 (2009).
- [241] D. B. Strasfeld, S.-H. Shim, and M. T. Zanni, *Adv. Chem. Phys.*, **141**, 1 (2009).
- [242] C. T. Middleton, D. B. Strasfeld, and M. T. Zanni, *Opt. Express*, **17**, 14526 (2009).

- [243] H. Itoh, T. Urakami, S.-i. Aoshima, and Y. Tsuchiya, *Proceedings of the APLS 2002, The Third Asian Pacific Laser Symposium*, , 542 (2003).
- [244] J. C. Vaughan, T. Hornung, T. Feurer, and K. A. Nelson, *Opt. Lett.*, **30**, 323 (2005).
- [245] T. Hornung, J. C. Vaughan, T. Feurer, and K. A. Nelson, *Opt. Lett.*, **29**, 2052 (2004).
- [246] A. A. Maznev, T. F. Crimmins, and K. A. Nelson, *Opt. Lett.*, **23**, 1378 (1998).
- [247] A. M. Weiner, *Rev. Sci. Instrum.*, **71**, 1929 (2000).
- [248] J. A. Rogers and K. A. Nelson, *Physica B*, **219-220**, 562 (1996).
- [249] G. D. Goodno, G. Dadusc, and R. J. D. Miller, *J. Opt. Soc. Am. B*, **15**, 1791 (1998).
- [250] M. M. Wefers and K. A. Nelson, *J. Opt. Soc. Am. B*, **12**, 1343 (1995).
- [251] A. Präkelt, M. Wollenhaupt, A. Assion, C. Horn, C. Sarpe-Tudoran, M. Winter, and T. Baumert, *Rev. Sci. Instrum.*, **74**, 4950 (2003).
- [252] A. M. Weiner, D. E. Leaird, G. P. Wiederrecht, and K. A. Nelson, *Science*, **247**, 1317 (1990).
- [253] D. Meshulach and Y. Silberberg, *Nature*, **396** (1998).
- [254] N. Dudovich, B. Dayan, S. M. Gallagher Faeder, and Y. Silberberg, *Phys. Rev. Lett.*, **86**, 47 (2001).
- [255] N. Dudovich, D. Oron, and Y. Silberberg, *Phys. Rev. Lett.*, **92**, 103003 (2004).
- [256] C.-B. Huang, Z. Jiang, D. E. Leaird, J. Caraquitena, and A. M. Weiner, *Laser and Photon. Rev.*, **2**, 227 (2008).
- [257] J. C. Vaughan, T. Feurer, K. Stone, and K. Nelson, *Opt. Express*, **14**, 1314 (2006).
- [258] M. M. Wefers, K. A. Nelson, and A. M. Weiner, *Opt. Lett.*, **21**, 746 (1996).
- [259] J. C. Vaughan, T. Feurer, and K. A. Nelson, *J. Opt. Soc. Am. B*, **19**, 2489 (2002).
- [260] A. W. Albrecht, J. D. Hybl, S. M. Gallagher Faeder, and D. M. Jonas, *J. Chem. Phys.*, **111**, 10934 (1999).
- [261] J. C. Vaughan, *Two-Dimensional Ultrafast Pulse Shaping and its Application to Coherent Control and Spectroscopy*, PhD thesis, Massachusetts Institute of Technology, 2005.
- [262] B. Xu, J. M. Gunn, J. M. Dela Cruz, V. V. Lozovoy, and M. Dantus, *J. Opt. Soc. Am. B*, **23**, 750 (2006).
- [263] R. Trebino, *Frequency-Resolved Optical Gating: The Measurement of Ultrashort Laser Pulses*, Springer, 2002.
- [264] E. H. G. Backus, S. Garrett-Roe, and P. Hamm, *Opt. Lett.*, **33**, 2665 (2008).
- [265] L. Lepetit, G. Cheriaux, and M. Joffre, *J. Opt. Soc. Am. B*, **12**, 2467 (1995).
- [266] C. Dorrer, *J. Opt. Soc. Am. B*, **16**, 1160 (1999).
- [267] C. Dorrer, N. Belabus, J.-P. Likforman, and M. Joffre, *J. Opt. Soc. Am. B*, **17**, 1795 (2000).
- [268] C. Dorrer, *Opt. Lett.*, **24**, 1532 (1999).

- [269] M. H. Levitt, P. K. Madhu, and C. E. Hughes, *J. Mag. Res.*, **155**, 300 (2002).
- [270] D. M. Jonas, S. A. Diddams, J. K. Ranka, A. Stentz, R. S. Windeler, J. L. Hall, and S. T. Cundiff, *Science*, **288**, 635 (2000).
- [271] M. D. Sturge, *Phys. Rev.*, **127**, 768 (1962).
- [272] H. Mayer, U. Rössler, and M. Ruff, *Phys. Rev. B*, **47**, 12929 (1993).
- [273] K. W. Stone, *Coherent multi-exciton dynamics in semiconductor nanostructures via two-dimensional Fourier Transform optical spectroscopy*, PhD thesis, Massachusetts Institute of Technology, 2009.
- [274] K. A. Nelson and M. D. Fayer, *J. Chem. Phys.*, **72**, 5202 (1980).
- [275] K. A. Nelson, R. Caselegno, R. J. D. Miller, and M. D. Fayer, *J. Chem. Phys.*, **77**, 1144 (1982).
- [276] M. D. Fayer, *Ann. Rev. Phys. Chem.*, **33**, 63 (1982).
- [277] V. M. Huxter and G. D. Scholes, *J. Chem. Phys.*, **125**, 144716 (2006).
- [278] J. M. Anna, M. J. Nee, C. R. Baiz, R. McCanne, and K. J. Kubarych, *J. Opt. Soc. Am. B*, **27** (2010).
- [279] K. Nagayama, P. Bachmann, K. Wuetrich, and R. R. Ernst, *J. Mag. Res.*, **31**, 133 (1978).
- [280] L. P. Deflores, R. A. Nicodemus, and A. Tokmakoff, *Opt. Lett.*, **32**, 2966 (2007).
- [281] A. Miller, M. Ebrahimzadeh, and D. M. Finlayson, editors, *Semiconductor quantum optoelectronics: from quantum physics to smart devices : Proceedings of the Fiftieth Scottish Universities Summer School in Physics, St. Andrews, June 1998*, Bristol and Philadelphia, 1999, Taylor and Francis US.
- [282] J. T. Fourkas, R. Trebino, and M. D. Fayer, *J. Chem. Phys.*, **97**, 69 (1992).
- [283] K. B. Ferrio and D. G. Steel, *Phys. Rev. Lett.*, **80**, 786 (1998).
- [284] E. C. Fulmer, P. Mukherjee, A. T. Krummel, and M. T. Zanni, *J. Chem. Phys.*, **120**, 8067 (2004).
- [285] L. Yang and S. Mukamel, *Phys. Rev. Lett.*, **100**, 057402 (2008).
- [286] T. Östreich, *Phys. Rev. B*, **64**, 245203 (2001).
- [287] W. Langbein, T. Meier, S. W. Koch, and J. M. Hvam, *J. Opt. Soc. Am. B*, **18**, 1318 (2001).
- [288] T. Meier, S. W. Koch, P. Brick, C. Ell, G. Khitrova, and H. M. Gibbs, *Phys. Rev. B*, **62**, 4218 (2000).
- [289] V. I. Klimov, A. A. Mikhailovsky, D. W. McBranch, C. A. Leatherdale, and M. G. Bawendi, *Science*, **287**, 1011 (2000).
- [290] H. G. Breuning, T. Voss, I. Ruckmann, J. Gutowski, V. M. Axt, and T. Kuhn, *J. Opt. Soc. Am. B*, **20**, 1769 (2003).
- [291] S. R. Bolton, U. Neukirch, L. J. Sham, and D. S. Chemla, *Phys. Rev. Lett.*, **85**, 2002 (2000).

- [292] V. M. Axt, S. R. Bolton, U. Neukirch, L. J. Sham, and D. S. Chemla, *Phys. Rev. B*, **63**, 115303 (2001).
- [293] T. Meier, C. Sieh, E. Finger, W. Stolz, W. W. Rühle, P. Thomas, S. W. Koch, and A. D. Wieck, *phys. stat. sol. (b)*, **238**, 537 (2003).
- [294] J. A. Wheeler, *Geons, Black Holes, And Quantum Foam: A Life in Physics*, Norton and Company, 1998.
- [295] J. Gribbin, *The Scientists: A History of Science Told Through the Lives of Its Greatest Inventors*, Random House Trade Paperbacks, 2004.
- [296] A. Einstein, B. Podolsky, and N. Rosen, *Phys. Rev.*, **47**, 777 (1935).
- [297] N. Bohr, *Phys. Rev.*, **48**, 696 (1935).
- [298] E. Schrödinger, *Proc. Cambridge Phil. Soc.*, **31**, 555 (1935).
- [299] A. Aczel, *Entanglement*, Plume, 2003.
- [300] Z. I. Alferov, The double heterostructure: Concept and its application in physics, electronics and technology, in *Nobel Lecture*, 2000.
- [301] T. Voss, I. Rückmann, J. Gutowski, V. M. Axt, and T. Kuhn, *Phys. Rev. B*, **73**, 115311 (2006).
- [302] T. S. Humble and J. A. Cina, *J. Phys. Chem. B*, **110**, 18879 (2006).
- [303] P. Kner, S. Bar-Ad, M. B. Marquezini, D. S. Chemla, and W. Schäfer, *Phys. Rev. Lett.*, **78**, 1319 (1997).
- [304] N. A. Fromer, C. Schüller, D. S. Chemla, T. V. Shahbazyan, I. E. Perakis, K. Maranowski, and A. C. Gossard, *Phys. Rev. Lett.*, **83**, 4646 (1999).
- [305] K. M. Dani, J. Tignon, M. Breit, D. S. Chemla, E. G. Kavousanaki, and I. E. Perakis, *Phys. Rev. Lett.*, **97**, 057401 (2006).
- [306] J. R. Danielson, Y.-S. Lee, J. P. Prineas, J. T. Steiner, M. Kira, and S. W. Koch, *Phys. Rev. Lett.*, **99**, 237401 (2007).
- [307] S. Wilson, *Electron Correlation in Molecules*, Clarendon Press, Oxford, 1984.
- [308] P. G. Savvidis, J. J. Baumberg, R. M. Stevenson, M. S. Skolnick, D. M. Whittaker, and J. S. Roberts, *Phys. Rev. Lett.*, **84**, 1547 (2000).
- [309] A. Huynh, J. Tignon, O. Larsson, P. Roussignol, C. Delalande, R. André, R. Romestain, and L. S. Dang, *Phys. Rev. Lett.*, **90**, 106401 (2003).
- [310] S. Kundermann, M. Saba, C. Ciuti, T. Guillet, U. Oesterle, J. L. Staehli, and B. Deveaud, *Phys. Rev. Lett.*, **91**, 107402 (2003).
- [311] J. Keeling, F. M. Marchetti, M. H. Szymanska, and P. B. Littlewood, *Semicond. Sci. Technol.*, **22**, R1 (2007).
- [312] J. R. Tischler, M. S. Bradley, Q. Zhang, T. Atay, A. Nurmikko, and V. Bulović, *Organic Electronics*, **8**, 94 (2007).

- [313] J. Wenus, S. Ceccarelli, D. G. Lidzey, A. I. Tolmachev, J. L. Slominskii, and J. L. Bricks, *Organic Electronics*, **8**, 120 (2007).
- [314] M. S. Bradley, J. R. Tischler, Y. Shirasaki, and V. Bulović, *Phys. Rev. B*, **78**, 193305 (2008).
- [315] S. L. Sewall, R. R. Cooney, K. E. H. Anderson, E. A. Dias, D. M. Sagar, and P. Kambhampati, *J. Chem. Phys.*, **129**, 084701 (2008).
- [316] S. L. Sewall, A. Franceschetti, R. R. Cooney, A. Zunger, and P. Kambhampati, *Phys. Rev. B*, **80**, 081310(R) (2009).
- [317] B. J. Walker, G. P. Nair, L. F. Marshall, V. Bulović, and M. G. Bawendi, *J. Am. Chem. Soc.*, **131**, 9624 (2009).
- [318] J. E. Halpert, J. R. Tischler, G. P. Nair, B. J. Walker, W. Liu, V. Bulović, and M. G. Bawendi, *J. Phys. Chem. C*, **113**, 9986 (2009).
- [319] A. Buchleitner, C. Viviescas, and M. Tiersch, editors, *Entanglement and Decoherence: Foundations and Modern Trends*, volume 768 of *Lecture Notes in Physics*, Springer-Verlag, 2009.
- [320] M. P. A. Branderhorst, P. Londero, W. Piotr, C. Brif, R. L. Kosut, H. Rabitz, and I. A. Walmsley, *Science*, **320**, 638 (2008).
- [321] G. D. Scholes, *J. Phys. Chem. Lett.*, **1**, 2 (2010).
- [322] M. Sarovar, A. Ishizaki, G. R. Fleming, and K. B. Whaley, *Nature Physics (accepted)*, (2010).
- [323] V. Boyer, A. M. Marino, R. C. Pooser, and P. D. Lett, *Science*, **321**, 544 (2008).
- [324] O. Roslyak and S. Mukamel, *Phys. Rev. A*, **79**, 063409 (2009).
- [325] O. Roslyak, C. A. Marx, and S. Mukamel, *Phys. Rev. A*, **79**, 033832 (2009).
- [326] D. J. Ulness, J. C. Kirkwood, and A. C. Albrecht, *J. Chem. Phys.*, **108**, 3897 (1998).
- [327] K. C. Wilson, B. Lyons, R. Mehlenbacher, R. Sabatini, and D. W. McCamant, *J. Chem. Phys.*, **131**, 244512 (2009).
- [328] R. Mehlenbacher, B. Lyons, K. C. Wilson, Y. Du, and D. W. McCamant, *J. Chem. Phys.*, **131**, 214502 (2009).
- [329] M. Cho, D. A. Blank, J. Sung, K. Park, S. Hahn, and G. R. Fleming, *J. Chem. Phys.*, **112**, 2082 (2000).
- [330] O. Golonzka, N. Demirdöven, M. Khalil, and A. Tokmakoff, *J. Chem. Phys.*, **113**, 9893 (2000).
- [331] S. Garrett-Roe and P. Hamm, *J. Chem. Phys.*, **130**, 164510 (2009).

Curriculum Vitae

Daniel B. Turner

Massachusetts Institute of Technology, Department of Chemistry, Room 6-026
77 Massachusetts Avenue, Cambridge MA 02139, USA

Phone: +1 617 253 1956

Email: dbt@mit.edu

Education

2010 Ph.D. Physical Chemistry, Massachusetts Institute of Technology, Cambridge MA (4.8/5.0 GPA)
2004 B.A. Mathematics & B.A. Chemistry, Concordia College, Moorhead MN (3.9/4.0 GPA)

Professional and Academic Experience

2005 – present Graduate Research and Teaching Assistant, Department of Chemistry, **Massachusetts Institute of Technology**, Cambridge MA
Advisor: Prof. Keith A. Nelson
2004 – 2005 Advanced Process Development Engineering, **Hutchinson Technology Inc.**, Hutchinson MN
Managers: Mr. Steve Young & Dr. Robert Henry
2003 (summer) REU Student, Chemistry Department, **Cornell University**, Ithaca NY
Advisor: Prof. John A. Marohn
2002 (summer) REU Student, Chemistry Department, **University of Minnesota**, Minneapolis MN
Advisor: Prof. David A. Blank
2000 – 2004 Undergraduate Student, Chemistry Department, **Concordia College**, Moorhead MN
Advisor: Prof. Darin J. Ulness

Honors

2005 National Science Foundation Graduate Research Fellowship
2005 National Defense Science and Engineering Graduate Fellowship
2003 Barry M. Goldwater Scholarship

Publications

2010 **10. Two-dimensional correlation spectra of excitons in GaAs quantum wells**
D. B. Turner, P. Wen, D. H. Arias, and K. A. Nelson *manuscript in preparation*
9. The COLBERT spectrometer: Coherent multidimensional spectroscopy made easier
D. B. Turner, K. W. Stone, K. Gundogdu, and K. A. Nelson *manuscript in preparation*
8. Coherent two-exciton dynamics measured using fifth-order COLBERT spectroscopy
D. B. Turner, P. Wen, D. H. Arias, and K. A. Nelson *manuscript in preparation*
7. Coherent spectroscopic measurements of high-order electronic correlations in quantum wells
D. B. Turner and K. A. Nelson *submitted*

2009 **6. Three-dimensional electronic spectroscopy of excitons in GaAs quantum wells**
D. B. Turner, K. W. Stone, K. Gundogdu, and K. A. Nelson
Journal of Chemical Physics **131**, 144510 (2009)
Selected as a *JCP Editors' Choice* paper for 2009
Highlighted in: Physics Today, 17–20, November 2009
5. Exciton-exciton correlations revealed by two-quantum, two-dimensional Fourier transform optical spectroscopy
K. W. Stone, D. B. Turner, K. Gundogdu, S. T. Cundiff, and K. A. Nelson
Accounts of Chemical Research **42**, 1452 (2009)
4. Two-quantum 2D FT electronic spectroscopy of biexcitons in GaAs quantum wells
K. W. Stone, K. Gundogdu, D. B. Turner, X. Li, S. T. Cundiff, and K. A. Nelson
Science **324**, 1169 (2009)

2007 **3. Multidimensional coherent spectroscopy made easy**
K. Gundogdu, K. W. Stone, D. B. Turner, and K. A. Nelson
Chemical Physics **341**, 89–94 (2007)

2003 **2. Factorized time correlation diagram analysis of Raman induced Kerr effect spectroscopy using noisy light**
D. B. Turner, and D. J. Ulness
Journal of Chemical Physics **119**, 10745 (2003)

2002 **1. Factorized time correlation diagram analysis of paired causal systems excited by twin stochastic driving functions**
D. P. Biebighauser, D. B. Turner, and D. J. Ulness
Physical Review E **65**, 026142 (2002)